CHEMICAL COMPOSITION AND ORIGIN OF AEROSOL PARTICLES INVOLVED IN SUMMERTIME ARCTIC CLOUD PROCESSES

Dissertation
zur Erlangung des Grades
'Doctor rerum naturalium (Dr. rer. nat.)' der Fachbereiche:

08: Physik, Mathematik und Informatik
09: Chemie, Pharmazie und Geowissenschaften
10: Biologie,
Unimedizin

Max Planck Graduate Center
mit der Johannes Gutenberg-Universität Mainz

angefertigt am Max-Planck-Institut für Chemie

Oliver Eppers

geboren in Trier

Mainz, 9. September 2021

1. Berichterstatter: Prof. Dr. Peter Hoor
2. Berichterstatter: PD Dr. Johannes Schneider

Tag der mündlichen Prüfung: 9. November 2021

ABSTRACT

The Arctic climate is warming rapidly compared to other regions of the globe with drastic implications for its environment (e.g. sea ice loss). Aerosol particles are an important factor for the energy budget in this polar region as they interact directly or indirectly via cloud formation and processing with solar and terrestrial radiation. However, the interaction between aerosol and clouds in the Arctic is still not fully understood. This study focuses on the occurrence of different aerosol species and their influence on cloud processes in the summertime Arctic. Airborne in-situ measurements of particle composition were conducted in the European Arctic using the single particle mass spectrometer ALABAMA. Ambient aerosol particles and cloud particle residues in the diameter range between 250 nm and 1.6 μm were chemically analyzed. More than 240000 single particle mass spectra were obtained in total during the flights, almost 45000 of them from cloud residuals sampled in clouds. Different particle types were identified by detection of characteristic ion signal markers. This chemical particle analysis was complemented by further measurements of aerosol and cloud properties, trace gases as well as air mass history simulations.

This study has found that Arctic cloud residual composition was dominated by triethyl- and/or diethylamine, which were observed for the first time in Arctic aerosol particles. In addition to amines, also sea spray, dicarboxylic acids, nitrate, iodine and elemental carbon were enriched inside the cloud residuals. In contrast, particles in ambient air contained mainly trimethylamine and sea spray inside the boundary layer and ammonium sulfate in the free troposphere. Only little contribution of triethyl- and/or diethylamine to particle composition in ambient air was observed, suggesting these amines were taken up by the cloud droplets from the gas-phase. This hypothesis was further supported by the observed correlation between the ethylated amine fraction and cloud liquid water content indicating their high solubility. Outside the Arctic, a significant contribution of these amines was found in clouds at mid-latitudes as well, suggesting a general importance of amines for cloud processes. Moreover, the cloud residual composition of clouds, which were thermodynamically decoupled from the surface, showed similarities to above-cloud particle composition. Thus, the thermodynamic structure of the clouds seems to play a critical role for the contribution of surface-related aerosol species to Arctic clouds.

ZUSAMMENFASSUNG

Das arktische Klima zeigt eine rapide Erwärmung im Vergleich zu anderen Regionen der Erde, mit drastischen Folgen für ihre Umgebung (z.B. Verlust der Meereisbedeckung). Aerosolpartikel stellen einen wichtigen Faktor für die Energiebilanz dieser polaren Region dar, da sie sowohl direkt als auch indirekt über die Bildung und Beeinflussung von Wolken mit solarer und terrestrischer Strahlung wechselwirken. Die Wechselwirkung zwischen Aerosolpartikel und Wolken in der Arktis ist jedoch noch immer nicht vollständig verstanden. Der Schwerpunkt dieser Arbeit liegt auf dem Vorkommen verschiedener Aerosolspezies und ihren Einfluss auf Wolkenprozesse im arktischen Sommer. Dazu wurden flugzeuggetragene in-situ Messungen der chemischen Zusammensetzung von Aerosolpartikeln in der europäischen Arktis unter Verwendung des Einzelpartikel-Massenspektrometers ALABAMA durchgeführt. Umgebungsaerosol und Wolkenpartikel-Residuen mit Durchmessern zwischen 250 nm und 1.6 μm wurden chemisch analysiert. Insgesamt wurden dabei über 240000 Massenspektren aufgezeichnet, fast 45000 davon innerhalb von Wolken als Residuen von Wolkenpartikeln. Verschiedene Partikeltypen wurden über das Vorhandensein charakteristischer Ionen-Markersignale identifiziert. Diese chemische Partikelanalyse wurde unterstützt durch Messungen der Eigenschaften von Aerosol- und Wolkenpartikel, Spurengasmessungen sowie Simulationen der Luftmassenhistorie.

Diese Arbeit konnte zeigen, dass die Zusammensetzung arktischer Wolkenresiduen von Triethyl- und/oder Diethylamin dominiert wurden, die erstmals in arktischen Aerosolpartikel beobachtet werden konnten. Neben Aminen wurden auch Seesalz, Dicarboxylsäuren, Nitrat, iodhaltige Verbindungen und elementarer Kohlenstoff verstärkt in Wolkenresiduen gefunden. Im Gegensatz dazu bestanden die Partikel außerhalb von Wolken innerhalb der atmosphärischen Grenzschicht hauptsächlich aus Trimethylamin und Seesalz, oberhalb der Grenzschicht aus Ammoniumsulfat. Der Beitrag von Triethyl- bzw. Diethylamin außerhalb von Wolken war allerdings gering, sodass der Eintrag zu Wolken vermutlich über die Gasphase abläuft. Diese Hypothese wurde durch eine beobachtete Korrelation zwischen dem Anteil des ethylartigen Amins und dem Wolken-Flüssigwassergehalt unterstützt, was für die gute Löslichkeit dieser Substanz spricht. Ein signifikanter Beitrag dieser Amine konnte auch außerhalb der Arktis in Wolken in mittleren Breiten gefunden werden, was die allgemeine Bedeutung der Amine für Wolkenprozesse hervorhebt. Des Weiteren zeigte

die Zusammensetzung der Residualpartikel aus Wolken, die thermodynamisch entkoppelt vom Boden waren, Ähnlichkeiten zur Aerosolzusammensetzung oberhalb der Wolke aufwiesen. Daher spielt die thermodynamische Struktur der Wolken vermutlich eine wichtige Rolle für den Beitrag von Partikeln aus bodennahen Quellen für die Entstehung und die Eigenschaften von arktischen Wolken.

CONTENTS

1

INTRODUCTION

1.1 MOTIVATION

The Arctic region experiences drastic changes owing to global warming in recent decades (Jeffries et al., 2013). In fact, surface temperatures increased up to three times faster compared to the rest of the globe (Bindoff et al., 2014). This enhanced warming is known as *Arctic Amplification* (Serreze and Barry, 2011) and is associated with consequences also for other regions in mid-latitudes (Francis and Vavrus, 2012). A major driver for this regional enhanced trend is the so-called ice/snow-albedo feedback (Curry et al., 1995; Serreze and Barry, 2011). In more detail, the warming of the polar environment reduces the sea ice extent (Chapman and Walsh, 1993; Stroeve et al., 2012), which further lowers the reflectivity and, thus, more energy is absorbed by the surface and emitted to the surroundings (Curry et al., 1995; Serreze and Barry, 2011). On the other hand, also further feedback processes are involved in this amplified warming, including aerosol particles and clouds (Wendisch et al., 2017).

Globally, the net radiative effect of clouds is cooling (Raschke et al., 2016). In contrast, as the polar environment is characterized by highly reflective ice surfaces and low amounts of solar radiation, clouds mainly contribute to Arctic warming, in particular during the dark winter months (Intrieri et al., 2002; Shupe and Intrieri, 2004). However, model inter-comparison studies showed significant discrepancies in the calculated Arctic cloud feedback (Zelinka et al., 2013; Pithan and Mauritsen, 2014). One important reason for these uncertainties is the incomplete understanding of aerosol-cloud interaction (ACI) processes around the North Pole (Pithan and Mauritsen, 2014; Wendisch et al., 2017; Wendisch et al., 2019; Schmale et al., 2021).

In terms of Arctic aerosol particles, the research interest began with observations of long-range transported pollution to the polar region in the last century which was characterized as the chronic *Arctic haze* phenomenon occurring in spring (e.g. Megaw and Flyger, 1973; Radke and Hobbs, 1984; Rahn et al., 1977; Shaw, 1984; Schnell and Raatz, 1984). Therefore, mostly anthropogenic aerosol particles and their cloud effect were reviewed in the context of *Arctic Amplification* in early studies (Garrett et al., 2002).

In recent years, the research focus shifted towards local natural aerosol particles and precursors in the Arctic and their interaction with clouds (Willis et al., 2018; Schmale et al., 2021). During summer, when aerosol concentrations are generally low in the Arctic, the contribution of marine biogenic sources to atmospheric particulate matter becomes more important (Willis et al., 2017). Simultaneously, the occurrence of clouds in the Arctic environment is highest in summer (Mioche et al., 2015; Shupe et al., 2011). Under these conditions, small changes in the amount of cloud-active particles can have a significant impact on the cloud radiative effect (Mauritsen et al., 2011). With the ongoing decline in Arctic sea ice, precursor gases and particles with local marine origin will become even more relevant in the near future (Browse et al., 2014). However, the role of local marine particles for Arctic cloud processes is still highly uncertain (Willis et al., 2018).

One reason for these uncertainties is the sparsity of in-situ data of aerosol-cloud interaction in the Arctic (Schmale et al., 2021). Most of the previous field studies derived the effect of aerosol particles only indirectly using an instrumentation which is based on artificial activation of cloud particles (e.g. Bigg and Leck, 2001; Lance et al., 2011; Martin et al., 2011; Leck and Svensson, 2015; Burkart et al., 2017b). On the other hand, sampling of cloud residual particles after evaporation/sublimation of the water content allows for direct characterization of cloud-active aerosol. Nevertheless, very little in-situ data of cloud residuals exists in the Arctic to date (Zelenyuk et al., 2010; Karlsson et al., 2021). Therefore, the focus of the current thesis was the characterization of ambient aerosol and cloud residual particles in the summertime Arctic in order to improve the representation of aerosol-cloud interaction processes in climate models.

1.2 CURRENT KNOWLEDGE OF ARCTIC AEROSOL PARTICLES AND CLOUDS

Aerosol particles are an important factor for the *Arctic Amplification* phenomenon since they influence the Arctic surface radiative budgets directly and indirectly via ACI (Law and Stohl, 2007; Quinn et al., 2008; Shindell and Faluvegi, 2009; Najafi et al., 2015; Acosta Navarro et al., 2016). The net direct effect of Arctic aerosol has previously been regarded as cooling due to their scattering and absorption of incoming solar (shortwave) radiation (Quinn et al., 2008; Gagné et al., 2017). However, there are three direct aerosol-radiation processes which might contributed to recent Arctic warming. First, aerosol concentrations from pollution sources have decreased in the Arctic since the 1980s due to the reduction of primary particles and particle precursors emissions

(e.g. sulfur dioxide) in mid-latitudes (Gong et al., 2010; Breider et al., 2017). Thus, more solar energy reaches the Arctic surface due to a decreased aerosol optical depth. Second, the atmospheric warming effect of light-absorbing aerosol species, most notably black carbon (BC), is enhanced over highly reflective sea ice and snow surfaces (Law and Stohl, 2007; Quinn et al., 2008). Third, the deposition of absorbing particles on snow and ice lowers the surface albedo and thereby warms the lower troposphere (Flanner et al., 2007; Doherty et al., 2010; Hegg et al., 2010; Flanner, 2013). Considering the indirect effect of aerosol through cloud formation and altering, the net radiative impact is rather complex (Willis et al., 2018). However, measurements and modeling results indicate an overall warming effect of Arctic clouds throughout the year with the exception of the summer period (Intrieri et al., 2002; Shupe and Intrieri, 2004; Alterskjær et al., 2010; Döscher et al., 2014). Clearly, the presence of aerosol particles has a significant impact on the radiative balance and must be considered in the context of *Arctic Amplification*.

This section provides an overview of the current understanding of the physics, composition and origin of aerosol particles in the Arctic. Moreover, the peculiarity of Arctic mixed-phase clouds, the knowledge about cloud-interacting aerosols as well as the role of the thermodynamic structure on ACI are described within this section. Since the measurements in this study took place in May and June, the special focus of this section lies on aerosol characteristics during summer. The main processes controlling Arctic aerosol characteristics in the summertime marine lower troposphere are summarized in Fig. 1.1 and further explained in the following.

1.2.1 *Seasonality of Arctic aerosol properties*

Arctic aerosol particles are characterized by a strong seasonal cycle in their properties such as concentration, size and chemical composition (e.g. Shaw, 1995; Quinn et al., 2007; Engvall et al., 2008; Shaw et al., 2010; Sharma et al., 2013; Tunved et al., 2013; Breider et al., 2014; Asmi et al., 2016; Croft et al., 2016b; Nguyen et al., 2016; Freud et al., 2017; Lange et al., 2018; Leaitch et al., 2018). During late winter and early spring, aerosol mass concentrations reach their maximum and the particle sizes are dominated by the accumulation mode (Quinn et al., 2007; Freud et al., 2017). This phenomenon is often referred to as *Arctic Haze* (e.g. Clarke et al., 1984; Law and Stohl, 2007). Species like BC and sulfate, which are associated with long-range transport, dominate the composition of *Arctic Haze* (e.g. Barrie, 1986; Law and Stohl, 2007). In contrast, the summertime Arctic is characterized by low particle concentrations with

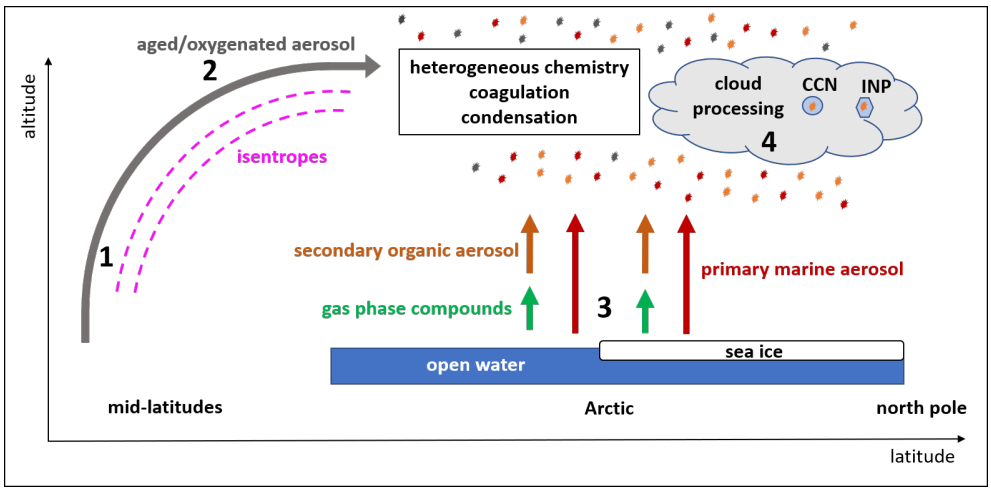

Figure 1.1: Schematic overview of the main processes controlling aerosol and cloud properties in the Arctic marine lower troposphere during summer. (1) Aerosol particles and precursor gases emitted by sources at lower latitudes are transported along isentropic surfaces (in the absence of diabatic processes) into the Arctic free troposphere. (2) The transported particles are aged due to different chemical and cloud processes occurring along this pathway (grey arrow). (3) Primary particles (red) and precursor gases (green) are emitted by open ocean surfaces as well as by melt ponds, leads and blowing snow. Secondary organic aerosol particles (orange) are formed via oxidation and heterogeneous reactions. (4) Once in the atmosphere, particles can further (photo-) oxidize, interact with each other via heterogeneous chemistry, coagulation and condensation, act as cloud condensation nuclei (CCN) or ice-nucleating particle (INP) to form clouds, or they can be altered through cloud processing.

main contributions from nucleation and Aitken mode particles (e.g. Croft et al., 2016b).

1.2.2 *Isentropic perspective and long-range transport*

One major driver of this seasonality is the transport of air masses from lower latitudes to the polar region (Klonecki et al., 2003). This northward transport can be described by applying the isentropic perspective (Carlson, 1981; Iversen, 1984). Due to surface cooling, the Arctic lower troposphere exhibits lower potential temperatures θ compared to the surrounding troposphere (Klonecki et al., 2003; Stohl, 2006). Thus, isolines of θ, the isentropes, form a dome-like structure over the Arctic which often is referred to as *Polar Dome* (Klonecki et al., 2003). In the absence of diabatic processes, air masses preferentially travel along isentropes (Iversen, 1984; Klonecki et al., 2003). Consequently, air parcels departing from regions with warmer potential temperatures θ compared to the

Arctic (e.g. from southern territories) will ascend along the sloping isentropes of the *Polar Dome* and will end up at higher vertical level in the polar region, whereas air of the Arctic boundary layer (BL) remains isolated inside this dome (see no. 1 in Fig. 1.1; Klonecki et al., 2003; Stohl, 2006; Law and Stohl, 2007; Bozem et al., 2019).

Following this isentropic concept, the seasonal variation of the *Polar Dome* provides an explanation for the seasonality in the properties of Arctic aerosol. In winter, parts of northern Eurasia are snow-covered and the polar front can extend much further south (as far as 40 °N; Barrie, 1986; Shaw, 1995; Law and Stohl, 2007). Therefore, pollution from these regions is emitted at low values of θ and is much more likely to reach the BL at northern latitudes (Carlson, 1981; Iversen, 1984). However, the summertime Arctic BL is much less affected by pollution transport from mid-latitudes for four reasons. First, the mean circulation patterns change with a transpolar route from Eurasia towards North America in winter to a circulation from the North Atlantic sector towards the Pacific Ocean in summer (Law and Stohl, 2007). Second, the Arctic front is located further north which excludes pollution sources from outside the Arctic for the *Polar Dome* (Klonecki et al., 2003; Stohl, 2006). Third, the reduced diabatic cooling and increased radiative heating in summer enhance the isolation of the Arctic lower troposphere (Klonecki et al., 2003; Stohl, 2006). Fourth, the transport efficiency of pollution particles is reduced due to significant wet removal of aerosol particles along the transport path (Browse et al., 2012; Croft et al., 2016b). As a consequence of these four mechanisms, the influence of long-range transport in summertime Arctic is restricted to the middle and upper troposphere, whereas the lower tropospheric Arctic air is more isolated from above compared to winter (Stohl, 2006; Schmale et al., 2011). Accordingly, the aerosol mass concentrations are low in the Arctic BL and local sources become more important in summer compared to winter because of the increased residence time inside the *Polar Dome* (Stohl, 2006; Schmale et al., 2011).

1.2.3 *Properties of particles from long-range transport*

The physicochemical properties of aerosol particles from long-range transport are characterized by chemical aging, cloud processing and wet removal along their pathway towards the Arctic (see no. 2 in Fig. 1.1). Aging of particles takes place due to oxidation of gas phase species resulting in lower-volatility products which either form secondary aerosol particles via new particle formation or condense on pre-existing particles (Kroll and Seinfeld, 2008; Croft et al., 2016b). Consequently, the particle size increases and the particle composition changes (Schmale et al., 2011; Croft et al., 2016b). Another aging process is

coagulation of particles which leads to larger particle sizes (Quennehen et al., 2012). In-cloud processing occurs via oxidation of dissolved gases like SO_2, organic species, ammonia or nitric acid. As a result, the released particle after droplet evaporation has grown and chemically changed due to the collection of non-volatile compounds compared to the pre-cloud particle (Croft et al., 2016b; Lange et al., 2018). In addition, interstitial coagulation with aerosol activated into cloud droplets increases particle sizes and, simultaneously, reduces the concentration of particles below ∼200 nm (Pierce et al., 2015; Croft et al., 2016b). Finally, wet scavenging of particles due to precipitation along their pathway towards the Arctic reduces the particle transport efficiency (Matsui et al., 2011a; Matsui et al., 2011b).

The chemical composition of aerosol particles transported to the Arctic is affected by three main types of sources: anthropogenic sources, vegetation fires and natural origin. Particles associated with anthropogenic emissions are mainly composed of sulfate, BC and organic matter (Willis et al., 2018). Sulfate particles are formed via oxidation of gas phase SO_2 (Rahn et al., 1980; Rahn and McCaffrey, 1980; Shindell et al., 2008; Breider et al., 2014) which is largely emitted by industrial sources (Smith et al., 2001). Aqueous phase oxidation and non-photochemical oxidation processes, e.g. via transition metals, contribute to sulfate transported to the Arctic as well (McCabe et al., 2006). A decreasing trend in Arctic sulfate concentrations has been observed since the 1980s due to decreasing anthropogenic sulfur emissions in Europe, North America and the former Soviet Union (Quinn et al., 2007; Breider et al., 2017). Simultaneously, the emissions in China increased by a factor of 3 between 1980 and 2006, illustrating the increasing importance of southeast Asian sources for the abundance of Arctic sulfate (Breider et al., 2017). Besides industrial sources, sulfate aerosol is also produced from natural sources, e.g. via oxidation of marine dimethyl sulfide (DMS) emissions (see Sect. 1.2.4). BC is generated from incomplete combustion processes (Bond et al., 2013) with vegetation fires as a major source, in particular for the Arctic summer. However, anthropogenic BC sources in northern Eurasia impact the lower Arctic troposphere (Köllner et al., 2021) whereas south Asian BC sources play a role for the middle and upper troposphere (Hirdman et al., 2010b; Backman et al., 2021). Similar to sulfate, BC shows a decreasing trend in the Arctic lower troposphere because of reduced emissions in most industrial regions, however, the importance of south Asian emissions (China and India) significantly increased for the middle and upper troposphere (Backman et al., 2021). Another important anthropogenic particle species is organic carbon (OC). OC summarizes a heterogeneity of different chemical compounds which are either primarily emitted or formed from gas-phase low-volatile organic compounds via photooxidation (Hallquist et al., 2009; Seinfeld and Pandis, 2016). The molecular composition of organic

matter varies significantly across Arctic sites depending on the proximity to specific sources and different chemical processing (Frossard et al., 2014; Hansen et al., 2014). Previous studies showed the contribution of alkanes, acids (e.g. phthalic acid and dicarbonylic acids), alcohols and organosulfates which have been associated with combustion processes, including fossil fuel and biomass burning (BB; Fu et al., 2009a; Brock et al., 2011; Schmale et al., 2011; Fu et al., 2013; Frossard et al., 2014; Hansen et al., 2014; Leaitch et al., 2018).

During spring and summer, vegetation fires can be an important source of transported particulate matter from mid-latitudes. Several studies reported a significant contribution of BB emissions in North America and Siberia to Arctic aerosol in the free troposphere during these seasons (e.g. Paris et al., 2009; Schmale et al., 2011; Bian et al., 2013; Thomas et al., 2013; Xu et al., 2017). Episodical events of BB can also impact the Arctic near surface (Stohl et al., 2007). The composition of aerosol particles from BB is dominated by organic compounds (Kondo et al., 2011; Köllner et al., 2021). These particles result from emissions of primary organic particles or organic precursor gases at the fire source and subsequent secondary organic aerosol (SOA) formation. However, the contribution of SOA to vegetation fire aerosol in the Arctic remains poorly constraint (Hecobian et al., 2011; Quennehen et al., 2012). Furthermore, processes during transport (e.g. oxidation) affect the BB particles and they become less volatile and more water soluble (Jimenez et al., 2009; Schmale et al., 2011; Lathem et al., 2013). The molecular composition of OC from natural fires is therefore mainly determined by water-soluble organics, like acids, carbonyls and carbohydrates such as levoglucosan which is often used as an important organic tracer for BB (Fu et al., 2013; Hansen et al., 2014; Leaitch et al., 2018). Furthermore, particles from BB are often potassium-rich since potassium is a common constituent of plant material (Silva et al., 1999; Schill et al., 2020). In addition to OC, vegetation fires are also a major source of BC particles in Arctic summer (Stohl, 2006; Bian et al., 2013; Breider et al., 2014; Evangeliou et al., 2016; Xu et al., 2017). Measurements of fire particles often show BC which is thickly coated with organics, indicating enhanced aging and processing during transport (Kondo et al., 2011; Lathem et al., 2013). Finally, vegetation fires are also associated with the formation of secondary aerosol particles, including inorganic material, such as ammonium, nitrate and sulfate (Fisher et al., 2011; Breider et al., 2014). During transport to the Arctic, ammonium nitrate or sulfate particles are formed via reactions of the oxidation products of SO_2 or NOx with ammonia, mainly in the aqueous phase (Fisher et al., 2011; Seinfeld and Pandis, 2016).

Particles that are of natural origin and are transported into the Arctic can be classified in three types. First, sea spray aerosol from regions with open

ocean contributes significantly to the Arctic particle concentration and sizes of the particles (Huang and Jaeglé, 2017). Especially during winter, when wind speeds over the northern oceans are high and the local production of sea spray as well as biological activity is low within the Arctic, transport of sea spray particles can play an important role (Huang and Jaeglé, 2017; Leaitch et al., 2018). During summer, the local emissions of sea spray becomes more important (see Sect. 1.2.4). Second, mineral dust originating from the Gobi and Sahara deserts has been observed in the Arctic (Rahn et al., 1977; VanCuren et al., 2012; Huang et al., 2015). Dust particles are largely important for ice nucleation (see Sect. 1.2.6; Irish et al., 2018) and can significantly influence the radiative properties of high albedo surfaces (Stone et al., 2007; Groot Zwaaftink et al., 2016). However, little is known on the quantitative contribution of mineral dust from global deserts to Arctic aerosol (Willis et al., 2018). Third, sulfur emissions from volcanoes can be an important source for sulfate transported to the Arctic. Patris et al. (2002) studied sulfur isotopes in Greenland ice cores and found that volcanic sulfate contributes significantly to deposited sulfate in pre-industrial periods. Only few observations exist in order to quantify the volcanic impact (Norman et al., 1999; Leaitch et al., 2018) but it is suggested that volcanic events influence the amount of Arctic sulfate aerosol episodically (Willis et al., 2018).

In summary, long-range transport controls the abundance of Aitken and accumulation mode particles in the Arctic, especially during summer, when aerosol concentrations in the Arctic are low. As described in this section, a variety of different source emissions and aging processes during transport lead to complex features in particle size distribution and chemical composition.

1.2.4 *Predominance of natural particles during Arctic summer*

The Arctic region is mostly a marine and coastal environment, in particular during summer, when more open water surfaces are present due to the seasonal sea ice retreat. In addition, anthropogenic pollution sources are scarce with only some local emissions from shipping, oil and gas extractions as well as domestic activities (Aliabadi et al., 2015). Therefore, local sources of aerosol particles are mostly given by ocean, soils and vegetation surfaces. Together, these sources emit a range of primary particles and precursor gases for secondary aerosol formation (see no. 3 in Fig. 1.1). The resulting aerosol particles are mainly composed of a mixture of sea spray, sulfate, methanesulfonic acid (MSA), ammonium, amines, iodine and organic matter.

Sea spray is one of the major primary particle types that is emitted locally. Similar to transport, a complex mixture of inorganic salts and organic matter is mostly emitted by open water surfaces (e.g. open ocean, polyneas, leads; Prather et al., 2013). The main mechanism behind sea spray emissions is wind-driven wave breaking (Blanchard, 1989). Hence, air is trapped beneath the water surface and rises up as bubbles towards the surface again. There, the bubbles generate film and jet drops of ocean water which are released to the atmosphere (Blanchard and Woodcock, 1957; Blanchard, 1989). Once the droplets evaporate, aerosol particles of non-volatile species remain in the atmosphere (Blanchard and Woodcock, 1980; Bigg and Leck, 2008; Karl et al., 2013; Prather et al., 2013). Another possibility for sea salt production in the Arctic is the emission from snow and ice surfaces which is either related to frost flowers (Seguin et al., 2014; Xu et al., 2016) or to blowing snow (Yang et al., 2008; Huang and Jaeglé, 2017). However, both mechanisms are difficult to distinguish (Hara et al., 2017; Willis et al., 2018) and, thus, their individual contribution is still an open question (Willis et al., 2018). Since each of those formation processes depend on wind speed, the seasonal maximum sea salt concentration is reached during winter and spring when wind speeds are high (Deshpande and Kamra, 2014; May et al., 2016; Kirpes et al., 2018).

The composition of primary marine aerosol is mostly determined by inorganic salts (e.g. sodium chloride) and is often accompanied by different organic matter, in particular during summer (Bigg and Leck, 2008; Prather et al., 2013). Among these organic species, MSA, protein-like substances, organosulfates, polysaccharides, alcohol functional groups and insoluble microgels exist (Fu et al., 2013; Frossard et al., 2014; Fu et al., 2015; Zeppenfeld et al., 2019). In addition, aging of sea salt occurs due to reactions with organic, sulfuric and nitric acids forming internal mixtures of salt with secondary organics, sulfate and nitrate (Prather et al., 2013; Sierau et al., 2014; Chi et al., 2015; Kirpes et al., 2018). Both, organic matter and aged sea salt, can be important for cloud formation by serving as cloud condensation nuclei (CCN) or ice nucleating particles (INP; Leck and Svensson, 2015; Wilson et al., 2015).

During summer, when sea salt concentrations are low and the influence of long-range transport to the Arctic BL is weak, secondary aerosol particles become more relevant. These secondary particles from gas-phase precursors are induced by new particle formation (NPF) events which are characterized by high concentrations of nucleation-mode particles (Kulmala et al., 2004; Zhang et al., 2012). Such NPF events were frequently observed in the summertime Arctic BL in association with marine precursor gases (e.g. Leaitch et al., 2013; Asmi et al., 2016; Nguyen et al., 2016; Dall'Osto et al., 2017; Freud et al., 2017). The main drivers for NPF remain still unclear, however, the presence of clouds

might play an important role (Willis et al., 2018). More specifically, particle removal via cloud scavenging establishes favorable conditions for NPF due to low condensation sinks (Collins et al., 2017). In addition, photochemistry by the available sunlight during summer has a strong impact on the occurrence of NPF events (Ström et al., 2009; Freud et al., 2017).

A prominent marine precursor for secondary particles is DMS which is an important contributor to Arctic sulfate production (e.g. Levasseur, 2013; Park et al., 2013; Becagli et al., 2016; Mungall et al., 2016; Park et al., 2017; Jarníková et al., 2018; Ghahremaninezhad et al., 2019). DMS is produced via bacterial breakdown of dimethylsulfoniopropionate which is generated by marine microalgae and phytoplankton (Carpenter et al., 2012; Becagli et al., 2016). Once emitted to the atmosphere, DMS further reacts to form sulfuric acid or MSA (Hoffmann et al., 2016). Both oxidation products can play a role in secondary aerosol formation by forming stable sulfate clusters (Kulmala et al., 2000; Bzdek et al., 2011; Dawson et al., 2012), MSA, however, may contribute more to the growth of existing particles by condensation due to its higher vapor pressure (Leaitch et al., 2013; Seinfeld and Pandis, 2016; Willis et al., 2016). Accordingly, DMS emissions lead to the formation of sulfate particles in the Arctic BL.

Basic precursor gases, like ammonia and amines, play an important role in the formation of secondary aerosol with sulfuric acid in the Arctic. The abundance and their individual contribution to secondary particle formation is still highly uncertain (Willis et al., 2018). Ammonia is emitted locally from seabird guano as several studies found elevated ammonia levels associated with nearby seabird colonies (Blackall et al., 2007; Croft et al., 2016a; Wentworth et al., 2016). Boreal fires can also contribute episodically to Arctic ammonia concentrations, however, their influence is limited by the short atmospheric lifetime of ammonia (1-2 days; Lutsch et al., 2016; Lutsch et al., 2019a). Marine open water (e.g. ocean, melt ponds, leads), on the other hand, act as a sink for gas phase ammonia (Johnson et al., 2008; Wentworth et al., 2016). The knowledge of sources and abundance of amines in the Arctic region is very limited. Dall'Osto et al. (2012) found particles containing amines at Mace Head, Ireland, in air masses from polar marine regions. Another study showed the abundance of amino acids in Arctic aerosol with marine background (Scalabrin et al., 2012). In addition, trimethylamine (TMA) have been found as component of organic aerosol particles at a coastal site in Alaska during summer (Gunsch et al., 2017). Recently, single particle aerosol measurements in the Canadian high Arctic demonstrated the abundance of TMA in particulate matter which could be related to inner-Arctic marine biogenic sources (Köllner et al., 2017; Köllner, 2020). In other regions of the globe, emissions of gas phase amines from marine biota to the atmosphere were observed which play an important role for aerosol

chemistry (Gibb et al., 1999; Facchini et al., 2008; Ge et al., 2011a; Dall'Osto et al., 2019; van Pinxteren et al., 2019b). Together with ammonia, gas phase amines act as stabilizers for sulfuric acid clusters and, thus, are important contributors to NPF processes (Facchini et al., 2008; Ge et al., 2011a; Almeida et al., 2013; Kürten et al., 2016). The aerosol acidity, Henry's law coefficient and the amount of both species determine their individual role in acid neutralization (Pratt et al., 2009; Ge et al., 2011b).

For amines, two additional pathways may exist for secondary aerosol formation: First, amines are highly water-soluble in terms of Henry's law coefficient (Ge et al., 2011b; Leng et al., 2015b; Leng et al., 2015a). Therefore, they may dissolve in available cloud water droplets where the acid-base reactions and other cloud processing can occur (Ge et al., 2011b; Rehbein et al., 2011). Second, gas phase amines can oxidize and form species with lower volatility, like amides, nitramines and imines which promote secondary aerosol formation (Angelino et al., 2001; Murphy et al., 2007; Ge et al., 2011b).

Iodine oxides are another species associated with NPF and growth processes in coastal environments (e.g. Carpenter, 2003; O'Dowd and De Leeuw, 2007; Sipilä et al., 2016). Measurements in the Arctic marginal ice zone revealed a connection between increased iodic acid concentrations and the formation of ultrafine particles in spring and the summer-to-autumn transition (Allan et al., 2015; Sipilä et al., 2016; Baccarini et al., 2020). Baccarini et al. (2020) observed an increase in iodic acid concentrations over the Arctic pack ice region during autumn, possibly related to freezing onset and a seasonal ozone rise. This abundance of iodic acid triggered NPF events contributed to particle growth and, thus, potentially influence cloud properties (Baccarini et al., 2020). Gas-phase iodine can be produced by micro-algae below the sea ice and is transported via brine channels or cracks to the atmosphere (Hill and Manley, 2009; Saiz-Lopez et al., 2015). Another pathway can be the release of iodine from the snowpack and frozen saline surfaces via photochemical reactions (Abbatt et al., 2012; Raso et al., 2017; Halfacre et al., 2019).

Finally, other condensible organic species can also contribute to particle nucleation and subsequent growth. The current knowledge of sources and involved species, however, is still very limited in the Arctic (Willis et al., 2018). Several studies reported volatile organic compounds (VOC), like fatty acids, monoterpenes and isoprene, which are known as aerosol precursors (Fu et al., 2009b; Schollert et al., 2014; Kramshøj et al., 2016; Kim et al., 2017; Mungall et al., 2017). Among several SOA tracers, a variety of dicarboxylic acids (DCA) have been measured at different Arctic sites (e.g. Kerminen et al., 1999; Fu et al., 2009b; Kawamura et al., 2012; Fu et al., 2013; Hansen et al., 2014). However, the abundance of DCA in summer is lower compared to spring because of the weak

influence of long-range transport from lower latitudes. For example, Köllner et al. (2021) observed particles containing DCA in the Canadian Arctic only when air masses arrived from outside the Arctic. On the other hand, natural sources in the Arctic become more important by retreating sea ice and increased biological activity (Kawamura et al., 1996; Kerminen et al., 1999; Kawamura et al., 2010; Kawamura et al., 2012). In addition to marine production, also terrestrial sources for VOC and nitrogen-containing species may contribute to Arctic SOA (Schollert et al., 2014; Kramshøj et al., 2016; Kramshøj et al., 2018). In short, the origin and involved species of organic aerosol in the Arctic are poorly constrained and further studies are needed with the focus on organic species.

1.2.5 *Peculiarity of Arctic clouds*

Clouds are a crucial compound for the Arctic surface energy balance and, therefore, important to understand the Arctic Amplification (Serreze and Barry, 2011; Wendisch et al., 2019). However, their quantitative impact on the accelerated warming is still associated with large uncertainties (Schmale et al., 2021). As mentioned earlier, the net radiative effect of clouds to the Arctic surface is warming, except for midsummer when the incoming solar radiation is at its maximum and surface albedo is low (Intrieri et al., 2002; Shupe and Intrieri, 2004; Alterskjær et al., 2010; Döscher et al., 2014). Specifically, the sign and strength of these cloud effects depend on latitude (amount of solar radiation), surface albedo, aerosol properties and cloud properties, like liquid water content and temperature (Shupe and Intrieri, 2004; Sedlar et al., 2011; Döscher et al., 2014). The interaction of aerosol with clouds is a key mechanism which contributes significantly to the existing uncertainties (Wendisch et al., 2017; Wendisch et al., 2019; Schmale et al., 2021).

The Arctic region is characterized by high cloud frequencies throughout the year with a significant fraction of liquid and mixed-phase clouds (Shupe, 2011). These cloud types contribute substantially to the energy fluxes as longwave cloud radiative forcing is very sensitive to the liquid water path (Shupe and Intrieri, 2004). Several measurements at different Arctic sites as well as spaceborne observations revealed an annual cycle in the cloud occurrence and phase (Shupe, 2011; Mioche et al., 2015). In summer and autumn, the fraction of liquid phase clouds is largest, whereas mixed-phase clouds are a frequent feature in winter and spring (Shupe and Intrieri, 2004; Cesana et al., 2012; Morrison et al., 2012).

Another special characteristic of Arctic clouds is the longevity of mixed-phase clouds (Morrison et al., 2012). Usually, the lifetime of this cloud type is limited due to the fast growth of ice-crystals at the expense of liquid cloud droplets which is known as the Wegener-Bergeron-Findeisen (WBF) process. In the Arctic region, however, they can persist for multiple days (Shupe et al., 2006; Morrison et al., 2012). Morrison et al. (2012) summarized several factors for the observed persistence of Arctic mixed-phase clouds. First, the longevity is largely driven by a feedback pathway in which liquid water, radiation and turbulence is involved. In particular, supercooled liquid water in the upper part of the cloud leads to strong radiative cooling causing a decrease in static stability. Consequently, upward motions and turbulence are triggered which promote condensational growth of cloud droplets. Furthermore, advection of humid air from lower latitudes often results in strong moisture inversions above the cloud which provides enough water vapor for sustaining the liquid phase inside the cloud via entrainment from above (Morrison et al., 2012; Sedlar et al., 2012). Surface energy and moisture from open water sources (e.g. open ocean, leads) feed the cloud with water vapor as well if the cloud is dynamically coupled to the surface (Zuidema et al., 2005). An additional factor in sustaining the liquid phase are aerosol particles available for cloud formation. Since the concentrations of INP can be very low in the Arctic, their availability is critical for the WBF mechanism (Morrison et al., 2012; Wex et al., 2019). As a further consequence of the limited INP amount, cloud ice often only forms if liquid droplets are present. Thus, an intensive depletion of liquid water at the expense of ice formation and growth, as would occur for the WBF process, might not be possible since the liquid would be missing for further ice formation (Lance et al., 2011; Morrison et al., 2012). In summary, the combination of these processes leads to the persistence of Arctic mixed-phase clouds, their individual contribution, however, is still an open question (Wendisch et al., 2019).

Besides the INP concentration as critical factor for cloud ice formation, the abundance and properties of available CCN play also an important role for the cloud radiative effect. In particular, when the CCN concentrations are very low ($< 10\,\mathrm{cm}^{-3}$), small increases in the amount of CCN can have a significant impact on the cloud LWP and, thus, enhance the warming longwave emissions of the cloud (Mauritsen et al., 2011). This critical range of lacking CCN abundance for cloud formation is referred to as *tenuous cloud regime* (Mauritsen et al., 2011). In conclusion, the interaction of aerosol particles with clouds are a critical component for Arctic radiative fluxes.

1.2.6 *Cloud-interacting particles in the Arctic*

Aerosol particles and precursors can interact with clouds by acting as CCN or INP for cloud formation or by being mixed into the clouds where they can alter their properties due to cloud processing (see process no. 4 in Fig. 1.1; Seinfeld and Pandis, 2016). The concentration of CCN shows in general a seasonal cycle similar to the total particle concentration in the Arctic (Karlsson et al., 2021). Winter- and springtime CCN abundance can reach values of up to $1000\,\mathrm{cm}^{-3}$ because of the dominance of accumulation mode particles (Moore et al., 2011). During summer, the CCN concentration is often very low but can increase episodically (Bigg and Leck, 2001; Wylie and Hudson, 2002; Burkart et al., 2017b). For instance, measurements in the central Arctic Ocean from July to September showed concentrations varying over three orders of magnitude ranging from 1 up to $1000\,\mathrm{cm}^{-3}$ (Bigg and Leck, 2001). The general low CCN concentrations in summer are largely driven by the lack of accumulation mode particles which are commonly activated to cloud droplets. Under these conditions, supersaturations can become high enough that a significant fraction of particles below 100 nm can be activated (Korhonen et al., 2008; Croft et al., 2019). Indeed, several studies reported the activation of particles in the Aitken mode which can take place down to particle sizes of $\sim 20\,\mathrm{nm}$ (Korhonen et al., 2008; Leaitch et al., 2016). In short, the size effect is hypothesized to be the dominant factor for CCN concentrations (Dusek et al., 2006; Zelenyuk et al., 2010; Moore et al., 2011). However, particle composition and mixing state might also be important, especially during summer when the availability of cloud active particles is limited.

Under these conditions, when long-range transport can be neglected, aerosol species from marine biogenic sources represent an important class of CCN-active particles. Previous studies in the Arctic highlighted the CCN-contribution of sulfur-containing secondary aerosol which is formed via DMS oxidation (Leaitch et al., 2013; Willis et al., 2016). Furthermore, marine secondary organic aerosol (MSOA), which is mostly internally mixed with sulfate, contributes significantly to formation of cloud droplets (Willis et al., 2016). Another important aerosol type for cloud droplet activation are primary particles from the ocean, like marine microgels (Orellana et al., 2011). However, a study using κ-Köhler theory hypothesized a large fraction of organic aerosol being insoluble (Martin et al., 2011). As a result, an increase in organic fraction might decrease the CCN-activity of tropospheric particles in the Arctic summer (Martin et al., 2011; Leck and Svensson, 2015). On the other hand, MSOA might contribute to cloud droplet formation via particle growth to CCN-active size (Burkart et al., 2017a; Willis et al., 2017; Willis et al., 2018).

When particles from long-range transport reach the Arctic atmosphere, species from anthropogenic, biomass burning and natural sources play an important role for the CCN burden. The transported aerosol material is often dominated by oxygenated organic compounds leading to high O:C-ratios (Fu et al., 2009a; Moore et al., 2011). Among these species, DCA is a prominant agent in the Arctic (e.g. Fu et al., 2009a; Köllner et al., 2021). Because of the hygroscopicity of oxygenated species (Jimenez et al., 2009), the CCN-activity significantly increases if the Arctic atmosphere is influenced by sources from mid-latitudes, in particular during winter and spring (Moore et al., 2011).

In comparison to CCN active particles, less is known on the number and composition of Arctic INP (Willis et al., 2018). Concentrations of INP are in general lower than $1\,\mathrm{L}^{-1}$ but can increase to higher values episodically (e.g. Fountain and Ohtake, 1985; Bigg, 1996; Prenni et al., 2009; McFarquhar et al., 2011; Mason et al., 2016; Creamean et al., 2018; Irish et al., 2019; Wex et al., 2019; Hartmann et al., 2020). Mineral dust from local sources and regions at lower latitudes is known as efficient ice nucleus and contributes significantly to Arctic INP (Mason et al., 2016; Groot Zwaaftink et al., 2016; Creamean et al., 2018; Irish et al., 2019; Si et al., 2019). Another important INP source could be the Arctic Ocean. Global measurements of seawater samples illustrated elevated INP concentrations and high freezing temperatures at the sea surface microlayer (SML; Wilson et al., 2015; DeMott et al., 2016; Chance et al., 2018). Accordingly, primary marine aerosol from the Arctic Ocean have been identified as potential INP source (Creamean et al., 2019; Zeppenfeld et al., 2019). In addition, Hartmann et al. (2020) found effective INP in the Arctic troposphere in combination with marine local air masses. However, many uncertainties remain regarding the role of marine Arctic aerosol for ice nucleation (Schmale et al., 2021).

1.2.7 *Thermodynamic structure of Arctic clouds*

The contribution of particles originating from Arctic surfaces depends strongly on the thermodynamic structure of the cloud (Morrison et al., 2008; Shupe et al., 2013; Li et al., 2017). In particular, the position of thermodynamically stable inversion layers, i.e. temperature and moisture inversions, determine the vertical pathway for aerosol particles and moisture into the cloud (Sedlar and Tjernström, 2009; Sedlar et al., 2012; Shupe et al., 2013; Li et al., 2017). In the Arctic, different scenarios for the thermodynamic profile have been observed in the past (Sedlar and Tjernström, 2009; Shupe et al., 2013; Sotiropoulou et al., 2014; Creamean et al., 2021).

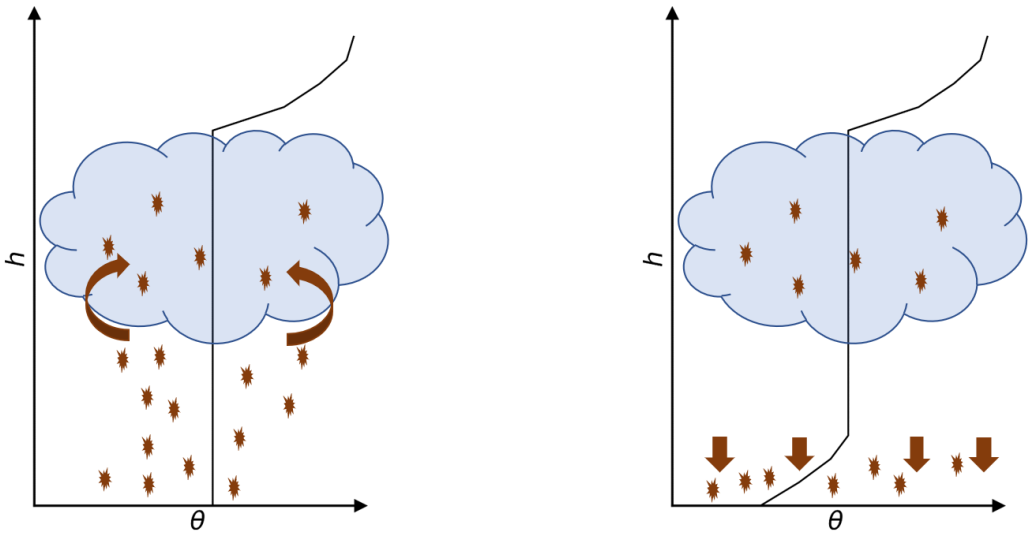

(a) coupled cloud **(b)** decoupled cloud

Figure 1.2: Schematic vertical profile of potential temperature θ for a surface-coupled cloud (a) and a decoupled cloud (b). Arrows indicate the mixing pathways of aerosol particles into the cloud. An increase of θ with altitude corresponds to a stable stratification.

One discrimination can be made for the thermodynamic structure below-cloud. If the cloud mixed-layer extends down to the surface, the cloud is referred to as surface-coupled cloud (see Fig. 1.2a). Consequently, aerosol particles and precursor gases from the surface can directly be mixed into the cloud via upward motion and turbulence (Shupe et al., 2013). In contrast, the presence of a near-surface stable stratification prohibits the upward mixing of aerosol into the cloud above (see Fig. 1.2b). In this case, the cloud is thermodynamically decoupled from the surface, thus, horizontal advection and mixing from above the cloud are the dominant drivers for aerosol and moisture transport to the cloud (Shupe et al., 2013; Sotiropoulou et al., 2014).

For the cloud top structure, another two regimes can be defined. First, the inversion base can be collocated with the cloud top height (see Fig. 1.3a) which is classified as a cloud capped by inversion (CCI; Sedlar and Tjernström, 2009; Sedlar et al., 2012). On the other hand, the cloud top can extend up to a few hundred meters into the inversion layer, resulting in a cloud inside the inversion (CII; Sedlar and Tjernström, 2009; Sedlar et al., 2012; see Fig. 1.3b). This CII case is considered to occur with strong temperature and moisture inversions at cloud top (Sedlar et al., 2012). The location of inversion base below cloud top promotes the moisture transport into the clouds from above. On the other hand, aerosol particles aloft can be mixed into the cloud via entrainment in the

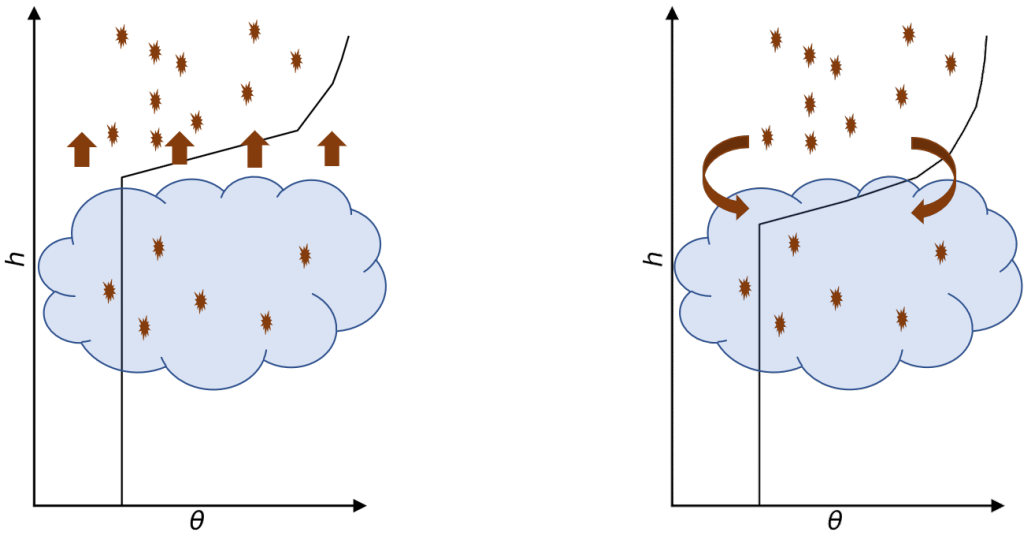

(a) cloud capped by inversion (CCI) **(b)** cloud inside inversion (CII)

Figure 1.3: Schematic vertical profile of potential temperature θ similar to Fig. 1.2 but for the cloud capped by inversion (CCI; a) and the cloud inside inversion (CII) case (b).

upper part of the cloud (Sedlar et al., 2012; Tjernström et al., 2014). Clearly, the vertical location of stable inversion layers can be decisive for the aerosol contribution from below or above the cloud. However, their quantitative input to cloud formation and processes is still unknown (Schmale et al., 2021).

1.3 OBJECTIVES AND STRUCTURE OF THE THESIS

As described in the previous sections, the current understanding of aerosol particles in the Arctic is already robust, however, some questions remain open, especially for aerosol-cloud interaction processes. Schmale et al. (2021) outlined current deficits in aerosol-related processes in the Arctic some of which were already pointed out in the previous sections. In short, the main knowledge gaps exists in the properties of cloud forming particles (CCN and INP), their origin and the processing of particles and precursors in clouds. For instance, the effect of aerosol chemical composition on cloud processes is still highly debated.

A large part of the incomplete knowledge of aerosol-cloud interaction processes is due to a lack of in-situ observations. Most of the knowledge is based on comparison of particle measurements with observed CCN or INP concentrations, however, these quantities are only inferred from artificial particle activation inside the instruments. Only a few studies exists with measurements of particles

directly involved in Arctic clouds (e.g. Zelenyuk et al., 2010; Baccarini et al., 2020; Karlsson et al., 2021). Directly involved means that cloud particle residues were analyzed remaining after evaporating the cloud particles (droplet or ice crystal). The information about chemical composition of cloud residuals is further restricted. To the author's knowledge, only one previous aircraft-based measurements took place in Alaska where a single particle mass spectrometer was connected with a counterflow virtual impactor (CVI) inlet to analyze the cloud particle residues' composition (McFarquhar et al., 2011).

For this reason, the following research questions were addressed in this thesis:

- Which particle types can be found in summertime Arctic clouds and how does their composition differ from ambient air?
- How does the thermodynamic structure of clouds vary between different meteorological and surface conditions and does this effect the chemical composition of cloud particle residues?
- Does the chemical composition of Arctic cloud residues differ from mid-latitudinal clouds?
- Which role plays long-range transport for the clouds during Arctic summer?

In this thesis, the combination of a single particle mass spectrometer with a CVI inlet system is used to characterize the chemical composition of cloud residual particles. Here, the focus will lie especially in the contribution and mixing state of MSOA.

The structure of the current thesis is the following: In Chapter 1, the current understanding of aerosol particles and aerosol-cloud interaction processes is introduced and the existing knowledge gaps are emphasized. In the following Chapter 2, the instruments and methods for this study are described. In particular, the main instrument of this thesis, the single particle mass spectrometer ALABAMA, is introduced and characterized. Furthermore, complementary instruments and the resulting data sets for this study are presented briefly. In Chapter 3, the airborne campaign of this study, the "Arctic CLoud Observations Using airborne measurements during polar Day" (ACLOUD; Wendisch et al., 2019), is presented together with an overview of the meteorological conditions during the airborne experiments. Chapter 4 contains the results from the airborne measurements of ambient aerosol and cloud particle residue composition. In the final Chapter 5, the results are summarized and combined with an outlook for further measurements on aerosol-cloud interaction in the Arctic region.

2

METHODS

The main focus of the thesis is the chemical characterization of Arctic aerosol particles and cloud particle residuals. To analyze the chemical composition of atmospheric particles, the Aircraft-based Laser ABlation Aerosol MAss spectrometer (ALABAMA) was deployed on the Polar 6 aircraft. In the following sections, the main working principle, measurement efficiencies and the particle classification of the ALABAMA are described. Furthermore, complementary measurements of different trace gases, additional aerosol instrumentation and cloud properties are introduced. In addition, the Lagrangian models for air mass history calculation are described.

2.1 LASER ABLATION/IONIZATION AEROSOL MASS SPECTROMETER ALABAMA

2.1.1 *Working principle of ALABAMA*

The main instrument used in the thesis is the single particle mass spectrometer ALABAMA (Brands et al., 2011; Clemen et al., 2020). Figure 2.1 shows a schematic view of the ALABAMA setup. It consists in principle of three different sections.

In the first section, particles enter the instrument and are focused into a narrow particle beam. This is achieved by a constant pressure inlet (CPI; Molleker et al., 2020) and an aerodynamic lens. The CPI consists of an in-house manufactured O-ring which is either squeezed or relaxed by a bottom and top metal plate, depending on the upstream pressure. As a result, the O-ring acts as a critical orifice by changing its inner diameter which determines the volumetric flow rate into the ALABAMA. For airborne sampling with changing ambient pressure conditions, this flexibility is important to maintain a constant mass flow into the instrument. A detailed description of the CPI similar to the one used in the ALABAMA is given by Molleker et al. (2020). After the CPI, the particles pass a Liu-type aerodynamic lens containing a series of orifices with different diameters (Liu et al., 1995a; Liu et al., 1995b; Liu et al., 2007) which focuses the particles into a narrow beam. At the exit of the first section, a skimmer

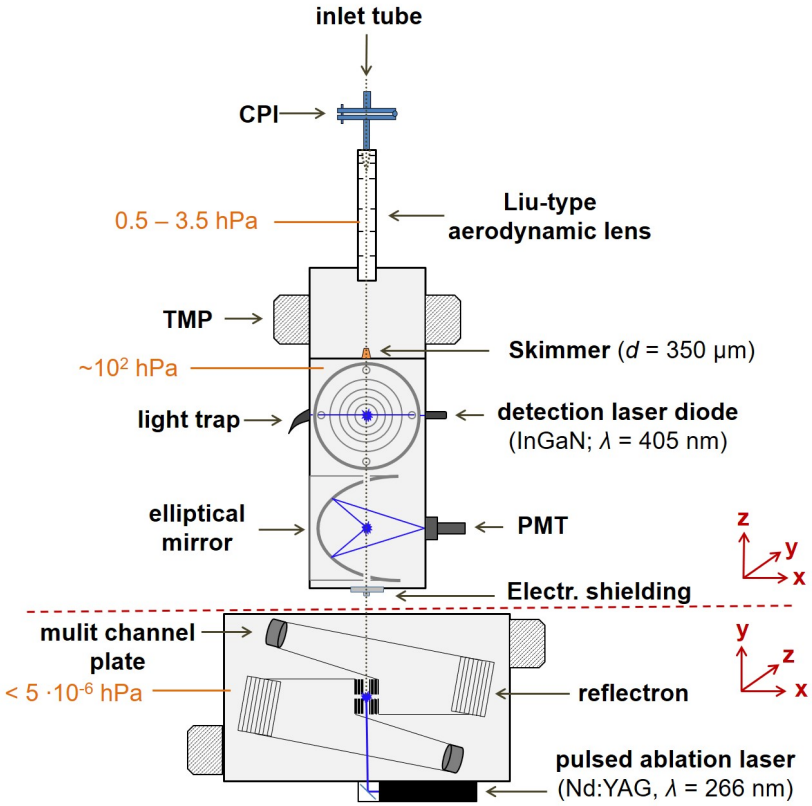

Figure 2.1: Schematic overview of the ALABAMA (modified according to Brands et al., 2011 and Clemen et al., 2020). Acronyms are defined as follows: CPI = constant pressure inlet; PMT = photomultiplier tube; TMP = turbo molecular pump. The view of the scheme changes from the upper part to the mass spectrometer part indicated by the two coordinate systems on the right-hand side. Pressure regimes for the individual sections are given as numbers on the left hand side as well.

with a diameter of 350 nm is installed to reduce the amount of air reaching the following sections. The combination of CPI, aerodynamic lens and skimmer ensures an efficient transmission of particles in the size range of 100 nm up to $\sim 2\,\mu$m.

The second part of the instrument is the detection unit. There, the particles pass through two orthogonal laser beams from InGaN laser diodes (wavelength $\lambda =$ 405 nm). The scattered light is guided by elliptical mirrors towards photomultiplier tubes (PMTs) where the light signals are detected at both laser stages. Signal amplifiers support the detection of very small particles down to 100 nm. Via the elapsed time of the particles between the two detection stages, the particle velocity can be determined (DeCarlo et al., 2004). Using a calibration with particles of known size, density and shape (in this case: polystyrene latex (PSL) particles), the vacuum-aerodynamic diameter (d_{va}) can be derived (see section 2.1.2). In addition, the particle velocity is used to trigger the ablation

laser (pulsed frequency-quadrupled Nd:YAG laser, wavelength $\lambda = 266\,\text{nm}$, max. repetition rate 20 Hz, pulse length $\sim 6\,\text{ns}$; Quantel, 2008).

Finally, the particles arrive in the actual mass spectrometer section where the ablation laser pulse takes place. A successfully detected and sized particle is hit by the high-energy laser pulse so that the particle evaporates and simultaneously ionizes. Following this ablation/ionization process, the generated positive and negative ions are guided into a mass spectrometer (Z-shaped bipolar ToF-MS; TOFWERK AG, Thun, Switzerland). The ions reach the multi-channel detector plates at the end of the Z-shaped extraction paths with a certain flight time depending on their mass-to-charge ratios (m/z). Thus, a bipolar mass spectrum up to m/z 250 is recorded for each particle hit.

The main limitation of this laser-induced ablation/ionization method is the difficulty of quantifying aerosol mass concentrations due to highly variable ion signals (Sullivan and Prather, 2005; Murphy, 2007; Köllner, 2020). This variability occurs due to several factors. First, the particles can experience different laser intensities when they are hit by the ablation laser. This is due to a combination of the particle beam divergence, the Gaussian shape of the laser beam profile and inhomogeneities within the spatial laser beam profile (Wenzel and Prather, 2004; Brands, 2009; Clemen et al., 2020). Second, the ionization efficiency changes with the chemical composition of the particles (e.g. Bhave et al., 2002). Third, the fragmentation of particles varies due to different laser intensities as well as differences in particle size, structure and composition (e.g. Bhave et al., 2002; Cai et al., 2006; Sultana et al., 2017). Fourth, matrix effects can lead to suppression of ion signals from major compounds by minor constituents (Gross et al., 2000; Reilly et al., 2000; Hatch et al., 2014). In addition, the diversity of organic compounds can challenge the molecular identification of specific organic particle species (Sullivan and Prather, 2005; Murphy, 2007). In short, the combination of these effects is still not fully understood (Murphy, 2007). As a consequence, a quantification of certain particulate compounds via the ablation/ionization process is almost impossible. Despite these limitations, this method provides an important advantage for the analysis of aerosol processes. In fact, it allows the investigation of mixtures of different chemical compounds, the so-called internal mixing state (Sullivan and Prather, 2005; Köllner, 2020). In addition, the quantification of certain particle compounds can be approximated by using aerosol concentrations from complementary measurements or from the concentration of detected particles by the ALABAMA (see Sect. 2.2.4; Froyd et al., 2019; Köllner, 2020).

2.1.2 *Calculation of particle size*

When passing through the aerodynamic lens, the particles accelerate depending on their particle size. Thus, particles travel through the evacuated part of the ALABAMA with a certain velocity v_p depending on their size (Klimach, 2012). Consequently, the information on v_p can be used to derive the size of individual particles. Therefore, the flight time of the particles between the two detection lasers is measured via an internal clock system with a processor frequency of 25 MHz and the time counter value *upcount*, so one *upcount* corresponds to 40 ns. Using the known distance between the two detection lasers of 0.07 m, the particle velocity v_p is determined by:

$$v_p = \frac{0.07\,\mathrm{m} \cdot 25\,\mathrm{MHz}}{upcount}. \tag{2.1}$$

The resulting velocity is not only a function of particle size, but also depends on shape and density. As both properties are highly variable among atmospheric particles, a specific size parameter is introduced which refers to particles of a certain shape and density. The diameter of a spherical particle with a density of 1 g cm^{-3} that has the same velocity v_p as the particle of interest is called the aerodynamic diameter d_a. For the free-molecular regime, like the evacuated part of the ALABAMA, the equivalent diameter is called vacuum-aerodynamic diameter d_{va} (DeCarlo et al., 2004).

To obtain particle sizes from the determined velocities v_p, calibration measurements with particles of known shape and size are necessary. For this study, two sets of calibration measurements were conducted: one set during the ACLOUD field experiments (11 June 2017) and one after ACLOUD (17 July 2017). As calibration particles, monodisperse PSL particles of different sizes in the range between 210 nm and 1.68 μm were dispersed in purified water and sequentially passed through the experimental setup which is described in the following. First, the PSL-water mixtures were nebulized using an atomizer. After nebulization, the small droplets passed through a diffusion drier with silica gel where all the liquid evaporated. Finally, the remaining PSL particles reached the ALABAMA where v_p values were measured and the number of successfully detected particles C_{coinc} was counted. More specifically, C_{coinc} gives the number of particles which were detected by both detection stages in a pre-defined time interval. In Fig. A.1 and A.2 in the appendix, the resulting C_{coinc}-histograms of measured v_p for each PSL size can be found for the first and second set of calibration measurements, respectively. Using the median *upcount* values, the particle velocity v_p was

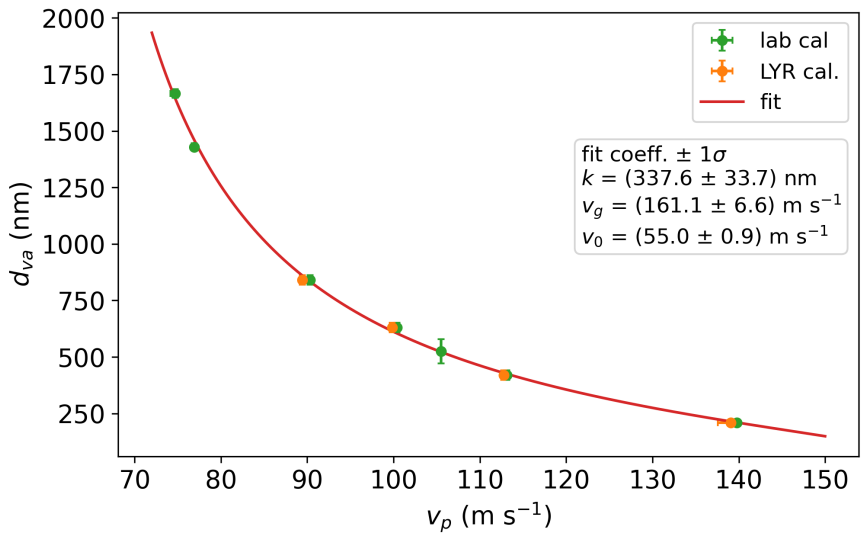

Figure 2.2: Vacuum-aerodynamic diameter (d_{va}) as a function of particle velocity (v_p) calculated from a PSL size calibration during the ACLOUD campaign (LYR cal.; orange) and after the campaign (lab cal.; green). The fit function (red line) is calculated based on Eq. 2.2, the fit coefficients are shown in the text box. Uncertainty analyses are given in Sect. A.5.

calculated for each PSL particle size via Eq. 2.1. In Fig. 2.2, the PSL median size, given as d_{va}, are visualized as a function of the corresponding v_p values.

From a differential equation describing the particle's acceleration at the exit of the aerodynamic lens, Klimach (2012) derived a mathematical equation which relates the diameter d_{va} to the velocity v_p as follows:

$$d_{va} = \frac{k}{\ln(\frac{v_g - v_0}{v_g - v_p})} \tag{2.2}$$

with the particle velocity before the gas expansion v_0, the gas velocity after the expansion v_g and the size calibration factor k. The fit coefficients k, v_g and v_0 can be determined by fitting the measured particle velocities to the particle diameters using Eq. 2.2. With this calibration curve, the d_{va} from unknown particles can be calculated from the measured velocities (v_p). The resulting fit curve is shown in Fig. 2.2, including the fit coefficient results in a text box.

The selected sizes of PSL particles covers almost the complete size range of particles analyzed during ACLOUD. In total, 99 % of all ablated/ionized particles during the conducted flights were in the range between 250 nm and 1.6 μm. Further information on the used PSL particles can be found in Tab. A.1 in the appendix.

2.1.3 *ALABAMA performance during ACLOUD*

The collection efficiency CE of the ALABAMA, i.e. the number of successfully ablated/ionized particles in relation to the number of particles reaching the inlet of the instrument, is determined by the transmission and detection efficiencies at the different stages of ALABAMA. It is defined as follows:

$$CE = DE \cdot HR, \tag{2.3}$$

where HR is the particle hit rate of the ablation laser. The detection efficiency DE describes the number concentration of successfully detected particles (N_{coinc}) by the ALABAMA, divided by the number concentration measured by a reference instrument (N_{ref}):

$$DE = \frac{N_{coinc}}{N_{ref}}. \tag{2.4}$$

Considering the detection of particles, losses can occur in the inlet and the focusing section of the instrument. In a laboratory characterization by Köllner (2020), the transmission efficiency of the Liu-type aerodynamic lens combined with the CPI orifice was measured for different particle sizes at a lens pressure p_{lens} of 2.5 hPa which is close to the p_{lens} settings of 2.4 hPa during ACLOUD. It was shown that the fraction of particles successfully entering the ALABAMA varied between 60 % for 840 nm (in d_{va}) particles up to more than 80 % for a particle diameter of 315 nm (Köllner, 2020). Moreover, these transmission efficiency values were stable for different upstream pressure conditions in the range of the observed ambient pressures during ACLOUD (500 hPa - 1000 hPa; Köllner, 2020). In contrast to these laboratory experiments, a new type of O-ring was used inside the CPI for the current thesis. It provides a smaller inner diameter (0.5 mm) compared to the former version (0.8 mm). This reduction in diameter improves the shape of the inner hole when the O-ring is pinched (Molleker et al., 2020). Thus, the transmission efficiency of the CPI should be increased compared to the earlier study of Köllner (2020).

As the detection section of the instrument is downstream of the CPI and the aerodynamic lens, DE comprises the efficiency of the optical detection as well as the previous discussed transmission efficiency of the inlet section. Therefore, DE depends on the upstream pressure (which corresponds to ambient pressure during in-flight operation), the lens pressure p_{lens} as well as particle size and

shape (e.g. Brands, 2009; Brands et al., 2011; Clemen et al., 2020; Köllner, 2020). These dependencies were characterized for the ALABAMA by previous laboratory experiments (Brands et al., 2011; Clemen et al., 2020; Köllner, 2020). Köllner (2020) measured the DE characteristics with the same setup of the ALABAMA compared to the current study. For a lens pressure of 2.5 hPa close to the value in this study, DE varied between 0.1 and 0.25 for different particle diameters with the most efficient detection between 400 nm and 600 nm (Köllner, 2020).

However, the obtained DE values by Köllner (2020) were in general lower compared to Brands et al. (2011) with a similar setup of the instrument. It was suggested that the additional particle losses occurred due to a partly clogged O-ring (Köllner, 2020). Furthermore, differences in the lens alignments might have contributed to the deviations (Köllner, 2020). Another reason for the reduced efficiency might have been the different wavelength of the detection lasers ($\lambda = 532$ nm) in the study by Brands et al. (2011) (Köllner, 2020). Clemen et al. (2020) analyzed the dependencies of DE using a new aerodynamic lens system. They found a detection efficiency close to unity in the size range between 200 nm and 2 μm, although the same detection laser devices as in Köllner (2020) and in the current study was used. Thus, the effect of the laser modifications might be negligible.

To characterize the detection efficiency DE for the ACLOUD field experiments, the number concentration N_{coinc} of the ALABAMA was compared with the number concentration obtained by complementary aerosol measurements N_{ref}. For this purpose, the raw particle counts signal of coinciding detections at both laser stages (C_{coinc}) was converted to N_{coinc} by using the volumetric flow through the ALABAMA (f_{ALA}). Based on measurements by Köllner (2020), f_{ALA} was estimated as (2.36 $\pm$ 0.05) cm^3 s-1. The concentration N_{coinc} was calculated as follows:

$$N_{coinc} = \frac{C_{coinc}}{f_{ALA}}. \tag{2.5}$$

For the reference concentration N_{ref}, measurements from the UHSAS and OPC instruments (see Sect. 2.3.2) were combined to yield the particle concentration $N_{250-1600}$ in the ALABAMA size range between 250 nm and 1.6 μm. Further details on the definition and calculation of $N_{250-1600}$ are given in Sect. 2.2.4. Note that the particle diameters measured by the ALABAMA are defined as vacuum-aerodynamic diameter (d_{va}), whereas the UHSAS and the OPC provide optical diameter (d_{opt}). As a result, the comparison of both size ranges can only be considered as approximation (Köllner, 2020).

Besides the detection efficiency, also the instrumental hit rate HR is an important parameter in the overall collection efficiency. It is defined as the particle number hit by the ablation laser and successfully ionized (C_{hits}) divided by the number of successfully detected particles (C_{coinc}) which trigger the ablation laser (Brands et al., 2011; Clemen et al., 2020; Köllner, 2020):

$$HR = \frac{C_{hits}}{C_{coinc}}. \tag{2.6}$$

Using Eq. 2.6, the HR for ACLOUD was determined for different particle sizes by dividing the ALABAMA size range in 20 logarithmic size bins. As shown in Fig. 2.3, a maximum HR of approx. 0.4 was reached for particle sizes of 1 μm (given as d_{va}) with a significant decrease below 150 nm to about less than 0.1 for 100 nm diameter. A similar decline of HR is observed for large particles. At 400 nm, an additional minimum occurs where HR drops to the half of the maximum plateau. A possible explanation for this minimum might be the high detection frequency, indicated by a maximum in the number of detected particles (C_{coinc}, also shown in Fig. 2.3), due to the highest detection efficiency of the ALABAMA in this size range. In more detail, the maximum shot repetition rate of the ablation laser was set to 8 Hz during ACLOUD. Thus, if occasionally more than eight particles per second were detected by the ALABAMA, HR must be smaller than one. Indeed, the detection frequency ν_{Coinc} was often larger than $8\,s^{-1}$ for particles of ~ 400 nm (see Fig. A.3) owing to the maximum DE in this size range. Consequently, a large portion of particles at this size were missed by the ablation laser, leading to a reduction of HR.

Similar to the detection efficiency DE, HR depends on the beam width and divergence of the particle beam in the evacuated part of the ALABAMA and, thus, is a function of particle size and shape (Brands et al., 2011; Clemen et al., 2020; Köllner, 2020). In addition, chemical composition, particle charge and the laser intensity play a role for the hit rate HR (Brands et al., 2011; Clemen et al., 2020; Köllner, 2020).

For the determination of the laser intensity, the laser energy was measured using an energy meter (EnergyMax-USB J-25MUV-193, Coherent, Wilsonville, OR, USA). During the ACLOUD measurement flights, the laser energy varied between 2.41 and 9.04 mJ with a mean value of 3.66 mJ. With a beam width of $(200 \pm 50)\,\mu$m (Roth, 2014) and a pulse length of 6 ns for the ablation laser, the energy can be converted to a laser intensity. Hence, for the measurements in this thesis, the laser intensity ranged from 1.01 to $3.77 \cdot 10^9$ W cm^{-2} with a mean value of $1.52 \cdot 10^9$ W cm^{-2}. However, Clemen et al. (2020) showed that the effective beam width diameter depends on the particle size and varies between

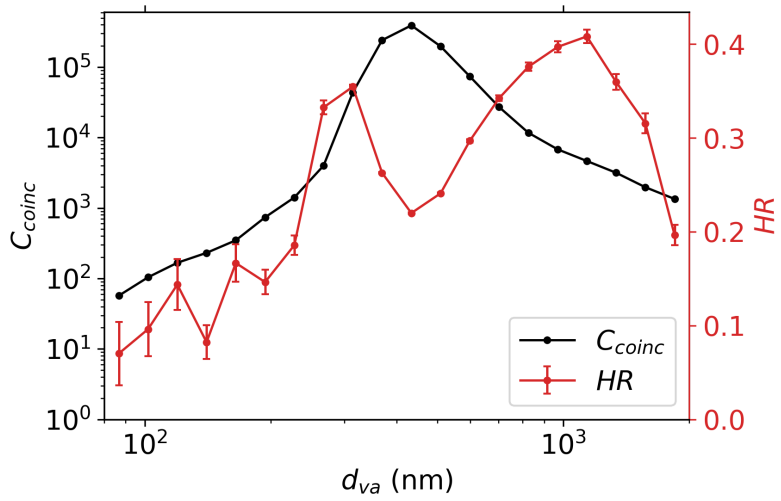

Figure 2.3: Number of successfully detected particles C_{coinc} and particle hit rate HR of the ALABAMA ablation laser as a function of particle size (d_{va}) for the ACLOUD field experiments. The given values were calculated for 20 logarithmic size bins between 80 nm and 2 μm. Uncertainty analyses are given in Sect. A.5.

200 and 600 μm for particle sizes between 200 nm and 1.8 μm. Thus, the laser intensity might be significantly lower for large particles with the minimum being in the order of $1{\cdot}10^8$ W cm^{-2}. As the true value of laser intensity lies somewhere in between the mentioned range of $1{\cdot}10^8$ W cm^{-2} and 3.77 $\cdot 10^9$ W cm^{-2}, the ionization energy in this study was in the order of magnitude of other single particle mass spectrometer (SPMS) studies (see Table A.2 in the appendix). Moreover, the laser intensity is small enough ($< 10^{10}$ W cm^{-2}) to avoid fragmentation of the particles to atomic ions (Murphy, 2007).

In Fig. 2.4, the vertical profiles for the detection efficiency (DE), hit rate (HR) and collection efficiency (CE) measured during the ACLOUD campaign are displayed which were calculated according to Eqs. 2.4, 2.6 and 2.3, respectively. DE increased with altitude from 0.6 near the surface to values close to unity in the highest flight levels. Similarly, the hit rate HR improved slightly towards higher altitudes, varying between 0.2 and 0.4, as for its size dependency. Consequently, CE also showed a positive trend with increasing height with 10 % of particles collected by the ALABAMA in the lowest flight levels and almost half of the particles in the upper part. These values were higher compared to the previous airborne measurements with the ALABAMA by Köllner (2020), where both, DE and HR, were approx. 50 % smaller. Thus, maximum CE values were smaller than 0.1 in the previous measurements.

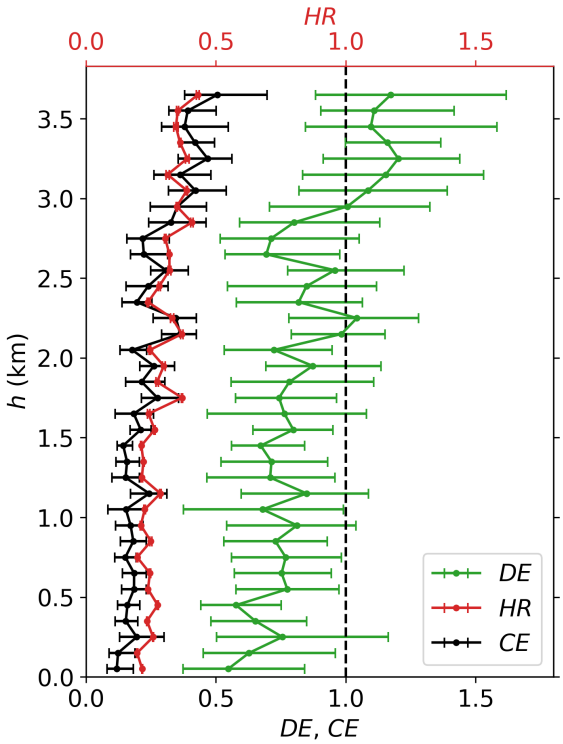

Figure 2.4: Vertical profiles of detection efficiency (DE), hit rate (HR) and collection efficiency (CE) for flights no. 7 - no. 18 (27 May - 16 June 2017) of the ACLOUD field campaign. The dashed line indicates the optimal efficiency of unity. Values are given as median within altitude intervals of 100 m, uncertainties correspond to the interquartile range within these intervals. The efficiencies for the remaining ACLOUD flights is shown in Fig. A.4 in the appendix. Uncertainty analyses are given in Sect. A.5.

The observed vertical gradient in the particle collection performance of the ALABAMA can be explained by two reasons. First, it was shown by Köllner (2020) that the transmission efficiency of the CPI depends on the upstream pressure, with decreasing transmission for increasing atmospheric pressure. However, as mentioned earlier, a different type of O-ring was used during ACLOUD compared to the Arctic measurements in Köllner (2020). Since Molleker et al. (2020) showed a transmission close to unity for upstream pressure of 1000 hPa up to a particle size of $\sim 2\,\mu$m, the CPI transmission was expected to be stable for varying ambient pressure conditions in the current study. Second, the changing particle size with preferentially small particles at lower altitudes might have contributed to a worse detection efficiency at the laser stages compared to the upper flight levels (Köllner, 2020). Besides these effects, the selected particle size range of the reference instruments for the DE calculation has to be regarded with caution. As mentioned earlier, the optical diameters

d_{opt} obtained by the UHSAS and OPC are not necessarily equal to the vacuum-aerodynamic diameters d_{va} of the ALABAMA measurements. Furthermore, the reference concentration is very sensitive to the selection of cut-off diameters, in particular for lower sizes. As a consequence, the given DE has to be considered as an approximation.

Considering the hit rate, this study revealed higher values compared to previous ALABAMA measurements in the Arctic by Köllner (2020). These differences correspond to modifications of the instrument. More specifically, an improved electrical shielding as well as a delayed ion extraction were implemented to the mass spectrometer section of the ALABAMA (Clemen et al., 2020). Laboratory experiments by Clemen et al. (2020) showed, that these modifications resulted in higher HR compared to previous ALABAMA studies.

To note, the last seven flights of ACLOUD (no. 19 - no. 25; 17 June - 26 June 2017) were excluded from the efficiency profiles in Fig. 2.4 as DE was significantly lower and more variable compared to the other flights (see Fig. A.4 in the appendix). An overview of the flight numbers and dates is given in Table B.1 in the appendix. During flight no. 18 (16 June 2017), the heating of the CVI inlet system broke, resulting in occasionally freeze-up of the inlet during the subsequent flights (see Sect. 2.3.1). Although these freeze-up periods were removed from the data sets, a potential influence on the ALABAMA measurements cannot be ruled out. Another possible explanation might be the different UHSAS reference instruments, as the reference UHSAS broke during flight no. 19 (17 June). Therefore, another UHSAS instrument was used as reference instrument for the remaining flights (see Sect. 2.3.2). However, a direct comparison of both UHSAS revealed only small differences in the measured aerosol concentrations (Ehrlich et al., 2019). Thus, the influence of the reference instrument exchange on the calculated DE is expected to be small. The majority of analyzed clouds were observed before this period of low DE. In addition, the analysis was focused on the qualitative differences of the particle composition between inside the clouds and cloud-free air rather than a quantitative perspective. Therefore, the lower DE should not impact the results of this study to a large extent.

2.2 PARTICLE CLASSIFICATION VIA ION MARKERS

The postprocessing of raw mass spectra towards individual particles to a categorization into various particle types requires complex data analysis. This section guides through the different steps which were necessary for the resulting particle classification.

In a first step, the ion flight time (t_{ToF}) dependend voltage signals detected by the multi-channel plates in the mass spectrometer part needs to be converted to mass to charge ratios m/z. For this purpose, the software package Concise Retrieval of Information from Single Particles (CRISP) was used to perform a m/z-calibration. The software makes use of the proportionality of t_{ToF} and $\sqrt{m/z}$ given by Klimach (2012):

$$t_{ToF} = a + b \cdot \sqrt{m/z}, \tag{2.7}$$

with the calibration coefficients a and b. Here, the coefficient a describes the shot-to-shot variability and b includes the properties of the electric field, like mass spectrometer high voltage and ion flight path distance (Klimach, 2012; Köllner, 2020). By integrating the raw voltage signal over time, the area below the voltage signal is calculated which results in the so-called particle stick spectra given as ion peak area in the unit mV $\cdot$ sample (Klimach, 2012; Köllner, 2020). The unit 'sample' refers to the sampling interval of the oscilloscope which was set to 2 ns. Thus, individual stick spectra of positive and negative ions were determined for all particles hit by the ablation laser.

In a second step, the individual spectra were classified into different categories of particle types. This classification, however, is rather complex due to the variety of different aerosol types and internal mixtures of various particle species as well as the described effects from the ablation/ionization process (see Sect. 2.1.1). In the past, different methods have been used to sort the individual spectra into certain particle classes.

One of these methods is the automated classification of spectra into different clusters using a clustering algorithm. In short, the clustering algorithm sorts individual stick spectra to the cluster which mean spectrum is nearest to the one considered. As a distance parameter, different function-based parameters, e.g. Pearson correlation or Euclidean metric, can be taken. As a result, the particles are assigned to different clusters depending on their dominant ion peaks which not necessarily means a chemical based connection between the members of a certain cluster. For the ALABAMA, clustering based on the fuzzy c-means and k-means algorithm have been applied in past studies (e.g. Roth et al., 2016; Schmidt et al., 2017; Schneider et al., 2017; Hünig, 2021). However, this clustering method shows issues with particle assignment in some cases.For instance, dominant ion peaks are decisive for the grouping into a given cluster. As a consequence, spectra with only weak ion peaks are neglected by the algorithm and may lead to incorrect classifications. This problem can be reduced by pre-scaling of ion peaks, for example by taken the square root, which decreases

relative differences of the signal intensities (Roth et al., 2016; Schmidt et al., 2017). Furthermore, the previous described variations in ionization efficiencies and matrix effects (see Sect. 2.1.1) can impact the automated classification using clustering procedures. In brief, these effects can cause misclassifications of certain spectra and, thus, lead to over- or underestimation of specific species' presence.

Another method is the usage of machine learning techniques for automated classification. This approach was used, for example, in a study by Christopoulos et al. (2018) who applied a random forest approach to classify different aerosol types. However, similar to the clustering method, chemical species with weak ion signal peaks and scarce occurrences can potentially be misclassified. Furthermore, machine learning algorithms require an extensive set of training data based on laboratory measurements of various particle types. Therefore, the application of this method is associated with high experimental and computational efforts.

As automated techniques show difficulties in estimating the total occurrences of certain chemical species in the analyzed particles, the particle spectra are grouped by using the so-called Marker method for this thesis. In contrast to the clustering method, which focuses on the mean intensities of individual ion peak intensities, the Marker method only considers the presence of characteristic ion peaks with signals above a background threshold value. In previous studies, this approach was used to target the existence of a certain particle type. For example, Tolocka et al. (2004) showed an improved identification of metal species with low signal intensities by using characteristic metal marker peaks. Another example is given in Roth (2014) who used characteristic marker ions to validate the resulting categories obtained by clustering. In a further study by Köllner (2020), the marker method was successfully applied for ALABAMA measurements in the Arctic region to identify different particle types, in particular, the amount of trimethylamine-containing particles.

Similar to Köllner (2020), the application of the Marker method in this study can be divided in four separate analyzing steps. First, important chemical species were identified via clustering using the fuzzy c-means algorithm to get an overview of occurring ions for all analyzed particles (not shown). In addition, knowledge about species found by previous measurements with SPMS in the Arctic was used to identify target species. Second, based on this knowledge, a list of characteristic marker ion signal peaks was selected for different chemical constituents (see Sect. 2.2.1). Third, a signal threshold was determined to differentiate background noise from true ion signals (see Sect. 2.2.2). Finally, the stick spectra of all analyzed particles were scanned by a self-written algorithm to identify the selected chemical species by the occurrence of their marker ions.

In this step, the internal mixing of some species was also classified as distinct particle type.

2.2.1 *Characteristic ion marker peaks*

In order to identify different chemical species, the ALABAMA mass spectra were scanned for the presence of characteristic ion marker signals. As the fragmentation of single particles with a common chemical composition is similar under similar ionization conditions (e.g. laser intensity, wavelength of the ablation laser), certain ion signals can be regarded as representative for the existence of respective chemical species. Based on previous laboratory and field measurements using SPMS, different characteristic ion markers were found for selected species which are listed in Table 2.1.

Table 2.1: Overview of different chemical species identified by given ion marker signals including the references (given as numbers, detailed references explained below the table).

Marker species (abbreviation)	**Ion markers**	**References**	**Comments**
Ammonium (amm.)	m/z +18 (NH_4^+)	3, 10, 18, 19	
Dicarboxylic acids (DCA)	at least two of the following ions: m/z -89 ($C_2HO_4^-$), -103 ($C_3H_3O_4^-$), -117 ($C_4H_5O_4^-$)	13, 21, 22	
Elemental carbon (EC)	at least six of the following ions: m/z +$n\cdot$ 12 (C_n^+) for n = 3, 4, ..., 12 and/or m/z -$n\cdot$ 12 (C_n^-) for n = 3, 4, ..., 12	2, 3, 10, 11, 15, 18, 19	Except m/z -96 due to isobaric interference with SO_4^-
Iodine (iod.)	m/z -175 (IO_3^-)	12	
Non-sea-spray (nss) nitrate	at least one of the following ions: m/z -46 (NO_2^-), -62 (NO_3^-)	3, 18, 19, 21	without any NaCl ion signals
Potassium (pot)	m/z +39/+41 (K^+)	3, 8, 11, 18, 19	isobaric interference with C_3H^+ at m/z +39 possible
Silicate (sil.)	m/z -60 (SiO_2^-), -76 (SiO_3^-)	9, 19	

Table continued on next page

Continued.

Marker species (abbreviation)	**Ion markers**	**References**	**Comments**
Sodium chloride (NaCl)	m/z +23 (Na^+), +81/+83 (Na_2Cl^+), -35/-37 (Cl^-), -93/-95 ($NaCl_2{}^-$)	2, 15, 16, 18, 19, 20	isobaric interference with $CH_3O_3S^-$ at m/z -95 possible
Sulfate (sulf.)	m/z -96 ($SO_4{}^-$), -97 ($HSO_4{}^-$)	3, 10, 11, 18, 19	
Triethyl-/Diethylamine (TEA/DEA)	m/z +86 ($C_5H_{12}N^+$)	1, 7, 14, 18, 21	with DEA/TEA ion signals larger than TMA signals
Trimethylamine (TMA)	m/z +58 ($C_3H_8N^+$), +59 ($(CH_3)_3N^+$)	1, 7, 10, 17, 18	with TMA ion signals larger than DEA/TEA signals
Vanadium (van.)	m/z +51 (V^+), +67 (VO^+)	6, 19, 23	

Given reference numbers are defined as follows: [1]Angelino et al. (2001), [2]Brands (2009), [3]Brands et al. (2011), [4]Dall'Osto and Harrison (2006), [5]de Foy et al. (2012), [6]Gaston et al. (2010), [7]Healy et al. (2015), [8]Hudson et al. (2004), [9]Kamphus et al. (2010), [10]Köllner et al. (2017), [11]Köllner et al. (2021), [12]Kürten et al. (2016), [13]Lee (2003), [14]Liu et al. (2020), [15]Pratt and Prather (2010), [16]Prather et al. (2013), [17]Rehbein et al. (2011), [18]Roth et al. (2016), [19]Schmidt et al. (2017), [20]Sierau et al. (2014), [21]Silva and Prather (2000), [22]Sullivan and Prather (2007), [23]Zanatta et al. (2020)

Additional to the marker species and the ion markers, the table contains the references for several studies where the respective ion markers were identified. Mainly measurements with ablation laser wavelengths of 266 nm were selected as reference to ensure comparable operating conditions to the ALABAMA measurements in this thesis. Besides the wavelength, further differences in the experimental conditions for the ionization process can occur due to different laser intensities. More specifically, variations in the laser intensity can result in different fragmentation of individual particles and, consequently, would require a different choice of marker ions. As described in Sect. 2.1.3, the laser intensity of the ALABAMA ranges roughly from $1 \cdot 10^8$ and $4 \cdot 10^9$ W cm^{-2}. In comparison with the studies listed in Table 2.1, these values are similar to laser intensities for the other SPMS studies (see Table A.2 in the appendix).

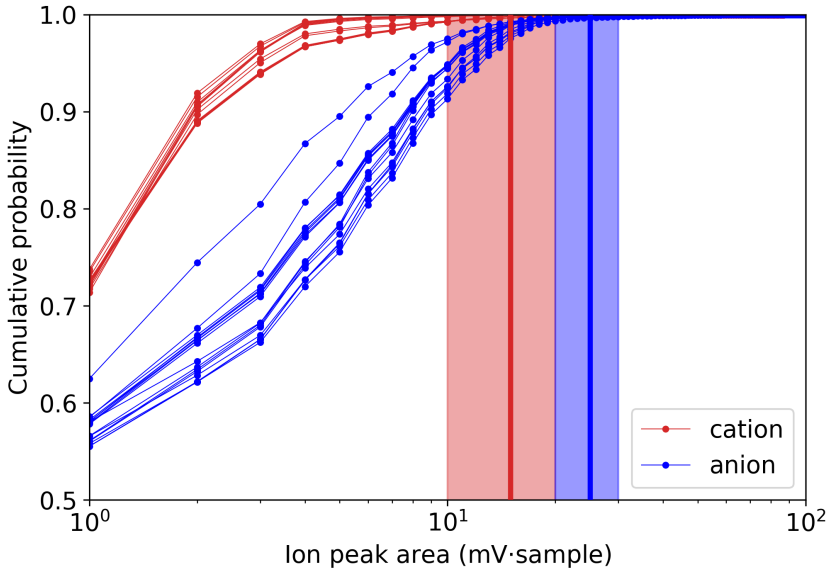

Figure 2.5: Cumulative probability distribution F_p for positive (cation; red) and negative (anion; blue) ion peak area of m/z values between $2-11$ (except m/z +7 which represents Li^+) and $245-250$ (assumed as non-occupied m/z values). Thick vertical lines indicate the selected threshold values. The red and blue shaded areas represent the uncertainty range of the defined background thresholds for cations and anions, respectively.

2.2.2 *Ion peak area thresholds*

In order to decide whether an ion signal peak is present or not, the background noise of the laser ablation/ionization must be determined. In other words, a certain threshold is needed above which a signal peak is defined as present. For this purpose, the ion signal peak intensities for mass-to-charge (m/z) ratios assumed as non-occupied were considered. In more detail, values of m/z 2-11 and m/z 245-250 were treated as background signals for both polarities. In addition, m/z +7 was excluded from positive background peaks because this peak corresponds to the Li^+ ion which can be a constituent of mineral dust (e.g. Gallavardin et al., 2008). The threshold value was then selected by counting the occurrence of these background signal peaks. Finally, the threshold was defined by the cumulative probability higher than 99 % for all non-occupied m/z values (Fig. 2.5). Consequently, the background thresholds for cation and anion spectra are 15 mV · sample and 25 mV · sample, respectively. In the literature, different threshold definitions were applied (e.g.Tolocka et al., 2004; Roth et al., 2016; Köllner et al., 2017). To account for the variability of the background signals, an interval of ±5 mV · sample was selected around the defined threshold values (see Sect. A.5).

Another possibility to determine the background noise is to run the ablation laser at a fixed shot frequency (Köllner, 2020). As the laser does not trigger particles in this case, the recorded mass spectra only provide background signals from the evacuated mass spectrometer chamber. Following this approach, 'background' mass spectra were measured before and after each research flight. The maximum ion signals of these spectra revealed values mostly within the defined variability range from the non-occupied m/z signals (not shown). Therefore, the threshold definitions indicated in Fig. 2.5 were used in this study to provide unique background thresholds for all analyzed single particle mass spectra.

2.2.3 *Determination of particle fractions*

When the characteristic ion signal peaks of a chemical species are known and a signal threshold has been determined, its abundance can be measured. This is done by counting the presence of the ion marker signals, i.e. signal intensities larger than the defined threshold, and relate this number to the total number of recorded spectra within a certain reference interval. In other words, the particle fraction (PF) containing the target species is determined for a binned reference variable. For instance, PF can be calculated for particular altitude bins, time bins or bins of individual meteorological parameters. To reduce the uncertainties of the identified fraction, the number of collected (i.e. detected and ablated/ionized) particles must be sufficient to achieve a good statistical representation. For this reason, only bins with more than 20 recorded spectra were included in this study.

2.2.4 *Scaling of particle fractions*

The obtained particle fraction (PF) by the ALABAMA only provides qualitative information about the presence of a species content. In order to achieve a more quantitative view, PF can be combined with the particle concentration measured by a reference instrument (Köllner, 2020). As the number of detected particles (C_{coinc}) can be converted to a number concentration (N_{coinc}; see Sect. 2.1.3), this can be used as reference concentration. For this purpose, the binned PF was multiplied by the mean of N_{coinc} for the respective bin:

$$PF_{scaled} = PF \cdot N_{coinc}. \tag{2.8}$$

Instead of N_{coinc} from the ALABAMA detection, also the concentration measurements by other aerosol instruments onboard of the aircraft (UHSAS and

OPC, see Sect. 2.3.2) can be used as reference. For instance, the number concentration $N_{250-1600}$ of particles in the size range between 250 and 1600 nm was chosen as benchmark for the detection efficiency (DE; see Sect. 2.1.3) of the ALABAMA. To note, the methods of size determination differ from each other, as discussed earlier. However, a comparison between $N_{250-1600}$ and N_{coinc} revealed only small differences between both approaches. In conclusion, the ALABAMA derived concentration N_{coinc} was selected as scaling reference for the particle fractions PF.

2.3 COMPLEMENTARY METHODS

The analysis of the ALABAMA measurements during the airborne field experiment was complemented by other measurement data collected onboard the aircraft, such as different aerosol and cloud properties, air mass parameters as well as trace gases. This section provides a brief introduction of the research aircraft and the additional instrumentation installed onboard the aircraft. Table 2.2 gives an overview of these complementary data sets used in this study and the corresponding instrumentation. Furthermore, the different modeling tools and included data sets for the air mass history analysis are described in this section.

Table 2.2: Overview of complementary data sets from different instruments used in this study, including parameters used in this study, measurement ranges, uncertainties and time resolution. The given information is partly adapted from Ehrlich et al., 2019.

Instrument	**Parameters used in this study**	**R: Range, A: accuracy, P: precision**	**time resolution**
Instrument	**Parameters used in this study**	**R: Range, A: accuracy, P: precision**	**time resolution**
CPC	$N_{>10}$	R: 10 nm–3 μm	3 s
OPC	$N_{250-1600}$	R: 250 nm–5 μm, A: 3 %	6 s
UHSAS-1	$N_{100-1000}$	R: 100 nm–1 μm	3 s
	$\mathrm{d}N/\mathrm{d}\log(d_p)$	R: 60 nm–1 μm, A: 10 %	3 s
UHSAS-2	$\mathrm{d}N/\mathrm{d}\log(d_p)$	R: 80 nm–1 μm, A: 10 %	3 s
CDP	N_{drop}	R: 2 –50 μm	
	LWC	A: 10 %	1 s
CIP	N_{ice}	R: 75 –1550 μm	1 s
Nevzorov probe	LWC	-	1 s
SID-3	N_{drop}	R: 5 –50 μm	1 s

Table continued on next page

Continued.

Instrument	**Parameters used in this study**	**R: Range, A: accuracy, P: precision**	**time resolution**
nose boom sensors	p	-	1 s
	T	A: 0.1 K	1 s
	RH	A: 0.4 %	1 s
	u, v	A: 0.2 m s^{-1}	1 s
Aerolaser ultrafast CO monitor	χ_{CO}	P: 1.5 ppb_v, A: 1.8 ppb_v	1 s
LI-7200	χ_{CO_2}	P: 0.05 ppm_v, A: 1.09 ppm_v	1 s
	χ_{H_2O}	P: 4 ppm_v, A: 18 ppm_v	1 s
Ozone Monitor 205	χ_{O_3}	P: 1.21 ppb_v	2 s

2.3.1 *Measurement platform and inlet systems*

The in-situ measurements of trace gases, aerosol and cloud properties as well as meteorological parameters took place on board of the *Polar 6* aircraft of the Alfred Wegener Institute (AWI, Bremerhaven, Germany). *Polar 6* is a DC-3 aircraft modified to a Basler BT-67 for flight operations in cold polar environmental conditions (Fig. 2.6; Herber et al., 2008). The cabin of the *Polar 6* is non-pressurized, thus, flight time at elevated levels of more than 4 km is limited due to the need of oxygen for pilots and operators of the installed instruments. Nevertheless, the maximum flight altitude during the ACLOUD campaign was approximately (approx.) 4.1 km. The flight speed during ACLOUD varied between 50 and 110 m s^{-1} with two modes at 65 and 100 m s^{-1} for intense in-situ sampling and ferry period to the measurement region, respectively. To achieve appropriate vertical resolutions during profile flights, ascent and descend rates of 100 to 300 m min^{-1} were chosen.

For the aerosol sampling, the *Polar 6* was equipped with two different inlet systems: a standard aerosol inlet and a CVI inlet (Fig. 2.7) operated by the Leibniz institute for tropospheric research (TROPOS, Leipzig, Germany). The standard aerosol inlet is a forward facing stainless steel inlet mounted on the front top of the aircraft ahead of the engines to avoid any impact of turbulence from the aircraft (Leaitch et al., 2016; Burkart et al., 2017a). The inlet tip consists of a shrouded diffusor (0.35 cm diameter at intake point). Inside the cabin, the aerosol inlet was connected to a 1.9 cm stainless steel manifold from which further sampling lines branches to the individual aerosol instruments. As

Figure 2.6: Picture of *Polar 6* aircraft (DC-3 modified to a Basler BT-67) from AWI.

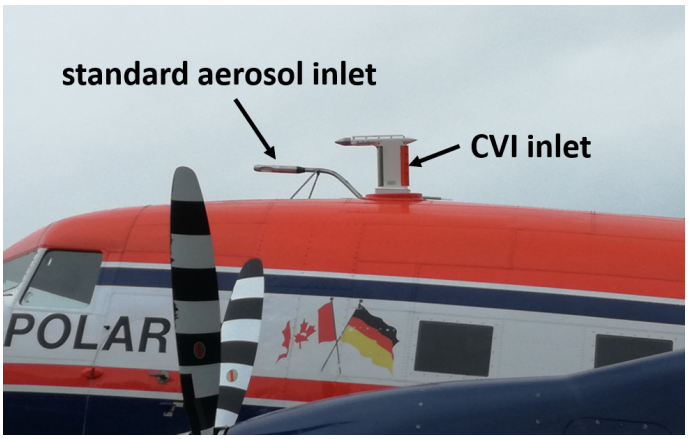

Figure 2.7: Picture of both aerosol inlets (standard aerosol inlet and CVI) mounted on top of the *Polar 6*.

the aerosol inlet is driven passively, the total air flow inside the inlet varies with the true air speed of the aircraft. By measuring the exhaust flow into the cabin (42 L min^{-1}) and using the instrument and bypass flow (13 L min^{-1}; Ehrlich et al., 2019), the inlet flow sums up to approx. 55 L min^{-1} for a flight speed of 90 m s^{-1}. Thus, considering the cross section at the intake point, the inlet was sampling under approx. isokinetic conditions ($\sim$ 86 m s^{-1} at the intake point). The particle transmission was near unity for particles in the size range between 20 nm and 1 μm and decreased to 80 % for 5 μm and down to 30 % for 10 μm (Ehrlich et al., 2019). Note that these transmission values are only valid for the inlet system. The particle size limitations for the individual instruments further depend on the corresponding sampling lines and the particle range of the instruments (see Sect. 2.1.3 and 2.3.2 for further details).

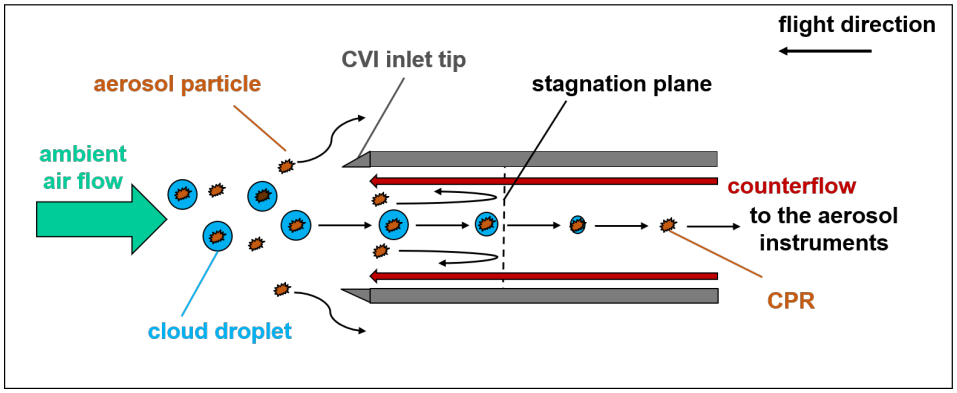

Figure 2.8: Illustration of the cloud particle residues (CPR) sampling with the counterflow virtual impactor (CVI) inlet. Only large particles (e.g. cloud droplets) overcome the stagnation plane generated by the counteracting flow inside the inlet. On their way towards the connected aerosol instruments, the water content evaporates leaving the remaining CPR.

Besides ambient aerosol particles, the analysis of cloud particle residues (CPR) was in focus of the in-situ measurements during ACLOUD. CPR are the residual particles after evaporation or sublimation of cloud droplets or ice crystals, respectively. In addition to the original CCN or INP of the cloud particle, the CPR can also contain scavenged particles or dissolved gaseous compounds. Therefore, the microphysical and chemical properties of CPR can provide important details on the aerosol properties, sources and aerosol-cloud interaction processes. To sample CPR particles, the CVI inlet was used to collect the non-precipitating cloud particles (droplets and ice crystals) and evaporates the water content (Ogren et al., 1985). As shown in Fig. 2.8, a counterflow is blowing out of the CVI inlet tip forming a stagnation plane inside the inlet. As a consequence, only particles larger than a certain size depending on the flow settings for this counterflow were collected. Smaller interstitial particles and gases are either completely deflected or decelerated inside the inlet and blown out of the CVI inlet (Ogren et al., 1985). Besides CPR, the CVI inlet was also applied to sample ambient aerosol particles by setting the counterflow to zero.

To determine particle concentrations for instruments connected to the CVI inlet, several effects must be considered and corrected. First, the enrichment factor (EF) of the CVI must be divided from the measured CPR concentrations for in-cloud measurements. EF is specified as the velocity ratio of the air volume flows in front to the flow inside the inlet tip (Ehrlich et al., 2019). For ambient sampling periods (with a counterflow of zero), EF was equal to one, whereas for sampling of CPR, EF increases to values of about 4.5 for most of the in-cloud periods. Second, the aspiration efficiency (AE) accounts for the effect

of a significant sideslip angle, i.e. a wind blowing sidewards with respect to the flight direction. This effect reduces the efficiency of cloud droplet collection for larger hydrometeors. During the ACLOUD experiments, AE varied between 0.2 and 0.8 (Ehrlich et al., 2019). Third, the overall sampling efficiency (SE) is determined by the ratio of cloud droplet number concentrations in the CVI sampling size range to the CPR concentration. As the mean cloud droplet size increases with height inside most of the sampled clouds, SE is often largest at cloud top and lowest at cloud base. For this study, only EF was included in the calculation of CPR concentrations. For this reason, the obtained in-cloud concentrations for CPR are lower than the expected CPR concentrations with regard to cloud droplet concentrations for droplets above the CVI cut-off size.

The ALABAMA and most of the other aerosol instruments (see Sect. 2.3.2) were connected to both inlet systems. To switch between the inlets, a three-way-valve was mounted upstream of the individual instruments. For CPR sampling, the valve was switched to the CVI inlet line. In case of ambient particle sampling, either the standard aerosol inlet or the CVI inlet in the ambient mode (counterflow switched off) was connected to the aerosol instruments. As the de-icing system of the standard aerosol inlet did not always work properly during ACLOUD and the inlet occasionally froze up, the CVI was permanently used as inlet system for the majority of flights. In this case, only the counterflow of the CVI was switched on while crossing a cloud. Otherwise, the instruments had to change inlet systems additionally when they were connected to the standard aerosol inlet before and after the cloud. In Sect. A.4 in the appendix, an intercomparison of ambient aerosol measurements for both inlet systems under similar atmospheric conditions is added. Furthermore, Table A.3 in the appendix provides an overview of the inlet configurations for the individual flights during ACLOUD. Further details on the inlets used in this thesis can be found in Ehrlich et al. (2019).

2.3.2 *Aerosol particle concentrations*

The *Polar 6* aircraft was equipped with further instrumentation to measure microphysical properties of atmospheric particles. A Condensation Particle Counter (CPC; model TSI-3010; Mertes et al., 1995) operated by TROPOS was deployed to measure concentrations of particles with diameters ranging from 10 nm up to 3 μm.

Two Ultra-High Sensitivity Aerosol Spectrometers (UHSAS; Cai et al., 2008) were installed in the aircraft to measure concentration and size distribution of particles. UHSAS-1 was operated by TROPOS, whereas UHSAS-2 was

supervised by AWI. Both UHSAS measured particles in the size range between 60 nm and 1 μm. However, the evaluation of the airborne measurements revealed that UHSAS-1 and UHSAS-2 could detect only particles larger than 60 nm and 80 nm, respectively (Ehrlich et al., 2019). In addition, UHSAS-1 broke during ACLOUD flight no. 19 (17 June, around 12 UTC). For this reason, the UHSAS dataset used in this thesis consists of UHSAS-1 data for flights no. 7 to 19 (27 May - 17 June) and UHSAS-2 data for flights no. 20 to 24 (18 June - 26 June). For the last flight of ACLOUD (no. 25; 26 June) and the ferry flights, no UHSAS data are available. The in-flight-comparison of both UHSAS showed a good agreement in the particle size distribution. Regarding the total concentration, UHSAS-1 indicated slightly higher values (up to 8 %) compared to UHSAS-2 for some flights (Ehrlich et al., 2019).

To measure the concentration and size of particles larger than 250 nm, an Optical Particle Counter (OPC, Grimm, model: 1.129) was operated in the ALABAMA rack. Due to sampling losses for very large particles, the upper size limit for the in-flight measurements was approx. 5 μm. While both, CPC and UHSAS data sets, offer a time resolution of 3 s, the measurements of the OPC took place in a time interval of 6 s. CPC and UHSAS-1 data are published as merged data set (Mertes et al., 2019, https://doi.org/10.1594/PANGAEA.900403), UHSAS-2 data (Zanatta and Herber, 2019, https://doi.org/10.1594/PANGAEA.900341) and OPC data (Eppers and Schneider, 2019, https://doi.org/10.1594/PANGAEA.901149) are published separately.

In comparison with the UHSAS, the OPC indicates an underestimation of aerosol number concentration (Fig. 2.9) in the overlapping size range. For this comparison, only particles between 300 and 700 nm optical diameter (d_{opt}) were included as both instruments can differ from each other in their lower and upper size range boundaries (Moore et al., 2021). Using the slope of the OPC-UHSAS correlation, a correction factor $m = (2.451 \pm 0.007)$ was found for the OPC (Fig. 2.9).

CPC, UHSAS and OPC, together, cover a broad size range for aerosol particles from 10 nm up to 5 μm. Therefore, the concentrations for individual size intervals within this broad range can be derived. For this study, three different concentrations were taken. First, the number concentration $N_{>10}$ measured by the CPC was used to cover the complete available size range. Second, the number concentration of accumulation mode particles $N_{100-1000}$ was derived as the sum of the UHSAS-1 size bins in the range between 100 nm and 1 μm. Finally, the reference concentration for the ALABAMA measurement $N_{250-1600}$ was calculated by combining the UHSAS size bins between 250 nm and 650 nm with the OPC size bins between 650 nm and 1.6 μm. Accordingly, $N_{250-1600}$ covers the complete size range of collected particles by the ALABAMA. To

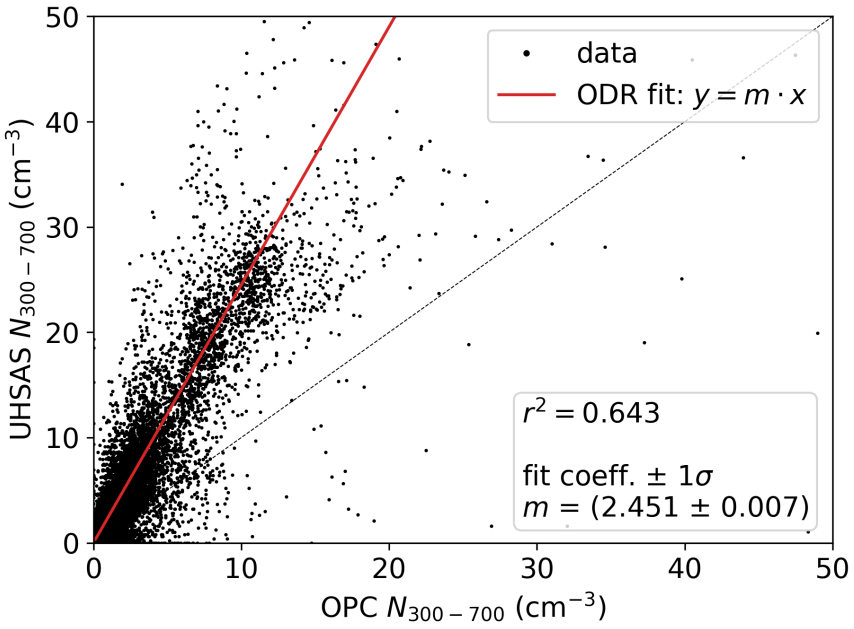

Figure 2.9: UHSAS vs. OPC aerosol number concentration in the size range between 300 and 700 nm (black dots) for the entire ACLOUD campaign and linear fit using orthogonal distance regression (ODR; red line). Fit coefficient and r^2 value are given in the description box.

note, the calculation of $N_{250-1600}$ is based on detection of optical particle size (d_{opt}), whereas the ALABAMA measures the vacuum aerodynamic diameter (d_{va}). Therefore, the reference diameters can be only regarded as approximation (see Sect. 2.1.3).

2.3.3 *Meteorological and trace gas data*

A set of atmospheric state parameters were measured onboard of the *Polar 6* by different sensors installed in a nose boom (Ehrlich et al., 2019). For this thesis, the 1 Hz merged data sets for air pressure (p), temperature (T), relative humidity (RH) and horizontal wind vectors (u and v) were used (Hartmann et al., 2019, https://doi.org/10.1594/PANGAEA.902849) A detailed description of the meteorological instruments can be found in Ehrlich et al., 2019.

A set of four different trace gases was measured during the ACLOUD field experiment: carbon monoxide (CO), carbon dioxide (CO_2), water vapor (H_2O) and ozone (O_3). Mixing ratios of these tracers were used as indicator for different air mass regimes. For example, enhancements in CO and CO_2 signals are characteristic for the influence of polluted air masses, like biomass burning

plumes or industrial emissions. In addition, the height of the planetary boundary layer (BL) can be estimated by gradients in trace gas mixing ratios.

CO was measured using the Aerolaser ultrafast CO monitor (Aerolaser, model AL5002; Gerbig et al., 1999; Scharffe et al., 2012). It makes use of the fluorescence emerging from the excitation of CO in the ultraviolet (UV) radiation range. In detail, UV radiation is produced by a resonance lamp excited by radio frequency discharge. An optical filter consisting of two CaF_2 lenses narrows the wavelength band of the emitted radiation to a wavelength λ of 150 nm which corresponds to the excitation value of CO. The fluorescence of the CO molecules is captured at a right angle by means of a PMT. Specific modifications of the instrument allow in-situ calibration during in-flight operations. During ACLOUD, calibrations were performed every 15 to 30 min using a National Institute of Standards and Technology (NIST) traceable calibration gas with a known CO concentration at atmospheric levels. Each calibration was followed by a zero measurement. Taken together, a complete calibration cycle (calibration plus zero measurement) took 110 s.

CO_2 and H_2O were measured simultaneously by the LI-7200 closed CO_2/H_2O analyzer from LI-COR Biosciences GmbH (Burba et al., 2010; Lampert et al., 2018). Specifically, the individual mixing ratios were obtained by using the absorption ratio of both species in the sample path. For this purpose, infrared light emitted by an optical source enters the sample path after passing a chopper filter wheel. Behind this sample path, the attenuated light intensity is measured by a temperature-controlled lead selenide detector. According to the attenuation law of Lambert–Beer, the light intensity reduces depending on the molecular absorption and, thus, on the density of CO_2 and H_2O. Using this relationship, the volume mixing ratios of both (χ_{CO_2} and χ_{H_2O}) can be derived. For the in-flight operations, the LI-7200 instrument was equipped with additional flow components for flow control as well as in situ calibrations. As for CO, a NIST traceable calibration standard with known CO_2 mixing ratio and H_2O close to zero was used. The calibration interval for the flight experiments was between 15 to 30 min for both gas phase species.

O_3 was measured by the 2B Technologies Dual Beam Ozone Monitor 205. Similar to the LI-7200, this instrument is based on the attenuation of light due to absorption of O_3. As ozone absorbs at a wavelength λ of 254 nm, UV light is used as radiation source. The light is guided through two separate measurement cells, one flushed with ozone and the other with ozone-filtered air. By detecting the respective intensity, the O_3 mixing ratio (χ_{O_3}) was derived. For flight no. 14 (8 June 2017), ozone data are only available from take-off to 12:58:36 UTC due to a failure of data acquisition. The trace gas data are published as a combined data set (Eppers et al., 2019; https://doi.org/10.1594/PANGAEA.901209).

2.3.4 *Cloud data*

A major goal of this study is the chemical characterization of residues from cloud particles, cloud droplets and ice crystals. For this reason, information about the microphysical properties of cloud residual particles, like number concentration and size, is required. To measure these properties, different cloud probing instruments were attached to the wings of the *Polar 6* aircraft.

In this thesis, the cloud droplet number concentration (N_{drop}) and size distribution from the Cloud Droplet Probe (CDP-2, hereafter abbreviated as CDP), operated by the Laboratoire de Météorologie Physique (LaMP, Clermont-Ferrand, France) are used (Dupuy et al., 2019, https://doi.org/10.1594/PANGAEA.899074). Since the CDP data are only available for ACLOUD flights no. 16 - 24, the size distribution data of liquid cloud particles from the the Small Ice Detector Mark 3 (SID-3), operated by the Karlsruhe Institute of Technology (KIT, Karlsruhe, Germany) were selected for the remaining flights (Schnaiter and Järvinen, 2019, https://doi.org/10.1594/PANGAEA.900261). To note, droplets were sampled in the size range of 2 - 50 μm and 5 - 45 μm using CDP and SID-3, respectively. For flights no. 8, 10, 15 and 23, no size and concentration data for cloud droplets are available.

Number concentration (N_{ice}) and size distribution of ice crystals were taken from the Cloud Imaging Probe (CIP; Dupuy et al., 2019, https://doi.org/10.1594/PANGAEA.899074), operated by KIT as well. Herein, the presence of ice crystals is defined by the availability of non-spherical particles. CIP size distribution for non-spherical particles are given in the size range between 75 μm and 3.2 mm.

Besides concentration and size, the liquid water content (LWC) derived from CDP is used for the analysis (Chechin, 2019, https://doi.org/10.1594/PANGAEA.906658). For flights without CDP data, LWC from the Nevzorov heated wire probe operated by the AWI was used instead. For flights no. 7, 8 and 23, no LWC data are available. Further information on the cloud probes installed on the *Polar 6* can be accessed in Ehrlich et al., 2019.

2.3.5 *Definition of aerosol sampling periods*

The ALABAMA was connected to both inlet systems onboard the *Polar 6*, the standard aerosol inlet and CVI inlet. The latter was used to sample CPR, whereas the standard aerosol inlet was only connected to our instruments for cloud-free measurements (see Sect. 2.3.1). To distinguish the CPR sampling periods from ambient particle measurements, a set of different parameters was

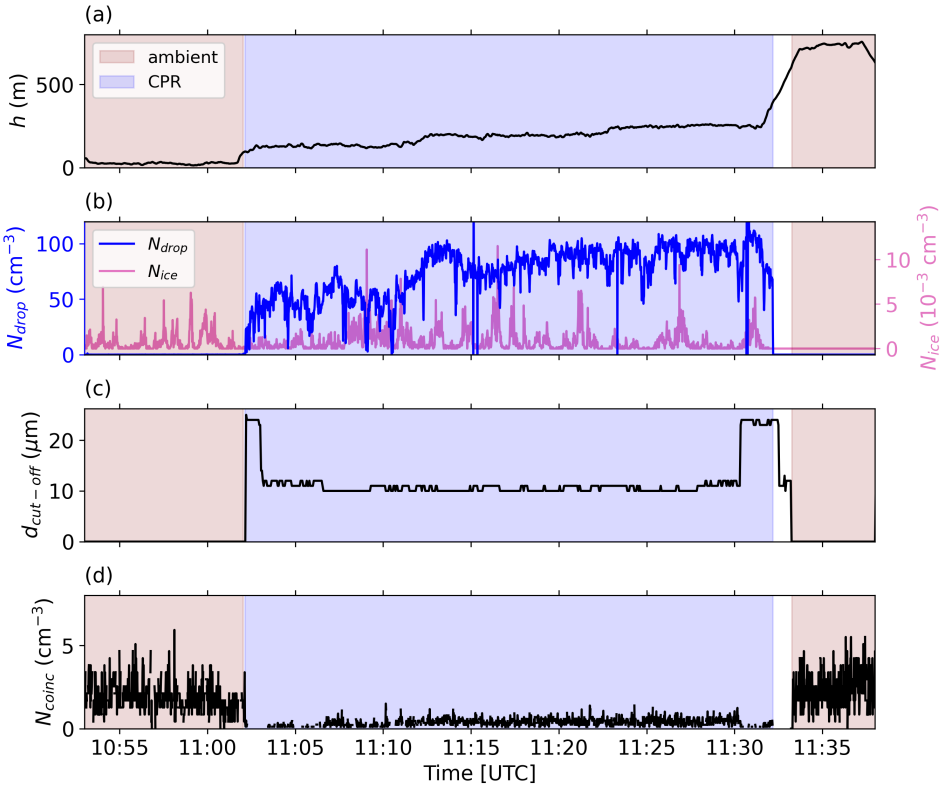

Figure 2.10: Exemplary time series of a cloud profile from ACLOUD flight no. 12 (4 June 2017), including flight altitude (h; a), cloud droplet number concentration (N_{drop}) and ice crystal number concentration (N_{ice}; b), cut-off size ($d_{cut-off}$) of the CVI inlet (c) and number concentration of detected particles by the ALABAMA (N_{coinc}; d). Periods of ambient aerosol and cloud particle residual (CPR) sampling are shaded in red and blue, respectively.

considered, as shown in an exemplary time series of a cloud transect during ACLOUD flight no. 12 (4 June; Fig. 2.10). In this example, the aircraft passed a cloud layer, starting below the cloud and ending up above the cloud, as indicated by the flight altitude (Fig. 2.10a).

The sampling periods were found via the following three steps: First, the presence of clouds was defined by the occurrence of cloud droplets ($N_{drop} > 0.5\,\mathrm{cm}^{-3}$) since the probed clouds were either pure liquid or mixed-phase clouds. As shown in the example (Fig. 2.10b), N_{ice} was not useful for cloud identification due to observations of precipitating ice crystals below cloud base as well as lacking ice-phase particles for some cloud cases. Second, the lower cut-off diameter $d_{cut-off}$ for the CVI inlet transmission indicated periods when the CVI was in CPR sampling mode. More precisely, CPR from cloud droplets larger than the given cut-off size were collected when $d_{cut-off} > 0\,\mu\mathrm{m}$ (Fig. 2.10c). In contrast, if $d_{cut-off}$ was equal to zero, the counteracting air flow inside the CVI was switched off, thus, ambient aerosol particles were sampled

by the CVI inlet. Third, a concentration of detected particles by ALABAMA (N_{coinc}) greater than zero reveals if particles entered the instrument and could potentially be ablated/ionized (Fig. 2.10d). In some cases, the presence of clouds could not be directly measured due to missing data of cloud parameters (see Sect. 2.3.4). Instead, the cloud sampling period was estimated manually using the combination of the second ($d_{cut-off} > 0\,\mu$m) and third step ($N_{coinc} > 0\,\mathrm{cm}^{-3}$).

Based on these indicators, two different flags were introduced for the ALABAMA measurements: an ambient flag and a CPR flag (color shaded periods in Fig. 2.10a-d). If both flags were zero, it means that either the counteracting CVI flow was running outside the cloud or the ALABAMA inlet was closed due to zero measurements or in-flight adjustments (see white shaded period in Fig. 2.10a-d).

In summary, the ALABAMA sampling periods for ambient particles and CPR were distinguished based on cloud presence, CVI inlet flow and number concentrations of detected particles.

2.3.6 *Air mass history modeling*

To infer the origin of aerosol particles, analysis of the air mass history using dynamical modeling tools is essential. In this study, two different Lagrangian tools were applied: the FLEXible PARTicle dispersion model (FLEXPART) and the LAGRangian ANalysis TOol (LAGRANTO) trajectory model. Both models were run with operational data from the European Centre for Medium-Range Weather Forecast (ECMWF) with 0.125 ° horizontal resolution and 137 vertical hybrid sigma-pressure levels. The temporal resolution of the meteorological data was 6 hours. In the following, both air mass history models are described in more detail.

Dispersion model FLEXPART

The dispersion model FLEXPART was developed for simulations of long-range and mesoscale transport, diffusion, dry and wet deposition as well as radioactive decay of tracers released from a certain source (Stohl et al., 2005). In this thesis, FLEXPART, version 10, was used. In principle, the model calculates trajectories of a multitude of infinitesimal small air parcels, so-called particles, by applying the following advection equation:

$$X(t + \Delta t) = X(t) + v(X, t) \cdot \Delta t, \tag{2.9}$$

with the position vector of the particle X, wind vector v, time t and time increment Δt (Stohl et al., 2005). Additionally, the calculation includes parametrizations for turbulent diffusion and convection (Stohl et al., 2005). As input data, the grid scale wind from the earlier described meteorological data set is used together with sub-grid scale turbulent and convective transport (Stohl et al., 2005).

For this air mass analysis, hypothetical particles were released from a receptor location and calculated 16 days backward in time. As release location, a certain volume was created around the airborne sampling location. For this purpose, the flights were divided in 2-min intervals. Within these intervals, the maximum and minimum position in terms of longitude, latitude and altitude mark the edges of each release volume. In this way, the dispersion simulation was executed for every 2-min interval, resulting in 40 to 175 releases for each flight, depending on the flight duration (78 to 355 min).

The output of the dispersion runs is the so-called potential emission sensitivity (PES) function. It refers to the sensitivity of an inert tracer, i.e. without deposition and chemical processes, sampled at the receptor related to the emission at a source of unit strength (Seibert and Frank, 2004; Stohl et al., 2005; Hirdman et al., 2010a; Köllner, 2020). As a consequence, the PES is proportional to the residence time of the air particles within these grid cells (Seibert and Frank, 2004; Hirdman et al., 2010a). The PES values are calculated for every six hours on a three-dimensional field, with horizontal grids of 0.25 ° spacing and eight vertical levels (0.2 , 0.4 , 1 , 2 , 3 , 4.5 , 8 and 15 km). Thus, the FLEXPART runs provide a four-dimensional PES map as output for every 2-min sampling interval.

To unveil potential ground sources for the observed aerosol particles, the four-dimensional FLEXPART PES maps were combined with a potential source inventory (PSI) map. For this purpose, the Northern hemisphere was manually divided into different geographical sectors similar to the study by Köllner (2020). The following regions were defined for the PSI map: Arctic, Alaska, northern Canada, southern North America, Pacific, Atlantic, Europe, Africa, Siberia and East Asia (see Fig. 2.11). To note, the Atlantic sector comprises the southern part of Greenland which is mainly covered by glacial ice. The southern boundary of the Arctic sector (73.5 °N) was selected based on the position of the *Polar Dome* in a previous Arctic aerosol study (Bozem et al., 2019). Apart from that, the *Polar Dome* location varies between different seasons and depends largely

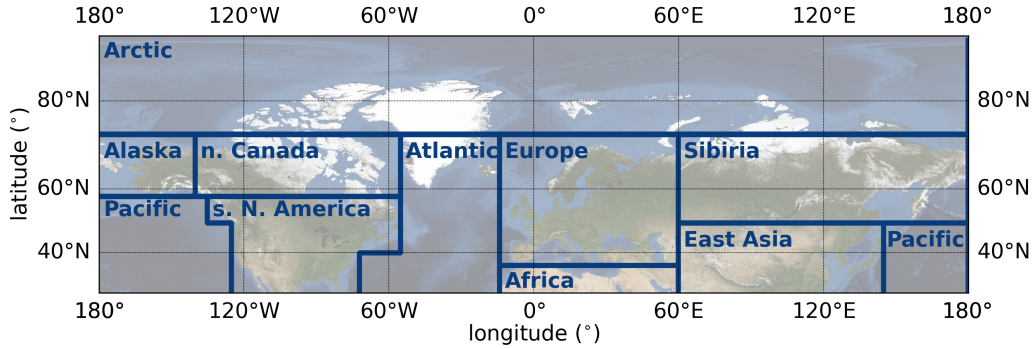

Figure 2.11: Map with defined geographical sectors for the potential source inventory (PSI). Abbreviations are defined as: n. Canada = northern Canada, s. N. America = southern North America.

on the meteorological situation (see Sect. 1.2.2; Bozem et al., 2019). Therefore, the sensitivity of the Arctic sector location was tested by shifting the bounding latitude 1.5 ° northwards and southwards, respectively, as further discussed in Sect. 3.2 as well as in Sect. B.2 in the appendix.

The combination of the PES maps and the PSI included the following steps. First, the PES grid data were summed up for the 16 days backward in time and the two lowest levels (0 - 400 m), resulting in a two-dimensional horizontal map of PES. The vertical levels (< 400 m) were selected to assure a high sensitivity to ground sources (Stohl et al., 2013). Second, PSI maps were generated specifying the geographical location of different source regions (Köllner, 2020). More precisely, the PSI maps consist of a two-dimensional flag which indicates the location of a specific source region on the same horizontal grid as the FLEXPART output. Third, the two-dimensional PES map is folded with the respective PSI map for a certain source type. Finally, the sum of PES within the matching grid cells with the source location is calculated and related to the total PES arriving at the receptor location.

Trajectory model LAGRANTO

The model LAGRANTO (Wernli and Davies, 1997; Sprenger and Wernli, 2015) was used to determine trajectories of the sampled air masses. It calculates trajectories of air parcels based on the meteorological wind fields as well. In comparison to other trajectory tools, LAGRANTO differs mainly in terms of spatial interpolation, the number of iterations used for one time step and the boundary layer implementation (Sprenger and Wernli, 2015).

In this study, LAGRANTO trajectories were initialized every 10 s at the location of airborne sampling and calculated for ten days backward in time. Together with the location of the calculated air parcels, also different state parameters (temperature, potential temperature, equivalent potential temperature, potential vorticity, specific humidity, cloud liquid and ice water content, Richardson number) were determined along the trajectories. The output of the simulated trajectories is returned for every hour. In summary, LAGRANTO provides some additional information on different properties along the trajectories, like the occurrence of clouds, which was used here to study the pathway of aerosol particles into the clouds.

2.3.7 *Data sets for potential particle sources*

Sea ice concentration

Considering sources for marine precursors and particles, the location of ice-free open ocean can be important. Therefore, satellite-based sea ice concentration data on daily basis from the University of Bremen were used (Spreen et al., 2008, https://seaice.uni-bremen.de/sea-ice-concentration/amsre-amsr2/). To compare the PES calculated by a FLEXPART simulation with the sea ice situation, the ice concentration was averaged for the respective time period of the corresponding simulations. In addition to the air mass history analysis, the sea ice concentration was used in this study to specify the surface conditions for the probed Arctic clouds. In particular, the surface conditions were classified as sea ice for concentrations $> 85\,\%$ and open water for concentrations $< 15\,\%$.

Fire maps

To study potential fire-related aerosol sources, satellite-based data sets of active fires obtained by the Visible Infrared Imaging Radiometer Suite (VIIRS) instrument were used. This instrument is installed onboard the Suomi National Polar-orbiting Partnership and NOAA-20 satellites (Schroeder and Giglio, 2021) which is jointly operated by the National Aeronautics and Space Administration (NASA) and the National Oceanic and Atmospheric Administration (NOAA). The VIIRS can detect active fires by thermal anomalies in the mid- and thermal infrared spectral range (Schroeder et al., 2014; Schroeder and Giglio, 2021).

In terms of the air mass history analysis, we are interested in the occurrence of fires within the time intervals of specific FLEXPART simulations. For this purpose, the fire observations are projected into a PSI map with the same

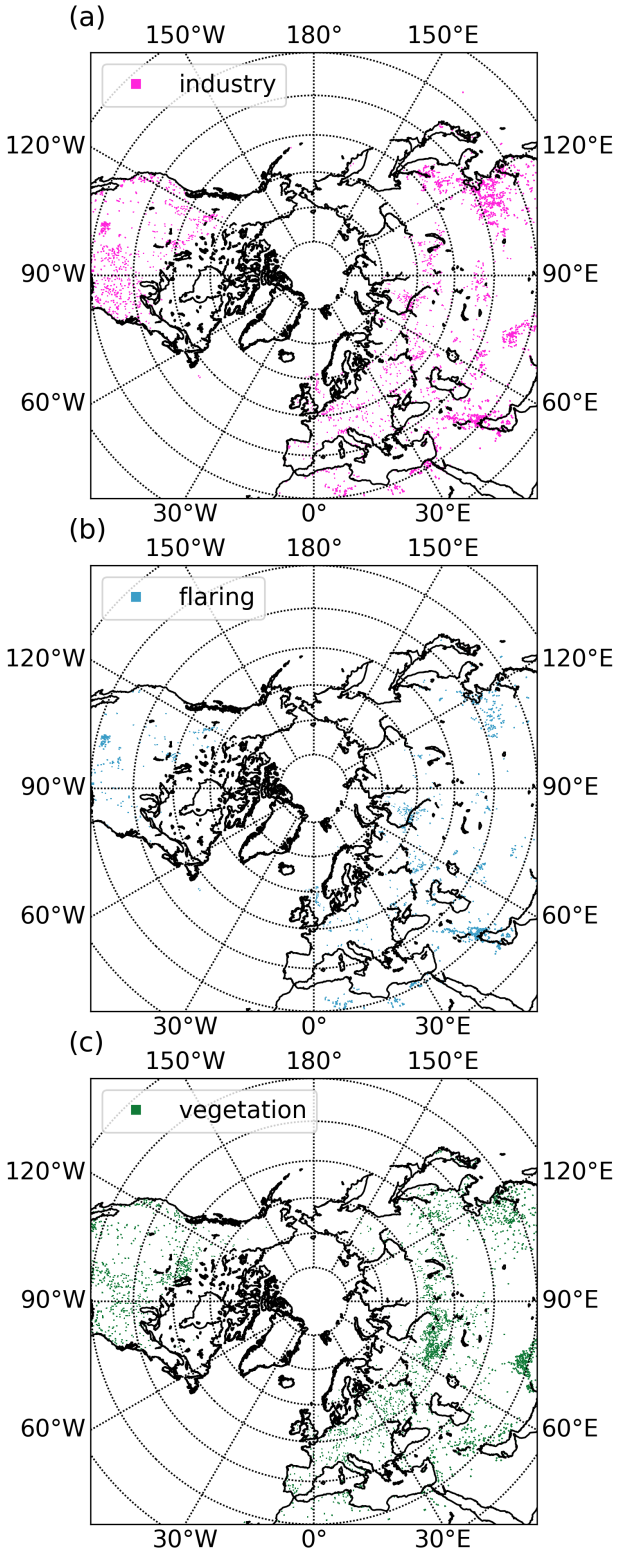

Figure 2.12: Maps with thermal anomalies within the FLEXPART output grid cells identified as industrial (a), gas flaring (b) and vegetation fires (c).

horizontal grid as the FLEXPART PES maps (0.25 ° resolution; see Sect. 2.3.6). Fires were identified by one or more observations of thermal anomalies per grid cell within the time period of the respective FLEXPART simulation.

In general, thermal anomalies include both natural vegetation fires and industrial fires (e.g. fossil-fuel combustion). To distinguish between the different fire types, a combination of data products from the VIIRS instrument was applied. First, the near real-time VIIRS 375 m Active Fire product was used to identify fire spots in a certain time period before the measurements (Schroeder and Giglio, 2021). The data were downloaded from NASA (2021). Second, the VIIRS Nightfire product provides estimates of the source emission temperatures by using the absence of solar reflectance in short-wave infrared spectral range (Elvidge et al., 2013; Elvidge et al., 2016). Using this emission temperature, industrial fire sources can be further sub-classified into gas flaring sources and other industrial fire sources. The emission of gas flares can be identified by fire spots in the VIIRS Nightfire data with emission temperatures between 1600 and 2000 K (Elvidge et al., 2016). For other industrial fires, an emission temperature above 840 K was considered (Liu et al., 2018; Köllner, 2020). The VIIRS Nightfire data were downloaded from EOG (2021).

As vegetation fires are scarce during winter in contrast to the summer period in middle and high northern latitudes, this seasonality was used as well to separate these natural fires from industrial combustion processes. Therefore, both VIIRS data sets were downloaded for two time periods: the winter period before the ACLOUD campaign (1 November 2016 until 31 January 2017) and the fire period relevant for the campaign (11 May 2017 until 26 June 2017).

Using the two VIIRS data sets and the seasonality, the fire types were classified based on three possible scenarios for a specific grid cell. First, if one or more fires occurred in the grid cell within the respective time period of the specific FLEXPART run and the same grid cell indicated an industrial fire event at least once during the winter period, this fire grid cell was assigned to an ‘industrial’ fire. Second, if the grid cell indicated a flaring fire in the VIIRS Nightfire data and occurred in the FLEXPART period as well, the cell was assigned to a ‘flaring’ fire. Finally, if no fire was detected within the grid cell in winter but a fire was detected within the FLEXPART period, the cell was assigned to a ‘vegetation’ fire. In Fig. 2.12a-c, the locations of the three fire types are exemplary shown for the time period between 20 May and 4 June 2017. This period was used for the FLEXPART simulations of a pollution case study in Sect. 4.2.2.

3

MEASUREMENT CAMPAIGN ACLOUD

3.1 CAMPAIGN OVERVIEW AND SCIENTIFIC GOALS

The aerosol and cloud observations presented in this thesis were conducted during the aircraft field campaign ACLOUD which took place in the surroundings of Svalbard (Norway) with the base airport situated at Longyearbyen, Svalbard (Wendisch et al., 2019). The period of aircraft operations was in late spring/early summer from 23 May to 26 June 2017. With the main goal of studying Arctic mixed-phase clouds and their role in the amplified warming of the polar environment, measurements were conducted using two research aircrafts from AWI: *Polar 5* and *Polar 6*. The *Polar 5* was mainly equipped with remote sensing instruments to observe the clouds from above (Ehrlich et al., 2019; Wendisch et al., 2019). Additionally, instruments for trace gas, aerosol and cloud sampling were installed onboard of the *Polar 6* to obtain in-situ information about the air mass as well as aerosol and cloud parameters (see Sect. 2.3.1). Thus, the flight patterns of the *Polar 6* mostly contain vertical profiles as well as cloud transects.

In total, 19 research flights were conducted for both airplanes, 16 of them as co-located flights, summing up to 165 flight hours. As shown by the overview of the *Polar 6* flights in Fig. 3.1, the majority of flight hours were spend in the transition zone between open ocean and closed sea ice surfaces in the northwest of Svalbard. Remarkably, clouds were sampled during each of the 19 flights of the *Polar 6*, as indicated by the blue-colored sections in Fig. 3.1. The flight altitude for the *Polar 6* varied between 70 m above sea level for below-cloud measurements up to 4 km, whereas the *Polar 5* spent most of the time above 3 km. The scientific goals and conducted flights of ACLOUD are summarized in more detail by Wendisch et al. (2019). In short, the main goals of the campaign were the characterization of boundary layer clouds with remote sensing and microphysical measurements, vertical mapping of aerosol particles, satellite validation, comparison with ground-based observations and measurements of turbulent and radiative fluxes. Table B.1 in the appendix gives an overview of all 19 flights of *Polar 6*. Furthermore, a summary of the complete data set from ACLOUD can be found in Ehrlich et al. (2019).

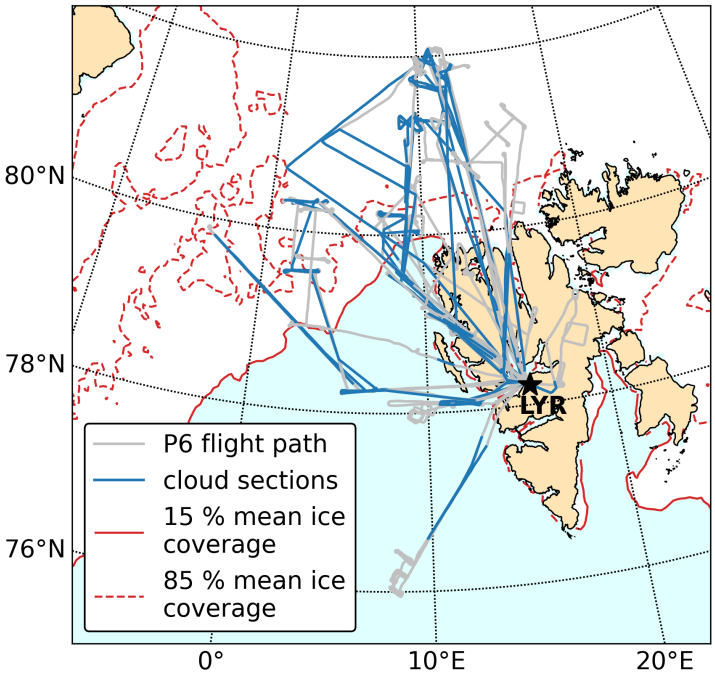

Figure 3.1: Map of all 19 flights during ACLOUD, including flight track (grey), periods of measurements inside clouds (blue) and mean sea ice concentration as 15 % contour (red solid line) and 85 % contour (red dashed line) from satellite data (see Sect. 2.3.7). The black asterisk indicates the location of the base airport in Longyearbyen (LYR).

In parallel to the ACLOUD airborne activities, a ship-based field campaign called "Physical feedbacks of Arctic planetary boundary level Sea ice, Cloud and AerosoL" (PASCAL) was conducted using the German icebreaker *Polarstern* in the vicinity of Svalbard. The first leg of PASCAL (PS 106/1) which took place in the drift ice northwest of Svalbard (reaching up to 82 °N) was coordinated with the ACLOUD flight activities. Together with different instruments onboard of the *Polarstern*, an ice-floe camp was established nearby the ship between 5 and 14 June with various measurement activities. Both, ACLOUD and PASCAL, were performed in the framework of the "ArctiC Amplification: Climate Relevant Atmospheric and SurfaCe Processes, and Feedback Mechanisms" $(AC)^3$ project (https://www.ac3-tr.de/).

3.2 ATMOSPHERIC CONDITIONS DURING ACLOUD

During the ACLOUD campaign, the measurement region was affected by different synoptical conditions. A detailed overview on the meteorological con-

ditions during ACLOUD can be found in Knudsen et al. (2018). In general, the ACLOUD experiments can be divided in three key periods: a cold period (CP; 23 - 29 May 2017), a warm period (WP; 30 May - 12 June) and a neutral period (NP; 13 - 26 June). The three periods differ in the characteristics of the air masses with respect to composition and thermodynamic structure as well as cloud occurrence as described in the following.

3.2.1 *Cold air mass period*

The first period was characterized by cold and dry air masses, with surface temperatures in Svalbard mostly below 0 °C. This cold air outbreak (CAO) was driven by a low pressure system north of Svalbard which created a northerly wind flow in the Fram Strait and at the Svalbard archipelago (Knudsen et al., 2018).

The cold and dry character of the CP is further confirmed by the atmospheric conditions during both *Polar 6* flights (27 and 29 May), especially inside the BL below 600 m above sea level. There, the potential temperature (θ) was below 270 K with relative humidity (RH) of about 50 % close to the surface (see Fig. 3.2a). Above 100 m, RH is closer to saturation which reflects the presence of clouds inside the BL as well as up to 2 km. This cloud layer was topped by a second stable inversion layer, marked by a strong increase in θ and O_3 mixing ratios (see Fig. 3.2a, c). Furthermore, particle number concentrations of accumulation mode particles ($N_{100-1000}$) indicate an increase above 2 km, together with slightly enhanced mixing ratios of CO and CO_2 (see Fig. 3.2b, d). Hence, the air mass above 2 km might be affected by pollution sources. It should be pointed out, that an additional layer of dry air mass stands out in the vertical profile (Fig. 3.2a-d) at roughly 1 km with reduced CO and CO_2 as well as increased O_3. This feature is produced by calculating the median for both flights during the CP. As shown by the individual data points of θ in Fig. B.4 in the appendix, the location of the stable inversion layer clearly differs between both flights. In addition, the statistical coverage inside individual 100 m-bins varies in the altitude range between 1 and 1.5 km. Therefore, a sudden shift in the individual air mass properties (see Fig. 3.2a-d) occurred when the impact of the individual flight on the median value weakened/strengthened due to these statistical features.

In order to characterize the air mass origin, the PES from the FLEXPART simulations were used in combination with the PSI maps of different geographical regions (see Sect. 2.3.6). Considering the PES fraction for the CP, the air in the lowest 2 km originated mainly from the inner Arctic with a contribution of

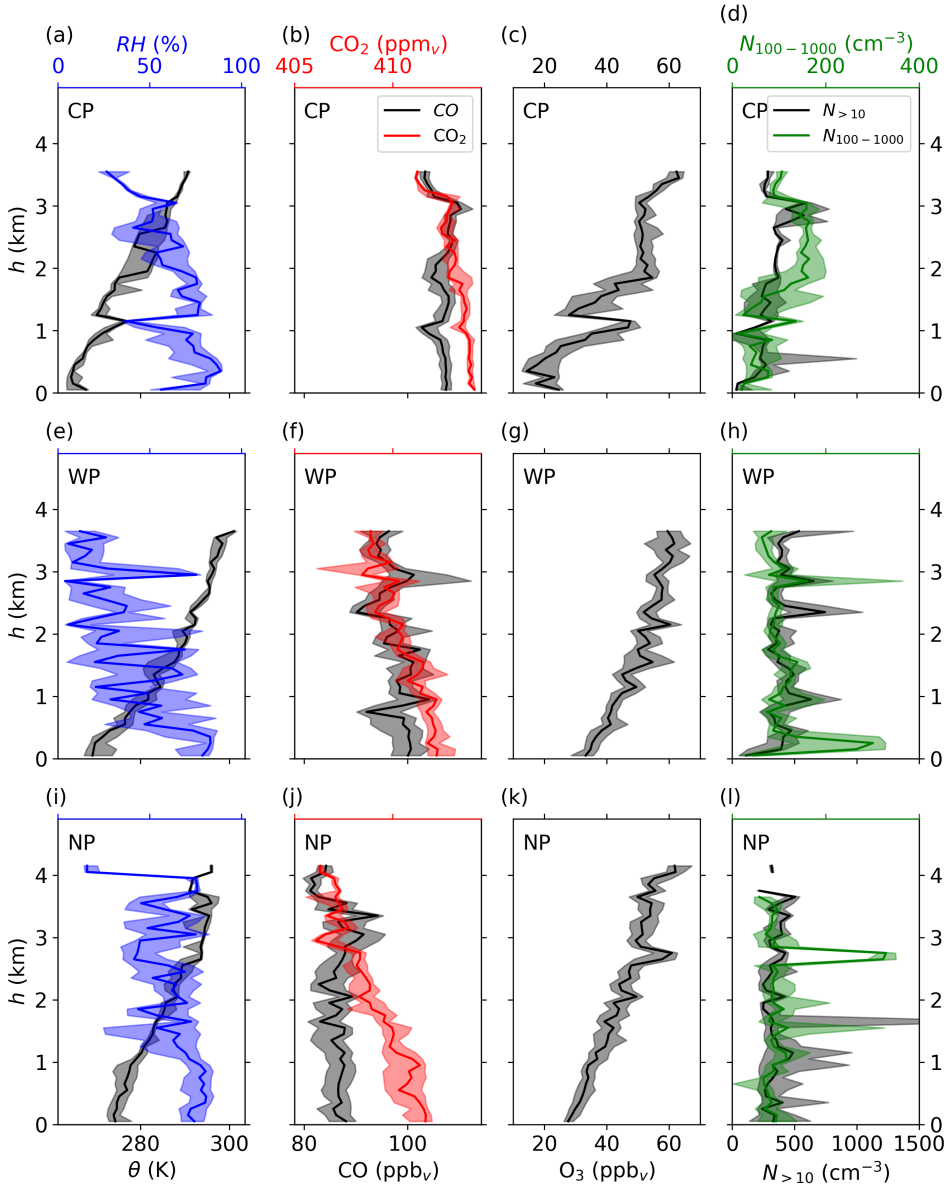

Figure 3.2: Vertical profiles of median (solid lines) and interquartile range (shaded) during the three different synoptical periods during ACLOUD: the cold period (CP; a-d), the warm period (WP; e-h) and the neutral period (NP; i-l) for potential temperature (θ; black) and relative humidity (RH; blue; a, e, i), trace gas volume mixing ratios for carbon monoxide (CO; black) and carbon dioxide (CO_2; red; b, f, j), the ozone (O_3) volume mixing ratio (c, g, k) and particle number concentrations for particles larger than 10 nm ($N_{>10}$; black) as well as particles in the size range between 100 nm and 1 μm ($N_{100-1000}$; green; d, h, l). To avoid any cloud-related effects, in-cloud periods were excluded for the shown particle concentrations (d, h, l). The effect of in-cloud measurements on the aerosol concentrations is shown in Fig. B.3 in the appendix.

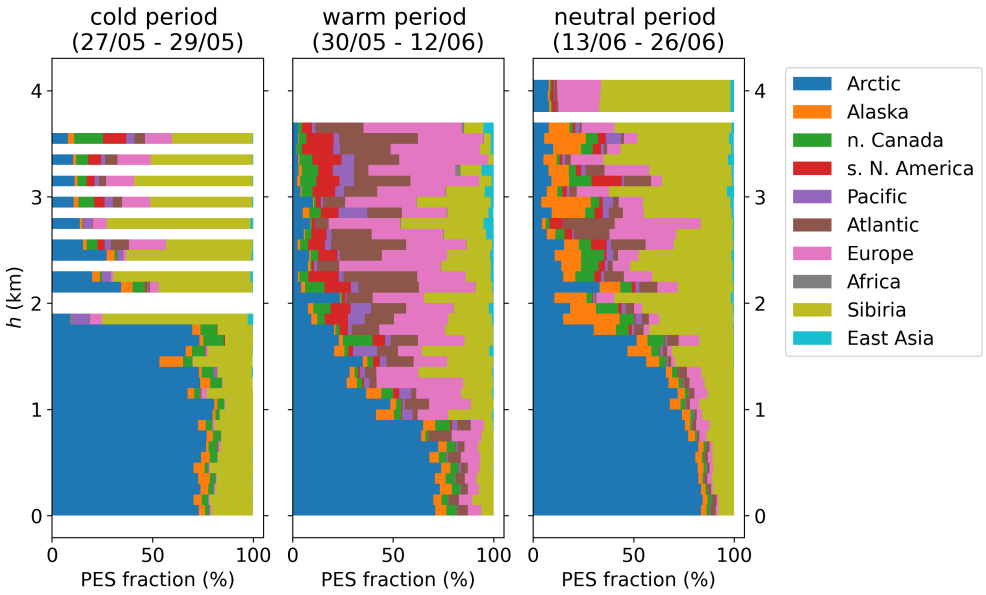

Figure 3.3: Vertically-binned cumulative contribution of source regions to sampling altitude for the three different synoptical periods during ACLOUD: the cold period (a), the warm period (b) and the neutral period (c). The contribution is given as fraction of the potential emission sensitivity ($PESF$) which is predicted by the FLEXPART model. Abbreviations are defined as: n. Canada = northern Canada, s. N. America = southern North America. Further details on the FLEXPART simulations and the source region definitions are described in Sect. 2.3.6.

about 75 % (Fig. 3.3a). In contrast, the fraction of Siberian influence increases above this level with only minor Arctic PES fraction. These differences in air mass history might explain the second inversion layer observed at the same altitude (Fig. 3.2a, c). Additionally, small contributions from mid-latitudinal regions like Europe and North America were calculated as well which might explain the increase of pollution tracers and accumulation mode particles.

Wendisch et al. (2019) summarized the cloud occurrence and phases for the ACLOUD campaign, based on the cloud time series which is adapted in Fig. 3.4. As shown by this time series, the CP was influenced by clouds inside the BL and in the free troposphere above, as already indicated by RH (Fig. 3.2a). This observation is further supported by the satellite-derived cloud-top heights ranging from 0.5 km to 1.5 km (Fig. 3.4a). As a consequence, the clouds were partly decoupled from the surface due to their high extent. Furthermore, the clouds contained a significant fraction of ice which can be explained by the cold temperatures just below freezing point during the CP.

In summary, the cold period was characterized by cold and dry air masses arriving mostly from the inner Arctic without significant contribution of pollution

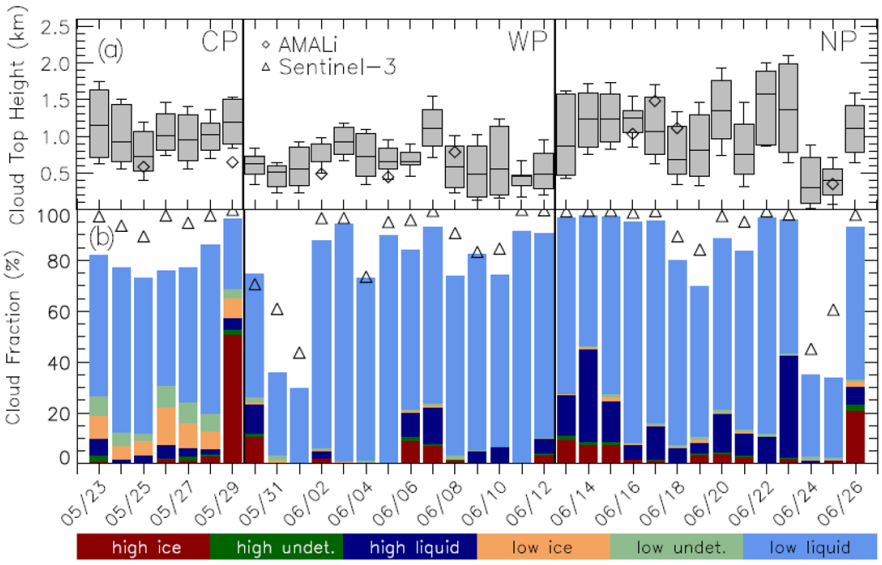

Figure 3.4: Time series of daily means for cloud top height of low-level clouds ((a; boxes show median and the interquartile range, whiskers indicate the standard deviation added to or subtracted from the mean cloud-top height), and cloud fraction of different cloud types (b) as derived from the MODIS cloud product (Collection 6.1). All values were derived for the area of airborne observations (77.5 - 80 °N, 0 - 10.5 °E and 80 - 82.5 °N, 0 - 20 °E), excluding the Svalbard archipelago. Additionally, cloud-top heights from the Airborne Mobile Aerosol Lidar (AMALi) onboard of the *Polar 5* are included as open diamonds in (a) and daily mean cloud fractions derived from the Sentinel-3 Sea and Land Surface Temperature Radiometer (SLSTR) are shown by triangles in (b). The figure is by courtesy of Wendisch et al. (2019).

sources at lower latitudes. From the climatological perspective, this CAO was extraordinary strong for this time of the year (Knudsen et al., 2018).

3.2.2 *Warm air mass period*

After 29 May, a sharp increase in surface temperature was observed in Ny Alesund (Svalbard) with a temperature increase to 17 °C until the 31 May (Knudsen et al., 2018). This temperature increase marked the transition to the next distinct period. In the following two weeks, the environment of Svalbard was affected by advection of warm and moist air masses with dominating southwesterly winds. This warm air intrusion was mainly induced by a high pressure system located south of Svalbard (Knudsen et al., 2018). In detail, two distinct warm air advection events were observed during this WP (Knudsen et al., 2018). During the first warm air event (30 May - 5 June), air was advected from the eastern Arctic Ocean to the measurement region. Thereby, the warming

occurred either due to Foehn effect from crossing the Svalbard islands or due to thermodynamic heating above the open ocean south of the islands (Knudsen et al., 2018). During the second sub-event, additional moistening of the atmosphere occurred, related to an atmospheric river event reaching Svalbard from the east (Knudsen et al., 2018).

The vertically-resolved tracer profiles yield several findings. First, warm air intruding to the Arctic free troposphere is indicated by higher values of θ compared to the CP (Fig. 3.2e). Second, the BL top height decreased significantly towards the WP with θ and O_3 values starting to rise already below 500 m above sea level (Fig. 3.2e, g). Third, a sharp inversion layer separated the moist BL with partially high particle concentrations from the warm and dry air masses aloft (Fig. 3.2e, h). It should be noted that the actual inversion layer was stronger than shown in Fig. 3.2e-h. By calculating the median profile for all WP flights, the inversion is smoothed due to the flight-to-flight variations in the BL height. Finally, a peak in particle concentrations ($N_{>10}$ and $N_{100-1000}$) occurred together with a maximum in CO mixing ratios at about 3 km which might reveal the presence of a pollution layer. This pollution signal is further analyzed in Sect. 4.2.

Regarding the origin, the influence of southerly air masses is evident, in particular for the free troposphere. Indeed, the PES fraction from the European and Atlantic sector is significantly enhanced above 1 km (Fig. 3.3b). This might also explain the presence of elevated pollution layers in the tracer profiles mentioned above. In contrast, the BL is largely influenced by inner-Arctic air and might reach further up in the ECMWF model compared to the observed BL height. A closer look to the trajectories displayed that the approaching air from northern Eurasia and the Nordic Seas crossed open ocean surfaces before reaching the region of interest. As a result, the air in the lowest levels was moistened by the water surfaces which is depicted by RH close to 100 %.

The moistening of the BL is also illustrated by the occurrence of low-level clouds with cloud-top heights of approx. 500 m (Fig. 3.4a). As the temperatures increased compared to the previous period, the vast majority of clouds were classified as liquid-only clouds (Fig. 3.4b). Throughout the WP, the sharp inversion layer covered the moist BL. Consequently, most of the observed clouds were coupled with the surface which is further analyzed in Sect. 4.3.3.

In short, the WP was influenced by warm air advection from mid-latitudinal regions which arrived in the Arctic free troposphere. Due to the cold Arctic surfaces, the air mass inside the BL was separated from the warmer air above by pronounced temperature inversions. Furthermore, the air passed open ocean surfaces while approaching the measurement region which led to additional

moistening of the BL. As a consequence, surface coupled clouds were frequently found inside the BL. In contrast to the CAO, this warm air advection period can be classified as usual for late spring in terms of the climatology (Knudsen et al., 2018).

3.2.3 *Neutral air mass period*

During the last phase of ACLOUD, a mixture of air masses showing characteristics of both, CP and WP, influenced the measurement region which led to the classification as neutral period (NP). Indeed, the air temperature was between the levels of the cold and warm phases, with values close to 0 °C and winds from different directions (Knudsen et al., 2018). Compared to the other periods, moist air masses with high *RH* were occasionally observed at different vertical levels (Fig. 3.2i). Similarly, the cloud-top height was more variable and reached up to 2 km in the satellite data (Fig. 3.4a). By the aircraft, cloud layers at even higher levels (> 3.5 km) were observed (not shown). Moreover, the FLEXPART PES fractions show contribution of inner Arctic air masses up to approx. 1.5 km for the NP. Above, the Siberian sector contributes the most, but also European and North American influence was noticed (Fig. 3.3c). Finally, more variable conditions were observed regarding the particle and trace gas concentrations with occasionally higher values above 1 km. In particular, the median profile of accumulation mode particles peaked in the altitude range between 2.5 and 3 km (Fig. 3.2l). This feature was accompanied by a small maximum in the ozone profile (Fig. 3.2j) as well as higher fractions of European and Atlantic air masses (Fig. 3.3c). However, individual flight profiles revealed rather high variability in accumulation mode particles ($N_{100-1000}$) above 1.5 km than a distinct maximum at certain levels (not shown). This is further supported by fluctuating median CO mixing ratios in (Fig. 3.2j). Indeed, both pollution tracers (CO and CO_2) obtained lower mixing ratios compared to the other air mass periods without sharp maxima, suggesting minor contribution of combustion-related sources during the NP.

Overall, the NP can be characterized as a combination of both, cold and warm period, with inner-Arctic air masses dominating up to 1.5 km. Above, the impact of more distant sources increased significantly leading to a sporadically high abundance of accumulation mode particles. However, the contribution of industrial or fire sources was low in contrast to the WP where a distinct maximum in CO was observed. To note, there was no significant influence of strong low pressure systems during the five weeks of flight operations.

4

RESULTS FROM THE ACLOUD 2017 CAMPAIGN

In the following, the results from the ALABAMA measurements from the ACLOUD campaign are presented. To address the central questions of this thesis (see Sect. 1.3), the vertical distribution of particle types will be presented. Furthermore, a pollution layer event during the WP will be characterized in terms of its aerosol properties and origin. Finally, the chemical characterization of analyzed CPR is described. The Arctic CPR composition is discussed in comparison to out-of-cloud particles, the influence of cloud thermodynamic structure, the particle origin, and their differences to mid-latitudinal cloud composition.

4.1 PARTICLE COMPOSITION IN THE ARCTIC LOWER TROPOSPHERE

In order to discuss the composition of CPR, the information about ambient particle chemical properties is important. Therefore, this section provides an overview of the particle types which were found in the summertime Arctic lower troposphere during ACLOUD. For this purpose, the overall statistics of collected particle spectra and identified particle classes are presented. Moreover, the vertical distribution for the individual particle types is demonstrated and related to the air mass periods of the ACLOUD campaign.

4.1.1 *Statistics of observed particles*

During ACLOUD, a total of 242065 particles were successfully ablated/ionized by the ALABAMA. Among these particles, 20 % were sampled inside clouds as CPR (Table C.1). For 96 % of all analyzed particles, the particle size could be determined. More than 80 % of the collected mass spectra contained signals for both polarities. For 3344 particles, no significant ion signals were found above the background threshold. In the remaining spectra, primarily signals at positive ions (cations) were present, whereas the fraction of spectra with single negative ion signals (0.02 %) was negligible.

Based on the marker method described in Sect. 2.2.1, the recorded particle spectra were scanned for the presence of ion signals that are characteristic for

Table 4.1: Overview of the absolute and relative abundance of different chemical species in the particles analyzed by the ALABAMA during the ACLOUD campaign, including potential sources (summarized from literature in Sect. 1.2).

Species	**No. of particles (relative contribution in %)**	**Potential sources (from Sect. 1.2)**
Ammonium (amm.)	198 631 (82.06 %)	secondary formation, long-range transport, local seabird colonies
Sulfate (sulf.)	184 025 (76.02 %)	secondary formation, DMS as Arctic presursor, long-range transport
Amine	139 962 (57.82 %)	secondary formation, marine biogenic precursor gases, long-range transport
* with trimethylamine (TMA)	100 562 (41.54 %)	
* with tri-/diethylamine (TEA/DEA)	39 400 (16.28 %)	
Potassium (pot)	122 935 (50.79 %)	local sources, inorganic salts, long-range transport
Sea spray (NaCl)	41 864 (17.29 %)	open water surfaces, sea ice, also transported sea spray material
Dicarboxylic acids (DCA)	14 988 (6.19 %)	local and remote VOC as precursors
Vanadium (van.)	10 911 (4.50 %)	heavy oil fuel combustion
Elemental carbon (EC)	3 416 (1.41 %)	combustion, vegetation fires
Non-sea-spray nitrate (nss nit.)	2 423 (1.00 %)	long-range transport
Iodine (iod.)	2 276 (0.94 %)	open ocean surfaces
Silicate (sil.)	1 704 (0.70 %)	mineral dust, soil-related
other signals	15 108 (6.24 %)	

the individual species. Table 4.1 provides an overview of the frequencies of particles containing a certain species. It is apparent from this table that particles containing ammonium (82 %), sulfate (76 %) and amines (58 %; including both, trimethylamine- (TMA) and tri-/diethylamine- (TEA/DEA) containing particles) were most abundant in this study. As all of these species are associated with secondary particle formation via acid-base reactions (see Sect. 1.2.4), the internal mixing of these species is of particular interest. For this reason, hierarchical markering was used to determine the abundance of particles including mixtures of amines, ammonium and/or sulfate. In Fig. 4.1, the hierarchical order is demonstrated. In more detail, the particles were first checked for amine-content, followed by sulfate- and finally ammonium-signatures. Since most of the identified amine spectra also included the characteristic ion signal for ammonium (m/z +18; NH_4^+), the specification of ammonium-amine-mixtures was skipped for this classification. In addition, potassium-containing particles were excluded from this particle classification although they occurred for half of the analyzed particles. Potassium is one of the most abundant species in the Earth's crust and often related to aerosol from biomass burning (Silva et al., 1999; Sullivan and Prather, 2005; Schill et al., 2020). However, since the ionization energy of potassium is low, distinct m/z signals of K^+ ions appear in the mean mass spectra of all analyzed species (see Fig. C.17-C.20 in the appendix).

As described in Sect. 2.2.1, two types of amines were distinguished in this study based on the marker method: trimethylamine (TMA) and tri-/diethylamine (TEA/DEA). TMA was already observed in the summertime Arctic associated with marine biogenic sources (see Sect. 1.2.4; Köllner et al., 2017; Köllner, 2020). The other particulate amine type (TEA/DEA) with an ethyl-structure was analyzed for the first time in the Arctic environment. Regarding their fractional occurrence, the majority of amine-containing particles was identified as TMA (see Table 4.1). However, TEA/DEA-containing particles still accounted for almost 30 % of the analyzed amine particles which mostly appeared inside clouds (see Sect. 4.3).

In Fig. 4.2, the mean mass spectra of both amine species are displayed. For TMA, the mean spectrum shows significant ion signal peaks at the characteristic markers m/z +58 ($C_3H_8N^+$) and m/z +59 ($C_3H_9N^+$; see Fig. 4.2a). However, the TMA-spectra are dominated by sulfate and potassium peaks on average, with smaller contributions of sea spray (NaCl), nitrate and further organic signals. In contrast, the spectra for TEA/DEA show a clear signal at m/z +86 ($C_5H_{12}N^+$) in addition to m/z +58 and +59 (Fig. 4.2b). Furthermore, a small signal peak at +101 ($C_6H_{15}N^+$) is present which corresponds to the molecular peak of TEA. Therefore, the identified TEA/DEA type might represent TEA

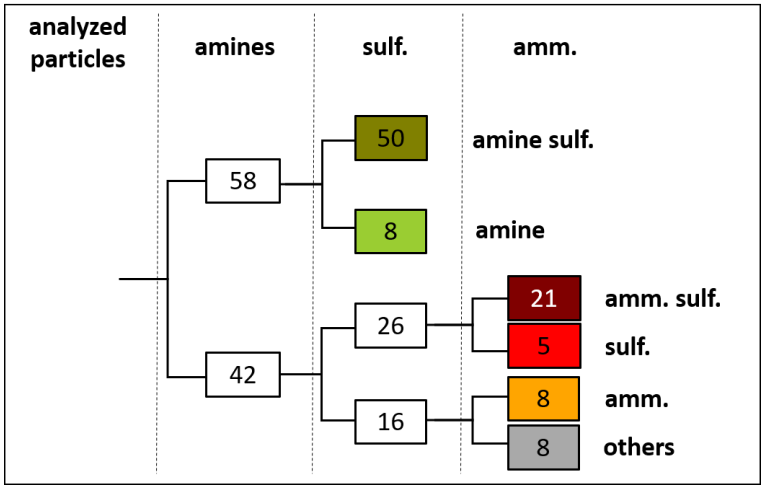

Figure 4.1: Schematic overview of the decision tree for the hierarchical markering. All analyzed particles were checked for amine, sulfate (sulf.) and ammonium (amm.) marker ion signals in the given order from left to right. Numbers represent the fraction of particles containing the individual mixing state based on the 242065 collected particle spectra during ACLOUD. The colored boxes indicate the obtained particle types used in this study. It must be noted, that the internal mixing of amines with ammonium was not considered since most of the amines contained an ammonium-signal as well which might also appear due to amine-fragmentation (Angelino et al., 2001).

rather than DEA in this study. This idea is further supported by the correlation of all m/z positions to the characteristic ion markers m/z +58 for TMA and m/z +86 for TEA/DEA (see Fig. C.16 in the appendix). Indeed, the correlation of the molecular signal m/z +101 and the protonated ion m/z +100 for TEA to the marker signal m/z +86 is high. Thus, it is likely that the mass spectra denoted here as TEA/DEA represent TEA. Nevertheless, the notation as 'TEA/DEA' is kept for this thesis since the identification of TEA by the ALABAMA needs to be confirmed by laboratory measurements.

Besides the species discussed above, the following species were also identified in the analyzed spectra: sea spray (NaCl), DCA, vanadium (van.), EC, non-sea-spray nitrate (nss nit.), iodine (iod.) and silicate (sil.). As shown in Table 4.1, their abundance was much lower compared to ammonium, sulfate and amines, with percentages mostly below 10 %. Therefore, these particles were only checked for the occurrence of the respective species, instead of considering internal mixtures with other species. NaCl-containing particles, referred to as sea spray, still account for a fifth of the sampled particles. However, since they were primarily externally mixed with the three dominating species (ammonium, sulfate and amines), internal mixtures of sea spray containing particles with those substances were neglected as well. An overview of the average mass

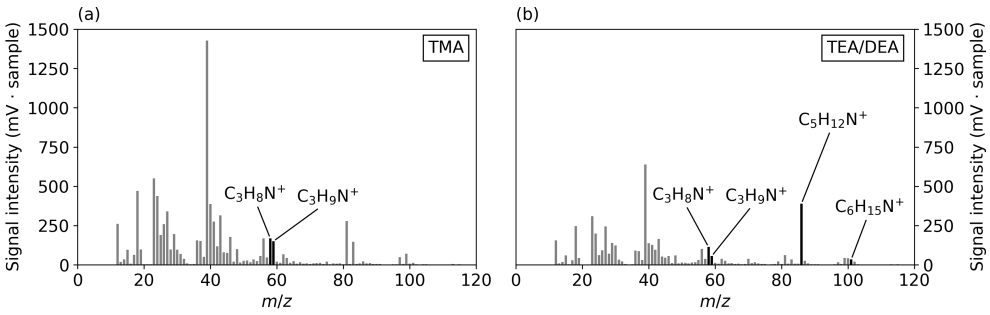

Figure 4.2: Mean positive mass spectrum of all analyzed particles for (a) trimethylamine- (TMA) containing and (b) tri-/diethylamine- (TEA/DEA) containing particles. Characteristic peaks are denoted.

spectra for particles containing the individual species is given in Sect. C.4 in the appendix.

4.1.2 *Vertical distribution of particle types*

In this section, the vertical structure of the previously defined particle types will be described based on the three air mass periods during ACLOUD (CP, WP and NP; see Sect. 3.2). For this purpose, the particle fractions (PF) and the scaled particle fraction (PF_{scaled}) were determined for the individual particle types within certain altitude bins (bin width of 100 m) for each period. In general, the chemical composition exhibits a different composition between the lowest vertical levels corresponding to the Arctic BL and the free troposphere above, in particular for the WP which was characterized by strong temperature inversions topping the BL (see Sect. 3.2.2).

For the three most abundant particle species, the following relationships were observed from the vertically-resolved composition (see Fig. 4.3). First, the fraction of amine-containing particles decreased with altitude. Second, amines and ammonium, both, were internally mixed with sulfate with only a few percent of both substances not containing sulfate. Third, with decreasing amine-content, the ammonium sulfate fraction increased towards higher altitudes. Forth, considering the amine sub-classification, almost all ambient amine particles contained TMA but only a few of them contained TEA/DEA which mostly occurred in the NP (Fig. 4.4). Finally, the scaled fractions confirm the trends for these particle types. However, the increase of scaled TMA fraction towards lower altitudes was only noticed during the WP. For the other two periods, the total aerosol number concentrations were significantly lower close to the surface (see Fig. 3.2d, l). As a result, all particle types dropped at the lowest levels. In

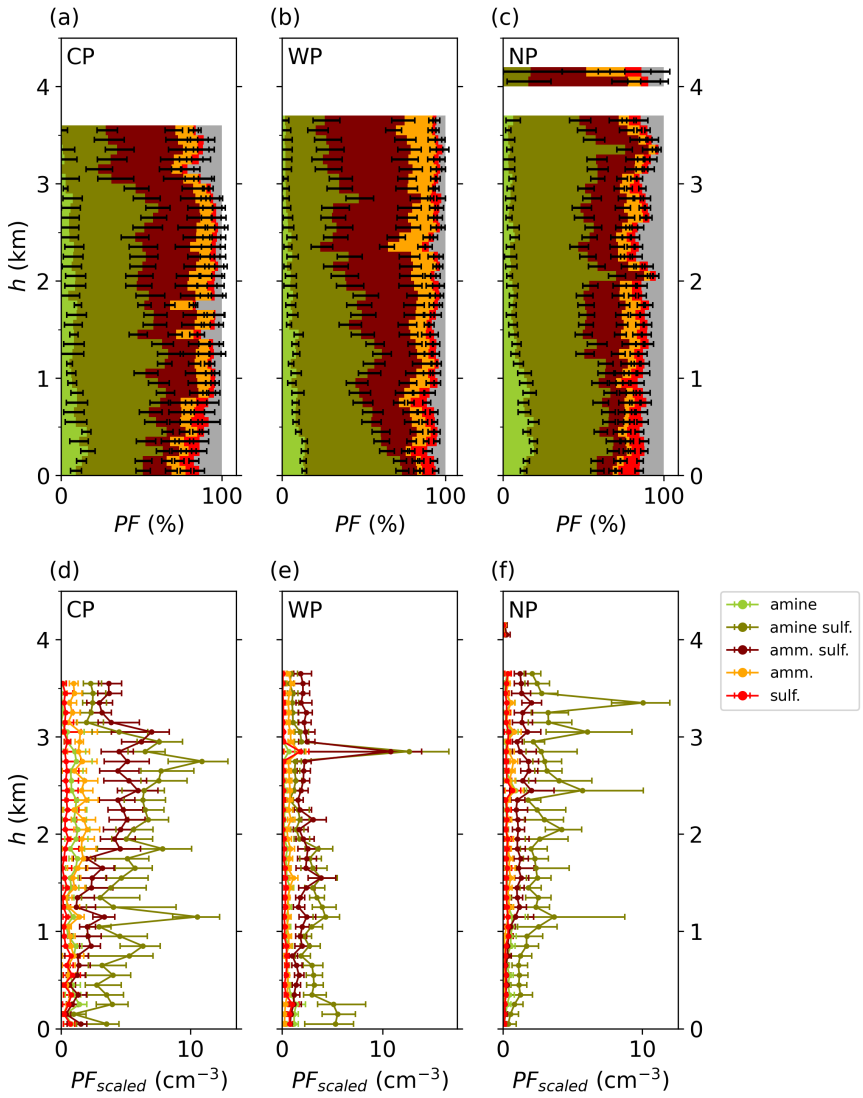

Figure 4.3: Vertically-resolved amine-, ammonium- and sulfate-containing particles as well as their internal mixtures analyzed by the ALABAMA during the cold (CP; a, d), the warm (WP; b, e) and the neutral (NP; c, f) air mass period. The particle fractions (PF) are displayed in (a), (b) and (c), the scaled particle fraction (PF_{scaled}) in (d), (e) and (f), respectively. The acronyms are defined as follows: amine sulfate (amine sulf.), ammonium sulfate (amm. sulf.), ammonium (amm.) and sulfate (sulf.). Altitude bins with less than 20 recorded particle spectra are excluded. Bins with less than 20 analyzed particles were removed from this overview. Further details about the determination of PF, PF_{scaled} and the corresponding uncertainties are provided in Sect. 2.2.3, 2.2.4 and A.5, respectively.

short, the vertical distribution of aerosol composition indicates a potential surface-based Arctic source for TMA.

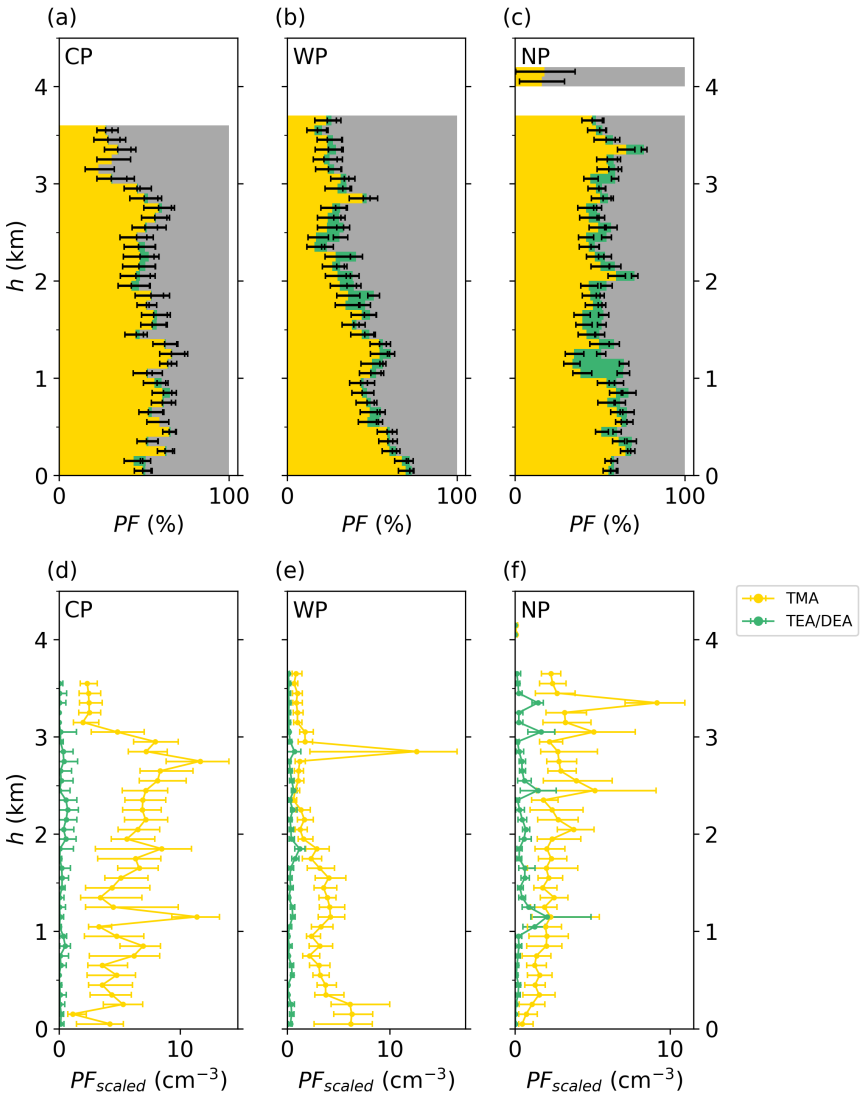

Figure 4.4: Vertically-resolved distribution of particles containing trimethylamine (TMA) and tri-/diethylamine (TEA/DEA) analyzed by the ALABAMA during the cold (CP; a, d), the warm (WP; b, e) and the neutral (NP; c, f) air mass period. The particle fractions (PF) are displayed in (a), (b) and (c), the scaled particle fraction (PF_{scaled}) in (d), (e) and (f), respectively. Altitude bins with less than 20 recorded particle spectra are excluded. Bins with less than 20 analyzed particles were removed from this overview. Further details about the determination of PF, PF_{scaled} and the corresponding uncertainties are provided in Sect. 2.2.3, 2.2.4 and A.5, respectively.

The vertical profiles of particles containing the other investigated particle species for the three periods are displayed in Fig. 4.5. As shown in this figure, NaCl particles revealed a similar trend to particulate amines with decreasing abundance with altitude, even though the reduction is smaller compared to TMA. Interestingly, sea spray fractions remained high when air masses originated

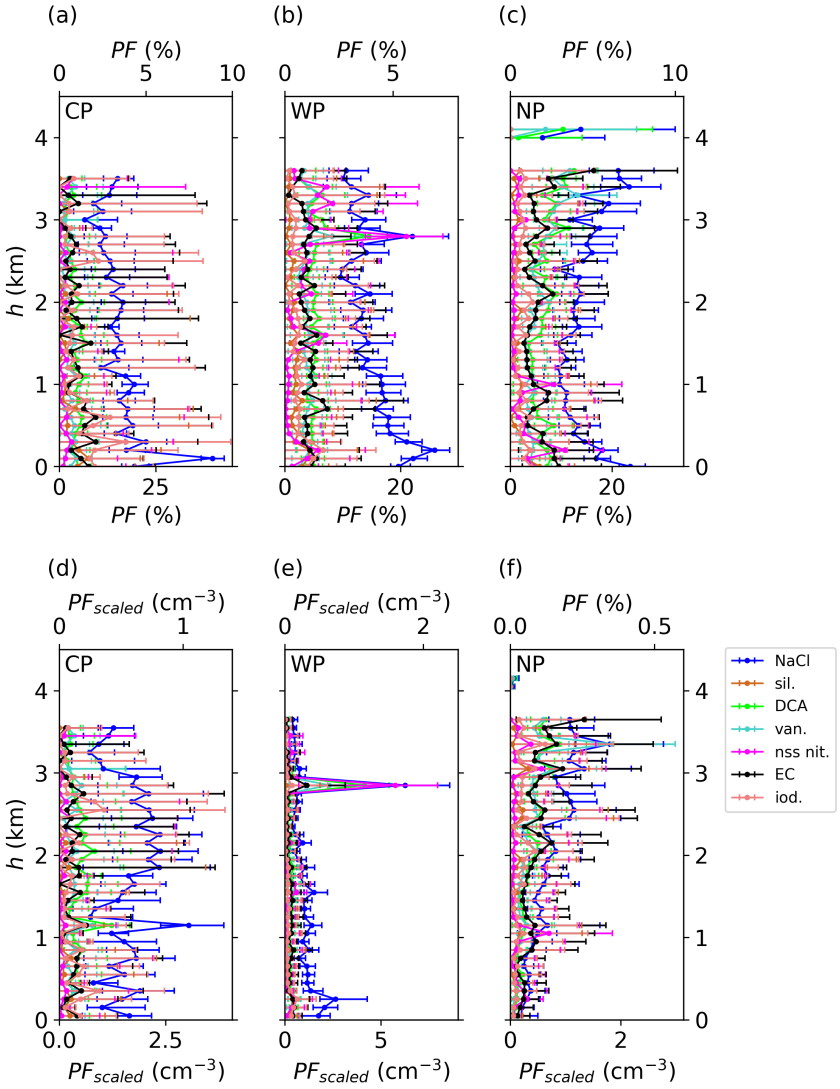

Figure 4.5: Vertically-resolved distribution of particles containing further species analyzed by the ALABAMA during the cold (CP; a, d), the warm (WP; b, e) and the neutral (NP; c, f) air mass period. The particle fractions (PF) are displayed in (a), (b) and (c), the scaled particle fraction ($PF \cdot N$) in (d), (e) and (f), respectively. The acronyms are defined as follows: sea spray (NaCl), silicium (sil.), dicarboxylic acids (DCA), vanadium (van.), nss nitrate (nss nit.), elemental carbon (EC) and iodine (iod.). Bins with less than 20 analyzed particles were removed from this overview. Further details about the determination of PF, PF_{scaled} and the corresponding uncertainties are provided in Sect. 2.2.3, 2.2.4 and A.5, respectively.

from closed sea ice areas as observed during the cold period. This suggests a sea ice-related source for NaCl-containing particles in addition to the open ocean. Similarly to sea spray, the fraction of iodine-containing particles slightly dropped with height but the significance is very low because of low statistics

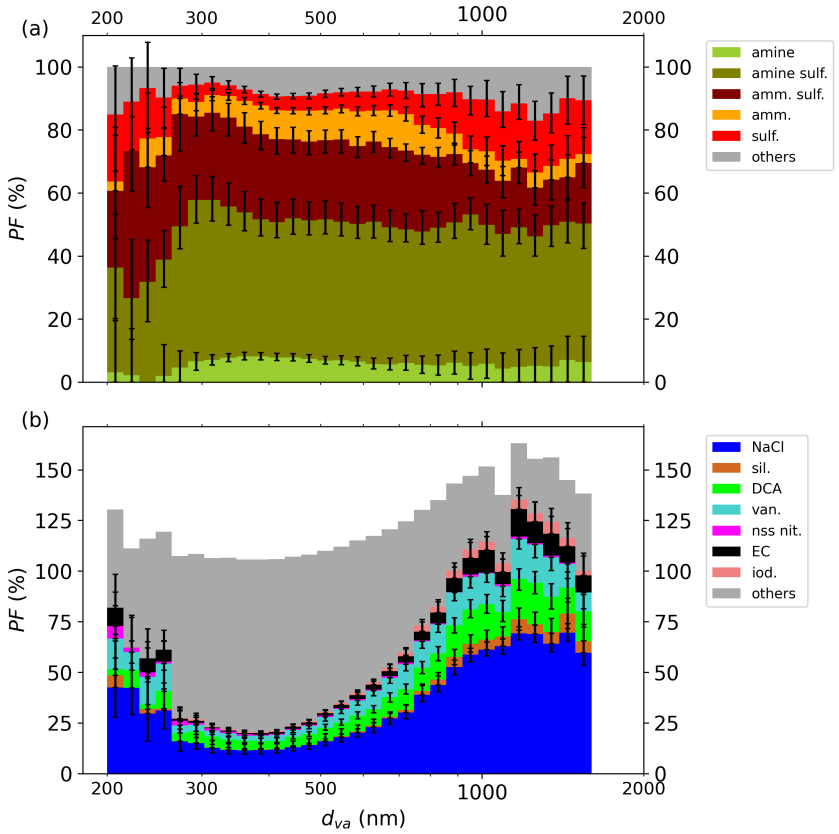

Figure 4.6: Size distribution with particle fraction (PF) of ambient particles containing different chemical species analyzed by the ALABAMA for substances from hierarchical markering (a) and for further identified species (b). To note, accumulated PF of the latter exceeds 100 % since internal mixing of these species is not considered. Therefore, accumulated PF beyond 100 % describes the degree of internal mixing among these substances. Bins with less than 20 analyzed particles were removed from this overview. Further details about the determination of PF and the corresponding uncertainties are provided in Sect. 2.2.3 and A.5, respectively.

for this particle type (see Table 4.1). The appearance of EC and nss nitrate particles did not change vertically and between the periods. For vanadium- and DCA-containing aerosol particles, at least a weak rise in the scaled fractions was obtained during the NP. Fig. 4.5 also shows a noticeable peak for most of the substances at 3 km during the WP. Indeed, this layer containing a large variety of substances marks the presence of polluted air masses from mid-latitudes, as will be further detailed in Sect. 4.2.

Besides the vertical distribution, also the size-resolved chemical composition of ambient particles suggests the occurrence of several species in aged air masses. From the size distribution in Fig. 4.6b, substances such as EC, DCA, vanadium, iodate, silicate and sea spray (NaCl) were enriched for large particles. Furthermore, an overlap among the PF of those species in the upper size

range indicated a high degree of internal mixing for these large particles. In addition, the increasing fraction of sea spray-containing particles was internally mixed with either sulfate, corresponding to the 'sulfate only' particles in Fig. 4.6a, or with nitrate. For these reasons, the composition of particulate matter with diameters of $\sim 1\,\mu$m might relate these particles to chemical aging. In contrast, amine and ammonium sulfate-containing particles dominated the particle composition for small particles (Fig. 4.6a) with around 25 % of the other species at 400 nm. Thus, particles in this size range might represent more freshly formed atmospheric particles.

4.1.3 *Summary and discussion with literature*

The presented ALABAMA results of ambient aerosol composition will now be discussed in the context of the current knowledge about Arctic aerosol particles during summer. In previous field experiments, the chemical composition of single particles was mainly limited to ground- and ship-based experiments (e.g. Sierau et al., 2014; Gunsch et al., 2017). So far, only two studies of aircraft-based measurements of the single particle composition were reported in the Arctic, one located in Alaska (Zelenyuk et al., 2010) and the second conducted in the Canadian Arctic (Köllner et al., 2017; Köllner et al., 2021). Therefore, the results presented in this study add valuable information on the vertically-resolved particle composition to the current knowledge of Arctic aerosol.

One interesting finding is that ambient particles during ACLOUD often contained a mixture of sulfate and amines, represented by TMA. Particles containing this internal mixture showed a decreasing tendency with increasing altitude, in particular for meteorological situations with a clearly defined separation of BL air and the free troposphere. This result reflects those of Köllner et al. (2017) who also found frequently internal mixing of TMA and sulfate in the Canadian Arctic with a maximum in the BL. Furthermore, Dall'Osto et al. (2019) related the presence of low-molecular weight amines, including TMA, to micro-biota of sea ice and sea ice-influenced ocean in the Southern Ocean. Prior laboratory and chamber studies demonstrated acid-base reactions (for example with sulfuric acid) as important pathway for aminium salt formation (e.g. Angelino et al., 2001; Murphy et al., 2007). Therefore, the high degree of internal mixing with sulfate indicated the neutralization of sulfuric acid and MSA as important pathway for the formation of TMA-containing particles. Overall, the high abundance of TMA inside the BL further supports previous findings of a marine biogenic origin for these secondary amine particles. In Sect.

4.3.5, the observation of amine particles will be further discussed in the context of Arctic clouds.

As evident from the literature, ammonia competes with amines in neutralizing available acids (e.g sulfuric acid; Murphy et al., 2007; Pratt et al., 2009; Ge et al., 2011b). More specifically, amines are stronger bases compared to ammonia (Ge et al., 2011b; Liu et al., 2018). In the presented measurements, ammonium-containing particles were internally mixed with sulfate to a large extent, suggesting their secondary nature formed by acid-base reactions. Especially in the Arctic free troposphere where the TMA-content in the particles declined ammonium sulfate particles were dominant. Simultaneously, air mass history revealed an important contribution of long-range transport to the abundance of particles containing ammonium-sulfate mixtures. This result is in agreement with previous studies reporting significant contribution of ammonium and gas-phase ammonia from outside the Arctic (Fisher et al., 2011; Lutsch et al., 2019b; Köllner et al., 2021). However, inner-Arctic ammonia sources, such as seabird guano emissions (Croft et al., 2016a; Wentworth et al., 2016), might have contributed as well. Indeed, the internal mixture of TMA sulfate particles with ammonium inside the BL corroborates these earlier studies.

An substantial contribution to marine secondary aerosol is expected to originate from distinct NPF events (e.g. Burkart et al., 2017b; Dall'Osto et al., 2017). Aerosol concentrations onboard of *Polarstern* showed two NPF events occurring above the sea ice northwest of Svalbard: the first NPF on 1 June and the second on 18 June (Kecorius et al., 2019). One day after the first event, a high concentration of accumulation mode particles was observed by the airborne instruments above the sea ice. These particles might have resulted from the previous NPF event after subsequent growth. During the flight on 18 June, indeed, high concentrations of small particles between 10 and 60 nm were measured inside the BL onboard of the *Polar 6*. However, these particles could not be analyzed by the ALABAMA as they were too small.

Another interesting finding of the current study was the observation of sea salt particles in inner-Arctic air masses originating from the sea ice. In accordance with the presented results, previous work have demonstrated the production of sea salt aerosol from sea ice surfaces from frost flowers and blowing snow (Yang et al., 2008; Seguin et al., 2014; Xu et al., 2016; Huang and Jaeglé, 2017). These observations were associated with high wind speeds during winter and spring (e.g. Leaitch et al., 2013; Huang and Jaeglé, 2017). However, the current study suggests that NaCl-containing particles from sea ice surfaces can contribute significantly to Arctic aerosol during cold air outbreak events in early summer.

Besides NaCl, also particle types associated with natural origin were observed during ACLOUD. Several studies reported a contribution of iodic acid (HIO_3) to NPF and particle growth in the Arctic, especially during the spring-to-summer and the summer-to-autumn transition periods (Allan et al., 2015; Sipilä et al., 2016; Baccarini et al., 2020; He et al., 2021). However, the findings of the current study demonstrated only a minor contribution of iodine to the observed particles. Baccarini et al. (2020) observed iodine-related NPF events linked with high ozone values and freezing onset in the Arctic Ocean. As the ozone levels were relatively low inside the BL during ACLOUD and the campaign was affected by melting rather than re-freezing of the ice, the influence of iodine on NPF might be low in summer compared to spring and late summer/autumn. Nevertheless, it can not be excluded that iodine was present in particles smaller than the ALABAMA size range.

Considering mineral dust, a potential contribution of transported material from mid-latitudes was reported in previous literature, in particular during spring (e.g. Rahn et al., 1977; VanCuren et al., 2012; Huang et al., 2015; Groot Zwaaftink et al., 2016). The results of the current study, however, cannot confirm a large contribution of dust-containing particles in early summer. It is important to note, that here only silicium-content was considered as reference for dust. There are more potential signatures for mineral dust in single particle mass spectrometry, such as potassium, calcium, iron and magnesium ion signal peaks (Gallavardin et al., 2008).

To conclude, the Arctic lower troposphere was characterized by a high abundance of sulfate-, ammonium- and TMA-containing particles. During the WP, in particular, substances associated with marine origin, like sea spray- and TMA-containing particles were enriched inside the BL. In the upper flight levels, where the amine content was reduced, ammonium sulfate particles were dominating the particle composition analyzed by the ALABAMA. The observed particle fractions of typical combustion species were very low, except for an elevated pollution layer during the WP, which will be further characterized in the following section. Together with the low mixing ratios of pollution tracers (see Sect. 3.2), it can be concluded that the influence of polluted air masses was weak throughout the ACLOUD campaign.

4.2 CHARACTERIZATION OF A DISTINCT POLLUTION EVENT

During the WP, a distinct layer of polluted air masses was identified in the average vertical profiles at almost 3 km. In this section, the chemical and physical

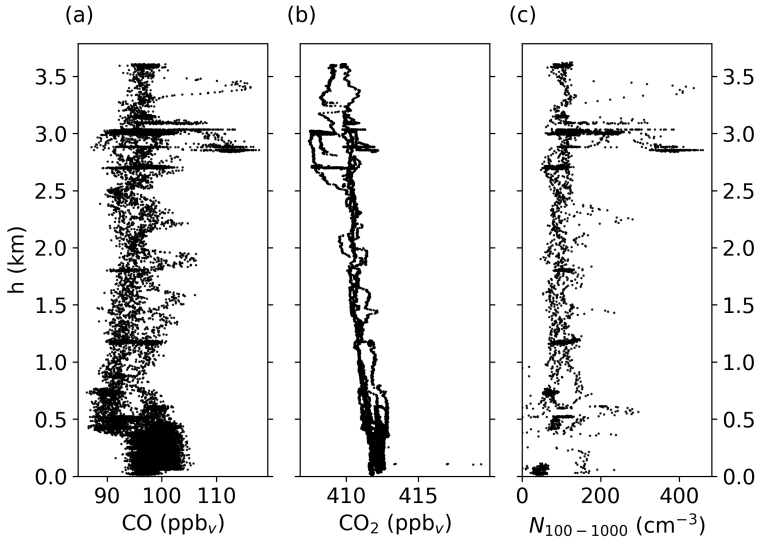

Figure 4.7: Vertical profiles recorded during ACLOUD flight no. 12 (4 June 2017) for trace gas measurements of CO (a) and CO_2 (b), as well as the number concentrations of parcticles between 100 nm and 1 μm ($N_{100-1000}$) measured by UHSAS-1.

properties are presented. In addition, the potential origin of particles within this layer is discussed.

4.2.1 *Chemical and physical aerosol properties*

From the results of individual ACLOUD flights, the occurrence of this elevated pollution layer could be dated to flight no. 12 on 4 June. In the beginning and at the end of this flight, vertical profiles up to 3.6 km were flown. The vertical profile of air mass tracers for the 4 June showed several peaks in CO and CO_2 mixing ratios between 2.8 and 3.5 km above sea level (4.7a, b). Similarly, the particle concentrations also revealed a higher variation in this altitude range, with a pronounced maximum at 2.9 km (4.7c). These enhanced signals were observed during the second profile segment at the end of this flight, but not in the segment after take-off. Therefore, only the last two hours of ACLOUD flight no. 12 (11:30 - 13:39 UTC) were used for the following analysis.

Based on a histogram of measured CO mixing ratios in the altitude range above 2.5 km, a threshold was determined to distinguish the polluted air from the background state. For CO below 105 ppb_v, the sampled air was defined as 'clean' background, whereas CO greater than 105 ppb_v indicated 'polluted' air (Fig. 4.8).

By applying this threshold, the following differences in the aerosol properties were observed between the polluted and clean air case. First, the polluted layer

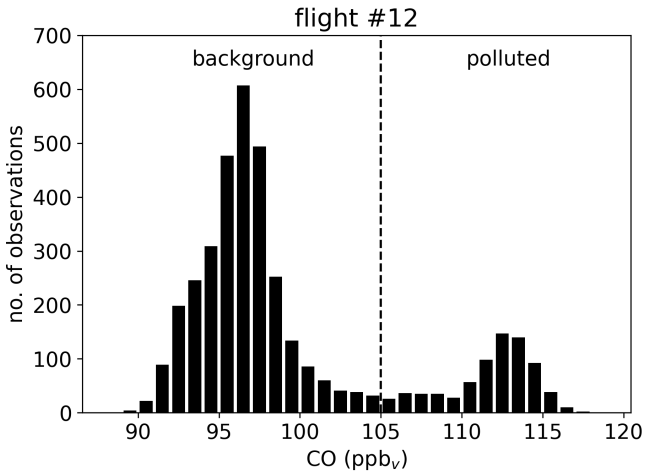

Figure 4.8: Histogram of measured CO mixing ratios during the last two hours (11:30 - 13:39 UTC) of ACLOUD flight no. 12 (4 June). The dashed line indicates the threshold at 105 ppb$_v$ defined for differentiation between background and polluted air mass.

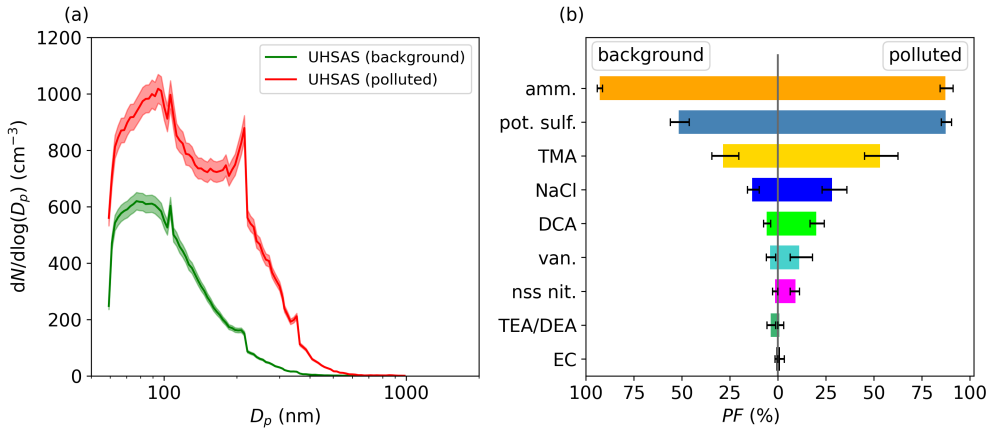

Figure 4.9: Comparison of ambient particle properties between background air mass and the pollution layer including (a) the average particle size distribution ($dN/dlog(d_p)$) obtained by UHSAS-1 and (b) the particle fraction (PF) of different chemical substances contained in the particles analyzed by the ALABAMA. The shaded area in (a) corresponds to the standard deviation. Uncertainty analyses are given in Sect. A.5.

revealed significantly higher concentrations on average with larger particle sizes (Fig. 4.9a). Moreover, the fraction of several chemical species inside the particles increased significantly towards the polluted air (Fig. 4.9b) as already shown in the previous section. Among these species, typical combustion and biomass burning tracers, such as potassium sulfate, vanadium and DCA, but also nitrate, sea spray and TMA were found. The latter demonstrates that TMA is not only

associated with a marine origin but can also be related to polluted air masses. Another combustion-related species, EC, was also slightly more abundant in the polluted air mass. However, due to the low statistics of this particle type, this trend was not significant. In contrast to these combustion-related particle types, TEA/DEA was rare in both cases with a decreasing tendency towards the polluted aerosol. Furthermore, the fraction of ammonium-containing particles declined moderately for the polluted case but remaining at a high fraction of more than 85 %. Overall, the particle fraction of most considered chemical species increased from background to polluted air (Fig. 4.9b), indicating a high degree of internal mixing among the particles associated with pollution.

4.2.2 *Potential origin of polluted air mass*

The general overview of air mass history during the WP already yielded a contribution of mid-latitudinal air to the Arctic free troposphere (see Sect. 3.2). In fact, the atmosphere above 1 km was influenced by the North American, European and Siberian sectors (Fig. 3.3b). To further investigate the sources of this particular layer on 4 June, more detailed air mass history analysis was applied. For this purpose, the FLEXPART PES was calculated for the last 16 days before the flight for the polluted and unpolluted case (see Sect. 2.3.6). As fire plumes are injected to the atmosphere in higher altitudes depending on the fire type, the fuel consumption and the prevailing meteorological conditions (e.g. Stohl, 2006; Kondo et al., 2011; Val Martin et al., 2018; Köllner, 2020), emissions between 1 and 4.5 km were considered for the PES maps. Additionally, the fire locations were identified using the satellite data described in Sect. 2.3.7.

From the resulting PES maps, a clear distinction in air mass origin could be inferred for background and polluted air above 2.5 km. For the background state, the model results revealed contribution from mainly two regions (Fig. 4.10a). First, high PES values were observed at western Siberia. Additional calculation of trajectories using LAGRANTO showed that air parcels ascended in the northern part of Russia into the middle troposphere and circulated around a high pressure system northeast of Svalbard, before descending towards the measurement region to the pressure level of the aircraft ($\sim$ 700 hPa; Fig. 4.11a). A second region indicating significant contribution was the northern part of Canada (Fig. 4.10a). The Canadian air moved across the Arctic Ocean in the middle and upper troposphere and joined the other branch of Russian air masses northeast of Svalbard (Fig. 4.11a). In contrast, the Siberian contribution weakened for the polluted air, whereas the region in Canada and the Pacific Ocean broadened (Fig. 4.10b). Both, the Siberian and North American PES coincided mostly with vegetation fire signals (Fig. 4.10). However, the Canadian

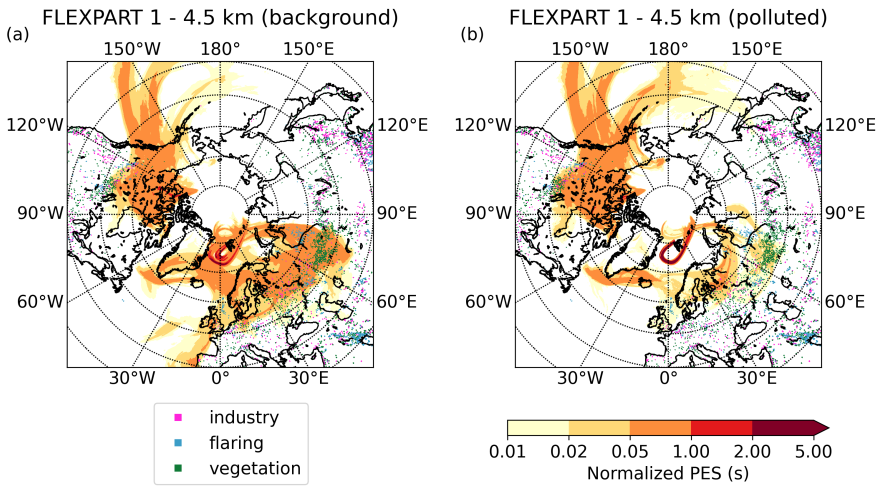

Figure 4.10: Air mass history map of normalized FLEXPART potential source emissivity (PES) for the background air mass (a) and the polluted layers (b). The PES was calculated for the last 16 days before the measurements in the model altitude range between 1 and 4.5 km (see Sect. 2.3.6) and normalized with respect to the number of FLEXPART particle releases. Additionally, satellite-derived locations of active fires during this 16-days-period for different fire types for different fire types are included (see Sect. 2.3.7).

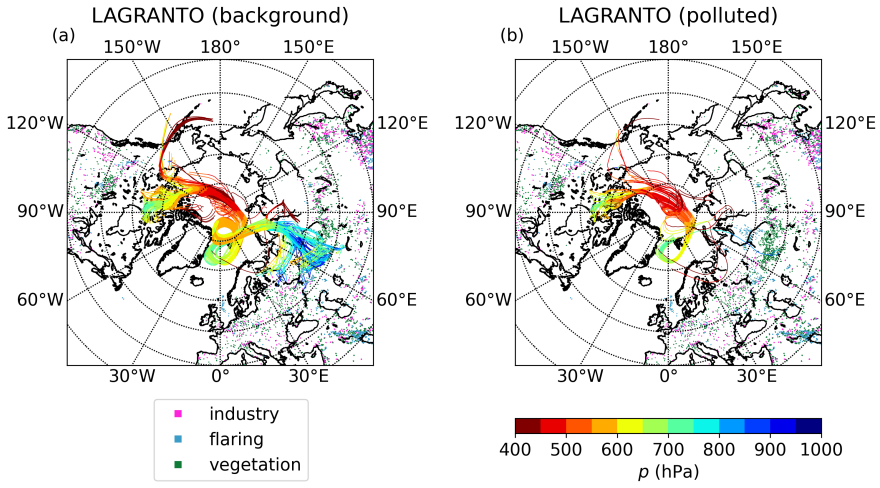

Figure 4.11: Map of calculated LAGRANTO trajectories for the background air mass (a) and the polluted layers (b). The trajectories were calculated for the last 10 days before the measurements (see Sect. 2.3.6). The color represents the atmospheric pressure (p) along the trajectories. Additionally, satellite-derived locations of active fires during this 16-days-period for different fire types for different fire types are included (see Sect. 2.3.7).

contribution to the modeled air mass origin remained high for the polluted case. In addition, the trajectories from Russian fire locations remained close to the surface while passing remote areas in northern Russia. Therefore, these

air masses were potentially mixed with clean air reducing the influence of fire pollution. In conclusion, the fire locations at central northern Canada might be responsible for the elevated pollution layer occurring in the Arctic free troposphere.

4.2.3 *Summary and discussion with literature*

As shown in the previous sections, an event of polluted air masses transported from lower latitudes was found in the Arctic free troposphere during summer. The impact of this event on aerosol microphysical and chemical properties was significant since the fire-related features were also noticeable in their average vertical profiles of the entire ACLOUD campaign. In the literature, the importance of episodical fire events on the atmospheric aerosol burden in the Arctic, particularly during spring and summer, has been discussed (e.g. Shindell et al., 2008; Brock et al., 2011; Schmale et al., 2011; Bian et al., 2013; Thomas et al., 2013; Breider et al., 2014; Evangeliou et al., 2016; Xu et al., 2017). Accordingly, the results from the current study further support the previous finding of episodic transport of wildfire emissions to Arctic regions. Such distinct pollution events are clearly separated from chronic *Arctic haze* events (Brock et al., 2011) which usually occur earlier in the year.

Regarding the geographical origin, the air mass history analysis indicated that polluted air mass originated from Canadian fire sources, whereas the background air arrived from northern Eurasia. In general, emissions from the North American and Eurasian sector dominated the origin of free tropospheric air during ACLOUD. These results are consistent with previous modeling studies showing contributions from Europe, Russia and North America to the lower and middle Arctic troposphere during summer (Stohl, 2006; Shindell et al., 2008). In contrast, the influence of southeast Asian sources which are associated with high BC emissions, are constrained to altitudes aloft (Stohl, 2006; Backman et al., 2021). Thus, the small contribution of southeast Asian air masses might be explained by the low maximum flight altitude of 4.2 km.

The chemical composition of particles within the pollution layer indicated an enrichment of wildfire-related species such as potassium, sulfate and nss nitrate. These results match those of earlier studies reporting significant contributions of biomass burning to the Arctic sulfate and nitrate burden (e.g. Kuhn et al., 2010; Fisher et al., 2011; Breider et al., 2014; Köllner et al., 2021). In addition to these compounds, the abundance of vanadium in Arctic aerosol increased with increasing influence of polluted air masses. Accordingly, this suggests an

additional input of heavy-oil fuel combustion to the observed pollution layer (Ault et al., 2010; Gaston et al., 2010).

Interestingly, the abundance of detected EC particles by the ALABAMA was very low within the observed pollution layer. This finding is consistent with results from Köllner et al. (2021) who reported no significant contribution of vegetation fires to the EC abundance obtained by the ALABAMA. However, these results are contrary to findings from previous studies (e.g. Hirdman et al., 2010b; Bond et al., 2013; Breider et al., 2014). This discrepancy of the ALABAMA EC might be explained by the following reasons. First, aged BC particles resulting from biomass burning sources are often thickly coated with organic material (Paris et al., 2009; Brock et al., 2011; Kondo et al., 2011). Thus, the laser energy maybe was not sufficiently high to reach the BC core inside the particles. Second, a large fraction of vegetation fire particles are known to contain potassium which is also confirmed by the results in the previous sections. Since the potassium-content is associated with high signal peaks for the K^+ ion (m/z +39) owing to its high ionization efficiency, a suppression of other signal peaks by matrix-effects is possible. Furthermore, the presence of sulfate and nitrate in aged soot might have contributed to the suppression of EC ion signals. Taken together, the combination of these effects might have suppressed the carbon cluster ion signals which are characteristic for soot.

Another important finding of this case study was the enhancement of TMA in biomass burning-related air compared to the background air. Hence, besides the marine contribution to TMA abundance in Arctic aerosol discussed in Sect. 4.1.3, vegetation fires might play an important role for the presence of particulate amines in the Arctic summer as well. Results from previous field measurements also observed amines inside combustion-related particles in the Arctic. Gunsch et al. (2019) measured TMA and other alkylamine ion signals in plumes from oil and gas extraction activities in the Alaskan Arctic. In addition, Köllner et al. (2017) reported increased fractions of TMA-containing particles in air masses from mid-latitudinal vegetation fires. However, a large variety of possible sources for TMA (Ge et al., 2011a) are known and further potential pathways into the particle phase via oxidation and condensation exists (Murphy et al., 2007; Seinfeld and Pandis, 2016). Therefore, a clear statement on their origin in air masses associated with long-range transport is difficult.

In summary, the maximum aerosol concentration observed at 3 km during the WP corresponded to a distinct pollution event observed during the flight on 4 June. The aerosol chemical composition and elevated CO levels further indicated the presence of combustion-related air at this altitude. Furthermore, the air mass history calculation showed evidence of vegetation fire origin with air parcels departing from Canada. Interestingly, the particle composition

also demonstrated increased abundance of TMA for the polluted case. Thus, long-range transport of fire-related air represents another relevant source for TMA-containing particles in the summertime Arctic.

4.3 CLOUD PARTICLE RESIDUAL COMPOSITION OF SUMMERTIME ARCTIC CLOUDS

So far, the chemical characterization of aerosol particles in ambient air was described. The following sections will focus on the chemical composition of CPR. The first part of this section will give an overview of all sampled CPR during ACLOUD and will discuss their chemical composition in the context of ambient composition. In particular, the role of amine-containing particles will be examined. Furthermore, the influence of cloud thermodynamic structure and the Arctic surfaces on properties of CPR will be demonstrated based on case studies. Finally, the cloud residual composition of Arctic clouds will be directly compared to clouds at southern latitudes.

4.3.1 *General cloud residual composition during ACLOUD*

In order to relate the chemical properties of CPR to ambient particle composition, the cloud flight sections were divided in three categories: above-cloud, inside-cloud and below-cloud. As 'below' and 'above' cloud, sampling periods of ambient aerosol were selected in the proximity to the corresponding cloud layer. More specifically, these periods were chosen to be at a similar horizontal location as the clouds (within a few kilometers) and mostly less than 500 m away from the cloud layer in the vertical to allow for comparibility. The vertical distance of below-cloud measurements to the cloud base was often closer than 500 m as the majority of probed clouds were located at low altitudes. Above the cloud, the selected vertical distance was extended for cases where the statistics of analyzed particles was not sufficient for the analysis. However, in the absence of polluted air masses, the vertical differences in the Arctic free-tropospheric particle properties were often low. The 'inside-cloud' measurements refer to the sampled CPR. Based on the three cloud-relative categories, the particle fraction (PF) was derived for each case by adding up all cloud transects during ACLOUD analyzed by the ALABAMA. It must be noted that the results for the scaled particle fraction (PF_{scaled}) is not shown because of missing corrections of CPR concentration measurements with regard to sampling efficiency (see Sect. 2.3.1).

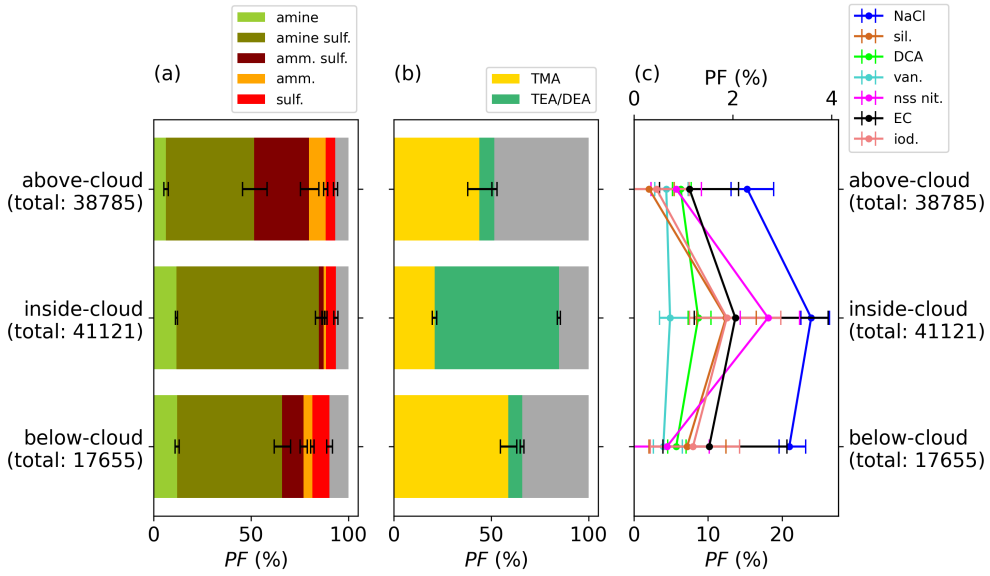

Figure 4.12: Overview of vertical profiles including CPR and ambient aerosol composition for all ACLOUD flights for species from hierarchical markering, the amine types (b) and further species (c). The 'inside-cloud' results corresponds to the chemical composition of CPR, whereas below-/above-cloud sampling periods refer to ambient particle composition in vertical proximity to the clouds (mostly within 500 m away from the respective cloud). The acronyms are defined as follows: amine sulfate (amine sulf.), ammonium sulfate (amm. sulf.), ammonium (amm.) and sulfate (sulf.), trimethylamine (TMA), tri-/diethylamine (TEA/DEA), sea spray (NaCl), silicium (sil.), dicarboxylic acids (DCA), vanadium (van.), nss nitrate (nss nit.), elemental carbon (EC) and iodine (iod.).

As shown in Fig. 4.12, several differences in the chemical composition between clouds and ambient particles were evident. The most striking result from this figure is the high abundance of amine particles inside the clouds with more than 80 % of all sampled CPR containing amines (Fig. 4.12a). More specifically, the majority of amines found inside the clouds were TEA/DEA particles (Fig. 4.12b). In contrast, the out-of-cloud measurements revealed only a small fraction of particles being composed of this type of amines (see Sect. 4.1.2). Instead, TMA particles were present, especially below the clouds which corroborates the vertical distribution of TMA in ambient air (see Fig. 4.4). Both observed amine types were to a large degree internally mixed with sulfate. In short, the different occurrences of TEA/DEA between in-cloud and out-of-cloud measurements suggests an important role of this amine type in cloud processes.

Besides the increased amine content, also the other chemical compounds indicated differences in their abundance between cloud residuals and particles in ambient air (Fig. 4.12c). The fraction of sea spray particles (NaCl) were similar

to below-cloud measurements with slightly higher values inside the clouds, but their abundance significantly decreased above the clouds. This corresponds to the expected role of sea spray particles in cloud formation. Furthermore, other chemical species, such as EC, DCA, nss nitrate and iodine, were slightly more frequent in CPR compared to outside of clouds. This might be explained either by wet deposition or by cloud activation of particles containing these substances. For vanadium-containing particles, no significant difference could be discovered between the three categories.

In the following, the chemical characteristics of Arctic cloud residuals will be further discussed for selected examples. The special focus for this discussion lies on amine-containing particles. Since the statistics of particles containing DCA, EC, iodine and silicate was low for individual cloud cases, these species will be omitted for the further discussion.

4.3.2 *Importance of amine-containing particles in cloud processes*

Due to lacking TEA/DEA particles in ambient air, it is hypothesized that this amine species observed in CPR originated from the gas phase. This suggestion is further supported by laboratory measurements of the Henry's law coefficient describing the solubility of substances in liquid aerosol and cloud particles for TMA and TEA (Leng et al., 2015b; Leng et al., 2015a). In Fig. 4.13, a comparison of the solubility for both substances is shown. From this figure, it is apparent that TEA preferentially dissolves to available aerosol particles compared to TMA. More specifically, the fraction of TEA in aqueous phase reaches 100 % for a liqiud water content (LWC) of 0.1 g m^{-3} which is comparable to the values obtained for the observed clouds in this study (see Fig. 4.14b for example). In contrast, 20 % of TMA still remain in the gas phase under these LWC conditions.

In order to investigate the solubility effect as possible reason for the enriched TEA/DEA content in cloud particles, their vertical distribution inside the clouds was investigated in more detail. For this purpose, those cloud cases were selected where several horizontal legs had been flown inside the clouds at different vertical levels. As a consequence, the the number of particles collected by the ALABAMA on these legs was sufficient ($C_{coinc} > 100$) to derive the chemical composition for each vertical level. To account for changing CPR concentrations between the legs, the particle fraction (PF) was scaled with the mean concentration of successfully detected particles for each leg. Since the selected clouds were located at slightly different altitudes, the resulting PF_{scaled} was analyzed relative to the height inside the clouds by introducing

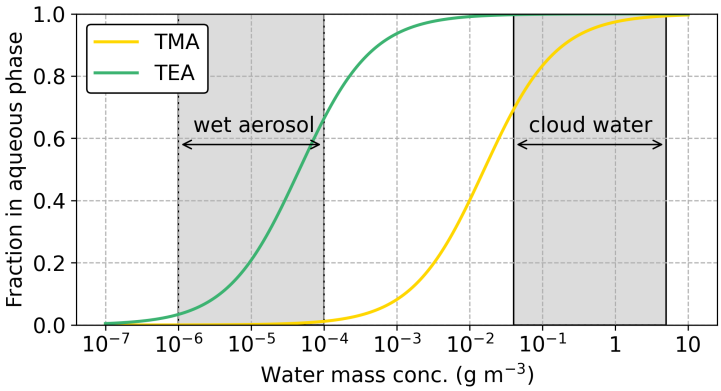

Figure 4.13: Solubility with respect to liquid water content for different amines for a pH of 5.6 and a temperature T of 278 K. The calculations of fraction in aqueous phase are based on Leng et al. (2015b) for trimethylamine (TMA) and Leng et al. (2015a) for triethylamine (TEA).

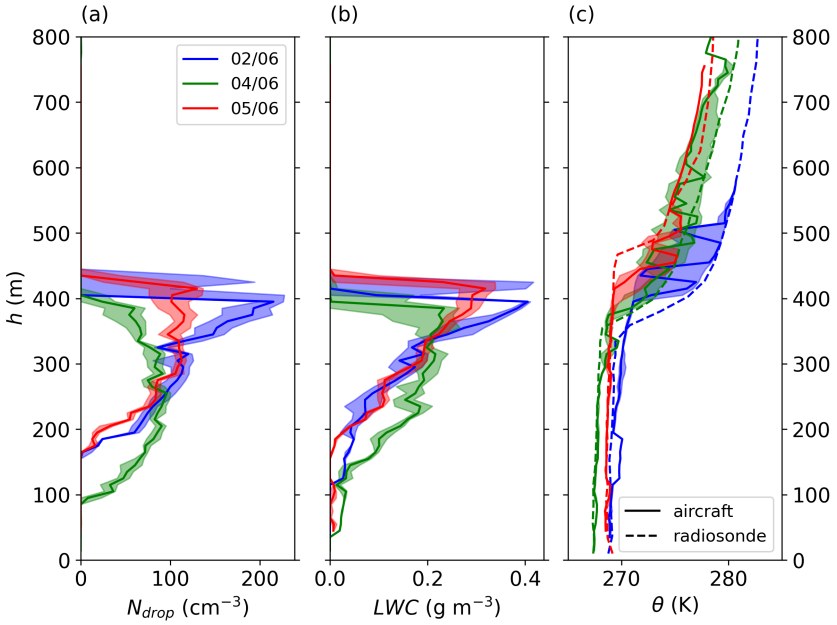

Figure 4.14: In-situ vertical profiles of median (solid) and interquartile range (shaded) for cloud droplet number concentration (N_{drop}; a), cloud liquid water content (LWC; b) and potential temperature (θ; c) for extensively probed clouds above sea ice. Different colors correspond to the different flight days during the warm period, with 2 June flight (blue), 4 June flight (green) and 5 June flight (red). In addition to the aircraft-based θ, measurements from radiosondes released from the nearby research vessel *Polarstern* were included (dashed lines in (c)).

the cloud-relative height (h_{cr}), i.e. $h_{cr} = 0$ for the cloud base height and $h_{cr} = 1$ for the cloud top level. The cloud levels were defined based on the presence of liquid water drops ($N_{drop} > 0\,\mathrm{cm}^3$ in Fig. 4.14a).

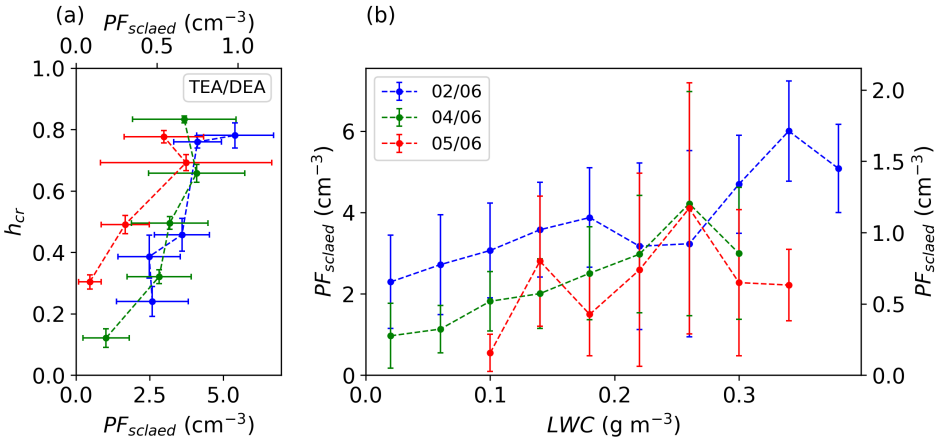

Figure 4.15: Cloud vertical profiles (given in cloud relative height h_{cr}) of scaled particle fractions (PF_{scaled}) for TEA/DEA-containing particles for the selected cloud cases (a) and PF_{scaled} of TEA/DEA-containing particles in dependency of the measured liquid water content (LWC) by the Nevzorov probe (see Sect. 2.3.4) inside the clouds above sea ice (b). The colors represents the flight day given in the legend. Uncertainty analyses are given in Sect. A.5.

To ensure the comparability of these cloud profiles, the cloud cases were further pre-selected for similar atmospheric conditions. In the end, three cloud profiles qualified for this comparison (F11C8 on 2 June, F12C7 on 4 June, F13C4 on 5 June), all of them located above sea ice surface during the WP. As shown in Fig. 4.14c, the thermodynamic profile was very similar for these clouds, representing surface-coupled clouds with a distinct temperature inversion close to the cloud top. The phase of cloud particles was primarily liquid showing a growth of droplet sizes with altitude. As a consequence, the cloud liquid water content ($CLWC$) increased towards cloud top. Accordingly, there should be in theory more uptake of dissolved species inside the CPR further up in the clouds.

If we now consider the CPR composition measured on the different cloud legs, the TEA/DEA-containing residuals revealed a vertical gradient as well. In terms of their scaled particle fraction (PF_{scaled}), CPR with TEA/DEA ion signals were more abundant for the upper part of the clouds (Fig. 4.15a). Similarly, their PF in CPR increased with height as well, except for the cloud on 2 June (see Fig. C.2 in the appendix) where the concentrations of cloud droplets increased towards cloud top. Furthermore, by directly comparing PF_{scaled} of TEA/DEA with the measured LWC, a correlation between both variables was observed (Fig. 4.15b). In short, this relationship supports the suggestion of gas phase TEA/DEA condensing on available cloud droplets as well.

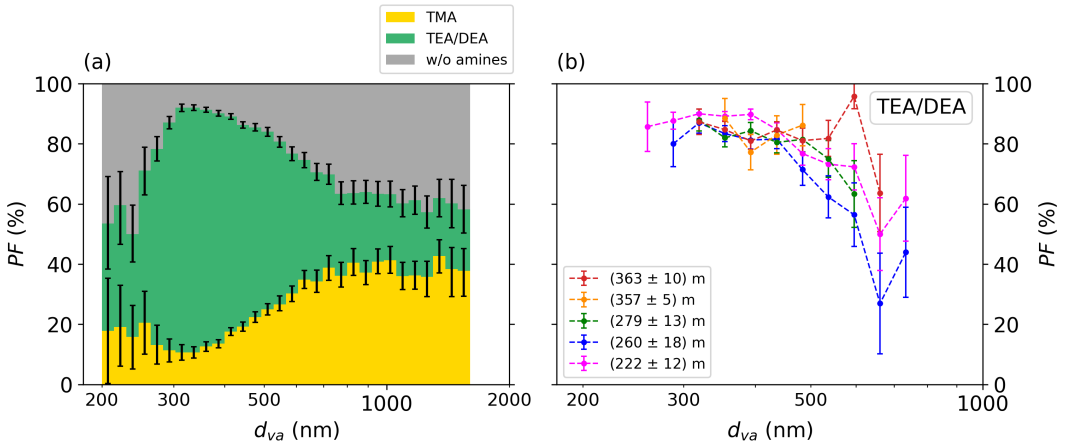

Figure 4.16: Size distribution of particle fraction (PF) of cloud residuals containing both amine types analyzed by ALABAMA (a) and size distribution of scaled CPR-fraction (PF_{scaled}) with TEA-/DEA-content for different vertical levels inside the clouds (b). Uncertainty analyses are given in Sect. A.5. Bins with less than 20 analyzed particles were removed from this overview.

In addition to the vertical trend, the TEA/DEA-containing particles revealed a specific feature regarding the size of CPR as well. More specifically, the fraction containing this amine type showed a maximum at small sizes for all analyzed cloud residuals (Fig. 4.16a). In contrast, TMA-containing particles dominated the larger CPR. Furthermore, vertically-resolved size distribution of CPR composition indicated an increasing contribution of TEA-/DEA-content at larger particle sizes further up in the clouds (Fig. 4.16b).

As the TEA/DEA particles appeared in cloud residuals, this rises the question about the fate of these particles after evaporation of the droplets. In this context, an interesting observation was made during the flight on 13 June. In the last flight hour of this flight, several cloud transects were flown through a cloud layer located above open water surface between 0.2 and 1 km altitude (Fig. 4.17a). In between, two 180 ° turns were conducted at 16:32 and 16:48 UTC, respectively. Thus, the examined cloud area was passed three times with one ascent and descent through the cloud for each leg. For the individual ascents and descents, changing cloud conditions were observed within this region. From the timeseries in Fig. 4.17b, it can be seen that the temperature profile indicated an inversion layer at 650 m. In most cases, the cloud extended above the inversion layer, occasionally as separated cloud layer (Fig. 4.17d). However, during the final climb through the cloud, the droplets above the temperature inversion layer disappeared. Instead, high particle concentrations were observed above the cloud (between 17:01 and 17:08 UTC) compared to the above-cloud segment before the cloud profiling (Fig. 4.17c). Furthermore, the relative humidity was still relatively high just above the cloud (Fig. 4.17b). Regarding the particle

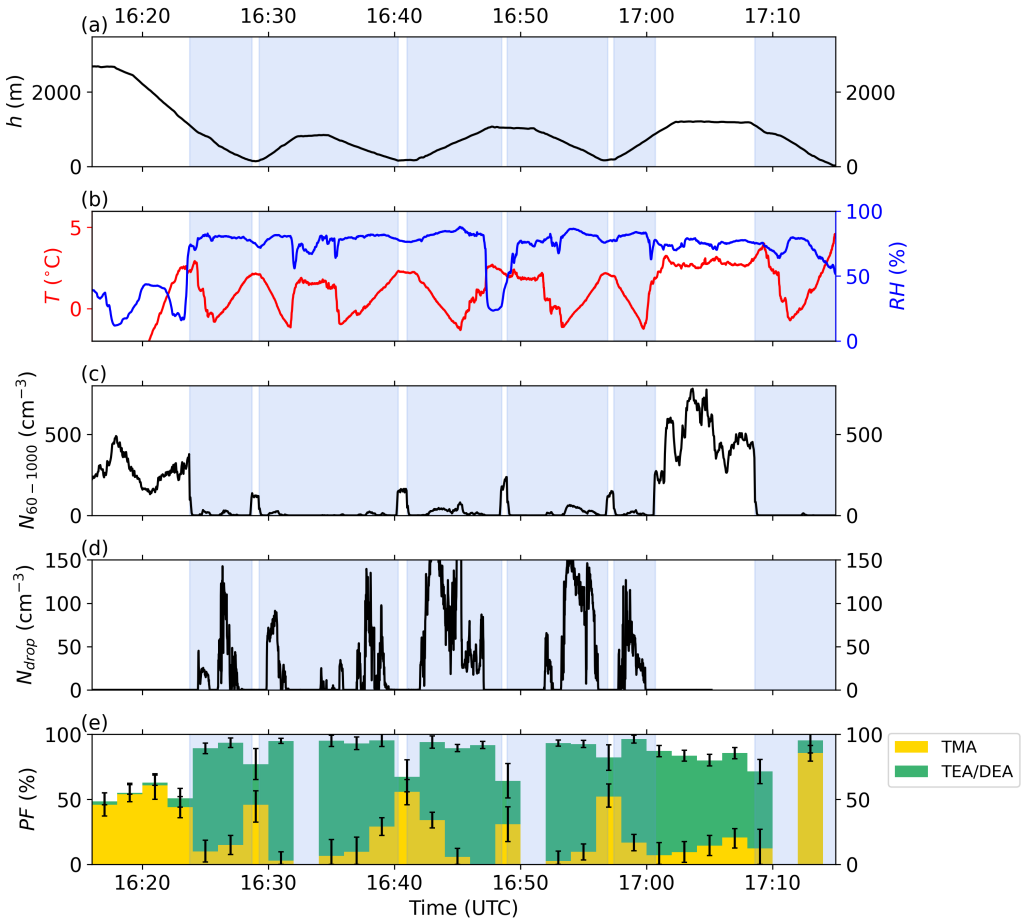

Figure 4.17: Timeseries of flight altitude (h; a), air temperature (T) and relative humidity (RH; b), cloud droplet number concentration (N_{drop}; c), aerosol particle number concentrations ($N_{60-1000}$) for particles between 60 nm and 1 μm (d) and particle fractions (PF) for trimethylamine- (TMA) and triethylamine-/diethylamine- (TEA/DEA) containing particles (e) during the final hour of ACLOUD flight no. 16 (13 June). The blue shaded time periods indicate CPR sampling mode inside clouds with CVI counterflow greater than zero. N_{drop} and $N_{60-1000}$ were obtained by SID-3 cloud probe and UHSAS-1, respectively. Uncertainty analyses are given in Sect. A.5.

composition, the TEA-/DEA-containing particles were not only found in CPR, but also in cloud-free air after leaving the cloud layer (Fig. 4.17e). Compared to the CPR composition inside the cloud, the particle fraction of TEA-/DEA-containing particles was very similar with values of roughly 70 %. In combination with the dissolving cloud above the inversion, this observation indicates the presence of cloud-processed particles after evaporation of the cloud elements.

Taken together, the correlation between TEA/DEA-content in CPR and LWC as well as its rarity in ambient air suggest the uptake of this species from the gas phase into Arctic cloud droplets. Furthermore, their presence in the aerosol phase nearby the clouds shown in the previous example supports hypothesis

that TEA/DEA-containing particles are formed inside the clouds. Therefore, this amine type might play an important role for the growth of existing cloud particles and for aqueous secondary aerosol formation. However, one important piece of evidence is still missing as no information about the abundance of gas-phase TEA/DEA was available during the ACLOUD campaign.

4.3.3 *Interplay between Arctic surfaces, cloud thermodynamic structure and the origin of CPR*

As shown in the previous sections, the CPR composition revealed differences compared to the chemical characteristics of ambient aerosol. Recent Arctic field studies discussed the critical role of the thermodynamic conditions on the origin regime (below-/above- cloud) of cloud-active aerosol particles and precursors (e.g. Shupe et al., 2013; Sotiropoulou et al., 2014; Tjernström et al., 2014). In particular, local sources from the Arctic surfaces are expected to be the dominating origin for thermodynamically surface-coupled clouds (see Sect. 1.2.7). Moreover, the surface conditions (sea ice/open water) is of particular importance for marine aerosol sources and can influence the thermodynamic structure of the clouds. Therefore, this section will focus on the impact of surface types and thermodynamic states on the chemical composition of CPR based on exemplary case studies.

The results presented here are mainly based on cloud flights during the WP. As described in Sect. 3.2.2, this air mass period was characterized by strong temperature inversions and the presence of low-level clouds. During the individual flights, the *Polar 6* aircraft often crossed these cloud layers above open water as well as above closed sea ice. Therefore, the cloud profiles with regard to the different surface conditions could be directly compared for these flights. In the following, two exemplary case studies with comparison of open water vs. sea ice cloud layers are presented. In addition, an example of a mid-level cloud ($\sim 3\,\mathrm{km}$) is given for the NP. Besides elevated clouds, this air mass period was characterized by low-level clouds and multiple cloud layers. However, aerosol concentrations were often very low for the low-level clouds, as already indicated in the period overview profile (see Fig. 3.2l), especially above sea ice. Therefore, the number of analyzed particles by the ALABAMA was mostly too low for significant results of a certain cloud profile. During the CP, the interpretation of cloud thermodynamics was challenging because of long horizontal flight sections within the cloud layer across the sea ice boundary (ACLOUD flight no. 7, 27 May). Furthermore, no information about cloud liquid water content is available on the second flight during the CP (ACLOUD flight no. 8, 29 May).

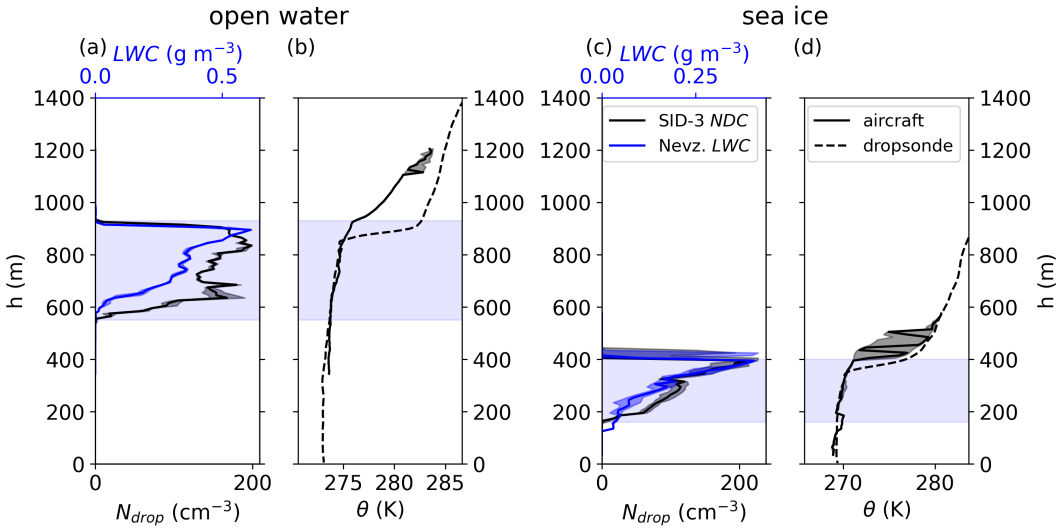

Figure 4.18: Comparison of vertical profiles of cloud properties including cloud liquid water content (LWC) and droplet number concentration (N_{drop}; a, c) as well as potential temperature (θ; b, d) for a cloud transect above open water (a, b) and above sea ice (c, d) during ACLOUD flight no. 11 (2 June), given as median (solid lines) and the interquartile range (shaded area). Additionally, a θ derived from a dropsonde released by the *Polar 5* (dashed line) and the vertical position of the clouds (light shaded areas) are included.

4.3.3.1 *Case study 1: Surface-coupled cloud layer above different surfaces*

In the first case on 2 June (ACLOUD flight no. 11), a low-level cloud layer was present which moved with the southwesterly flow from the open ocean across the sea ice. On this day, the *Polar 6* aircraft performed several cloud profiles by crossing the clouds from below to above and vice versa (see Fig. C.3 and C.4 in the appendix). In the following, two of these profiles are discussed: one above open water and one above sea ice surface.

As shown in Fig. 4.18, the thermodynamic profiles obtained by the aircraft revealed a sharp inversion layer at cloud top for both cloud transects. Below this layer, constant potential temperatures indicated a well-mixed BL. This is further supported by data from dropsondes which were released from the *Polar 5* aircraft in the proximity of the respective cloud transect location. As a result, both clouds, above open water and above sea ice, can be classified as surface-coupled clouds. However, the altitude of the cloud layer decreased towards sea ice (extending from 520 -900 m above open water; (160 -400 m above sea ice) due to colder surface temperatures above the ice (see Fig. C.5 in the appendix). In summary, it is expected that the cloud particles are influenced by surface sources, whereas the free tropospheric air is clearly separated from the cloud.

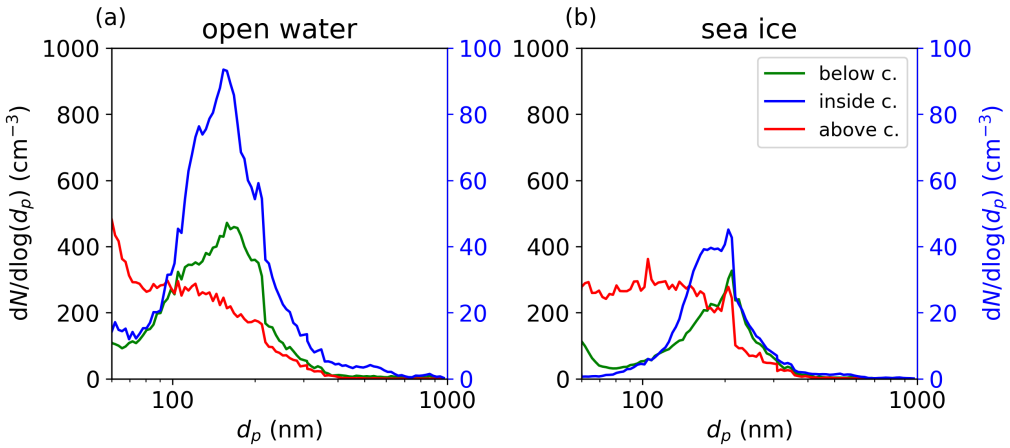

Figure 4.19: Comparison of particle size distributions for cloud profiles above open water (a) and above sea ice (b) during ACLOUD flight no. 11 (2 June). The binned number concentrations of particles in the size range between 60 nm and 1 μm were obtained by UHSAS-1 and averaged for below-, inside- and above-cloud flight segments, respectively. The shaded area corresponds to the standard deviation. Inside-cloud measurements correspond to size distributions of CPR. The right axes (in blue color) refer to the in-cloud measurements.

The resulting microphysical and chemical properties clearly confirm the expected influence of the surface regime for both coupled clouds. Dividing the measurements in the three cloud-relative categories (as described in Sect. 4.3.2), the particle sizes from below-cloud sampling overlapped with the cloud residual sizes, whereas the above-cloud aerosol was significantly smaller (Fig. 4.19). The ALABAMA composition analysis also indicated a similar abundance of different chemical species (PF) inside the CPR compared to below (Fig. 4.20). Above the cloud, particle fractions (PF) of amines and sea spray aerosol (NaCl) decreased significantly. However, regarding the particles inside the BL, their properties changed for the two surface conditions. More specifically, the particles above the ice-free surface were smaller and contained more NaCl and less amines compared to those above sea ice.

To further investigate the observed differences between open water and sea ice for this flight, the air mass history was compared for both cases applying the PES by FLEXPART. More specifically, the PES of the last 3 days before the measurements within the lowest 400 m was calculated. A comparison with the liquid water content of the LAGRANTO trajectories showed that the clouds appeared about 24 hours before the measurements in the model (see Fig. C.9-C.12 in the appendix). Therefore, the selected duration of the FLEXPART simulations seems reasonable. As shown in Fig. 4.21, the PES maps indicate small differences in the air mass origin. For the cloud above open ocean, the air

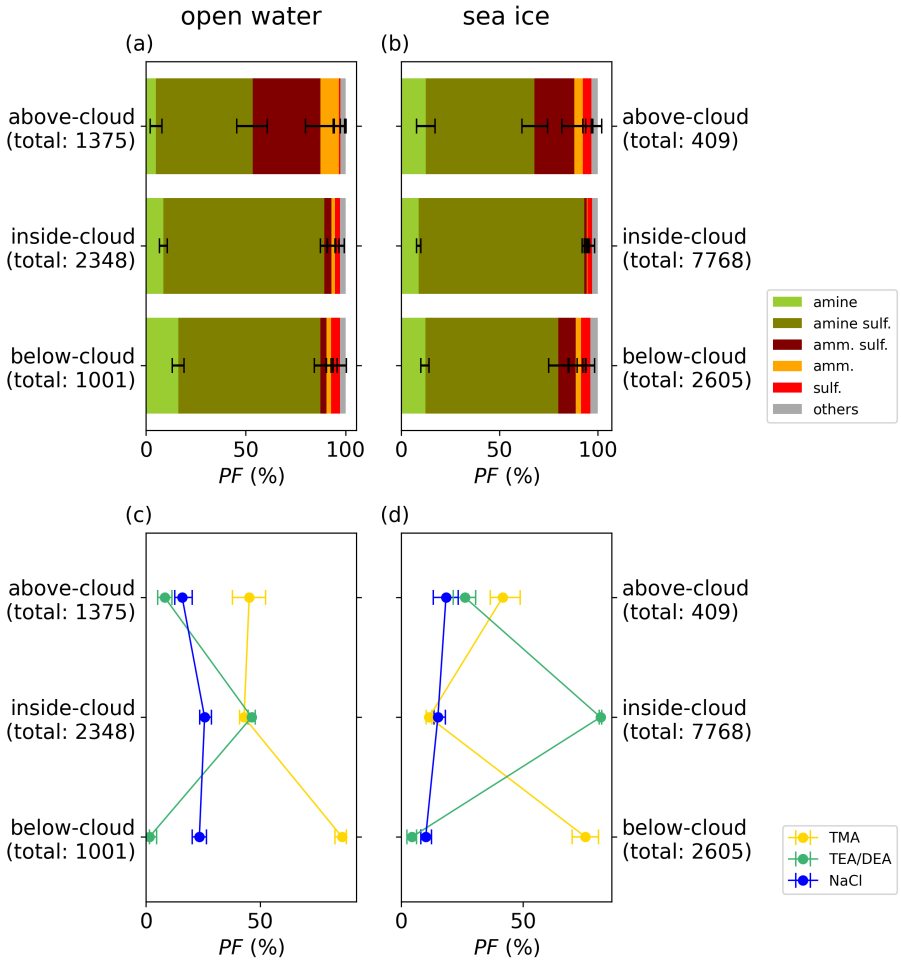

Figure 4.20: Comparison of particle chemical composition for cloud profile above open water (a, c) and above sea ice (b, d) during ACLOUD flight no. 11 (2 June). The profile is shown for particle types from hierarchical markering (a, b) as well as amine- and sea spray-containing particles (b, d). The acronyms are defined as follows: amine sulfate (amine sulf.), ammonium sulfate (amm. sulf.), ammonium (amm.) and sulfate (sulf.), trimethylamine (TMA), tri-/diethylamine (TEA/DEA) and sea spray (NaCl). The given numbers represents the total number of analyzed particles for the specific case. Uncertainty analyses are given in Sect. A.5.

passed the ocean surface west of Svalbard the day before reaching the aircraft position. In contrast, the air moved along the sea ice edge in the last hours before arriving at the sampling location. Thus, the enhanced amine fraction obtained above the sea ice might be associated with gas-phase amines released by the open water leads in the marginal ice zone.

To conclude the first case study, a clear influence of surface-related particles to the cloud residual physical and chemical properties was obtained for the coupled clouds above open ocean and sea ice. However, the particle composition inside the BL differed between both surface types in terms of amine- and

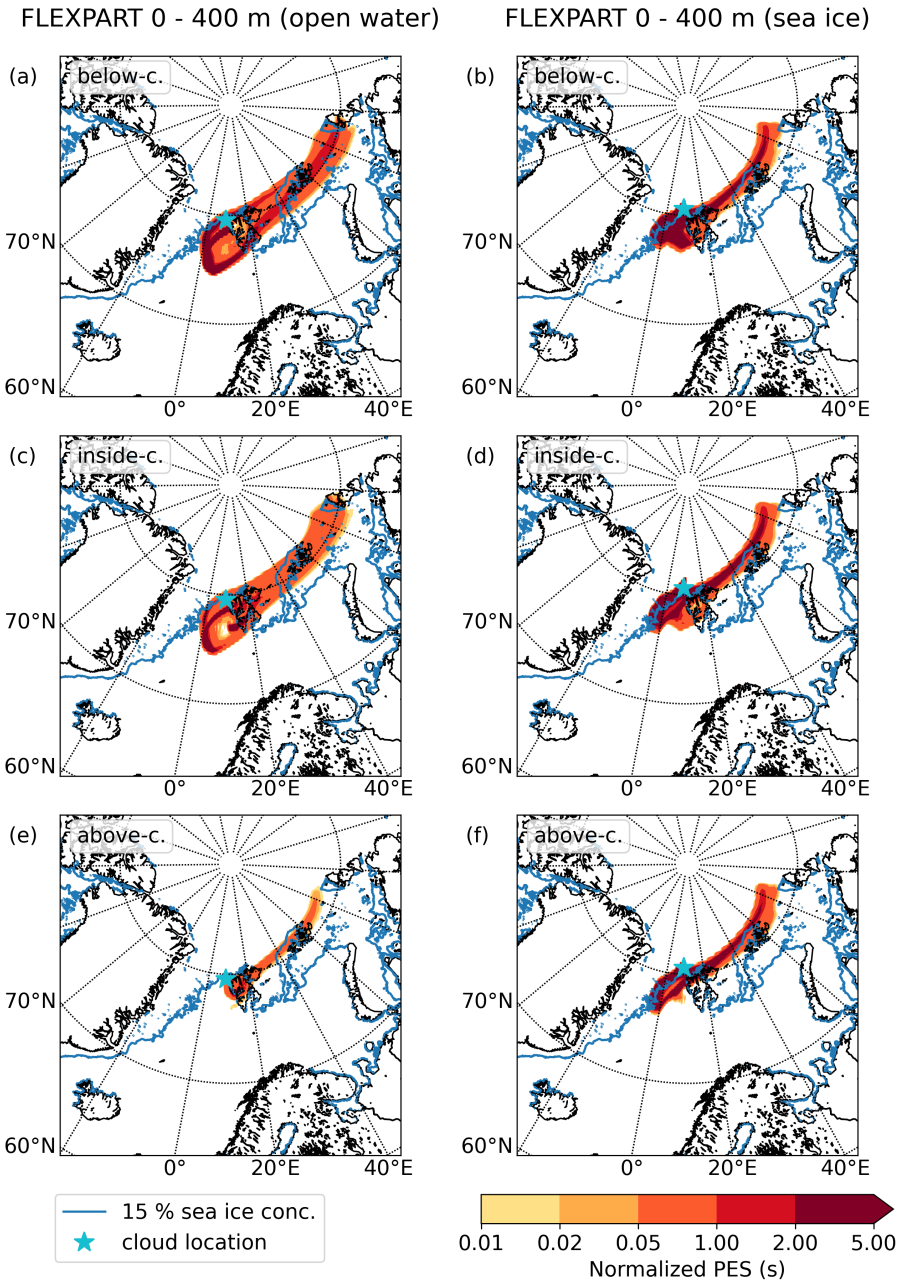

Figure 4.21: Air mass history for clouds (a, c, e) above open water and (b, d, f) above sea ice during ACLOUD flight no. 11 (2 June). The FLEXPART PES maps are shown for below-cloud (a, b), inside-cloud (c, d) and above-cloud (e, f) periods and normalized by the individual period duration. The cyan asterisks marks the location of the probed clouds. Additionally, the blue line indicates the 15-%-contour of the sea ice concentration (see Sect. 2.3.7). The PES was calculated for 3 days backwards in time (see Sect. 2.3.6).

sea spray-containing particles. The calculated air mass history suggests the amine particles originating from the marginal ice zone, whereas higher sea spray

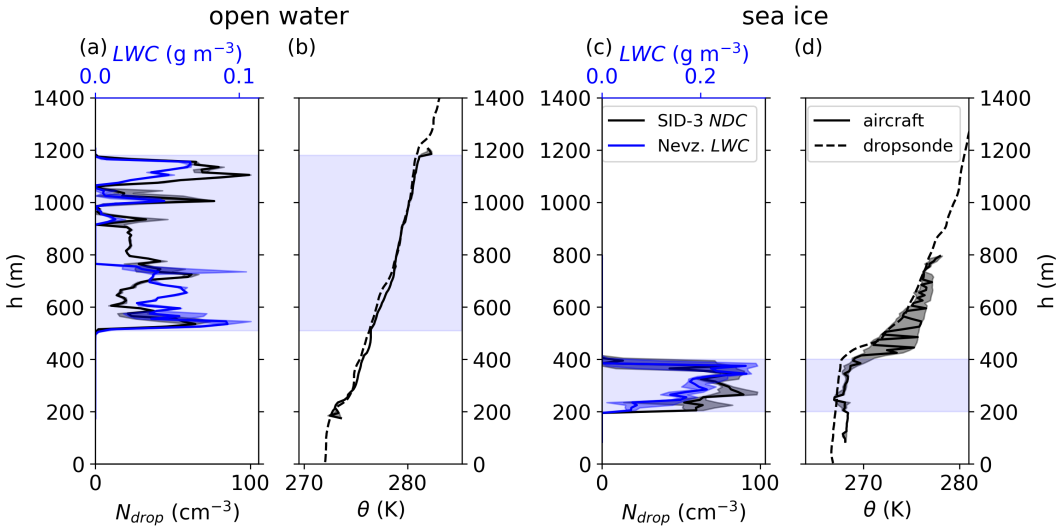

Figure 4.22: Comparison of vertical profiles of cloud properties including cloud liquid water content (LWC) and droplet number concentration (N_{drop}; a, c) as well as potential temperature (θ; b, d) for a cloud transect above open water (a, b) and above sea ice (c, d) during ACLOUD flight no. 14 (8 June), given as median (solid lines) and the interquartile range (shaded area). Additionally, a θ derived from a dropsonde released by the *Polar 5* (dashed line) and the vertical position of the clouds (light shaded areas) are included.

fractions were connected to longer residence time above the open ocean in the Fram Strait.

4.3.3.2 *Case study 2: Changing coupling states above different surfaces*

As a second example, clouds above open water and sea ice were contrasted for the flight on 8 June (ACLOUD flight no. 14). Similar to the first case, clouds were pushed towards the sea ice by a southwesterly wind. However, this time, the clouds above the open water were thermodynamically decoupled from the surface (Fig. 4.22). Indeed, the potential temperature (θ) illustrated an inversion at 200 m located below the cloud base height of 510 m. In addition, the air was very humid at this occasion, even above the cloud layer where the relative humidity was still above 50 % (see Fig. C.8 in the appendix). Above sea ice, the cloud is located below the inversion, demonstrating a surface-coupling.

Regarding particle properties, the decoupled cloud above the open ocean shows similarities between in-cloud particle composition and the aerosol chemical composition aloft. In particular, the amine content in terms of PF was comparable for both, CPR and above-cloud particulate matter, whereas sea spray-containing

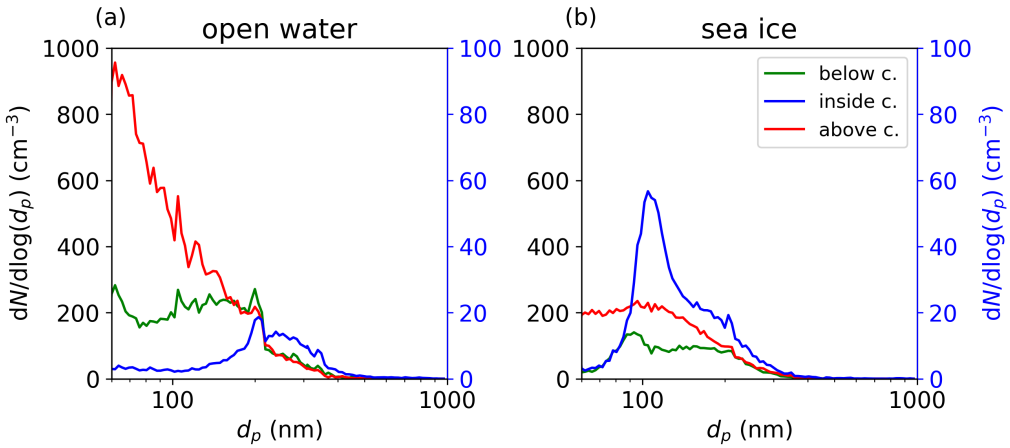

Figure 4.23: Comparison of particle size distributions for cloud profile (a) above open water and (b) above sea ice during ACLOUD flight no. 14 (8 June). The binned number concentrations of particles in the size range between 60 nm and 1 μm were obtained by UHSAS-1 and averaged for below-, inside- and above-cloud flight segments, respectively. The shaded area corresponds to the standard deviation. Inside-cloud measurements correspond to size distributions of CPR. The right axes (in blue color) refers to the in-cloud measurements.

particles mainly occurred below the cloud (Fig. 4.24). Interestingly, a significant contribution of nitrate was observed for the CPR as well. However, the attributions to below- or above-cloud influence was less clear considering the particle size distributions with similar concentrations below and above cloud in the size range of the sampled CPR ($\sim$ 200 nm; Fig. 4.23).

For the coupled sea ice cloud, the particle sizes suggest that the below-cloud regime was feeding the cloud. Indeed, the below-cloud size distribution showed a minimum at $\sim$ 120 nm coinciding with the peak in CPR particle sizes (Fig. 4.23). This coincidence might illustrate the cloud activation of particles from below according to Hoppel et al. (1994). Compared to previously discussed clouds, this cloud revealed smaller cloud residual sizes which could be due to the low particle concentrations in the BL leading to a higher supersaturation (Mauritsen et al., 2011; Croft et al., 2019). In contrast to the particle sizes, the chemical composition below and above the cloud was rather similar, thus, an attribution to cloud-influencing regimes was not possible based on the chemical information.

The FLEXPART air mass history calculations further support the suggested origin regimes from the in-situ measurements (Fig. 4.25). For the decoupled cloud, the PES maps attributed the sampled air masses below, inside and above the cloud to the northern European sector, moving across the Norwegian Sea

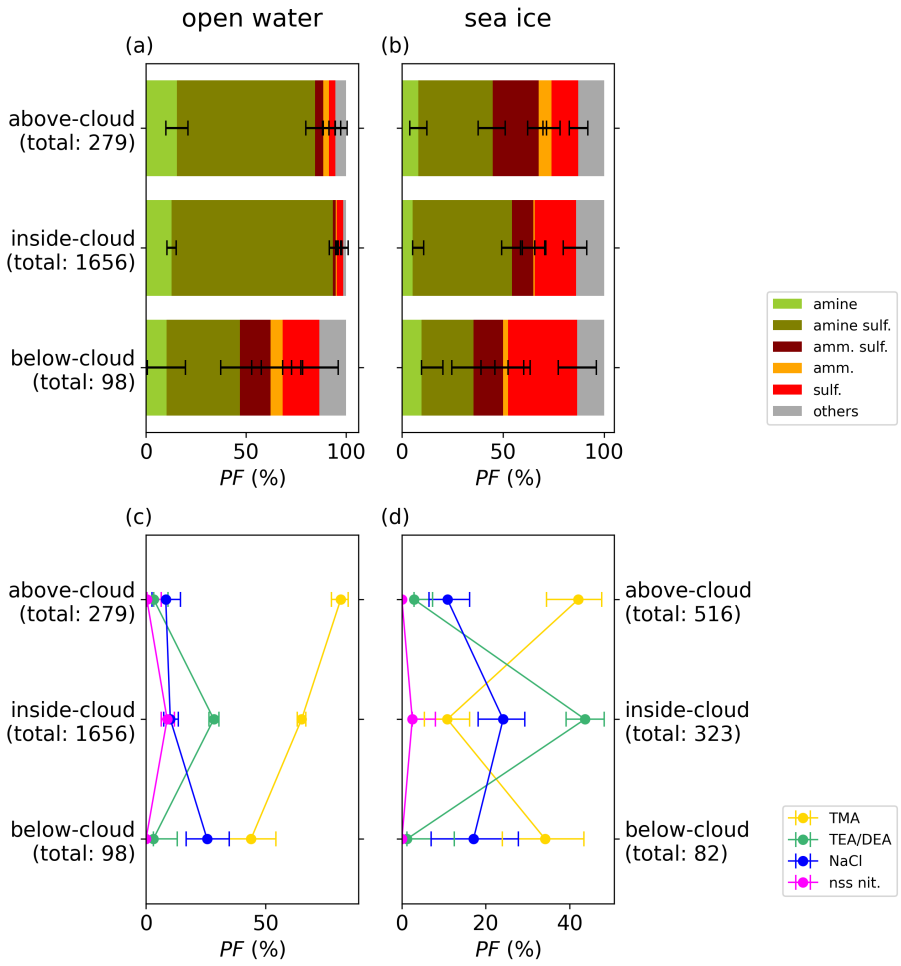

Figure 4.24: Comparison of particle chemical composition for cloud profile above open water (a) and above sea ice (b) during ACLOUD flight no. 14 (8 June). The profile is shown for particle types from hierarchical markering (a, b) as well as amine-, sea spray- and nitrate containing particles (b, d). The acronyms are defined as follows: amine sulfate (amine sulf.), ammonium sulfate (amm. sulf.), ammonium (amm.) and sulfate (sulf.), trimethylamine (TMA), tri-/diethylamine (TEA/DEA), sea spray (NaCl) and nss nitrate (nss nit.). The given numbers represents the total number of analyzed particles for the specific case. Uncertainty analyses are given in Sect. A.5.

towards Svalbard. Below the cloud, air masses approached the measurement location predominantly from the ice-covered Arctic Ocean between Svalbard and Franz-Josef-Land which might also explain the low amine content in the BL. These two source regions were also obtained for the cloud located above the ice. However, the contribution from northern Europe to this cloud was lower, especially below and inside the cloud.

In summary, the second case study was characterized by a different coupling state between the underlying surface conditions. For sea ice, the cloud was surface-coupled, similar to the previous example, which was also confirmed by

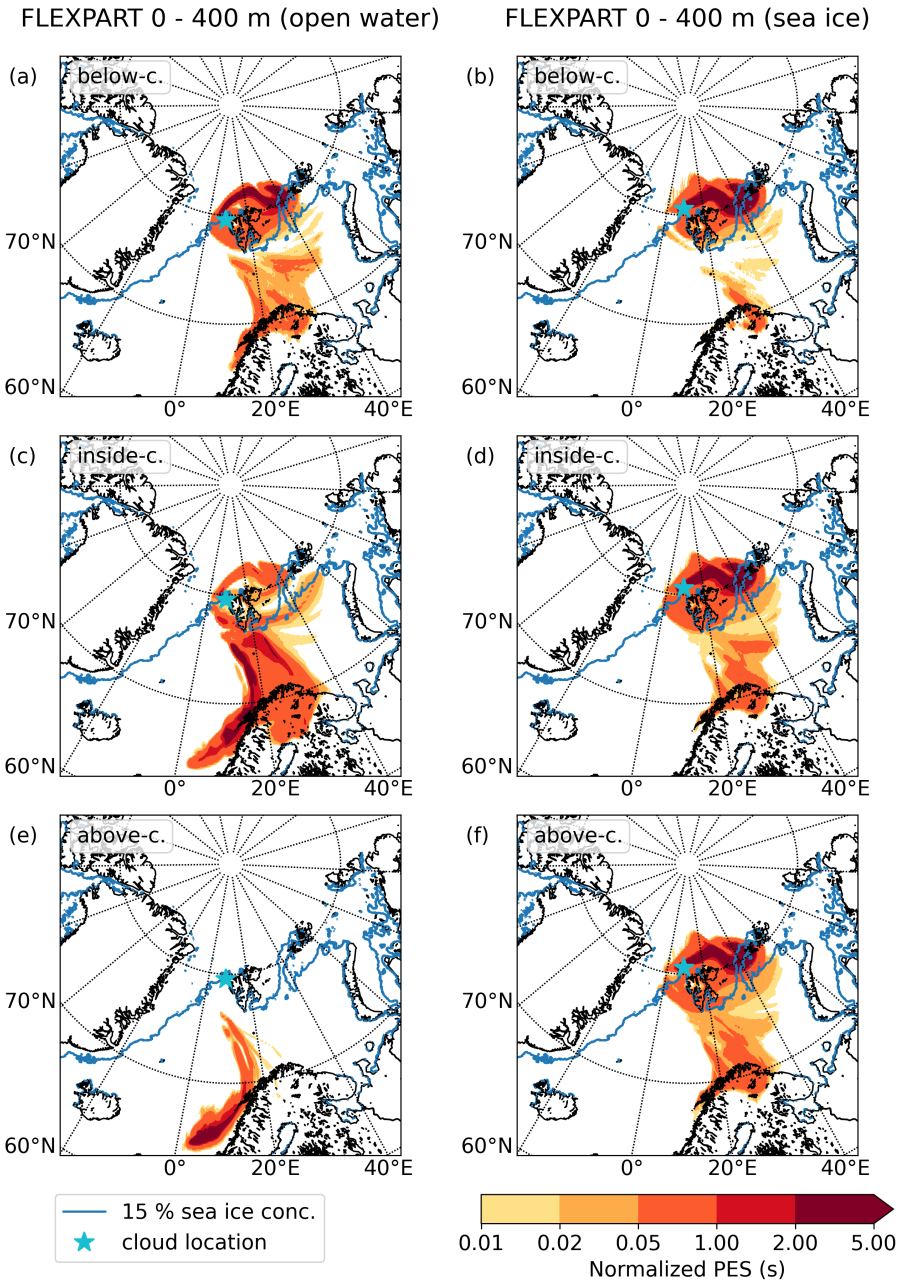

Figure 4.25: Air mass history for clouds above open water (a, c, e) and above sea ice (b, d, f) during ACLOUD flight no. 14 (8 June). The FLEXPART PES maps are shown for below-cloud (a, b), inside-cloud (c, d) and above-cloud (e, f) periods and normalized by the individual period duration. The cyan asterisks marks the location of the probed clouds. Additionally, the blue line indicates the 15-%-contour of the sea ice concentration (see Sect. 2.3.7). The PES was calculated for 3 days backwards in time (see Sect. 2.3.6).

the size distribution showing activation from the BL. On the other hand, the cloud thermodynamics above the open water indicated a separation between

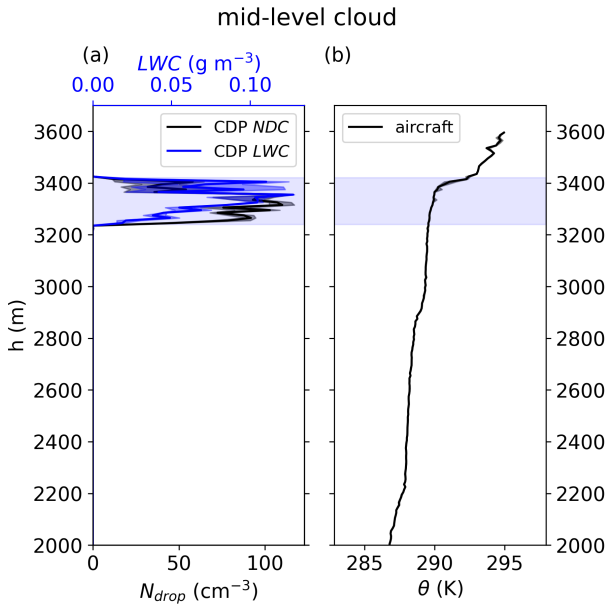

Figure 4.26: Vertical profiles of cloud properties including cloud liquid water content (LWC) and droplet number concentration (N_{drop}; a) and potential temperature (θ; b) for a cloud transect of a mid-level cloud layer during ACLOUD flight no. 19 (17 June), given as median (solid lines) and the interquartile range (shaded area). Additionally, the vertical position of the cloud (light shaded area) is included.

cloud and surface. Moreover, the chemical composition of CPR matched well with the aerosol composition above. The increased humidity for this cloud case suggests an important contribution of moisture transport to the decoupling of the cloud layer. Finally, the model-based air mass history analysis offered two distinct source regions, with European influence above the BL and inner-Arctic air masses inside the BL.

4.3.3.3 *Case study 3: Mid-level cloud layer*

Besides the low-level clouds in both previous examples, a few clouds at higher flight levels were crossed with the Polar 6 aircraft during ACLOUD. Because of their vertical distance to the surface, these cloud layers were located within the free troposphere decoupled from the surface. As an example, a cloud transect on 17 June (ACLOUD flight no. 19) is presented in the following. From Fig. 4.26, it can be seen that θ was rising below the cloud base height (3.2 km). Near the cloud top, the profile marked a distinct stable inversion layer with a tendency of a CII. However, no nearby dropsonde or radiosonde profile was available to confirm the aircraft-derived inversion layer position.

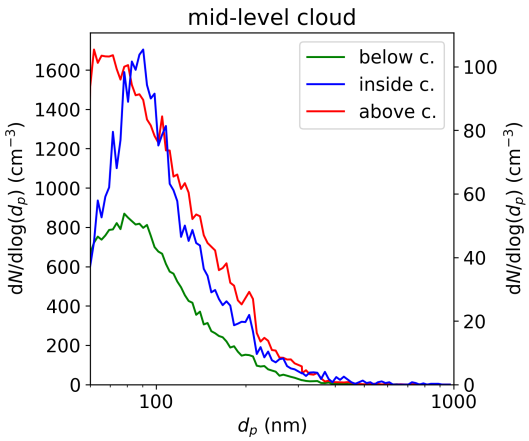

Figure 4.27: Particle size distributions for a cloud profile of a mid-level cloud during ACLOUD flight no. 19 (17 June). The binned number concentrations of particles in the size range between 60 nm and 1 μm were obtained by UHSAS-1 and averaged for below-, inside- and above-cloud flight segments, respectively. The shaded area corresponds to the standard deviation. Inside-cloud measurements correspond to size distributions of CPR. The right axes (in blue color) refers to the in-cloud measurements.

In contrast to the low-level cloud examples, the CPR characteristics were similar to the ambient background below and above the cloud layer. The size distributions for ambient particulate matter illustrated the dominance of Aitken mode particles with higher concentrations above the cloud (Fig. 4.27). Likewise, the mode diameter of cloud residuals was 100 nm. This smaller CPR sizes compared to the low-level clouds can be explained by low abundance of accumulation mode particles. As a consequence, a significant amount of particles smaller than 100 nm could be activated. Apart from the particle sizes, the chemical composition of CPR showed only small differences to both, below- and above- cloud properties. The most striking differences regarding the contained chemical composition were the increase of TEA/DEA as well as nss nitrate in the cloud residuals (Fig. 4.28). The latter might be formed in the clouds via gas-phase nitrogen oxide in the environmental air due to the lack of nitrate in ambient air. All in all, the analogy in size and chemical composition for below, inside and above the cloud suggests similar contribution of both ambient regimes to the cloud development. Indeed, the modeled air mass history indicated advection from northern Canada for all three categories (not shown).

Taken together, favored origin regimes from below or aloft could not be identified for the mid-level clouds based on particle size and composition despite the observed inversion in the upper part of the cloud. This suggests the cloud layer

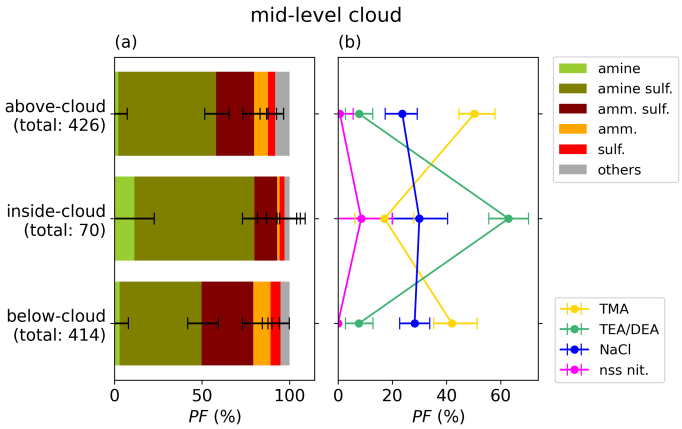

Figure 4.28: Comparison of particle chemical composition for cloud profile of a mid-level cloud during ACLOUD flight no. 19 (17 June). The profile is shown for particle types from hierarchical markering (a) as well as amine-, sea spray- and nitrate containing particles (b). The acronyms are defined as follows: amine sulfate (amine sulf.), ammonium sulfate (amm. sulf.), ammonium (amm.) and sulfate (sulf.), trimethylamine (TMA), tri-/diethylamine (TEA/DEA), sea spray (NaCl) and nss nitrate (nss nit.). The given numbers represents the total number of analyzed particles for the specific case. Uncertainty analyses are given in Sect. A.5.

being formed in homogeneous air masses with similar origin. Due to the elevated altitude, the cloud was significantly influenced by long-range transport which was illustrated by the presence of nitrate inside the CPR.

To conclude, this section illustrated that the thermodynamic structure significantly impacts the properties of particles involved in cloud processes. In particular for the WP, where strong temperature inversions separated the BL from the free troposphere, the differences between the air mass regimes feeding the clouds were significant. In contrast, almost no changes in particle properties between the below- and above-cloud regime could be identified for the mid-level clouds. It can be assumed that this is often the case for mid-level clouds in the Arctic as they are embedded in relative homogeneous air masses of the free troposphere.

4.3.4 *Chemical differences between Arctic and mid-latitudinal clouds*

In connection with the ACLOUD field experiments, ferry flights were conducted between Svalbard and Bremen (Germany) where the home base for the Polar aircrafts is located. The way from Svalbard back to Germany consisted of two ferry flights (Longyearbyen (Svalbard) to Trondheim (Norway) and Trondheim to Bremen (Germany)), both taking place on 29 June 2017. During these two

flights, the ALABAMA instrument and the CVI inlet system were operated. This provided the unique opportunity to directly compare the Arctic CPR composition with mid-latitude CPR composition under similar instrumental conditions.

As the main flight direction was southward in a flight altitude of $\sim 3\,\mathrm{km}$, the air mass transition from the Arctic to mid-latitudes can be examined in a meridional perspective. As shown in Fig. 4.29, several changes were observed for the air mass characteristics towards the south. First, the air temperature was monotonically increasing from the polar region to mid-latitudes (Fig. 4.29b). Second, relative humidity was declining towards Norway. South of 61 °N, the very dry conditions changed to high relative humidity close to saturation (Fig. 4.29b). Simultaneously, clouds were crossed by the aircraft marking the passage of a convective system above Denmark and northern Germany. Third, carbon monoxide mixing ratios dropped at 61 °N along with the appearance of the humid air mass. Within the convective system, CO values increased again which might be explained by the presence of updrafts advecting more polluted air masses from the BL. Taken together, these findings suggests a distinct air mass transition at 61 °N.

Regarding the ALABAMA measurements, 23 645 spectra were recorded during the two ferry flights. An overview of the detailed statistics regarding the data quality is provided in Table C.2 in the appendix. To facilitate a direct comparison with the Arctic aerosol composition, the particle type classification is kept identical to the previous section. As Fig. 4.29d,e illustrate, the air mass transition at 61 °N was observed in ambient particle composition as well. Indeed, the fraction of TMA and sulfate significantly decreased, whereas TEA- and nss nitrate-containing particles became more abundant further south.

During the passage of the convective clouds, a statistical significant amount of CPR were analyzed by the ALABAMA, indicated by the shaded regions in Fig. 4.29. In contrast to the Arctic cloud measurements, the ferry flights provided only horizontal flight sections through the clouds instead of a vertical flight pattern. Therefore, the results were divided into measurements inside-clouds (CPR) and outside-clouds (ambient aerosol). Specifically, for the out-of-cloud category, only particles for the last 5 min before the corresponding in-cloud segment were selected to directly contrast their composition to the particle types found inside the CPR.

Several differences were identified between the cloud residual composition and the particle types identified in cloud-free air (Fig. 4.30). First, the particle fraction of amine-containing particles is enhanced inside the clouds with respect to the content in ambient aerosol (Fig. 4.30a). Second, like in the Arctic

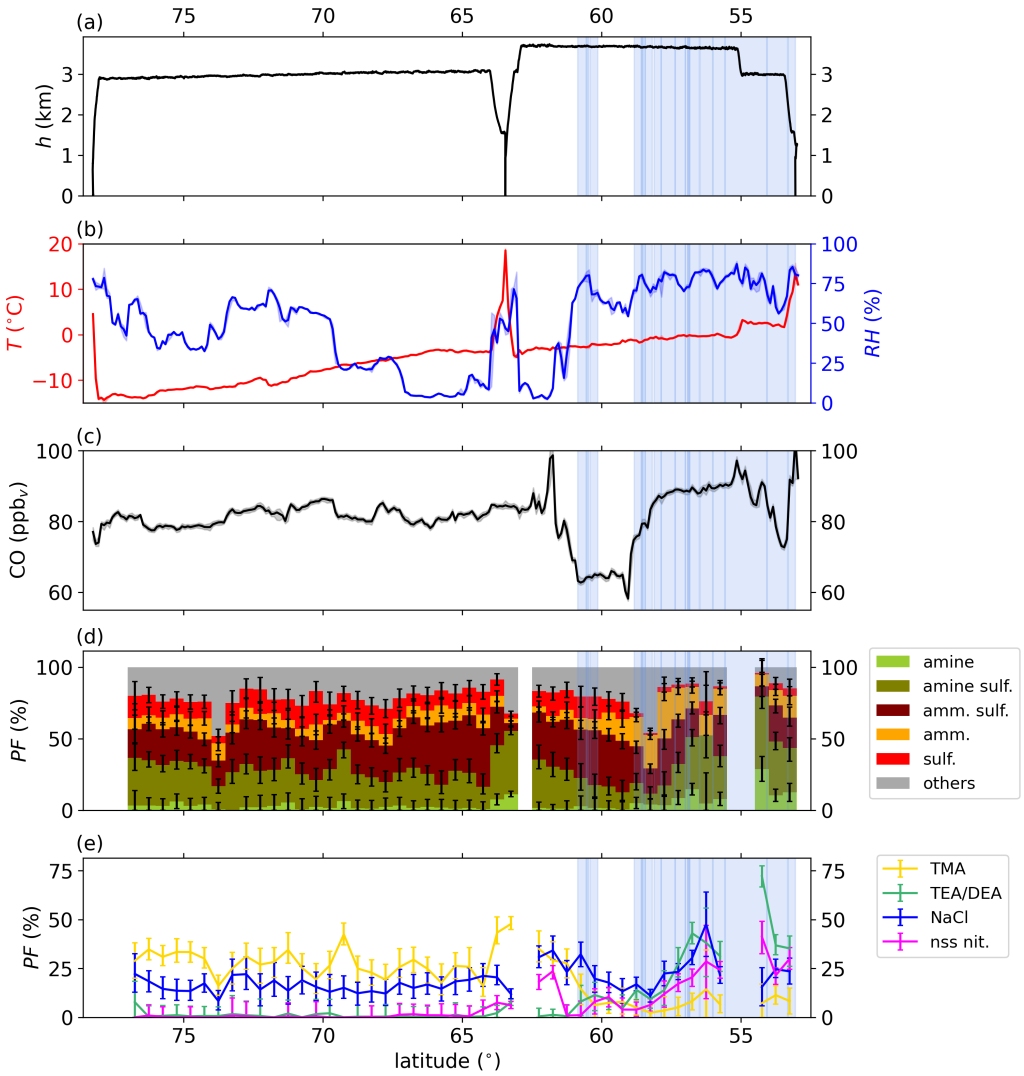

Figure 4.29: Meridional-resolved results of flight altitude (h, a), air temperature (T) and relative humidity (RH; b), (c) carbon monoxide (CO) mixing ratio (c) and the particle fraction (PF) of particle types from hierarchical markering (d) as well as amine-, sodium chloride- (NaCl) and non-sea-spray nitrate- (nss nit.) containing particles (e) measured during the two ferry flights (Longyearbyen to Trondheim; Trondheim to Bremen) on 29 June. Amines were distinguished between trimetyhlamine (TMA) and triethylamine/diethylamine (TEA/DEA). The blue shaded locations indicate measurements inside clouds. The shown PF refers to the occurrence of the individual chemical species in ambient particles, cloud residuals were excluded for this meridional overview. For CO, T and RH, median (solid lines) and interquartile range (shaded) were calculated for intervals of 0.1 °, the PF is determined for 0.5 ° bins. Bins with less than 20 analyzed particles were removed from this overview.

environment, a high abundance of TEA/DEA was observed inside the CPR (Fig. 4.30b). Third, there is a mixture of various species inside the CPR with particularly high contributions of nitrate and NaCl (Fig. 4.30c). In contrast,

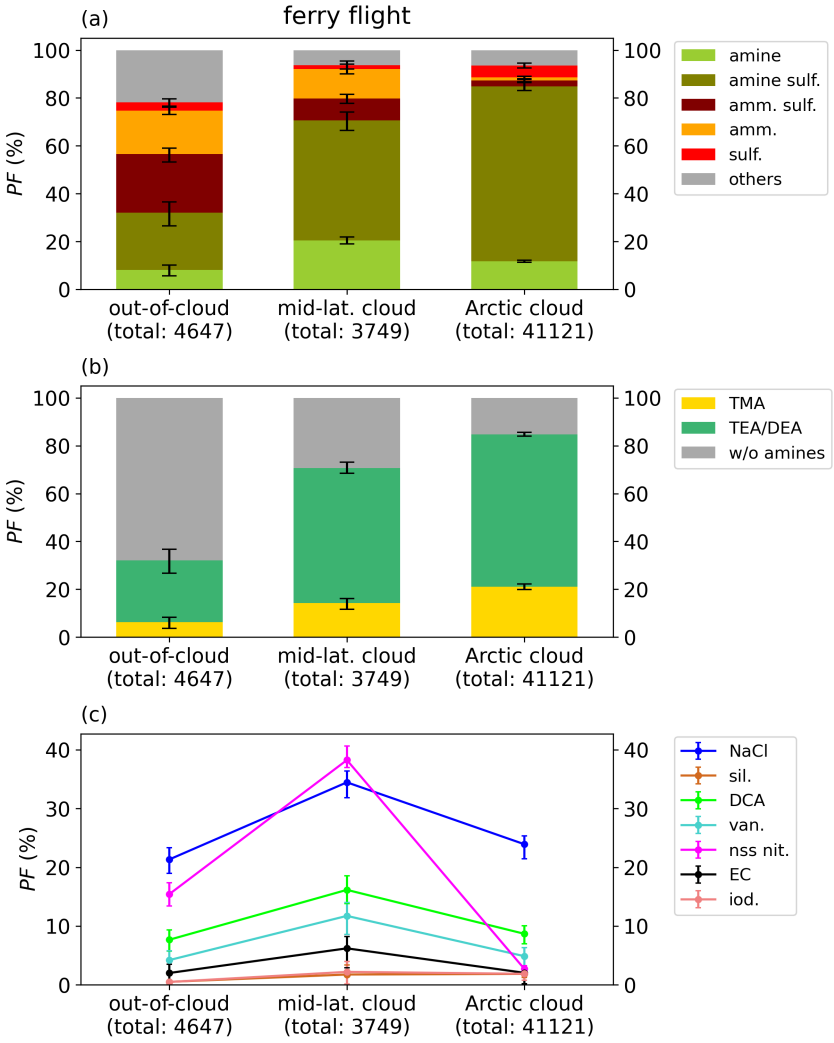

Figure 4.30: Overview of the CPR and ambient aerosol composition for the ferry flight from Trondheim (Norway) to Bremen (Germany) on 29 June. Particle fractions (PF) are presented for particle types from hierarchical maerkering (a), amine types (b) and further species (c). The acronyms are defined as follows: amine sulfate (amine sulf.), ammonium sulfate (amm. sulf.), ammonium (amm.) and sulfate (sulf.), trimethylamine (TMA), tri-/diethylamine (TEA/DEA), sea spray (NaCl), silicium (sil.), dicarboxylic acids (DCA), vanadium (van.), nss nitrate (nss nit.), elemental carbon (EC) and iodine (iod.).

these species were on average significantly less abundant in ambient air. However, as illustrated in Fig. 4.29, the fraction of TEA-/DEA- and nss nitrate-containing particles was elevated in the direct environment of the clouds where the relative humidity in ambient air was still high. Thus, this composition feature suggests the influence of evaporated cloud droplets, similar to the case in the Arctic in Sect. 4.3.2.

In comparison to the overall CPR composition in the Arctic (Fig. 4.12), the mid-latitudinal CPR indicated differences in the involved particle types. The most striking discrepancy is the abundance of nitrate-containing particles at mid-latitudes with a PF of almost 40 %. In the Arctic, nss nitrate was observed only in clouds which were associated with southerly air masses (e.g. Fig. 4.28 in Sect. 4.3.3.3). In addition to nitrate, further species, such as sea spray, DCA, vanadium and EC, were enriched inside the central European CPR. Interestingly, amines were identified to a large extent in mid-latitudinal cloud residuals as well, showing particularly high fractions of TEA/DEA. Hence, this amine type might be relevant for cloud processes beyond the Arctic.

Taken together, the probed clouds above northern Germany and Denmark revealed a similar domination of TEA/DEA in cloud residuals compared to Arctic CPR illustrating the importance of amine species for cloud processes. However, there were significant differences for other species, in particular for nitrate-containing particles. At mid-latitudes, their contribution to cloud residuals is significantly higher than in the polar environment, suggesting a lack of nitrate precursors, like nitrogen oxide, in the Arctic. It should be pointed out that the probed Arctic clouds were mainly low-level stratiform clouds, whereas the considered clouds at mid-latitudes were convective clouds associated with thunderstorms.

4.3.5 *Comparison with literature*

The current knowledge about aerosol species involved in Arctic cloud processes is very limited, in particular due to lacking in-situ observations of the cloud particle composition. In the past, only one airborne field campaign was conducted using a CVI inlet system combined with aerosol instruments in the polar regions (McFarquhar et al., 2011). On this occasion, also a single particle mass spectrometer similar to the ALABAMA was deployed, but only results of one cloud transect flight were reported in the literature (Zelenyuk et al., 2010). Furthermore, Leaitch et al. (2016) performed extensive aircraft-based measurements of aerosol concentrations in the direct surroundings of Arctic clouds during the NETCARE 2014 campaign. However, the cloud activation size of particles was estimated by ambient particles in this study instead of direct sampling of cloud residuals. For these reasons, the airborne measurements of CPR composition presented in the previous sections provide an important insight in Arctic cloud processes.

The most interesting finding in this study was the high abundance of TEA/DEA-containing particles inside cloud residuals, whereas they were rarely found in

ambient air. Prior studies have already shown a contribution of amines to cloud processing of aerosol particles. Rehbein et al. (2011), for instance, found a contribution of TMA to cloud and fog particles by SPMS measurements in Canada. Besides TMA, they reported ion signals at m/z +86 which might correspond to TEA, DEA or other amine compounds. In another study, it was observed that amines with characteristic ion signal peak for TEA/DEA occurred in mid-latitudinal cloud residuals (Roth et al., 2016). This observation is further supported by the presented results from the ferry flight to Germany in the current study. In the Arctic, neither TEA nor DEA have been noted in aerosol particles previously. Nevertheless, Dall'Osto et al. (2019) measured ion signals at m/z +86 in ambient particles in the sea ice-related Southern Ocean close to Antarctica.

The rarity of particulate TEA/DEA in ambient air compared to their abundance inside clouds suggests the condensation of these amine types takes place onto existing cloud droplets from the gas-phase. This hypothesis is further supported by previous findings from laboratory characterization measurements of different amines. More specifically, the Henry's law coefficients of both, TEA and DEA, are larger than for TMA under similar conditions (see Fig. 4.13; Ge et al., 2011b; Leng et al., 2015b; Leng et al., 2015a). Thus, TEA and DEA should preferentially dissolve in available cloud droplets compared to TMA. However, these findings raise the question regarding the fate of TEA/DEA-containing CPR after evaporation of the clouds. The ambient measurements in this study have, at least, indicated the presence of particulate TEA/DEA in the direct surrounding of clouds even though in low abundance. This observation suggests the alteration of particle properties due to the cloud processes involving TEA/DEA.

The previous airborne study of cloud residual composition in the Arctic did not directly report on a contribution of amines to clouds (Zelenyuk et al., 2010). Nevertheless, they measured enhanced fractions of a specific organic sulfate cluster (labeled as 'OrgSulf3'). As the involved species to this cluster were not further specified, it might correspond to the TEA-/DEA-containing particles from the current study. Moreover, Zelenyuk et al. (2010) concluded that the particle size was the controlling factor for cloud activation because most of the interstitial particles were smaller than 100 nm but chemically not very different from the cloud residuals. This cannot be directly confirmed by the current study since interstitial aerosol particles were not sampled. However, as TEA/DEA is hypothesized to condense on available cloud droplets from the gas phase, this study suggests that amine species play an important role to the growth of droplets and, thus, to precipitation.

TMA, DEA and TEA were the only alkylamine types that were identified in the recorded mass spectra of the ALABAMA. As discussed in Sect. 4.1.3, the observation of TMA in ambient air corroborates the findings of previous airborne measurements with the ALABAMA in the Canadian Arctic (Köllner et al., 2017). The prominent occurrence of the ion signal peak at m/z +86 ($C_5H_{12}N^+$), in particular for CPR, was analyzed in the Arctic for the first time. In comparison with literature, this ion signal is characteristic for both DEA and TEA (Angelino et al., 2001; Liu et al., 2020). The frequent combination with other typical ion signals for alkylamines, such as m/z +30 and +42, further suggests that these analyzed particles contain amines (Angelino et al., 2001). In addition to both ethylated amines, m/z +86 is associated with dipropylamine (DPA) as well (Angelino et al., 2001). Due to the lack of other characteristic signals for DPA at m/z +72 ($C_4H_{10}N^+$) and m/z +114 ($C_7H_{16}N^+$) in the recorded spectra (Angelino et al., 2001), this amine type was excluded for the presented analysis. Moreover, since the molecular ion signal of TEA at m/z +101 ($C_6H_{15}N^+$) was present in the majority of the m/z +86-containing spectra, these particles represented most probably TEA rather than DEA. Nevertheless, this hypothesis needs to be confirmed by laboratory studies of ethylated amines with the ALABAMA. Therefore, the notation as 'TEA/DEA' was kept for this study.

There are also other alkylamines which are linked to marine biogenic origin in literature, for instance monomethylamine and dimethylamine (e.g. Gibb et al., 1999; Ge et al., 2011a; van Pinxteren et al., 2019a). However, their presence in Arctic particulate matter could not be confirmed in the current study. As further discussed in Sect. C.3, the characteristic ion signals for other alkylamines could not be identified due to isobaric interference with other substances and/or were often lower than the background noise threshold of the ALABAMA.

Regarding the origin of cloud-interacting aerosol, the air mass history indicated the marine locations as dominant source. In particular for low-level clouds during the WP, the results from the dispersion model illustrated that the air parcels passed either above open or ice-covered ocean within the last few days before measurement. High sulfate and amine content further supports previous findings of the importance of marine precursors for cloud processes (e.g Leaitch et al., 2013; Willis et al., 2016). TMA and DEA, for instance, were previously observed in the marine BL associated with biogenic production in the ocean (e.g. Ge et al., 2011a; Köllner et al., 2017; van Pinxteren et al., 2019b). The occurrence of TEA was mostly reported in the context of engine emissions in past studies (Ge et al., 2011a; Gunsch et al., 2019). However, the findings from this study together with reports of TEA found in fish food processing (e.g.

Romero-González et al., 2012) suggest the Arctic ocean also representing a potential source for TEA.

It is known from literature, that the thermodynamic structure of Arctic clouds plays an important role for the origin of cloud residuals (Sedlar and Tjernström, 2009; Shupe et al., 2013; Tjernström et al., 2014). For example, Shupe et al. (2013) previously observed similarities of particle number concentration between in-cloud and above-cloud aerosol properties for decoupled clouds above the central Arctic ocean, whereas surface-coupled clouds showed a link of in-cloud aerosol from the local surface regime. As presented in Sect. 4.3.3, the results of the current study confirm this decisive role of the stable inversion layer location for the cloud particle chemical composition. In fact, if an inversion layer was separating the surface from the cloud layer, the CPR composition clearly indicated mixing of aerosol species from above into the clouds. In addition, the presence of decoupled clouds was linked to advection of moist air masses aloft, similar to what was observed by Shupe et al. (2013). Several studies suggested differences in the aerosol entrainment from above the cloud depending on the vertical location of the inversion in the upper part of the cloud (Sedlar et al., 2012; Sotiropoulou et al., 2014; Tjernström et al., 2014). However, the only example of a CII case presented in the current study was located at mid-levels where the differences in aersol composition were marginal between below and above the cloud. Therefore, this study could not demonstrate an entrainment from above-cloud for this CII-case. There might be more cases during ACLOUD with an extension of the cloud top inversion into the clouds. Nevertheless, since the *Polar 6* was moving relative to the cloud and the locations of the dropsonde releases did not match exactly the flight tracks of *Polar 6*, the accurate determination of the inversion position relative to the cloud top was difficult.

In the context of local marine aerosol, iodine was previously suggested to be involved in Arctic cloud formation owing to its contribution to NPF and particle growth (Baccarini et al., 2020). Indeed, the results in the previous sections indicated slightly higher occurrences of iodine in CPR compared to ambient air. However, the fraction of iodine-containing particles analyzed by the ALABAMA was generally low ($< 1\,\%$), thus, the statistical significance of this increase inside clouds is weak.

Concerning the impact of mineral dust on cloud processes, this study did not show an important contribution of such particles on Arctic clouds based on silicium-containing particles. As already discussed in Sect. 4.1.3, dust particles can be composed of other species as well. Thus, the markered silicium might not be fully representative. Furthermore, mineral dust is known as good INP. However, the vast majority of cloud particles sampled via the CVI inlet were liquid

cloud droplets rather than ice crystals. For this reason, its contribution to clouds might be further underestimated in the presented ACLOUD measurements.

Another finding of this study was a clear enhancement of nss nitrate in the measured CPR composition above northern central Europe compared to Arctic clouds. This result is consistent with prior studies of mid-latitudinal cloud composition showing high contribution of nitrate to clouds as well (e.g. Roth et al., 2016; Schneider et al., 2017) which could be explained by the uptake of gaseous nitric acid (Tilgner et al., 2005; Schneider et al., 2017). According to these data, we could infer that the role of nitric acid for Arctic clouds is limited by the low concentrations of nitric acid in polar environments.

In conclusion, the results from the Arctic CPR composition measurements showed a dominance of TEA/DEA inside the clouds. This particle type was reported for the first time in the Arctic environment. Interestingly, these ethylated amines were observed inside CPR at southern latitudes as well. Owing to the high solubility of DEA and TEA, indicated by their correlation with cloud liquid water content and the rarity of this amine type in ambient particulate matter, it is suggested that they dissolve in available cloud droplets from the gas phase. Thus, they might play an important role for the lifetime of Arctic clouds by supporting the growth of cloud droplets. In addition to amines, other species like sulfate, sea spray and oxygenated organics were also involved in cloud processes as they were found in CPR as well. Furthermore, the study illustrated the impact of the cloud thermodynamic structure on the origin of entrained particles, suggesting long-range transported particles to be important for decoupled clouds. Overall, this study revealed a closer look on aerosol-cloud interaction processes in the summertime Arctic adding crucial knowledge to the understanding of Arctic clouds.

5

CONCLUSIONS AND OUTLOOK

In order to improve the current understanding of aerosol-cloud interactions in the polar environment, this work focused on the chemical characterization of ambient aerosol particles and cloud particle residues (CPR) in the summertime Arctic. For this purpose, aircraft-based measurements were conducted in the region of Svalbard (Norway) using the single particle mass spectrometer ALABAMA. The number of previous airborne studies on aerosol chemical composition is very limited in the Arctic, in particular for cloud residuals with only one flight through Arctic clouds reported in the literature (Zelenyuk et al., 2010). In the following, the main findings of this study will be summarized with respect to the questions in Sect. 1.3. Furthermore, an outlook will be given towards ideas for future studies on Arctic aerosol-cloud interaction.

Particle types observed in summertime Arctic clouds

This study has found that the chemical composition of Arctic cloud residuals differs significantly from ambient particle composition in terms of amines. For ambient aerosol, trimethylamine- (TMA) containing particles were abundant, especially inside the marine boundary layer which supports previous findings from Köllner et al. (2017). In contrast, the CPR composition was dominated by triethyl-/diethylamine (TEA/DEA). This amine type was observed for the first time in the Arctic environment. The high abundance of TEA/DEA in cloud residuals suggests an important role of TEA and/or DEA in cloud processes.

Several indications for gas-to-particle conversion of these ethylated amines inside the clouds were found. First, only a small fraction of the collected particles in ambient air contained TEA/DEA which occurred particularly in proximity to clouds. Second, the abundance of TEA/DEA inside the CPR increased with cloud liquid water content for the examined cloud cases. Finally, the size distribution of CPR revealed that TEA/DEA was mostly found for small residuals with increasing tendency towards the upper part of the clouds. Taken together, these ethylated amines might contribute significantly to the growth of cloud droplets which would have further implications for the lifetime of Arctic clouds.

In addition to amines, also other substances were enriched inside the clouds, in particular sea spray aerosol. This suggests an important contribution to cloud particle activation by primary marine aerosol particles. Furthermore, species such as dicarboxylic acids (DCA), nitrate, iodine and elemental carbon (EC) were slightly more abundant inside CPR than in out-of-cloud aerosol, indicating a contribution either to formation or to processing of cloud particles. Overall, due to cloud processing, the analyzed cloud residuals often contained mixtures of several chemical species.

Comparison of Arctic clouds with mid-latitudinal clouds

The study has further shown that TEA/DEA might play a role for cloud processes beyond the Arctic environment. Measurements of CPR in convective clouds above northern central Europe indicated large fractions of cloud residuals containing the TEA/DEA particle type as well. Contrary to Arctic clouds, the contribution of nitrate and combustion-related species, such as DCA, vanadium and EC, to cloud particles was significantly larger at mid-latitudes owing to the proximity to industrial and agricultural sources.

Effect of the cloud thermodynamic structure

The results further illustrate that the chemical composition of Arctic CPR was significantly influenced by the thermodynamic structure of individual clouds. Case studies of thermodynamically surface-coupled clouds indicated a strong relationship of particle species found inside the cloud with the below-cloud regime. This coupling state was frequently observed during a warm air intrusion period above cold sea ice surfaces. Therefore, such meteorological conditions might favor the surface-based cloud activation and moistening. In contrast, thermodynamically decoupled clouds, which occurred predominantly above open water surfaces, showed similarities of CPR composition to the above-cloud regime indicating the importance of long-range transport to decoupled clouds in the Arctic. Similarly, clouds embedded in the Arctic free troposphere were more sensitive to aerosol species from mid-latitudes.

Influence of long-range transport on Arctic clouds

The contribution of transported pollution from mid-latitudes to the Arctic was generally low during the ACLOUD campaign, indicated by low mixing ratios

of carbonaceous pollution tracers and moderate concentrations of accumulation mode particles. Accordingly, the frequency of typical particle species associated with long-range transport, such as nitrate, EC and ammonium sulfate, was low as well and was restricted to vertical levels above the Arctic boundary layer. However, the observation of an elevated pollution layer demonstrated the episodical influence of biomass burning aerosol to the middle troposphere during the Arctic summer.

In conclusion, this study revealed new insights into the chemical composition of Arctic clouds which add valuable information to the current knowledge of aerosol-cloud interaction processes in the polar environment. In particular, the importance of amines to the formation and growth of cloud droplets has been shown. However, the detection of amines was limited to the particle phase in this study. To investigate their origin and the formation process of particulate amines in the Arctic, future field experiments in the polar region with complementary measurements of gas-phase amines in addition to particle composition analysis are needed. Furthermore, additional laboratory measurements of different amine species using the ALABAMA are required to improve the differentiation of TEA, DEA and other amine types. One limitation of the presented measurements is the lower size limit of the ALABAMA which inhibits sampling of cloud residuals in the Aitken mode. Therefore, the exploration of ambient aerosol and CPR in the Arctic should be complemented by instrumentation for chemical analysis of Aitken mode particles behind the CVI inlet. Moreover, a Lagrangian in-situ sampling strategy for aircraft measurements of Arctic clouds might provide more insights into the fate of evaporated cloud droplets. Additionally, coupling of the airborne measurements to the analysis of seawater samples could provide a further insight on the contribution of marine biogenic sources to atmospheric particles and clouds. Finally, airborne measurements are always restricted by a certain temporal and spatial coverage. For this reason, further airborne campaigns with the focus on aerosol-cloud interaction are needed in different Arctic locations and seasons, particularly during the dark winter season, where the cloud residual composition is still unknown.

A

SUPPLEMENTARY INFORMATION FOR CHAPTER 2

A.1 HISTOGRAMS OF ALABAMA SIZE CALIBRATION MEASUREMENTS

For the size calibration of the ALABAMA, two sets of calibration measurements were conducted (see Sect. 2.1.2). The first calibration measurement took place during the ACLOUD field campaign (11 June 2017), the second after the campaign (17 July 2017). For both sets of measurements, monodisperse PSL particles of different sizes were sequentially passed through the calibration setup (see Sect. 2.1.2). For each detected particle, the *upcount* value was measured by the ALABAMA, thus, the corresponding particle velocity v_p inside the vacuum was calculated with Eq. 2.1. In Fig. A.1 and A.2, the histogram of resulting v_p values are shown for the measurements during and after the campaign, respectively. In Table A.1, the manufacturer and particle sizes of the PSL standards used for these measurements are listed.

Table A.1: Overview of the PSL particle standards used for the ALABAMA size calibrations.

PSL manufacturer	Catalog no.	(d_{va}± uncertainty) nm
Polyscience, Inc.	64013-15	(210 ± 11) nm
Polyscience, Inc.	64017-15	(420 ± 21) nm
Sigma Aldrich	95585	(525 ± 53) nm
Polyscience, Inc.	64021-15	(630 ± 21) nm
Polyscience, Inc.	64025-15	(840 ± 21) nm
Thermo Scientific	4013A	(1365 ± 16) nm
Thermo Scientific	4016A	(1680 ± 19) nm

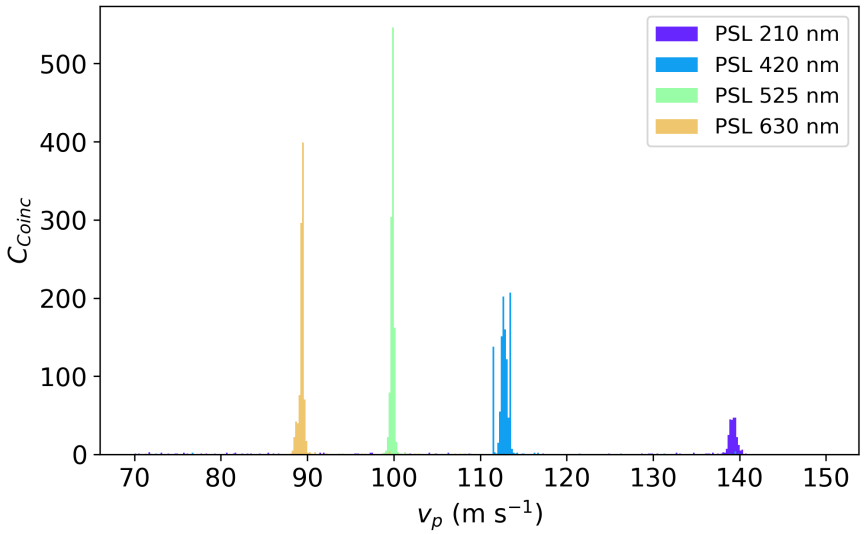

Figure A.1: Histogram of particle velocity (v_p) with number of particle dectections (C_{coinc}) by the ALABAMA for four different sizes (d_{va}) of PSL particles from a calibration measurement during the ACLOUD field campaign (11 June 2017).

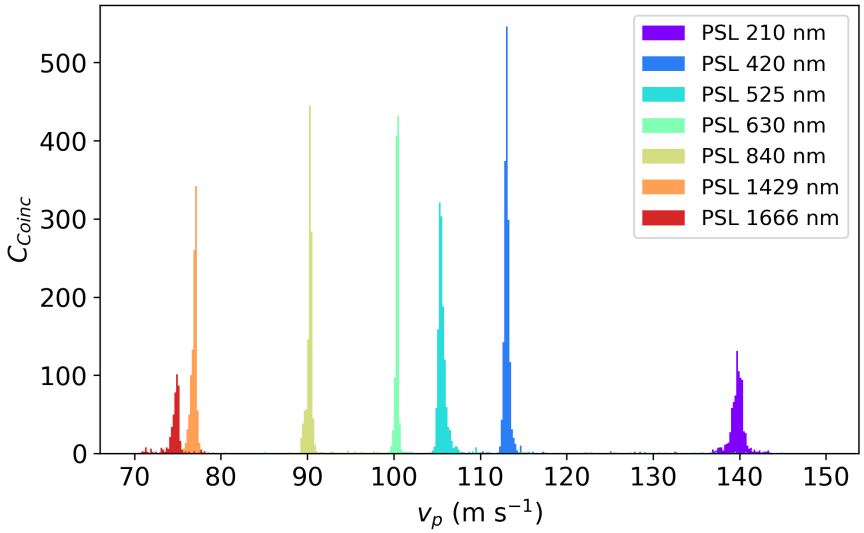

Figure A.2: Histogram of particle velocity (v_p) with number of particle dectections (C_{coinc}) by the ALABAMA for seven different sizes (d_{va}) of PSL particles from a calibration measurement after the ACLOUD field campaign (27 July 2017).

A.2 HIT RATE AND DETECTION EFFICIENCY

As described in Sect. 2.1.3, the hit rate (HR) of the ALABAMA ablation/ionization laser was limited by the maximum shot repetition rate of the laser (8 Hz). To analyze the effect of this limitation on the observed HR, the frequency of

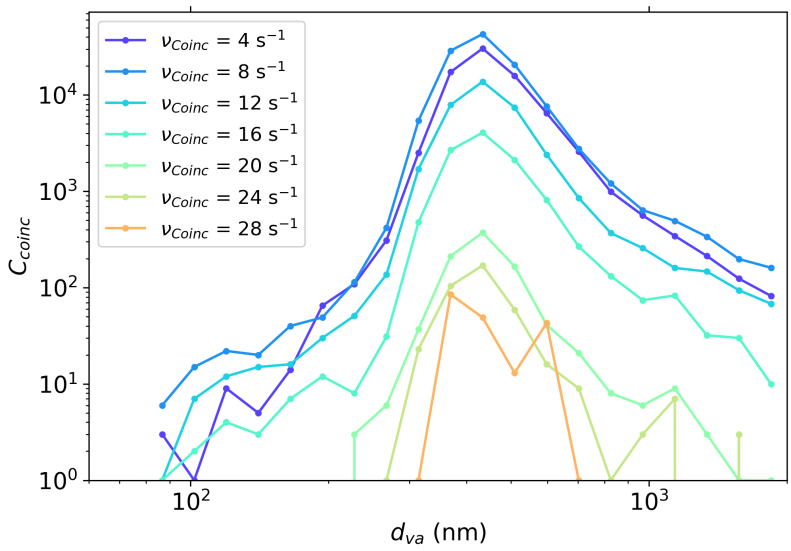

Figure A.3: Number of successfully detected particles C_{coinc} for different detection frequencies (ν_{Coinc}), i.e. C_{coinc} per second, as a function of particle size (d_{va}) for the ACLOUD field experiments. The given values were calculated for 20 logarithmic size bins between 80 nm and 2 μm.

detected particles ($\nu Coinc$) was considered. $\nu Coinc$ is defined by the number of detected particles (C_{coinc}) per time interval. To compare $\nu Coinc$ with the size-dependent HR (see Fig. 2.3), C_{coinc} of the corresponding $\nu Coinc$ values were calculated for different particle sizes (Fig. A.3). For $\nu Coinc$ values higher than the laser shot repetition rate, a large fraction of particles in the size range between 300 nm and 1 μm were detected by the ALABAMA. Since the laser could only shoot at eight particles per second, the remaining particles were missed at these frequencies. Therefore, HR must be smaller than one for ν_{Coinc} larger than 8 s^{-1}.

In Sect. 2.1.3, the vertical profile of the ALABAMA performance parameters, such as the detection efficiency (DE) and the hit rate (HR), was only shown for ACLOUD flights no. 7 - 18 (see Fig. 2.4. For the remaining flights no. 19 - 25, DE was significantly lower and more variable compared to the first set of flights (Fig. A.4).

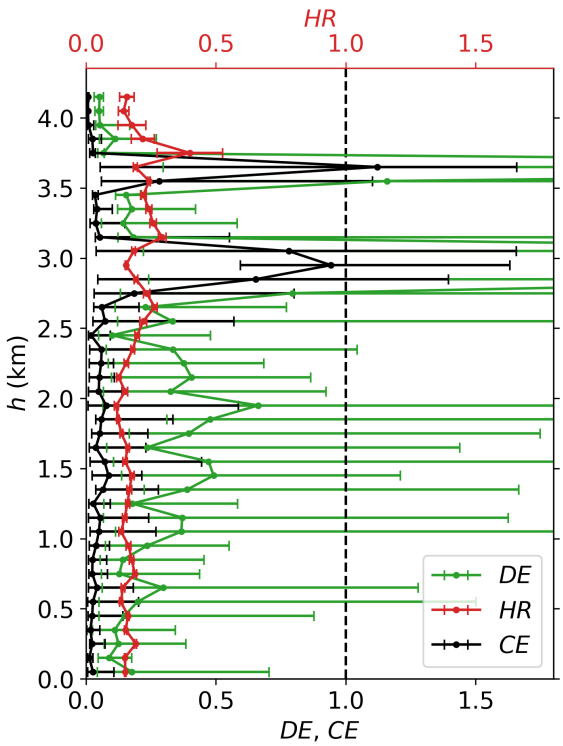

Figure A.4: Vertical profiles of detection efficiency (DE), hit rate (HR) and collection efficiency (CE) for flights no. 19 - no. 25 (17 June - 26 June 2017) of the ACLOUD field campaign. The dashed line indicates the optimal efficiency of unity. Values are given as median within altitude intervals of 100 m, uncertainties correspond to the interquartile range within these intervals. Uncertainty analyses are given in Sect. A.5.

A.3 OVERVIEW OF LASER INTENSITIES

The laser intensity of the ablation/ionization laser was estimated in the range between $1{\cdot}10^8$ W cm^{-2} and $3.77 \cdot 10^9$ W cm^{-2} for the current study. In Table A.2, this range is compared to laser intensities used in other SPMS studies.

A.4 COMPARISON OF INLET SYSTEM

During ACLOUD flight no. 8 (29 May 2017), the sampling of aerosol particles was compared between the two aerosol inlet systems (standard aerosol inlet and CVI inlet; see Sect. 2.3.1) in terms of particle concentrations and chemical composition. As shown in Fig. A.5a, a flight section in the free troposphere at about 1 km was selected during which the ALABAMA and the UHSAS-2 instruments switched from the CVI inlet to the standard aerosol inlet at 06:03:30

Table A.2: Overview of laser intensity or energy per pulse for different SPMS studies that were used as ion marker references (see Table 2.1) and for the experiments in the thesis. The given information is partly adapted from Köllner, 2020.

Studies	**Laser intensity or energy per pulse**
Angelino et al. (2001)	-
Prather et al. (2013)	1.2 - 1.5 mJ per pulse
Schmidt et al. (2017)	-
Brands et al. (2011)	$2.6 \cdot 10^9$ W cm^{-2}
Silva and Prather (2000)	10^8 - 10^9 W cm^{-2}
Brands (2009)	$3.8 \cdot 10^8$ - $2.6 \cdot 10^9$ W cm^{-2}
Arctic experiment ACLOUD 2017 (current study)	$1 \cdot 10^8$ - $4 \cdot 10^9$ W cm^{-2}

UTC. Since the UHSAS-1 which was continuously connected to the CVI inlet, the concentrations obtained by the UHSAS-1 were used as a reference. During the considered time period of approx. 7 min, the particle concentrations were constant at $\sim 200\,\mathrm{cm}^{-3}$ apart from minor fluctuations (Fig. A.5b).

Under these similar atmospheric conditions, the measurements of both, the UHSAS-2 and the ALABAMA, did not indicate apparent changes. In particular, the measured concentrations and particle sizes by the UHSAS-2 remained at a constant level before and after switching the inlet system (Fig. A.5b). Moreover, the chemical composition analysis by the ALABAMA revealed only small changes between both inlet systems (Fig. A.6). In summary, the measurements of the various aerosol properties seems to be not affected by the usage of different aerosol inlet systems.

Table A.3: Configuration of aerosol instruments and the inlet systems. Flight numbers indicate whether the instrument was switching during a flight between aerosol and CVI inlet or whether it remained connected to the CVI measuring ambient aerosol by switching off the counterflow of the CVI. This table is adapted from Ehrlich et al. (2019).

Instrument	**Aerosol and CVI inlet**	**CVI inlet only**
UHSAS-1, CPC	-	flight nos. 7-25
UHSAS-2, ALABAMA	flight nos. 7-10, 12, 15,19, 20, 22, 23	flight nos. 11, 13, 14, 16-18, 21, 24, 25

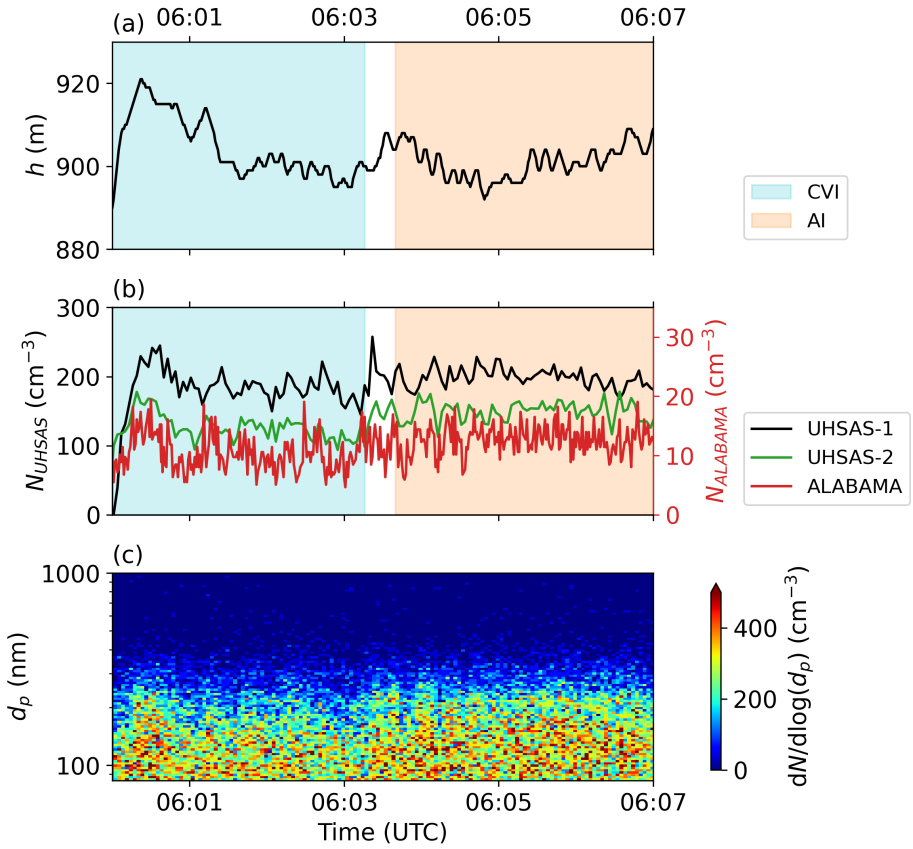

Figure A.5: Timeseries of fligt altitude (h; a), particle number concentrations obtained by both UHSAS instruments (N_{UHSAS}) and by the ALABAMA ($N_{ALABAMA}$; b) as well as the particle size distribution ($\mathrm{d}N/\mathrm{d}\log(d_p)$) obtained by UHSAS-2 while switching the aerosol inlet system during ACLOUD flight no. 8 (29 May 2017). $N_{ALABAMA}$ corresponds to the number concentration of successfully detected particles N_{coinc}. The color-shaded periods define the sampling periods connected to either the standard aerosol inlet (AI, orange) or the counterflow virtual impactor (CVI) inlet (green).

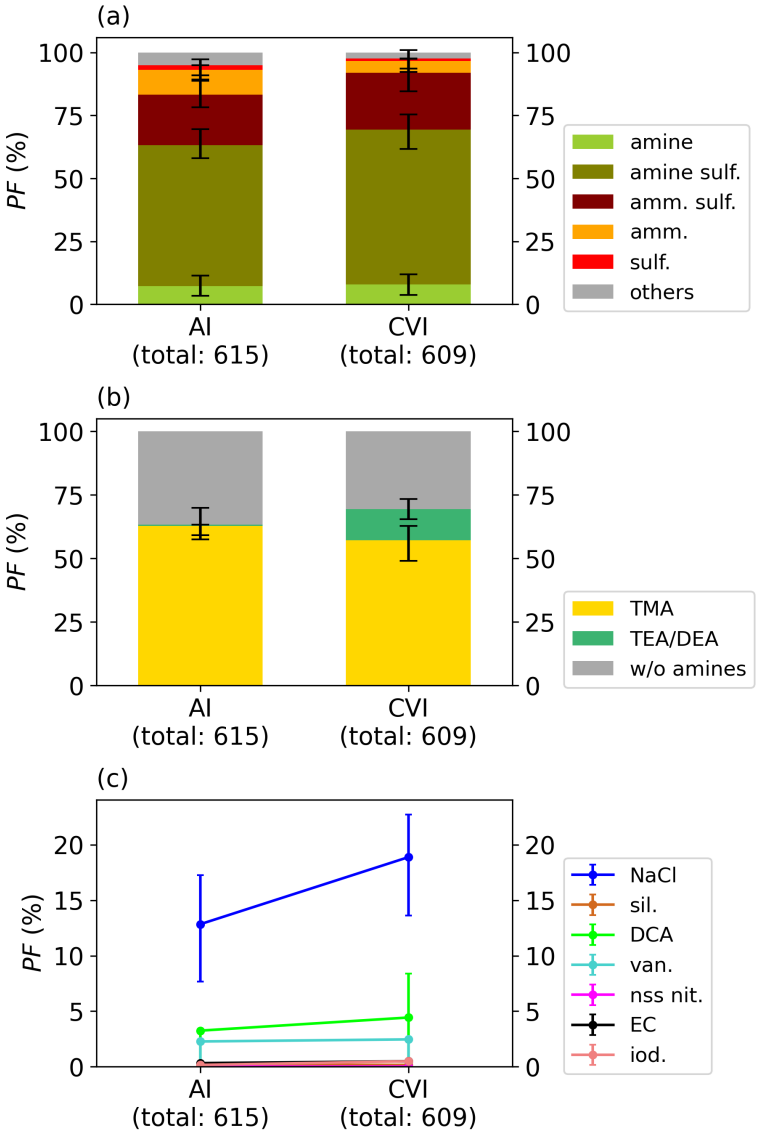

Figure A.6: Comparison of analyzed chemical composition obtained by the ALABAMA for the switching test between the two aerosol inlet systems: the standard aerosol inlet (AI) and the counterflow virtual impactor (CVI) inlet. The particle fraction (PF) is shown for the particle types from hierarchical markering (a), the amine types (b) and further markered species (c). The acronyms are defined as follows: amine sulfate (amine sulf.), ammonium sulfate (amm. sulf.), ammonium (amm.) and sulfate (sulf.), trimethylamine (TMA), tri-/diethylamine (TEA/DEA), sea spray (NaCl), silicium (sil.), dicarboxylic acids (DCA), vanadium (van.), nss nitrate (nss nit.), elemental carbon (EC) and iodine (iod.). Further details about the determination of PF and the corresponding uncertainties are provided in Sect. 2.2.3 and A.5, respectively.

A.5 UNCERTAINTY ANALYSIS

PSL particle size

The modal diameter (d_p) of PSL particles is provided by the manufacturers. The vacuum-aerodynamic diameter d_{va} is defined as follows:

$$d_{va} = \frac{\rho_p}{\rho_0 \chi} \cdot d_{ve}, \tag{A.1}$$

where ρ_p is the particle density, ρ_0 is the standard density of $1\,\mathrm{g\ m^{-2}}$ and χ represents the shape factor (DeCarlo et al., 2004). Using Eq. A.1 with the density for PSL ($\rho_{PSL} = 1.05\,\mathrm{g\ m^{-2}}$) and a shape factor ($\chi$) of 1 for spherical particles, the d_{va} for the PSL particles used in this thesis were obtained (Table A.1). Accordingly, the uncertainty for d_p provided by the manufacturer was converted to the uncertainty of d_{va} using Eq. A.1 (Table A.1).

Particle velocity

The absolute uncertainty of the particle velocity $\sigma_{v_p}^{abs}$ is determined by the lower and upper quartile of measured particle velocities v_p for a given PSL particle size (see histograms in Fig. A.1 and A.2).

Vertically-resolved detection efficiency and hit rate

The absolute uncertainty of the vertically-resolved detection efficiency (σ_{DE}^{vert}; see Fig. 2.4 and A.4) is determined by the lower and upper quartile of the measured detection efficiencies (DE) within a certain altitude bin. Likewise, the absolute uncertainty of the vertically-resolved hit rate (σ_{HR}^{vert}; see Fig. 2.4 and A.4) is determined by the lower and upper quartile of the hit rate (HR) distribution within a certain altitude bin.

Hit rate

The absolute uncertainty of the hit rate (σ_{HR}^{abs}) is calculated using binomial statistics (Clemen et al., 2020; Köllner, 2020):

$$\sigma_{HR}^{abs} = \frac{\sqrt{C_{hits}(1-HR)}}{C_{coinc}}, \tag{A.2}$$

with the particle number hit by the ablation laser and successfully ionized (C_{hits}), the number of successfully detected particles (C_{coinc}) which trigger the ablation laser and the hit rate (HR).

Collection efficiency

The absolute uncertainty of the vertically-resolved collection efficiency (σ_{CE}^{vert}; see Fig. 2.4 and A.4) is calculated using Gaussian propagation of uncertainties:

$$\sigma_{CE}^{vert} = \sqrt{(HR \cdot \sigma_{DE}^{vert})^2 + (DE \cdot \sigma_{HR}^{vert})^2} \tag{A.3}$$

Particle fraction

The absolute uncertainty of the ALABAMA particle fraction (σ_{PF}^{abs}) includes the uncertainty related to binomial statistics (σ_{PF}^{bin}) and the uncertainty related to the background signal definition (σ_{PF}^{bg}). It is defined as follows:

$$\sigma_{PF}^{abs} = \sqrt{(\sigma_{PF}^{bin})^2 + (\sigma_{PF}^{bg})^2}. \tag{A.4}$$

Since the successfull ablation/ionization of an individual particle by the ablation laser is well described as a Bernoulli process (Köllner, 2020), the uncertainty of PF partially result from binomial statistics. Thus, σ_{PF}^{bin} is defined as follows (Clemen et al., 2020; Köllner, 2020):

$$\sigma_{PF}^{bin} = \frac{\sqrt{C_{hits} \cdot PF \cdot (1-PF)}}{C_{hits}}, \tag{A.5}$$

with the number of successfully ionized particles by the ablation laser (C_{hits}) and the fraction of a specific particle type (PF).

σ_{PF}^{bg} is determined by adding/substracting the obtained PF using a 5 mV · sample lower/higher background threshold from PF with the original background signal threshold (see Sect. 2.2.2).

Scaled particle fraction

The absolute uncertainty of the scaled ALABAMA particle fraction ($\sigma_{PF_{sclaed}}^{abs}$) is calculated using Gaussian propagation of uncertainties:

$$\sigma_{PF_{scaled}}^{abs} = \sqrt{(N_{coinc} \cdot \sigma_{PF}^{abs})^2 + (PF \cdot \sigma_{N_{coinc}}^{abs})^2}, \tag{A.6}$$

with the absolute uncertainty of number concentration of detected particles by the ALABAMA ($\sigma_{N_{coinc}}^{abs}$). $\sigma_{N_{coinc}}^{abs}$ is determined as the standard deviation of the number concentration of detected particles by the ALABAMA N_{coinc} within a specific bin of the corresponding PF.

B

SUPPLEMENTARY INFORMATION FOR CHAPTER 3

B.1 ACLOUD FLIGHTS OF POLAR 6

Table B.1 gives an overview of the flight times of all *Polar 6* flights considered for the analysis in this study. The analysis covers all 19 conducted scientific flights with *Polar 6* during ACLOUD as well as the two ferry flights after the campaign. To note, the ACLOUD flight numbering for *Polar 6* starts with no. 7. Flights no. 1 - 3 were the ferry flights of both aircrafts (*Polar 5* & *6*) and no. 4 - 6 were the scientific flights of *Polar 5* only.

Table B.1: Overview of *Polar 6* flights considered in this study, including 19 scientific flights during the ACLOUD campaign and two ferry flights after the campaign. Flights no. 7 - 25 were conducted around Svalbard (Norway) with the base airport located in Longyearbyen. The first ferry flight (no. 26) was conducted from Longyearbyen (Norway) to Trondheim (Norway), the second ferry flight (no. 27) from Trondheim to Bremen (Germany).

Flight no.	**Date in 2017**	**Take-off–landing (UTC)**
7	27 May	13:02–16:27
8	29 May	05:11–09:17
9	30 May	09:18–13:30
10	31 May	14:59–19:03
11	2 June	08:27–14:09
12	4 June	10:06–15:39
13	5 June	10:43–14:44
14	8 June	07:30–13:20
15	9 June	07:56–09:18
16	13 June	14:57–17:16
17	14 June	12:54–17:37
18	16 June	04:40–10:31
19	17 June	10:10–15:55
20	18 June	12:25–17:50
21	20 June	07:37–13:27

Table continued on next page

Continued.

Flight no.	Date in 2017	Take-off–landing (UTC)
22	23 June	10:37–14:52
23	25 June	11:03–16:56
24	26 June	08:33–10:39
25	26 June	12:32–14:48
26	29 June	06:35–11:39
27	29 June	12:48–16:30

B.2 SENSITIVITY TO THE ARCTIC BOUNDARY DEFINITION

In Sect. 3.2, the contribution of different geographical origin regions to the measured air masses was presented. However, there is no clear geographical boundary for the definition of the Arctic region as it depends on the location of the *Polar Dome* (see Sect. 2.3.6). In this study, the value of the bounding latitude (73.5 °N) was selected from a previous study in the summertime Arctic (Bozem et al., 2019). This value might be different in the current study due to the variability of the *Polar Dome*. To test the sensitivity to the Arctic boundary definition, the bounding latitude was shifted by 1.5 ° northwards and southwards, respectively. In Fig. B.1 and B.2, the resulting vertical profiles of the source contribution are shown for a boundary latitude of 71 °N and 75 °N, respectively. In comparison to the original value in Fig. 3.3, the picture does not change qualitatively. Thus, the influence of the Arctic boundary definition on the analysis of air mass origin is expected to be small.

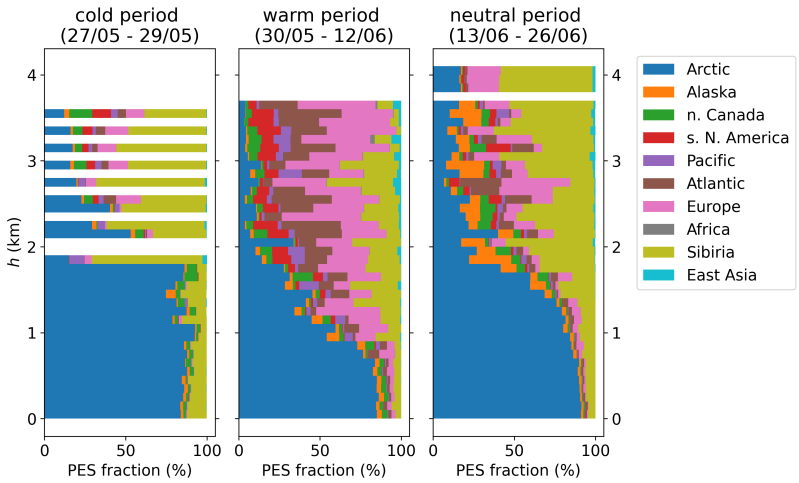

Figure B.1: Vertically-binned cumulative contribution of source regions as in Fig. 3.3, but with a southward shift of the Arctic boundary with a bounding latitude of 71 °N. The vertical profiles are shown for the three different synoptical periods during ACLOUD: the cold period (a), the warm period (b) and the neutral period (c). The contribution is given as fraction of the potential emission sensitivity ($PESF$) which is predicted by the FLEXPART model. Abbreviations are defined as: n. Canada = northern Canada, s. N. America = southern North America. Further details on the FLEXPART simulations and the source region definitions are described in Sect. 2.3.6.

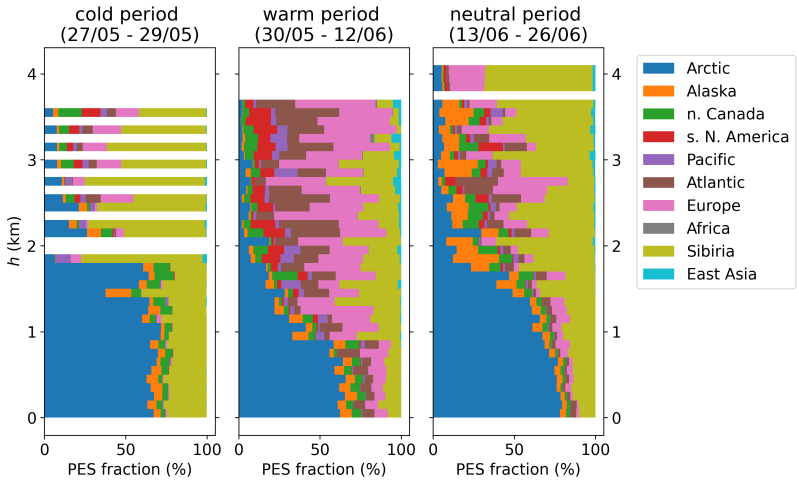

Figure B.2: Vertically-binned cumulative contribution of source regions as in Fig. 3.3, but with the Arctic region defined by a bounding latitude of 75 °N. The vertical profiles are shown for the three different synoptical periods during ACLOUD: the cold period (a), the warm period (b) and the neutral period (c). The contribution is given as fraction of the potential emission sensitivity ($PESF$) which is predicted by the FLEXPART model. Abbreviations are defined as: n. Canada = northern Canada, s. N. America = southern North America. Further details on the FLEXPART simulations and the source region definitions are described in Sect. 2.3.6.

B.3 ADDITIONAL FIGURES FOR THE AIR MASS CHARACTERIZATION

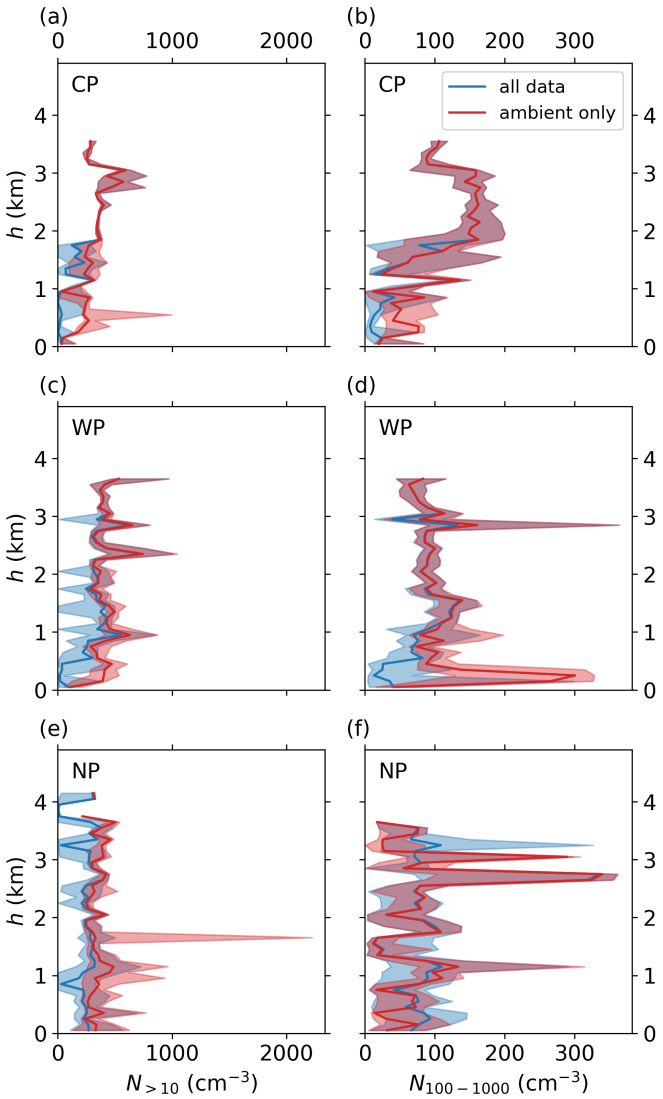

Figure B.3: Vertical profiles of median (solid lines) and interquartile range (shaded) during the three different synoptical periods during ACLOUD: the cold period (CP; a, b), the warm period (WP; c, d) and the neutral period (NP; e, f) for particle number concentrations for particles larger than 10 nm ($N_{>10}$; a, c, e) as well as particles in the size range between 100 nm and 1 μm ($N_{100-1000}$; b, d, f). The values were calculated for cloud-free air only (black) and for all data points (including in-cloud measurements).

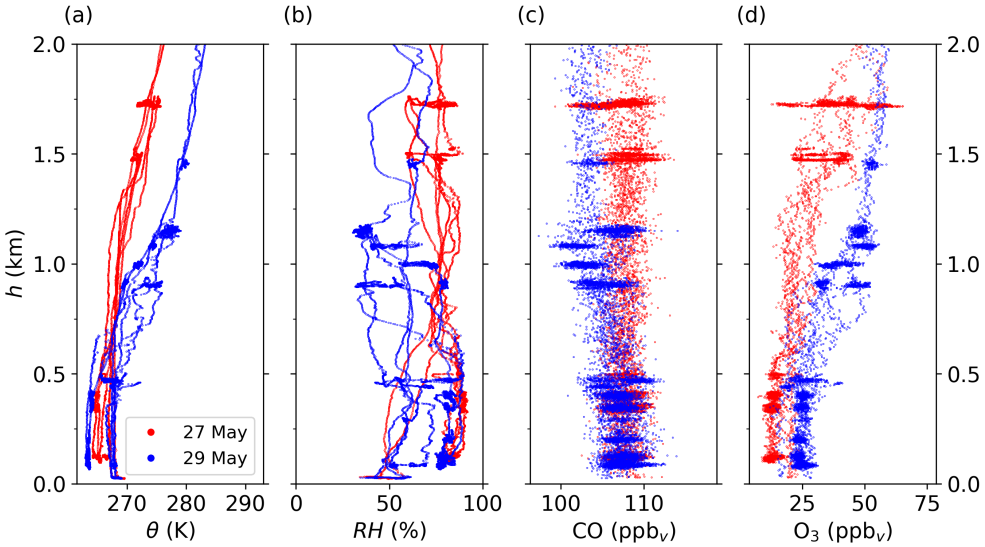

Figure B.4: Vertical profiles of individual data points for potential temperature (θ; a), relative humidity (RH; b), trace gas volume mixing ratios for carbon monoxide (CO; c) and ozone(O_3; d) for the two research flights during the CP on 27 May (red) and 29 May (blue).

C

SUPPLEMENTARY INFORMATION FOR CHAPTER 4

C.1 STATISTICS OF ANALYZED MASS SPECTRA DURING ACLOUD

Tables C.1 and C.2 summarize the statistics of analyzed particle spectra for the research flights during ACLOUD and the two ferry flights after the ACLOUD campaign, respectively.

Table C.1: Overview of mass spectra obtained by the ALABAMA during the ACLOUD campaign.

Selection	**no. of spectra (relative contribution in %)**
Analyzed particles	242 065 (100.00 %)
Analyzed CPR (inside clouds)	47 004 (19.42 %)
Particles with size information	232 379 (96.00 %)
Particles with dual polarity	198 058 (81.82 %)
Particles with single positive polarity	40 610 (16.78 %)
Particles with single negative polarity	53 (0.02 %)
Particles without any signal above threshold	3 344 (1.38 %)

Table C.2: Overview of mass spectra obtained by the ALABAMA during the ferry flights after the ACLOUD campaign.

Selection	**no. of spectra (relative contribution in %)**
Analyzed particles	23 645 (100.00 %)
Analyzed CPR (inside clouds)	3 749 (15.86 %)
Particles with size information	22 905 (96.87 %)
Particles with dual polarity	15 600 (65.98 %)
Particles with single positive polarity	7 450 (31.51 %)
Particles with single negative polarity	1 (<0.01 %)
Particles without any signal above threshold	7 449 (31.50 %)

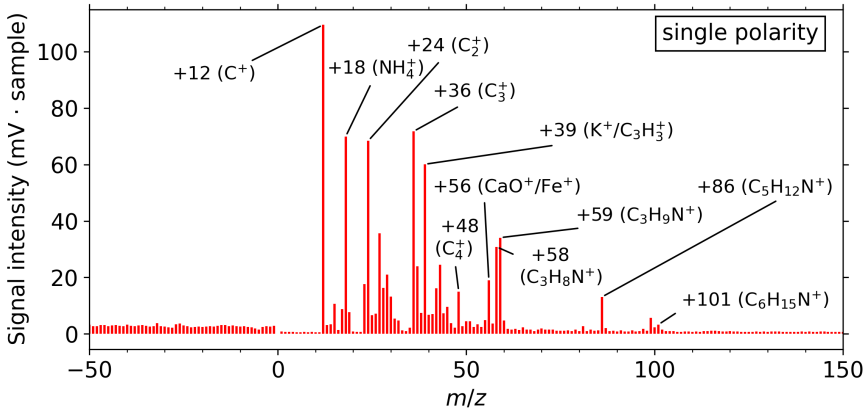

Figure C.1: Mean bipolar mass spectra of particles analyzed by the ALABAMA that showed only a single polarity.

C.2 ADDITIONAL FIGURES OF THE CLOUD COMPOSITION ANALYSIS

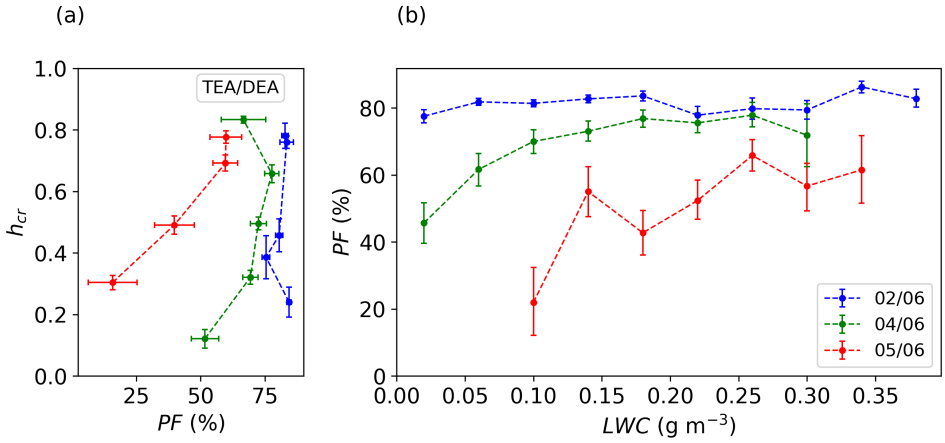

Figure C.2: Cloud vertical profiles (given in cloud relative height h_{cr}) of particle fractions (PF) for TEA/DEA-containing particles for the selected cloud cases (a) and PF of TEA/DEA-containing particles in dependency of the measured liquid water content (LWC) by the Nevzorov probe (see Sect. 2.3.4) inside the clouds above sea ice (b). The colors represents the flight day given in the legend. Uncertainty analyses are given in Sect. A.5.

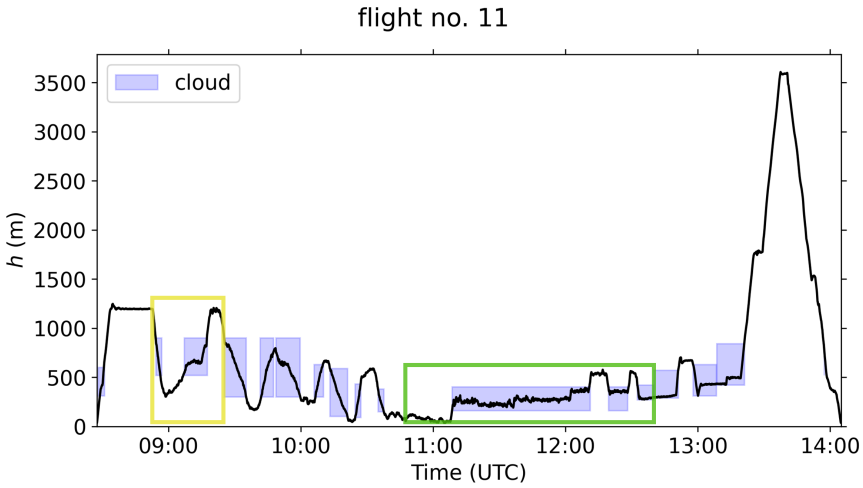

Figure C.3: Timeseries of flight altitude (h) during ACLOUD flight no. 11 (2 June 2017). The blue-shaded boxes indicate periods of in-cloud flight segments with estimated cloud height. In addition, the considered cloud events for the analysis above open water (yellow box) and above sea ice (green box) are highlighted.

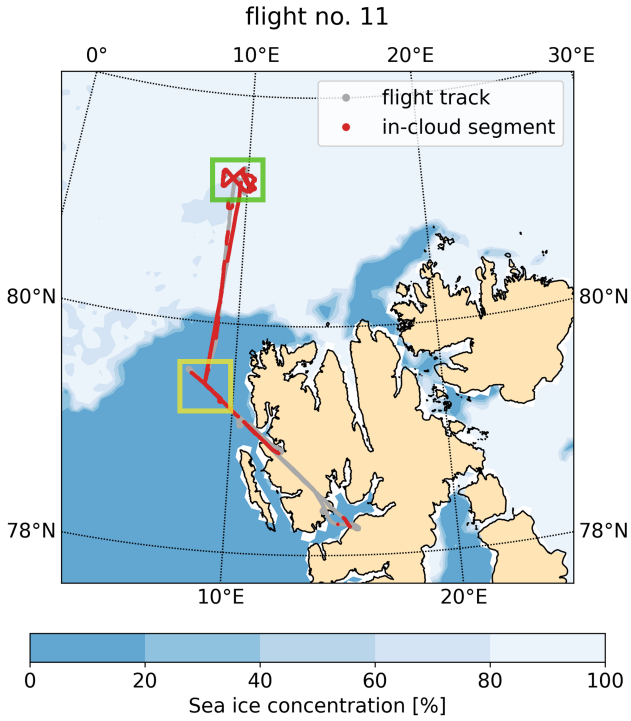

Figure C.4: Map of flight path (grey) and in-cloud flight segments (red) during ACLOUD flight no. 11 (2 June 2017). The colorbar indicates the sea ice concentration from satellite data (see Sect. 2.3.7). In addition, the considered cloud events for the analysis above open water (yellow box) and above sea ice (green box) are highlighted.

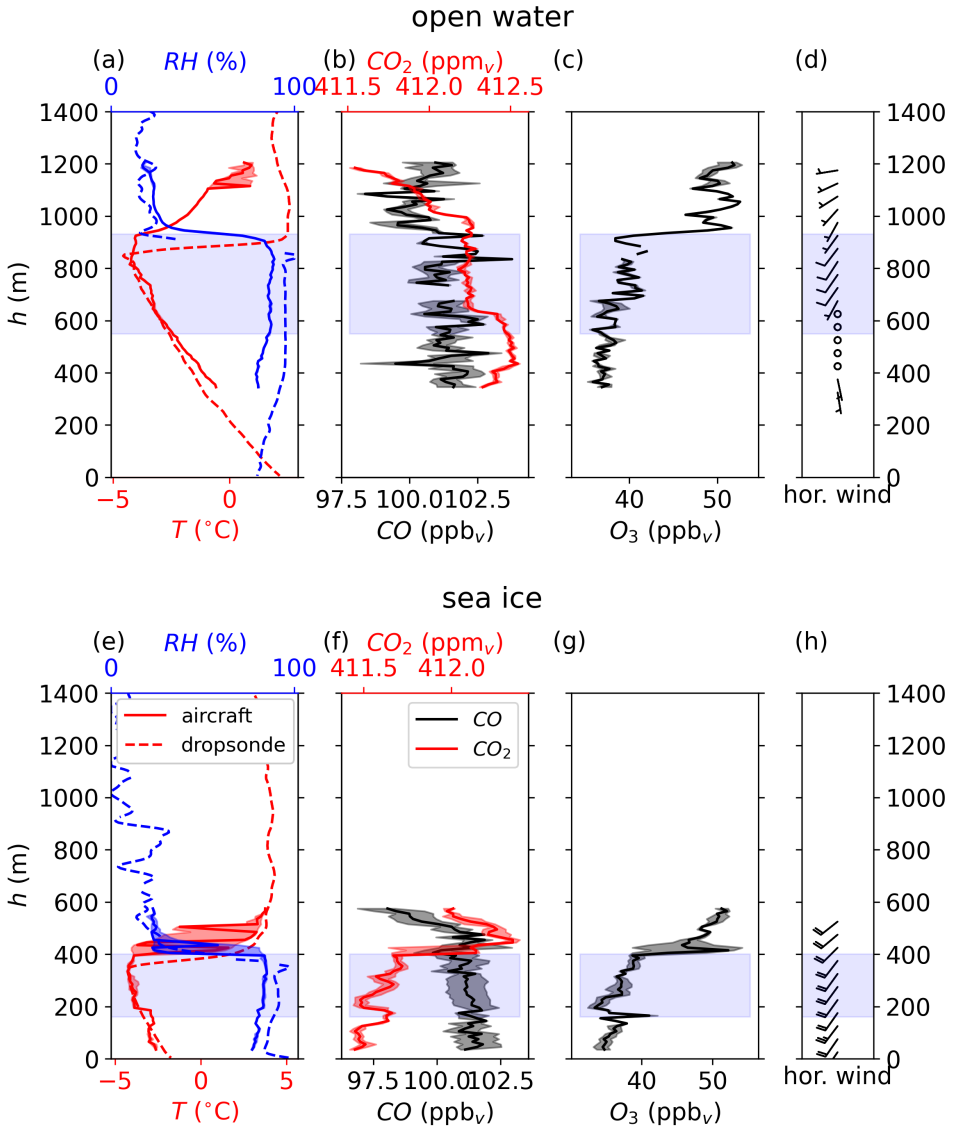

Figure C.5: Comparison of vertical profiles of cloud properties including temperature (T) and relative humidity (RH; a, e), CO and CO_2 volume mixing ratios (b, f), O_3 volume mixing ratio (c, g) as well as horizontal wind speed and direction (barbs; d, h) for a cloud transect above open water (a-d) and above sea ice (e-h) during ACLOUD flight no. 11 (2 June), given as median (solid lines) and the interquartile range (shaded area). Additionally, a θ derived from a dropsonde released by the *Polar 5* (dashed line) and the vertical position of the clouds (light shaded areas) are included.

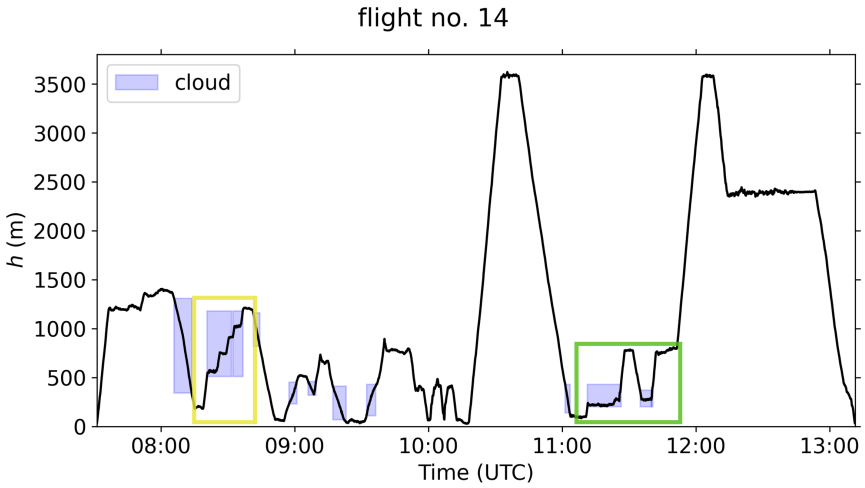

Figure C.6: Timeseries of flight altitude (h) during ACLOUD flight no. 14 (8 June 2017). The blue-shaded boxes indicate periods of in-cloud flight segments with estimated cloud height. In addition, the considered cloud events for the analysis above open water (yellow box) and above sea ice (green box) are highlighted.

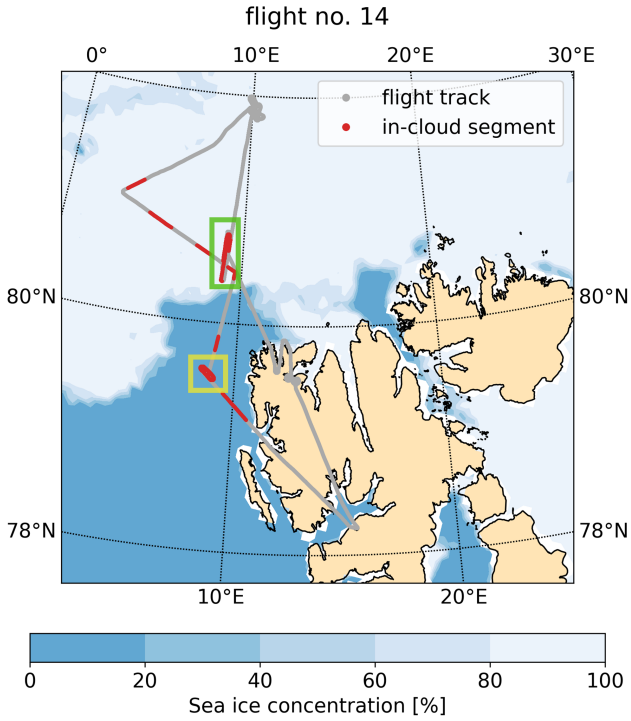

Figure C.7: Map of flight path (grey) and in-cloud flight segments (red) during ACLOUD flight no. 14 (8 June 2017). The colorbar indicates the sea ice concentration from satellite data (see Sect. 2.3.7). In addition, the considered cloud events for the analysis above open water (yellow box) and above sea ice (green box) are highlighted.

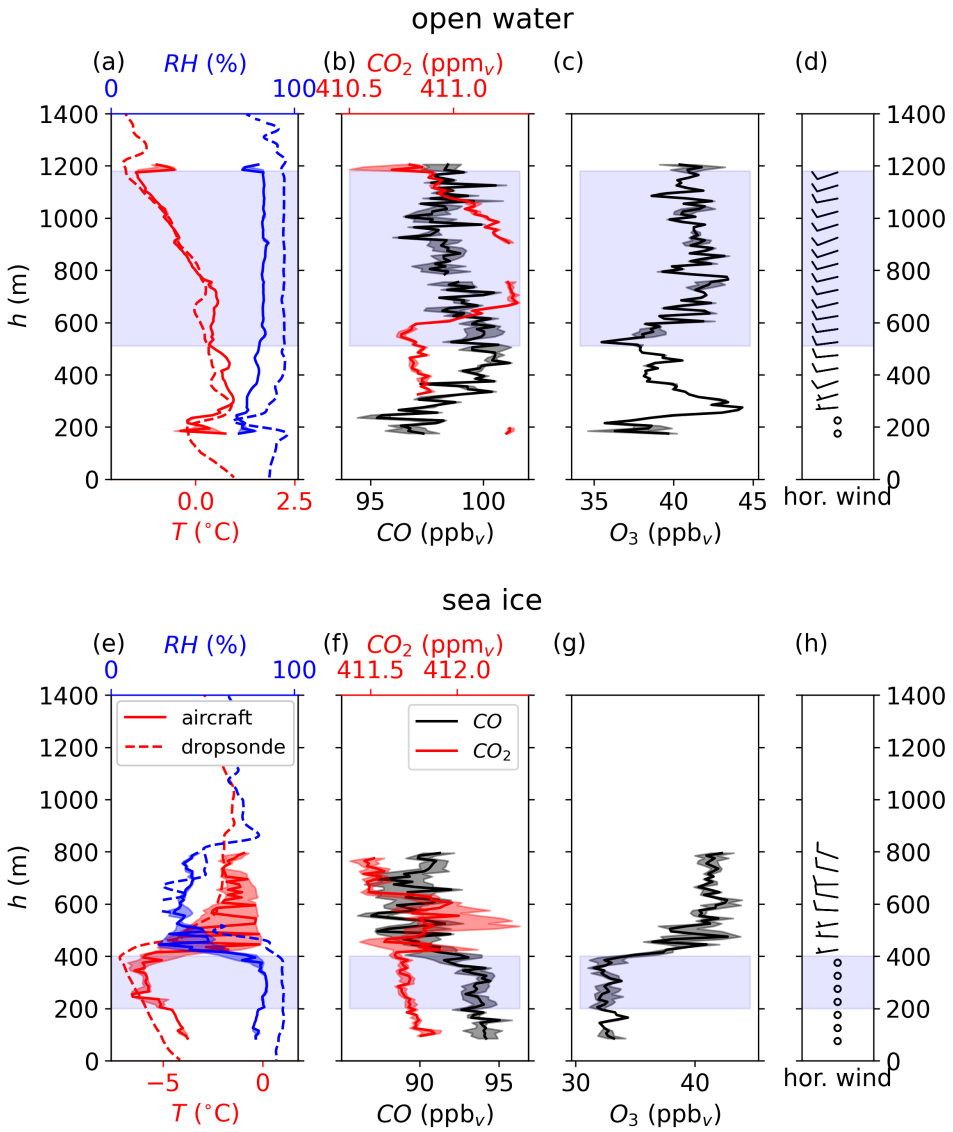

Figure C.8: Comparison of vertical profiles of cloud properties including temperature (T) and relative humidity (RH; a, e), CO and CO_2 volume mixing ratios (b, f), O_3 volume mixing ratio (c, g) as well as horizontal wind speed and direction (barbs; d, h) for a cloud transect above open water (a-d) and above sea ice (e-h) during ACLOUD flight no. 14 (8 June), given as median (solid lines) and the interquartile range (shaded area). Additionally, a θ derived from a dropsonde released by the *Polar 5* (dashed line) and the vertical position of the clouds (light shaded areas) are included.

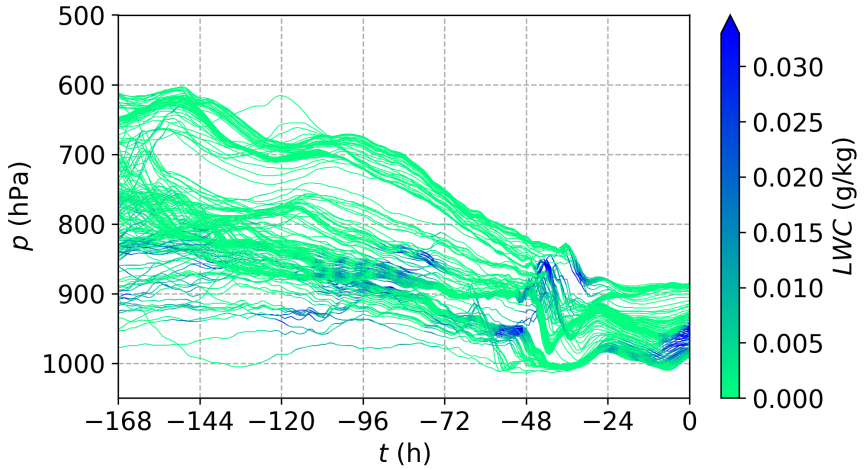

Figure C.9: Timeseries of vertically-resolved LAGRANTO trajectories colored by cloud liquid water content (LWC) for the open water case during ACLOUD flight no. 11 (2 June 2017).

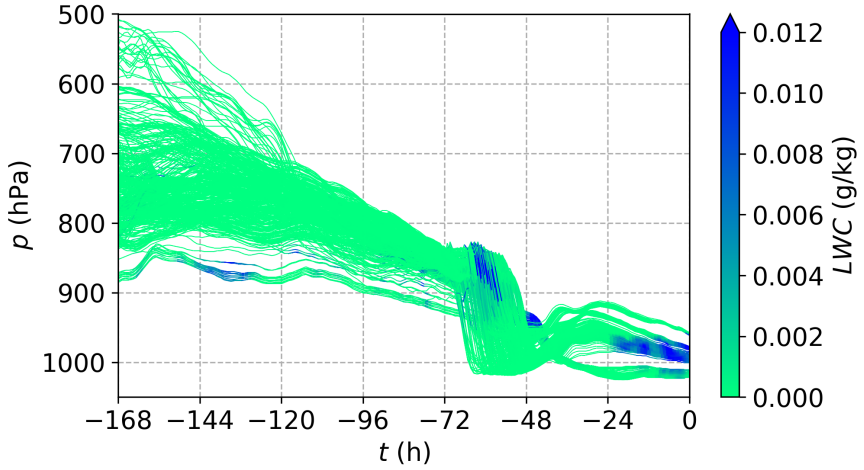

Figure C.10: Timeseries of vertically-resolved LAGRANTO trajectories colored by cloud liquid water content (LWC) for the sea ice case during ACLOUD flight no. 11 (2 June 2017).

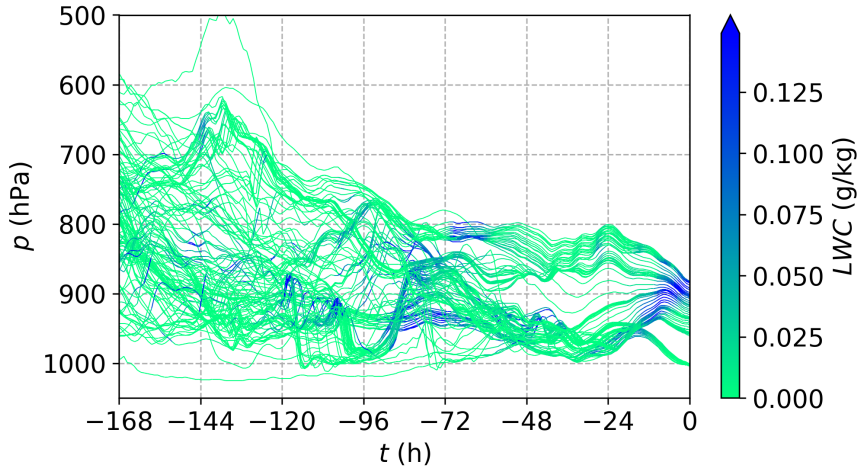

Figure C.11: Timeseries of vertically-resolved LAGRANTO trajectories colored by cloud liquid water content (LWC) for the open water case during ACLOUD flight no. 14 (8 June 2017).

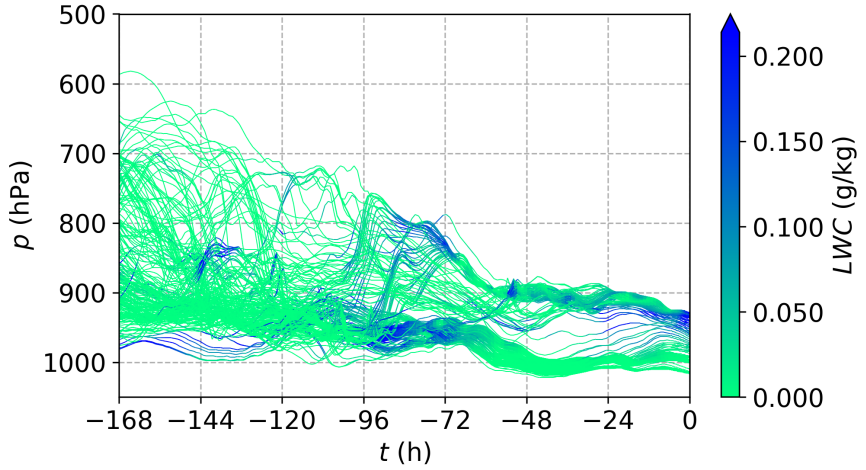

Figure C.12: Timeseries of vertically-resolved LAGRANTO trajectories colored by cloud liquid water content (LWC) for the sea ice case during ACLOUD flight no. 14 (8 June 2017).

C.3 ION SIGNALS OF DIFFERENT ALKYLAMINES AND AMINO ACIDS

In this study, three types of alkylamines were analyzed in the recorded mass spectra of the ALABAMA: DEA, TEA and TMA. Table C.3 gives an overview of the ion marker signals associated with these amine species. As shown in Fig. C.13, a significant fraction of these signals occurred above the background threshold. For the ion signal at m/z +74, only less than 10 % were higher than the background noise, suggesting the signal at m/z +86 representing rather TEA than DEA for the majority of its occurrence.

Table C.3: Overview of ion markers associated with the alkylamine species analyzed in this study, including isobaric interferences of other amine species and references. This table is partly adapted from Köllner (2020).

Ion markers	Marker species	Reference
m/z +58	diethylamine (DEA) and/or trimethylamine (TMA)	Angelino et al. (2001); Köllner et al. (2017)
m/z +59	TMA	Angelino et al. (2001); Köllner et al. (2017)
m/z +74	DEA	Angelino et al. (2001)
m/z +86	DEA, triethylamine (TEA) and/or dipropylamine (DPA)	Angelino et al. (2001)
m/z +101	TEA	Angelino et al. (2001)

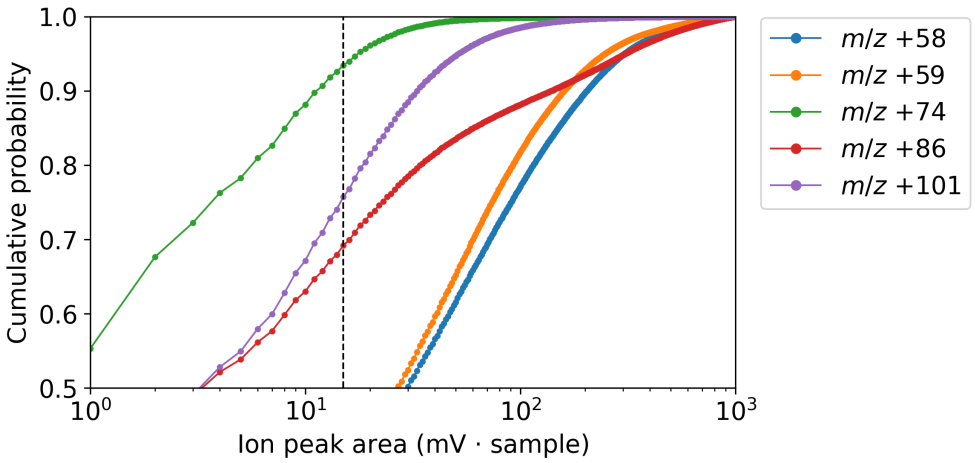

Figure C.13: Cumulative probability distributions of ion peak area values from ion signal peaks of alkylamines analyzed in this thesis (Table C.3).

Besides these amines, also other alkylamines have been identified by SPMS measurements in previous laboratory and field studies. Table C.4 summarizes the ion markers for different amine species reported by a laboratory study (Angelino et al., 2001) and a field study at five European sites (Healy et al., 2015). Primary amines, such as monomethylamine, were excluded from the discussion, as they are expected to produce ion signals at lower m/z values than the amine species focused in this study.

For most of the ion markers in Table C.4, the ion peak area was below the background noise for more than 90 % (Fig. C.14). Only for the ion signal at m/z +46, a larger contribution to identified ion signals above the background threshold was observed (Fig. C.14). However, dimethylamine and Na_2^+ have an isobaric interference at m/z +46 (Köllner et al., 2017). Since the signal at m/z +46 often occurred in combination with a signal at m/z +23 (for example in the bipolar mean spectrum for NaCl-containing particles; see Fig. C.18b), this ion signal represents more likely Na_2^+ than dimethylamine.

A small fraction of analyzed particles indicated ion signals at m/z +72 and +102 as well (Fig. C.14). These ion signals occurred in combination of ion markers associated with DEA/TEA (for example in the bipolar mean spectrum for TEA/DEA-containing particles; see Fig. C.17d). However, since the ion signal at m/z +114 was mostly absent in these particles, it is unlikely that this identified amine type corresponds to DPA.

Table C.4: Overview of different alkylamines (other than the three amine species in this study) as well as ion markers and references. This table is partly adapted from Köllner (2020).

Ion markers	**Marker species**	**Reference**
m/z +46	dimethylamine	Healy et al. (2015)
m/z +74	diethylamine (DEA) and/or dipropylamine (DPA)	Angelino et al. (2001)
m/z +102	DPA	Angelino et al. (2001)
m/z +114	DPA and/or tripropylamine (TPA)	Angelino et al. (2001)
m/z +143	TPA	Angelino et al. (2001)

The recorded mass spectra were also checked for the presence of ion signals corresponding to amino acids. In Table C.5, ion markers of different amino acids known from literature are listed. Indeed, a significant fraction of analyzed particles indicated ion signals at m/z +40, +56, +63 and +86 (Fig. C.15). The

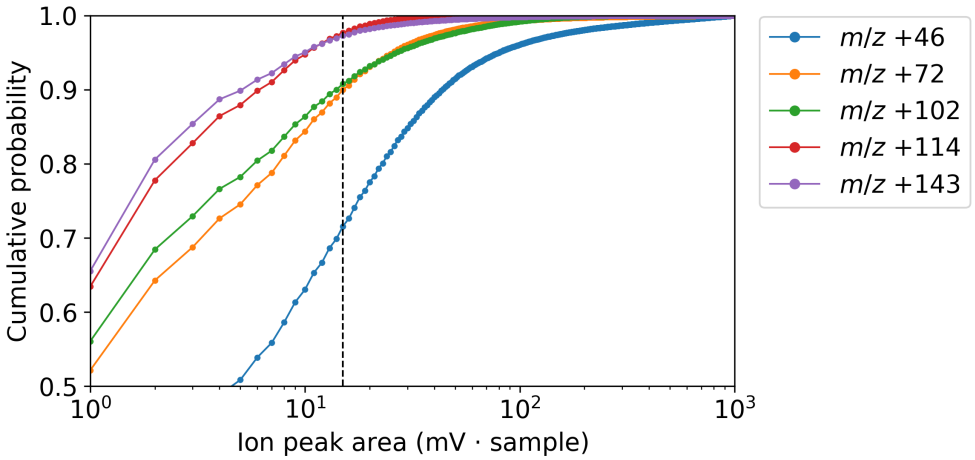

Figure C.14: Cumulative probability distributions of ion peak area values from ion signal peaks of different alkylamines (other than the three amine species in this study; Table C.4).

latter signal, however, is associated with the presence of amine particles due to its combination with other typical amine signals. Moreover, the ion signals at m/z +40, +56 and +63 have an isobaric interference with Ca^+ (m/z +40), CaO^+/Fe^+ (m/z +56) and Na_2OH^+ (m/z +63; Köllner et al., 2017). Thus, the assignment of these signals to amino acids is hindered.

Table C.5: Overview of different amino acids as well as ion markers and references. This table is partly adapted from Köllner (2020).

Ion markers	**Marker species**	**Reference**
m/z +40	Alanine, cysteine, glutamic acid, leucine, and/or proline	Schmidt et al. (2017)
m/z +56	Alanine, cysteine, glutamic acid, leucine, and/or proline	Schmidt et al. (2017)
m/z +63	Alanine, cysteine, glutamic acid, leucine, and/or proline	Schmidt et al. (2017)
m/z +76	Glycine	Silva and Prather (2000)
m/z +86	Leucine	Schmidt et al. (2017)
m/z +111	Proline	Schmidt et al. (2017)
m/z +130	Tryptophan	Schmidt et al. (2017)
m/z +132	Leucine	Schmidt et al. (2017)

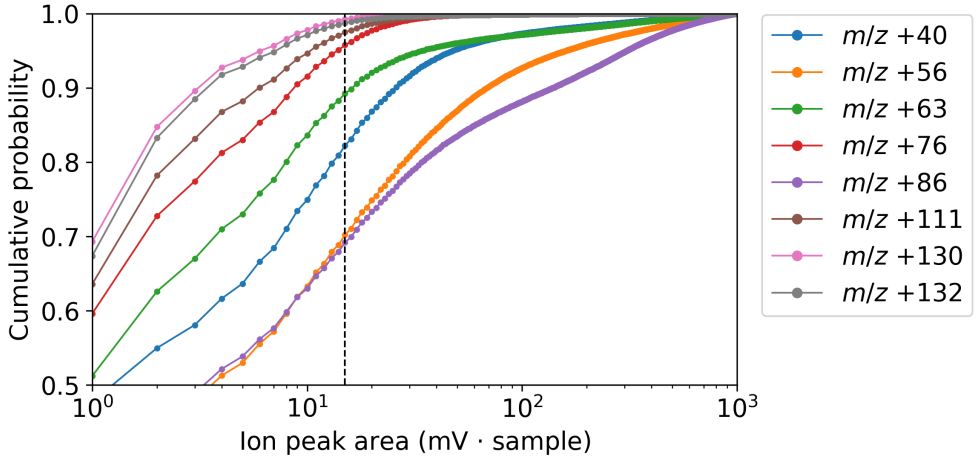

Figure C.15: Cumulative probability distributions of ion peak area values from ion signal peaks of different amino acids (Table C.5).

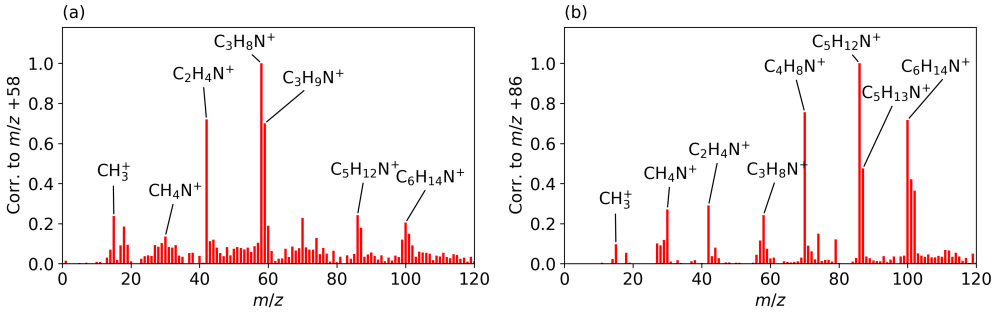

Figure C.16: Correlation of individual cation signals to the chracteristic ion signal of trimethylamine (TMA; m/z +58; a) and of tri-/dietyhlamine (TEA/DEA; m/z +86; a) of all analyzed particles.

C.4 ADDITIONAL MEAN MASS SPECTRA

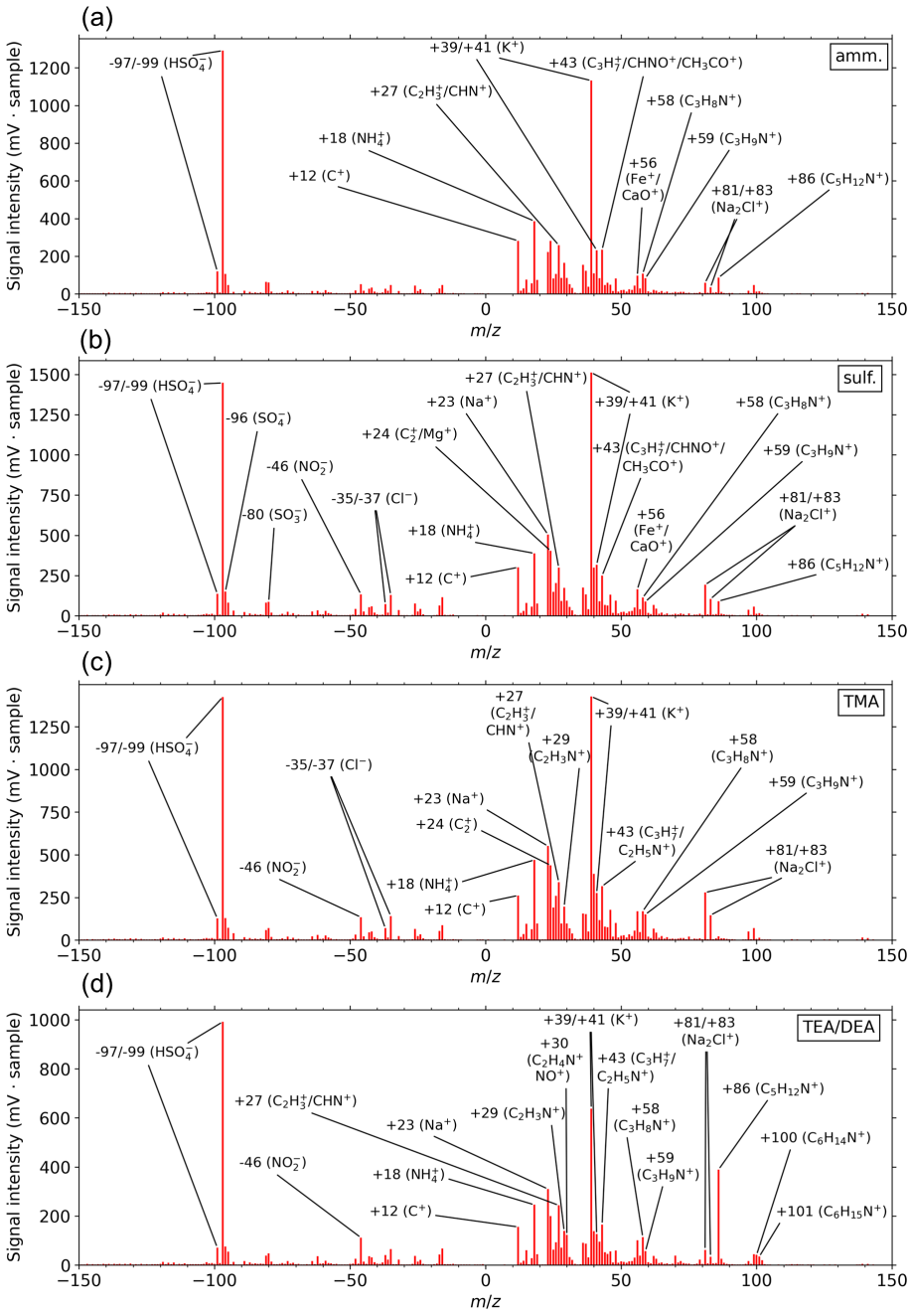

Figure C.17: Mean bipolar mass spectra of ammonium- (amm., a), sulfate- (sulf., b), trimethylamine- (TMA, c) and triethyl-/diethylamine- (TEA/DEA, d) containing particles analyzed by the ALABAMA.

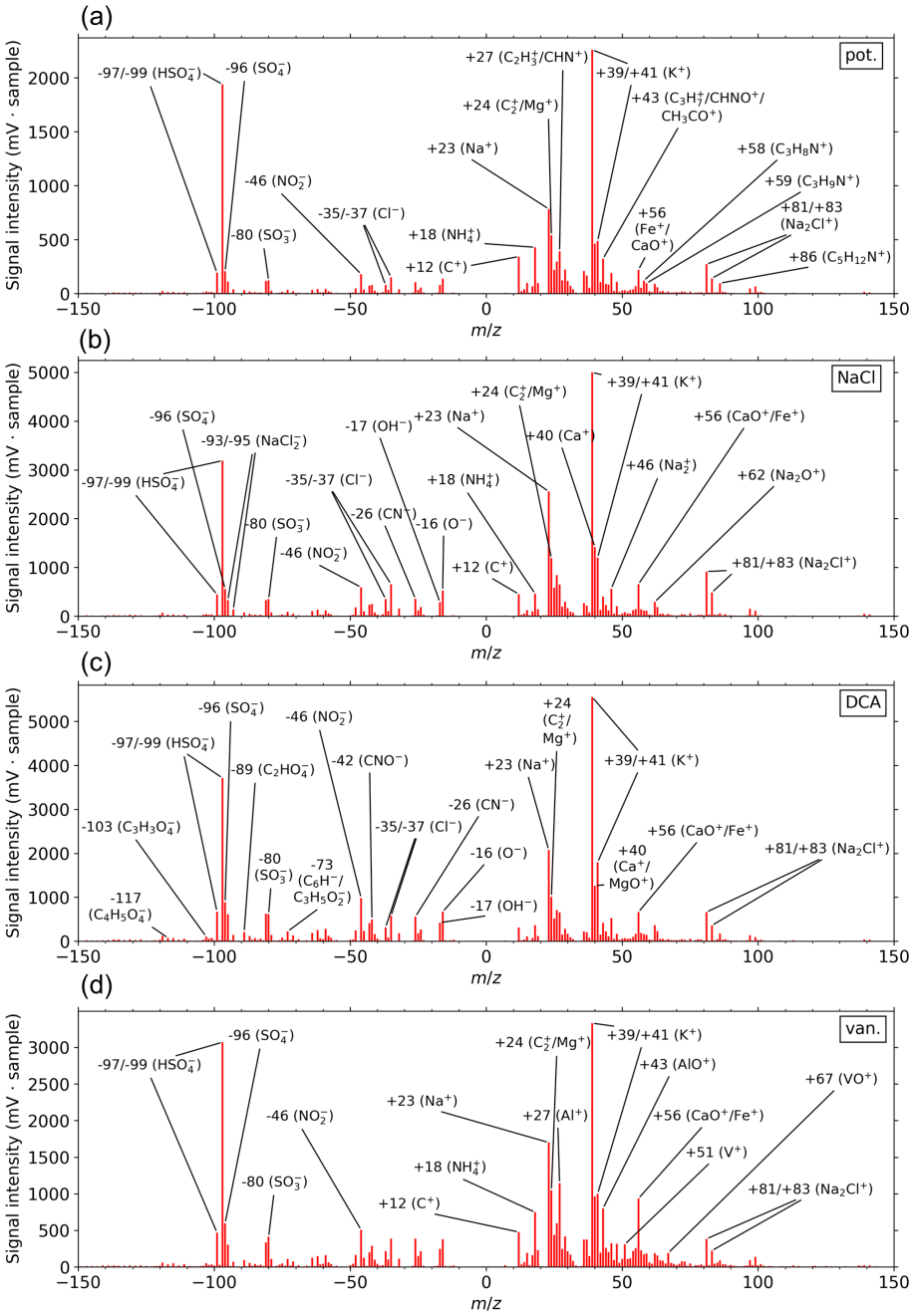

Figure C.18: Mean bipolar mass spectra of potassium- (pot., a), sea spray- (NaCl, b), dicarboxylic acids- (DCA, c) and vanadium- (van., d) containing particles analyzed by the ALABAMA.

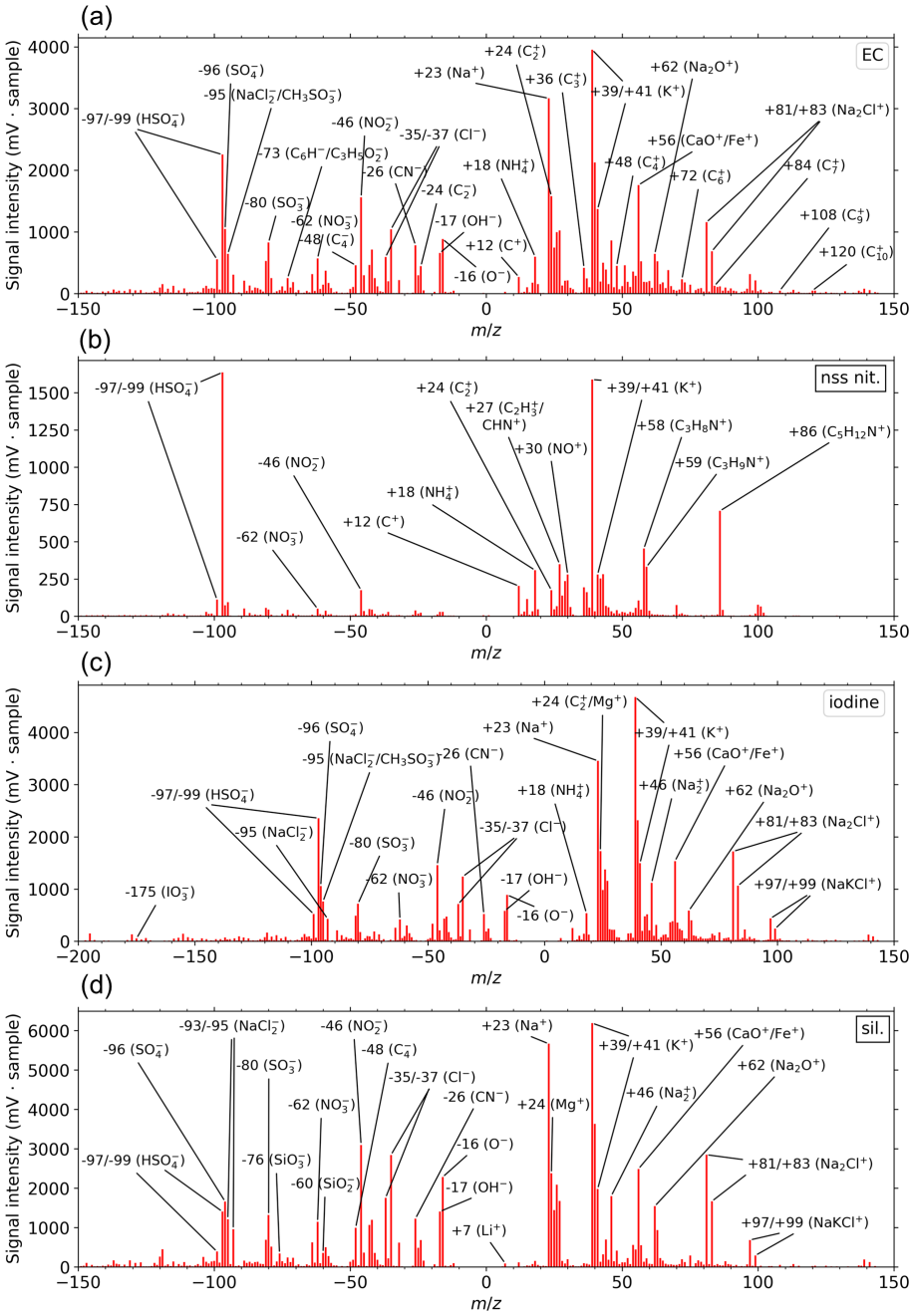

Figure C.19: Mean bipolar mass spectra of elemental carbon- (EC, a), non-sea-spray nitrate- (nss nit., b), iodine- (iod., c) and silicate- (sil., d) containing particles analyzed by the ALABAMA.

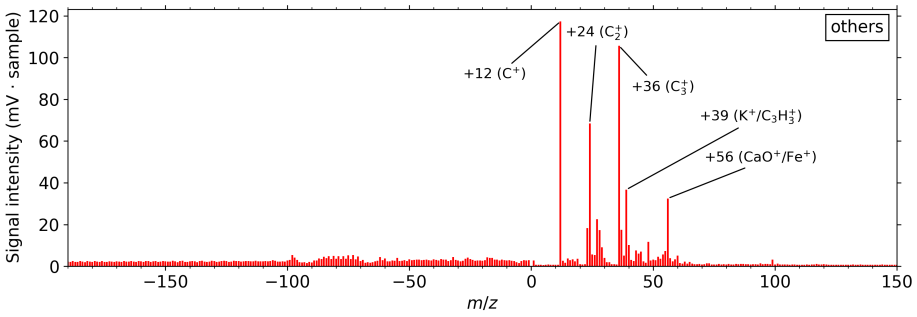

Figure C.20: Mean bipolar mass spectra of particles analyzed by the ALABAMA that could not be classified into one of the particle types. These particles are therefore summarized as 'others'.

BIBLIOGRAPHY

Abbatt, J. P. D., J. L. Thomas, K. Abrahamsson, C. Boxe, A. Granfors, A. E. Jones, M. D. King, A. Saiz-Lopez, P. B. Shepson, J. Sodeau, D. W. Toohey, C. Toubin, R. von Glasow, S. N. Wren, and X. Yang (2012). "Halogen activation via interactions with environmental ice and snow in the polar lower troposphere and other regions." *Atmospheric Chemistry and Physics*, 12, pp. 6237–6271. DOI: 10.5194/acp-12-6237-2012.

Acosta Navarro, J. C., V. Varma, I. Riipinen, Ø. Seland, A. Kirkevåg, H. Struthers, T. Iversen, H.-C. Hansson, and A. M. L. Ekman (2016). "Amplification of Arctic warming by past air pollution reductions in Europe." *Nature Geoscience*, 9, pp. 277–281. DOI: 10.1038/ngeo2673.

Aliabadi, A. A., R. M. Staebler, and S. Sharma (2015). "Air quality monitoring in communities of the Canadian Arctic during the high shipping season with a focus on local and marine pollution." *Atmospheric Chemistry and Physics*, 15, pp. 2651–2673. DOI: 10.5194/acp-15-2651-2015.

Allan, J. D., P. I. Williams, J. Najera, J. D. Whitehead, M. J. Flynn, J. W. Taylor, D. Liu, E. Darbyshire, L. J. Carpenter, R. Chance, S. J. Andrews, S. C. Hackenberg, and G. McFiggans (2015). "Iodine observed in new particle formation events in the Arctic atmosphere during ACCACIA." *Atmospheric Chemistry and Physics*, 15, pp. 5599–5609. DOI: 10.5194/acp-15-5599-2015.

Almeida, J. et al. (2013). "Molecular understanding of sulphuric acid–amine particle nucleation in the atmosphere." *Nature*, 502, pp. 359–363. DOI: 10.1038/nature12663.

Alterskjær, K., J. E. Kristjánsson, and C. Hoose (2010). "Do anthropogenic aerosols enhance or suppress the surface cloud forcing in the Arctic?" *Journal of Geophysical Research*, 115, p. D22204. DOI: 10.1029/2010JD014015.

Angelino, S., D. T. Suess, and K. A. Prather (2001). "Formation of Aerosol Particles from Reactions of Secondary and Tertiary Alkylamines: Characterization by Aerosol Time-of-Flight Mass Spectrometry." *Environmental Science & Technology*, 35, pp. 3130–3138. DOI: 10.1021/es0015444.

Asmi, E., V. Kondratyev, D. Brus, T. Laurila, H. Lihavainen, J. Backman, V. Vakkari, M. Aurela, J. Hatakka, Y. Viisanen, T. Uttal, V. Ivakhov, and A. Makshtas (2016). "Aerosol size distribution seasonal characteristics measured in Tiksi, Russian Arctic." *Atmospheric Chemistry and Physics*, 16, pp. 1271–1287. DOI: 10.5194/acp-16-1271-2016.

Ault, A. P., C. J. Gaston, Y. Wang, G. Dominguez, M. H. Thiemens, and K. A. Prather (2010). "Characterization of the Single Particle Mixing State of Individual Ship Plume Events Measured at the Port of Los Angeles." *Environmental Science & Technology*, 44, pp. 1954–1961. DOI: 10.1021/es902985h.

Baccarini, A., L. Karlsson, J. Dommen, P. Duplessis, J. Vüllers, I. M. Brooks, A. Saiz-Lopez, M. Salter, M. Tjernström, U. Baltensperger, P. Zieger, and J. Schmale (2020). "Frequent new particle formation over the high Arctic pack ice by enhanced iodine emissions." *Nature Communications*, 11, p. 4924. DOI: 10.1038/s41467-020-18551-0.

Backman, J., L. Schmeisser, and E. Asmi (2021). "Asian Emissions Explain Much of the Arctic Black Carbon Events." *Geophysical Research Letters*, 48. DOI: 10.1029/2020GL091913.

Barrie, L. A. (1986). "Arctic air pollution: An overview of current knowledge." *Atmospheric Environment*, 20, pp. 643–663. DOI: 10.1016/0004-6981(86)90180-0.

Becagli, S. et al. (2016). "Relationships linking primary production, sea ice melting, and biogenic aerosol in the Arctic." *Atmospheric Environment*, 136, pp. 1–15. DOI: 10.1016/j.atmosenv.2016.04.002.

Bhave, P. V., J. O. Allen, B. D. Morrical, D. P. Fergenson, G. R. Cass, and K. A. Prather (2002). "A Field-Based Approach for Determining ATOFMS Instrument Sensitivities to Ammonium and Nitrate." *Environmental Science & Technology*, 36, pp. 4868–4879. DOI: 10.1021/es015823i.

Bian, H. et al. (2013). "Source attributions of pollution to the Western Arctic during the NASA ARCTAS field campaign." *Atmospheric Chemistry and Physics*, 13, pp. 4707–4721. DOI: 10.5194/acp-13-4707-2013.

Bigg, E. K. (1996). "Ice forming nuclei in the high Arctic." *Tellus B: Chemical and Physical Meteorology*, 48, pp. 223–233. DOI: 10.3402/tellusb.v48i2.15888.

Bigg, E. K. and C. Leck (2001). "Cloud-active particles over the central Arctic Ocean." *Journal of Geophysical Research: Atmospheres*, 106, pp. 32155–32166. DOI: 10.1029/1999JD901152.

Bigg, E. K. and C. Leck (2008). "The composition of fragments of bubbles bursting at the ocean surface." *Journal of Geophysical Research*, 113, p. D11209. DOI: 10.1029/2007JD009078.

Bindoff, N., P. Stott, K. AchutaRao, M. Allen, N. Gillett, D. Gutzler, K. Hansingo, G. Hegerl, Y. Hu, S. Jain, I. Mokhov, J. Overland, J. Perlwitz, R. Sebbari, and X. Zhang (2014). "Detection and Attribution of Climate Change: from Global to Regional." *Climate Change 2013 – The Physical Science Basis: Working Group I. Contribution to the Fifth Assessment Report of the Intergovernmental Panel on Climate Change*. Ed. by T. Stocker, D. Qin, G.-K. Plattner, M. Tignor, S. Allen, J. Boschung, A. Nauels, Y. Xia, B. V., and M. P.M. Cambridge University Press. Cambridge, United Kingdom and New York, NY, USA. Chap. 10, pp. 867–952. DOI: 10.1017/CBO9781107415324.022.

Blackall, T. D., L. J. Wilson, M. R. Theobald, C. Milford, E. Nemitz, J. Bull, P. J. Bacon, K. C. Hamer, S. Wanless, and M. A. Sutton (2007). "Ammonia emissions from seabird colonies." *Geophysical Research Letters*, 34, p. L10801. DOI: 10.1029/2006GL028928.

Blanchard, D. C. and A. H. Woodcock (1957). "Bubble Formation and Modification in the Sea and its Meteorological Significance." *Tellus*, 9, pp. 145–158. DOI: 10.3402/tellusa.v9i2.9094.

Blanchard, D. C. (1989). "The Ejection of Drops from the Sea and Their Enrichment with Bacteria and Other Materials: A Review." *Estuaries*, 12, p. 127. DOI: 10.2307/1351816.

Blanchard, D. C. and A. H. Woodcock (1980). "The Production, Concentration, AND Vertical Distribution of the sea-salt aerosol." *Annals of the New York Academy of Sciences*, 338, pp. 330–347. DOI: 10.1111/j.1749-6632.1980.tb17130.x.

Bond, T. C. et al. (2013). "Bounding the role of black carbon in the climate system: A scientific assessment." *Journal of Geophysical Research: Atmospheres*, 118, pp. 5380–5552. DOI: 10.1002/jgrd.50171.

Bozem, H., P. Hoor, D. Kunkel, F. Köllner, J. Schneider, A. Herber, H. Schulz, W. R. Leaitch, A. A. Aliabadi, M. D. Willis, J. Burkart, and J. P. D. Abbatt

(2019). "Characterization of transport regimes and the polar dome during Arctic spring and summer using in situ aircraft measurements." *Atmospheric Chemistry and Physics*, 19, pp. 15049–15071. DOI: 10.5194/acp-19-15049-2019.

Brands, M et al. (2011). "Characterization of a Newly Developed Aircraft-Based Laser Ablation Aerosol Mass Spectrometer (ALABAMA) and First Field Deployment in Urban Pollution Plumes over Paris During MEGAPOLI 2009." *Aerosol Science and Technology*, 45, pp. 46–64. DOI: 10.1080/02786826.2010.517813.

Brands, M. (2009). "Aufbau und Charakterisierung eines flugzeuggetragenen Einzelpartikel-Massenspektrometers." PhD Thesis. Johannes Gutenberg-University, Mainz. DOI: 10.25358/openscience-2255.

Breider, T. J., L. J. Mickley, D. J. Jacob, C. Ge, J. Wang, M. Payer Sulprizio, B. Croft, D. A. Ridley, J. R. McConnell, S. Sharma, L. Husain, V. A. Dutkiewicz, K. Eleftheriadis, H. Skov, and P. K. Hopke (2017). "Multidecadal trends in aerosol radiative forcing over the Arctic: Contribution of changes in anthropogenic aerosol to Arctic warming since 1980." *Journal of Geophysical Research: Atmospheres*, 122, pp. 3573–3594. DOI: 10.1002/2016JD025321.

Breider, T. J., L. J. Mickley, D. J. Jacob, Q. Wang, J. A. Fisher, R. Y.-W. Chang, and B. Alexander (2014). "Annual distributions and sources of Arctic aerosol components, aerosol optical depth, and aerosol absorption." *Journal of Geophysical Research: Atmospheres*, 119, pp. 4107–4124. DOI: 10.1002/2013JD020996.

Brock, C. A. et al. (2011). "Characteristics, sources, and transport of aerosols measured in spring 2008 during the aerosol, radiation, and cloud processes affecting Arctic Climate (ARCPAC) Project." *Atmospheric Chemistry and Physics*, 11, pp. 2423–2453. DOI: 10.5194/acp-11-2423-2011.

Browse, J., K. S. Carslaw, S. R. Arnold, K. Pringle, and O. Boucher (2012). "The scavenging processes controlling the seasonal cycle in Arctic sulphate and black carbon aerosol." *Atmospheric Chemistry and Physics*, 12, pp. 6775–6798. DOI: 10.5194/acp-12-6775-2012.

Browse, J., K. S. Carslaw, G. W. Mann, C. E. Birch, S. R. Arnold, and C. Leck (2014). "The complex response of Arctic aerosol to sea-ice retreat." *Atmospheric Chemistry and Physics*, 14, pp. 7543–7557. DOI: 10.5194/acp-14-7543-2014.

Burba, G. G., D. K. Mcdermitt, D. J. Anderson, M. D. Furtaw, and R. D. Eckles (2010). "Novel design of an enclosed CO2/H2O gas analyser for eddy covariance flux measurements." *Tellus, Series B: Chemical and Physical Meteorology*, 62, pp. 743–748. DOI: 10.1111/j.1600-0889.2010.00468.x.

Burkart, J., A. L. Hodshire, E. L. Mungall, J. R. Pierce, D. B. Collins, L. A. Ladino, A. K. Lee, V. Irish, J. J. Wentzell, J. Liggio, T. Papakyriakou, J. Murphy, and J. Abbatt (2017a). "Organic Condensation and Particle Growth to CCN Sizes in the Summertime Marine Arctic Is Driven by Materials More Semivolatile Than at Continental Sites." *Geophysical Research Letters*, 44, pp. 10,725–10,734. DOI: 10.1002/2017GL075671.

Burkart, J., M. D. Willis, H. Bozem, J. L. Thomas, K. Law, P. Hoor, A. A. Aliabadi, F. Köllner, J. Schneider, A. Herber, J. P. Abbatt, and W. Richard Leaitch (2017b). "Summertime observations of elevated levels of ultrafine particles in the high Arctic marine boundary layer." *Atmospheric Chemistry and Physics*, 17, pp. 5515–5535. DOI: 10.5194/acp-17-5515-2017.

Bzdek, B. R., D. P. Ridge, and M. V. Johnston (2011). "Reactivity of methanesulfonic acid salt clusters relevant to marine air." *Journal of Geophysical Research*, 116, p. D03301. DOI: 10.1029/2010JD015217.

Cai, Y., D. C. Montague, W. Mooiweer-Bryan, and T. Deshler (2008). "Performance characteristics of the ultra high sensitivity aerosol spectrometer for particles between 55 and 800nm: Laboratory and field studies." *Journal of Aerosol Science*, 39, pp. 759–769. DOI: 10.1016/j.jaerosci.2008.04.007.

Cai, Y., A. Zelenyuk, and D. Imre (2006). "A High Resolution Study of the Effect of Morphology On the Mass Spectra of Single PSL Particles with Na-containing Layers and Nodules." *Aerosol Science and Technology*, 40, pp. 1111–1122. DOI: 10.1080/02786820601001677.

Carlson, T. N. (1981). "Speculations on the movement of polluted air to the Arctic." *Atmospheric Environment*, 15, pp. 1473–1477. DOI: 10.1016/0004-6981(81)90354-1.

Carpenter, L. J. (2003). "Iodine in the Marine Boundary Layer." *Chemical Reviews*, 103, pp. 4953–4962. DOI: 10.1021/cr0206465.

Carpenter, L. J., S. D. Archer, and R. Beale (2012). "Ocean-atmosphere trace gas exchange." *Chemical Society Reviews*, 41, pp. 6473–6506. DOI: 10.1039/c2cs35121h.

Cesana, G., J. E. Kay, H. Chepfer, J. M. English, and G. Boer (2012). "Ubiquitous low-level liquid-containing Arctic clouds: New observations and climate model constraints from CALIPSO-GOCCP." *Geophysical Research Letters*, 39, 2012GL053385. DOI: 10.1029/2012GL053385.

Chance, R. J., J. F. Hamilton, L. J. Carpenter, S. C. Hackenberg, S. J. Andrews, and T. W. Wilson (2018). "Water-Soluble Organic Composition of the Arctic Sea Surface Microlayer and Association with Ice Nucleation Ability." *Environmental Science & Technology*, 52, pp. 1817–1826. DOI: 10.1021/acs.est.7b04072.

Chapman, W. L. and J. E. Walsh (1993). "Recent variations of sea ice and air temperature in high latitudes." *Bulletin of the American Meteorological Society*, 74, pp. 33–47. DOI: 10.1175/1520-0477(1993)074<0033:RVOSIA>2.0.CO;2.

Chechin, D. (2019). "Liquid water content measured by the Nevzorov probe during the aircraft ACLOUD campaign in the Arctic". data set. Alfred Wegener Institute, Helmholtz Centre for Polar and Marine Research, Bremerhaven. DOI: 10.1594/PANGAEA.906658.

Chi, J. W., W. J. Li, D. Z. Zhang, J. C. Zhang, Y. T. Lin, X. J. Shen, J. Y. Sun, J. M. Chen, X. Y. Zhang, Y. M. Zhang, and W. X. Wang (2015). "Sea salt aerosols as a reactive surface for inorganic and organic acidic gases in the Arctic troposphere." *Atmospheric Chemistry and Physics*, 15, pp. 11341–11353. DOI: 10.5194/acp-15-11341-2015.

Christopoulos, C. D., S. Garimella, M. A. Zawadowicz, O. Möhler, and D. J. Cziczo (2018). "A machine learning approach to aerosol classification for single-particle mass spectrometry." *Atmospheric Measurement Techniques*, 11, pp. 5687–5699. DOI: 10.5194/amt-11-5687-2018.

Clarke, A. D., R. J. Charlson, and L. F. Radke (1984). "Airborne observations of Arctic aerosol, IV: Optical properties of Arctic haze." *Geophysical Research Letters*, 11, pp. 405–408. DOI: 10.1029/GL011i005p00405.

Clemen, H.-C., J. Schneider, T. Klimach, F. Helleis, F. Köllner, A. Hünig, F. Rubach, S. Mertes, H. Wex, F. Stratmann, A. Welti, R. Kohl, F. Frank, and S. Borrmann (2020). "Optimizing the detection, ablation, and ion extraction efficiency of a single-particle laser ablation mass spectrometer for application in environments with low aerosol particle concentrations." *Atmospheric Measurement Techniques*, 13, pp. 5923–5953. DOI: 10.5194/amt-13-5923-2020.

Collins, D. B. et al. (2017). "Frequent ultrafine particle formation and growth in Canadian Arctic marine and coastal environments." *Atmospheric Chemistry and Physics*, 17, pp. 13119–13138. DOI: 10.5194/acp-17-13119-2017.

Creamean, J. M., J. N. Cross, R. Pickart, L. McRaven, P. Lin, A. Pacini, R. Hanlon, D. G. Schmale, J. Ceniceros, T. Aydell, N. Colombi, E. Bolger, and P. J. DeMott (2019). "Ice Nucleating Particles Carried From Below a Phytoplankton Bloom to the Arctic Atmosphere." *Geophysical Research Letters*, 46, pp. 8572–8581. DOI: 10.1029/2019GL083039.

Creamean, J. M., G. de Boer, H. Telg, F. Mei, D. Dexheimer, M. D. Shupe, A. Solomon, and A. McComiskey (2021). "Assessing the vertical structure of Arctic aerosols using balloon-borne measurements." *Atmospheric Chemistry and Physics*, 21, pp. 1737–1757. DOI: 10.5194/acp-21-1737-2021.

Creamean, J. M., R. M. Kirpes, K. A. Pratt, N. J. Spada, M. Maahn, G. de Boer, R. C. Schnell, and S. China (2018). "Marine and terrestrial influences on ice nucleating particles during continuous springtime measurements in an Arctic oilfield location." *Atmospheric Chemistry and Physics*, 18, pp. 18023–18042. DOI: 10.5194/acp-18-18023-2018.

Croft, B., G. R. Wentworth, R. V. Martin, W. R. Leaitch, J. G. Murphy, B. N. Murphy, J. K. Kodros, J. P. Abbatt, and J. R. Pierce (2016a). "Contribution of Arctic seabird-colony ammonia to atmospheric particles and cloud-albedo radiative effect." *Nature Communications*, 7, pp. 1–10. DOI: 10.1038/ncomms13444.

Croft, B., R. V. Martin, W. Richard Leaitch, P. Tunved, T. J. Breider, S. D. D'Andrea, and J. R. Pierce (2016b). "Processes controlling the annual cycle of Arctic aerosol number and size distributions." *Atmospheric Chemistry and Physics*, 16, pp. 3665–3682. DOI: 10.5194/acp-16-3665-2016.

Croft, B. et al. (2019). "Arctic marine secondary organic aerosol contributes significantly to summertime particle size distributions in the Canadian Arctic Archipelago." *Atmospheric Chemistry and Physics*, 19, pp. 2787–2812. DOI: 10.5194/acp-19-2787-2019.

Curry, J. A., J. L. Schramm, and E. E. Ebert (1995). "Sea Ice-Albedo Climate Feedback Mechanism." *Journal of Climate*, 8, pp. 240–247. DOI: 10.1175/1520-0442(1995)008<0240:SIACFM>2.0.CO;2.

Dall'Osto, M., D. C. S. Beddows, P. Tunved, R. Krejci, J. Ström, H.-C. Hansson, Y. J. Yoon, K.-T. Park, S. Becagli, R. Udisti, T. Onasch, C. D. O´Dowd, R. Simó, and R. M. Harrison (2017). "Arctic sea ice melt leads to atmospheric new particle formation." *Scientific Reports*, 7, p. 3318. DOI: 10.1038/s41598-017-03328-1.

Dall'Osto, M., R. L. Airs, R. Beale, C. Cree, M. F. Fitzsimons, D. Beddows, R. M. Harrison, D. Ceburnis, C. O'Dowd, M. Rinaldi, M. Paglione, A. Nenes, S. Decesari, and R. Simó (2019). "Simultaneous Detection of Alkylamines in the Surface Ocean and Atmosphere of the Antarctic Sympagic Environment." *ACS Earth and Space Chemistry*, 3, pp. 854–862. DOI: 10.1021/acsearthspacechem.9b00028.

Dall'Osto, M., D. Ceburnis, C. Monahan, D. R. Worsnop, J. Bialek, M. Kulmala, T. Kurtén, M. Ehn, J. Wenger, J. Sodeau, R. Healy, and C. O'Dowd (2012). "Nitrogenated and aliphatic organic vapors as possible drivers for marine secondary organic aerosol growth." *Journal of Geophysical Research Atmospheres*, 117, pp. 1–10. DOI: 10.1029/2012JD017522.

Dall'Osto, M. and R. M. Harrison (2006). "Chemical characterisation of single airborne particles in Athens (Greece) by ATOFMS." *Atmospheric Environment*, 40, pp. 7614–7631. DOI: 10.1016/j.atmosenv.2006.06.053.

Dawson, M. L., M. E. Varner, V. Perraud, M. J. Ezell, R. B. Gerber, and B. J. Finlayson-Pitts (2012). "Simplified mechanism for new particle formation from methanesulfonic acid, amines, and water via experiments and ab initio calculations." *Proceedings of the National Academy of Sciences of the United States of America*, 109, pp. 18719–18724. DOI: 10.1073/pnas.1211878109.

De Foy, B., A. M. Smyth, S. L. Thompson, D. S. Gross, M. R. Olson, N. Sager, and J. J. Schauer (2012). "Sources of nickel, vanadium and black carbon in aerosols in Milwaukee." *Atmospheric Environment*, 59, pp. 294–301. DOI: 10.1016/j.atmosenv.2012.06.002.

DeCarlo, P. F., J. G. Slowik, D. R. Worsnop, P. Davidovits, and J. L. Jimenez (2004). "Particle Morphology and Density Characterization by Combined Mobility and Aerodynamic Diameter Measurements. Part 1: Theory." *Aerosol Science and Technology*, 38, pp. 1185–1205. DOI: 10.1080/027868290903907.

DeMott, P. J. et al. (2016). "Sea spray aerosol as a unique source of ice nucleating particles." *Proceedings of the National Academy of Sciences*, 113, pp. 5797–5803. DOI: 10.1073/pnas.1514034112.

Deshpande, C. G. and A. K. Kamra (2014). "Physical properties of the arctic summer aerosol particles in relation to sources at Ny-Alesund, Svalbard." *Journal of Earth System Science*, 123, pp. 201–212. DOI: 10.1007/s12040-013-0373-0.

Doherty, S. J., S. G. Warren, T. C. Grenfell, A. D. Clarke, and R. E. Brandt (2010). "Light-absorbing impurities in Arctic snow." *Atmospheric Chemistry and Physics*, 10, pp. 11647–11680. DOI: 10.5194/acp-10-11647-2010.

Döscher, R., T. Vihma, and E. Maksimovich (2014). "Recent advances in understanding the Arctic climate system state and change from a sea ice perspective: A review." *Atmospheric Chemistry and Physics*, 14, pp. 13571–13600. DOI: 10.5194/acp-14-13571-2014.

Dupuy, R., O. Jourdan, G. Mioche, C. Gourbeyre, D. Leroy, and A. Schwarzenböck (2019). "CDP, CIP and PIP In-situ arctic cloud microphysical properties observed during ACLOUD-AC3 campaign in June 2017". data set. LAMP / CNRS / UCA / OPGC. DOI: 10.1594/PANGAEA.899074.

Dusek, U., G. P. Frank, L. Hildebrandt, J. Curtius, J. Schneider, S. Walter, D. Chand, F. Drewnick, S. Hings, D. Jung, S. Borrmann, and M. O. Andreae (2006). "Size Matters More Than Chemistry for Cloud-Nucleating Ability of Aerosol Particles." *Science*, 312, pp. 1375–1378. DOI: 10.1126/science.1125261.

EOG (2021). URL: https://eogdata.mines.edu/products/vnf/ (visited on 08/30/2021).

Ehrlich, A. et al. (2019). "A comprehensive in situ and remote sensing data set from the Arctic CLoud Observations Using airborne measurements during polar Day (ACLOUD) campaign." *Earth System Science Data*, 11, pp. 1853–1881. DOI: 10.5194/essd-11-1853-2019.

Elvidge, C. D., M. Zhizhin, F.-C. Hsu, and K. E. Baugh (2013). "VIIRS nightfire: Satellite pyrometry at night." *Remote Sensing 5*, 9, pp. 4423–4449. DOI: 10.3390/rs5094423.

Elvidge, C. D., M. Zhizhin, K. Baugh, F.-C. Hsu, and T. Ghosh (2016). "Methods for Global Survey of Natural Gas Flaring from Visible Infrared Imaging Radiometer Suite Data." *Energies*, 9. DOI: 10.3390/en9010014.

Engvall, A.-C., R. Krejci, J. Ström, R. Treffeisen, R. Scheele, O. Hermansen, and J. Paatero (2008). "Changes in aerosol properties during spring-summer

period in the Arctic troposphere." *Atmospheric Chemistry and Physics*, 8, pp. 445–462. DOI: 10.5194/acp-8-445-2008.

Eppers, O., H. Bozem, and P. Hoor (2019). "Airborne in-situ measurement of carbon monoxide, carbon dioxide, water vapor and ozone during ACLOUD 2017". data set. Institute for Atmospheric Physics, University of Mainz. DOI: 10.1594/PANGAEA.901209.

Eppers, O. and J. Schneider (2019). "Airborne in-situ measurement of particle number concentration and size distribution using an optical particle counter during ACLOUD 2017". data set. Institute for Atmospheric Physics, University of Mainz. DOI: 10.1594/PANGAEA.901149.

Evangeliou, N. et al. (2016). "Wildfires in northern Eurasia affect the budget of black carbon in the Arctic-a 12-year retrospective synopsis (2002-2013)." *Atmospheric Chemistry and Physics*, 16, pp. 7587–7604. DOI: 10.5194/acp-16-7587-2016.

Facchini, M. C., S. Decesari, M. Rinaldi, C. Carbone, E. Finessi, M. Mircea, S. Fuzzi, F. Moretti, E. Tagliavini, D. Ceburnis, and C. D. O'Dowd (2008). "Important source of marine secondary organic aerosol from biogenic amines." *Environmental Science and Technology*, 42, pp. 9116–9121. DOI: 10.1021/es8018385.

Fisher, J. A. et al. (2011). "Sources, distribution, and acidity of sulfate–ammonium aerosol in the Arctic in winter–spring." *Atmospheric Environment*, 45, pp. 7301–7318. DOI: 10.1016/j.atmosenv.2011.08.030.

Flanner, M. G. (2013). "Arctic climate sensitivity to local black carbon." *Journal of Geophysical Research: Atmospheres*, 118, pp. 1840–1851. DOI: 10.1002/jgrd.50176.

Flanner, M. G., C. S. Zender, J. T. Randerson, and P. J. Rasch (2007). "Present-day climate forcing and response from black carbon in snow." *Journal of Geophysical Research Atmospheres*, 112, pp. 1–17. DOI: 10.1029/2006JD008003.

Fountain, A. G. and T. Ohtake (1985). "Concentrations and Source Areas of Ice Nuclei in the Alaskan Atmosphere." *Journal of Climate and Applied Meteorology*, 24, pp. 377–382. DOI: 10.1175/1520-0450(1985)024<0377:CASAOI>2.0.CO;2. arXiv: arXiv:1011.1669v3.

Francis, J. A. and S. J. Vavrus (2012). "Evidence linking Arctic amplification to extreme weather in mid-latitudes." *Geophysical Research Letters*, 39, pp. 1–6. DOI: 10.1029/2012GL051000.

Freud, E., R. Krejci, P. Tunved, R. Leaitch, Q. T. Nguyen, A. Massling, H. Skov, and L. Barrie (2017). "Pan-Arctic aerosol number size distributions: seasonality and transport patterns." *Atmospheric Chemistry and Physics*, 17, pp. 8101–8128. DOI: 10.5194/acp-17-8101-2017.

Frossard, A. A., L. M. Russell, S. M. Burrows, S. M. Elliott, T. S. Bates, and P. K. Quinn (2014). "Sources and composition of submicron organic mass in marine aerosol particles." *Journal of Geophysical Research: Atmospheres*, 119, pp. 12,977–13,003. DOI: 10.1002/2014JD021913.

Froyd, K. D., D. M. Murphy, C. A. Brock, P. Campuzano-Jost, J. E. Dibb, J.-L. Jimenez, A. Kupc, A. M. Middlebrook, G. P. Schill, K. L. Thornhill, C. J. Williamson, J. C. Wilson, and L. D. Ziemba (2019). "A new method to quantify mineral dust and other aerosol species from aircraft platforms using single-particle mass spectrometry." *Atmospheric Measurement Techniques*, 12, pp. 6209–6239. DOI: 10.5194/amt-12-6209-2019.

Fu, P. Q., K. Kawamura, J. Chen, B. Charrière, and R. Sempéré (2013). "Organic molecular composition of marine aerosols over the Arctic Ocean in summer: contributions of primary emission and secondary aerosol formation." *Biogeosciences*, 10, pp. 653–667. DOI: 10.5194/bg-10-653-2013.

Fu, P., K. Kawamura, and L. A. Barrie (2009a). "Photochemical and Other Sources of Organic Compounds in the Canadian High Arctic Aerosol Pollution during WinterSpring." *Environmental Science & Technology*, 43, pp. 286–292. DOI: 10.1021/es803046q.

Fu, P., K. Kawamura, J. Chen, and L. A. Barrie (2009b). "Isoprene, Monoterpene, and Sesquiterpene Oxidation Products in the High Arctic Aerosols during Late Winter to Early Summer." *Environmental Science & Technology*, 43, pp. 4022–4028. DOI: 10.1021/es803669a.

Fu, P., K. Kawamura, J. Chen, M. Qin, L. Ren, Y. Sun, Z. Wang, L. A. Barrie, E. Tachibana, A. Ding, and Y. Yamashita (2015). "Fluorescent water-soluble organic aerosols in the High Arctic atmosphere." *Scientific Reports*, 5, p. 9845. DOI: 10.1038/srep09845.

Gagné, M. È., J. C. Fyfe, N. P. Gillett, I. V. Polyakov, and G. M. Flato (2017). "Aerosol-driven increase in Arctic sea ice over the middle of the twentieth century." *Geophysical Research Letters*, 44, pp. 7338–7346. DOI: 10.1002/2016GL071941.

Gallavardin, S., U. Lohmann, and D. Cziczo (2008). "Analysis and differentiation of mineral dust by single particle laser mass spectrometry." *International Journal of Mass Spectrometry*, 274, pp. 56–63. DOI: 10.1016/j.ijms.2008.04.031.

Garrett, T. J., L. F. Radke, and P. V. Hobbs (2002). "Aerosol Effects on Cloud Emissivity and Surface Longwave Heating in the Arctic." *Journal of the Atmospheric Sciences*, 59, pp. 769–778. DOI: 10.1175/1520-0469(2002)059<0769:AEOCEA>2.0.CO;2.

Gaston, C. J., K. A. Pratt, X. Qin, and K. A. Prather (2010). "Real-Time Detection and Mixing State of Methanesulfonate in Single Particles at an Inland Urban Location during a Phytoplankton Bloom." *Environmental Science & Technology*, 44, pp. 1566–1572. DOI: 10.1021/es902069d.

Ge, X., A. S. Wexler, and S. L. Clegg (2011a). "Atmospheric amines - Part I. A review." *Atmospheric Environment*, 45, pp. 524–546. DOI: 10.1016/j.atmosenv.2010.10.012.

Ge, X., A. S. Wexler, and S. L. Clegg (2011b). "Atmospheric amines – Part II. Thermodynamic properties and gas/particle partitioning." *Atmospheric Environment*, 45, pp. 561–577. DOI: 10.1016/j.atmosenv.2010.10.013.

Gerbig, C., S. Schmitgen, D. Kley, A. Volz-Thomas, K. Dewey, and D. Haaks (1999). "An improved fast-response vacuum-UV resonance fluorescence CO instrument." *Journal of Geophysical Research: Atmospheres*, 104, pp. 1699–1704. DOI: 10.1029/1998JD100031.

Ghahremaninezhad, R., W. Gong, M. Galí, A.-L. Norman, S. R. Beagley, A. Akingunola, Q. Zheng, A. Lupu, M. Lizotte, M. Levasseur, and W. R. Leaitch (2019). "Dimethyl sulfide and its role in aerosol formation and growth in the Arctic summer – a modelling study." *Atmospheric Chemistry and Physics*, 19, pp. 14455–14476. DOI: 10.5194/acp-19-14455-2019.

Gibb, S. W., R. F. C. Mantoura, and P. S. Liss (1999). "Ocean-atmosphere exchange and atmospheric speciation of ammonia and methylamines in the region of the NW Arabian Sea." *Global Biogeochemical Cycles*, 13, pp. 161–178. DOI: 10.1029/98GB00743.

Gong, S. L., T. L. Zhao, S. Sharma, D. Toom-Sauntry, D. Lavoué, X. B. Zhang, W. R. Leaitch, and L. A. Barrie (2010). "Identification of trends and interannual variability of sulfate and black carbon in the Canadian High Arctic: 1981–2007." *Journal of Geophysical Research*, 115, p. D07305. DOI: 10.1029/2009JD012943.

Groot Zwaaftink, C. D., H. Grythe, H. Skov, and A. Stohl (2016). "Substantial contribution of northern high-latitude sources to mineral dust in the Arctic." *Journal of Geophysical Research: Atmospheres*, 121, pp. 13,678–13,697. DOI: 10.1002/2016JD025482.

Gross, D. S., M. E. Gälli, P. J. Silva, and K. A. Prather (2000). "Relative Sensitivity Factors for Alkali Metal and Ammonium Cations in Single-Particle Aerosol Time-of-Flight Mass Spectra." *Analytical Chemistry*, 72, pp. 416–422. DOI: 10.1021/ac990434g.

Gunsch, M. J., R. M. Kirpes, K. R. Kolesar, T. E. Barrett, S. China, R. J. Sheesley, A. Laskin, A. Wiedensohler, T. Tuch, and K. A. Pratt (2017). "Contributions of transported Prudhoe Bay oil field emissions to the aerosol population in Utqiaġvik, Alaska." *Atmospheric Chemistry and Physics*, 17, pp. 10879–10892. DOI: 10.5194/acp-17-10879-2017.

Gunsch, M. J., J. Liu, C. E. Moffett, R. J. Sheesley, N. Wang, Q. Zhang, T. B. Watson, and K. A. Pratt (2019). "Diesel Soot and Amine-Containing Organic Sulfate Aerosols in an Arctic Oil Field." *Environmental Science & Technology*, acs.est.9b04825. DOI: 10.1021/acs.est.9b04825.

Halfacre, J. W., P. B. Shepson, and K. A. Pratt (2019). "pH-dependent production of molecular chlorine, bromine, and iodine from frozen saline surfaces." *Atmospheric Chemistry and Physics*, 19, pp. 4917–4931. DOI: 10.5194/acp-19-4917-2019.

Hallquist, M. et al. (2009). "The formation, properties and impact of secondary organic aerosol: current and emerging issues." *Atmospheric Chemistry and Physics*, 9, pp. 5155–5236. DOI: 10.5194/acp-9-5155-2009.

Hansen, A. M., K. Kristensen, Q. T. Nguyen, A. Zare, F. Cozzi, J. K. Nøjgaard, H. Skov, J. Brandt, J. H. Christensen, J. Ström, P. Tunved, R. Krejci, and M. Glasius (2014). "Organosulfates and organic acids in Arctic aerosols: Speciation, annual variation and concentration levels." *Atmospheric Chemistry and Physics*, 14, pp. 7807–7823. DOI: 10.5194/acp-14-7807-2014.

Hara, K., S. Matoba, M. Hirabayashi, and T. Yamasaki (2017). "Frost flowers and sea-salt aerosols over seasonal sea-ice areas in northwestern Greenland during winter-spring." *Atmospheric Chemistry and Physics*, 17, pp. 8577–8598. DOI: 10.5194/acp-17-8577-2017.

Hartmann, J., C. Lüpkes, and D. Chechin (2019). "1Hz resolution aircraft measurements of wind and temperature during the ACLOUD campaign in 2017". data set. Alfred Wegener Institute, Helmholtz Centre for Polar and Marine Research, Bremerhaven. DOI: 10.1594/PANGAEA.902849.

Hartmann, M., K. Adachi, O. Eppers, C. Haas, A. Herber, R. Holzinger, A. Hünerbein, E. Jäkel, C. Jentzsch, M. Pinxteren, H. Wex, S. Willmes, and F. Stratmann (2020). "Wintertime Airborne Measurements of Ice Nucleating Particles in the High Arctic: A Hint to a Marine, Biogenic Source for Ice Nucleating Particles." *Geophysical Research Letters*, 47. DOI: 10.1029/2020GL087770.

Hatch, L. E., K. A. Pratt, J. A. Huffman, J. L. Jimenez, and K. A. Prather (2014). "Impacts of Aerosol Aging on Laser Desorption/Ionization in Single-Particle Mass Spectrometers." *Aerosol Science and Technology*, 48, pp. 1050–1058. DOI: 10.1080/02786826.2014.955907.

He, X.-c. et al. (2021). "Role of iodine oxoacids in atmospheric aerosol nucleation." *Science*, 371, pp. 589–595. DOI: 10.1126/science.abe0298.

Healy, R. M., G. J. Evans, M. Murphy, B. Sierau, J. Arndt, E. McGillicuddy, I. P. O'Connor, J. R. Sodeau, and J. C. Wenger (2015). "Single-particle speciation of alkylamines in ambient aerosol at five European sites." *Analytical and Bioanalytical Chemistry*, 407, pp. 5899–5909. DOI: 10.1007/s00216-014-8092-1.

Hecobian, A. et al. (2011). "Comparison of chemical characteristics of 495 biomass burning plumes intercepted by the NASA DC-8 aircraft during the ARCTAS/CARB-2008 field campaign." *Atmospheric Chemistry and Physics*, 11, pp. 13325–13337. DOI: 10.5194/acp-11-13325-2011.

Hegg, D. A., S. G. Warren, T. C. Grenfell, and A. D. Clarke (2010). "Sources of light-absorbing aerosol in arctic snow and their seasonal variation." *Atmospheric Chemistry and Physics*, 10, pp. 10923–10938. DOI: 10.5194/acp-10-10923-2010.

Herber, A., K. Dethloff, C. Haas, D. Steinhage, J. W. Strapp, J Bottenheim, T McElroy, and T Yamanouchi (2008). "POLAR 5 - a new research aircraft

for improved access to the Arctic." *ISAR-1, Drastic Change under the Global Warming, Extended Abstract*, pp. 54–57.

Hill, V. L. and S. L. Manley (2009). "Release of reactive bromine and iodine from diatoms and its possible role in halogen transfer in polar and tropical oceans." *Limnology and Oceanography*, 54, pp. 812–822. DOI: 10.4319/lo.2009.54.3.0812.

Hirdman, D., J. F. Burkhart, H. Sodemann, S. Eckhardt, A. Jefferson, P. K. Quinn, S. Sharma, J. Ström, and A. Stohl (2010a). "Long-term trends of black carbon and sulphate aerosol in the Arctic: Changes in atmospheric transport and source region emissions." *Atmospheric Chemistry and Physics*, 10, pp. 9351–9368. DOI: 10.5194/acp-10-9351-2010.

Hirdman, D., H. Sodemann, S. Eckhardt, J. F. Burkhart, A. Jefferson, T. Mefford, P. K. Quinn, S. Sharma, J. Ström, and A. Stohl (2010b). "Source identification of short-lived air pollutants in the Arctic using statistical analysis of measurement data and particle dispersion model output." *Atmospheric Chemistry and Physics*, 10, pp. 669–693. DOI: 10.5194/acp-10-669-2010.

Hoffmann, E. H., A. Tilgner, R. Schrödner, P. Bräuer, R. Wolke, and H. Herrmann (2016). "An advanced modeling study on the impacts and atmospheric implications of multiphase dimethyl sulfide chemistry." *Proceedings of the National Academy of Sciences*, 113, pp. 11776–11781. DOI: 10.1073/pnas.1606320113.

Hoppel, W. A., G. M. Frick, J. W. Fitzgerald, and R. E. Larson (1994). "Marine boundary layer measurements of new particle formation and the effects nonprecipitating clouds have on aerosol size distribution." *Journal of Geophysical Research*, 99, p. 14443. DOI: 10.1029/94JD00797.

Huang, J. and L. Jaeglé (2017). "Wintertime enhancements of sea salt aerosol in polar regions consistent with a sea ice source from blowing snow." *Atmospheric Chemistry and Physics*, 17, pp. 3699–3712. DOI: 10.5194/acp-17-3699-2017.

Huang, Z., J. Huang, T. Hayasaka, S. Wang, T. Zhou, and H. Jin (2015). "Short-cut transport path for Asian dust directly to the Arctic: a case study." *Environmental Research Letters*, 10, p. 114018. DOI: 10.1088/1748-9326/10/11/114018.

Hudson, P. K., D. M. Murphy, D. J. Cziczo, D. S. Thomson, J. A. de Gouw, C. Warneke, J. Holloway, H. J. Jost, and G. Hübler (2004). "Biomass-burning particle measurements: Characteristics composition and chemical processing."

Journal of Geophysical Research D: Atmospheres, 109, pp. 1–11. DOI: 10.1029/2003JD004398.

Hünig, A. (2021). "Development, characterization, and first field deployments of a novel aerosol mass spectrometer combining laser ablation and flash vaporization techniques for aircraft application at high altitudes." PhD Thesis. Johannes-Gutenberg University, Mainz, p. 309. DOI: 10.25358/openscience-5554.

Intrieri, J. M., C. W. Fairall, M. D. Shupe, P. O. Persson, E. L. Andreas, P. S. Guest, and R. E. Moritz (2002). "An annual cycle of Arctic surface cloud forcing at SHEBA." *Journal of Geophysical Research: Oceans*, 107, pp. 1–14. DOI: 10.1029/2000jc000439.

Irish, V. E., S. J. Hanna, M. D. Willis, S. China, J. L. Thomas, J. J. B. Wentzell, A. Cirisan, M. Si, W. R. Leaitch, J. G. Murphy, J. P. D. Abbatt, A. Laskin, E. Girard, and A. K. Bertram (2018). "Ice nucleating particles in the marine boundary layer in the Canadian Arctic during summer 2014." *Atmospheric Chemistry and Physics Discussions*, pp. 1–25. DOI: 10.5194/acp-2018-735.

Irish, V. E., S. J. Hanna, M. D. Willis, S. China, J. L. Thomas, J. J. B. Wentzell, A. Cirisan, M. Si, W. R. Leaitch, J. G. Murphy, J. P. D. Abbatt, A. Laskin, E. Girard, and A. K. Bertram (2019). "Ice nucleating particles in the marine boundary layer in the Canadian Arctic during summer 2014." *Atmospheric Chemistry and Physics*, 19, pp. 1027–1039. DOI: 10.5194/acp-19-1027-2019.

Iversen, T. (1984). "On the atmospheric transport of pollution to the Arctic." *Geophysical Research Letters*, 11, pp. 457–460.

Jarníková, T., J. Dacey, M. Lizotte, M. Levasseur, and P. Tortell (2018). "The distribution of methylated sulfur compounds, DMS and DMSP, in Canadian subarctic and Arctic marine waters during summer 2015." *Biogeosciences*, 15, pp. 2449–2465. DOI: 10.5194/bg-15-2449-2018.

Jeffries, M. O., J. E. Overland, and D. K. Perovich (2013). "The Arctic shifts to a new normal." *Physics Today*, 66, pp. 35–40. DOI: 10.1063/PT.3.2147.

Jimenez, J. L. et al. (2009). "Evolution of Organic Aerosols in the Atmosphere." *Science*, 326, pp. 1525–1529. DOI: 10.1126/science.1180353.

Johnson, M. T., P. S. Liss, T. G. Bell, T. J. Lesworth, A. R. Baker, A. J. Hind, T. D. Jickells, K. F. Biswas, E. M. S. Woodward, and S. W. Gibb

(2008). "Field observations of the ocean-atmosphere exchange of ammonia: Fundamental importance of temperature as revealed by a comparison of high and low latitudes." *Global Biogeochemical Cycles*, 22, GB1019. DOI: 10.1029/2007GB003039.

Kamphus, M., M. Ettner-Mahl, T. Klimach, F. Drewnick, L. Keller, D. J. Cziczo, S. Mertes, S. Borrmann, and J. Curtius (2010). "Chemical composition of ambient aerosol, ice residues and cloud droplet residues in mixed-phase clouds: Single particle analysis during the cloud and aerosol characterization experiment (CLACE 6)." *Atmospheric Chemistry and Physics*, 10, pp. 8077–8095. DOI: 10.5194/acp-10-8077-2010.

Karl, M., C. Leck, E. Coz, and J. Heintzenberg (2013). "Marine nanogels as a source of atmospheric nanoparticles in the high Arctic." *Geophysical Research Letters*, 40, pp. 3738–3743. DOI: 10.1002/grl.50661.

Karlsson, L., R. Krejci, M. Koike, K. Ebell, and P. Zieger (2021). "A long-term study of cloud residuals from low-level Arctic clouds." *Atmospheric Chemistry and Physics*, 21, pp. 8933–8959. DOI: 10.5194/acp-21-8933-2021.

Kawamura, K., K. Ono, E. Tachibana, B. Charriére, and R. Sempéré (2012). "Distributions of low molecular weight dicarboxylic acids, ketoacids and α-dicarbonyls in the marine aerosols collected over the Arctic Ocean during late summer." *Biogeosciences*, 9, pp. 4725–4737. DOI: 10.5194/bg-9-4725-2012.

Kawamura, K., H. Kasukabe, and L. A. Barrie (1996). "Source and reaction pathways of dicarboxylic acids, ketoacids and dicarbonyls in arctic aerosols: One year of observations." *Atmospheric Environment*, 30, pp. 1709–1722. DOI: 10.1016/1352-2310(95)00395-9.

Kawamura, K., H. Kasukabe, and L. A. Barrie (2010). "Secondary formation of water-soluble organic acids and α -dicarbonyls and their contributions to total carbon and water-soluble organic carbon: Photochemical aging of organic aerosols in the Arctic spring." *Journal of Geophysical Research*, 115, p. D21306. DOI: 10.1029/2010JD014299.

Kecorius, S. et al. (2019). "New particle formation and its effect on cloud condensation nuclei abundance in the summer Arctic: a case study in the Fram Strait and Barents Sea." *Atmospheric Chemistry and Physics*, 19, pp. 14339–14364. DOI: 10.5194/acp-19-14339-2019.

Kerminen, V.-M., K. Teinilä, R. Hillamo, and T. Mäkelä (1999). "Size-segregated chemistry of particulate dicarboxylic acids in the Arctic atmosphere." *Atmospheric Environment*, 33, pp. 2089–2100. DOI: 10.1016/S1352-2310(98)00350-1.

Kim, M. J., G. A. Novak, M. C. Zoerb, M. Yang, B. W. Blomquist, B. J. Huebert, C. D. Cappa, and T. H. Bertram (2017). "Air-Sea exchange of biogenic volatile organic compounds and the impact on aerosol particle size distributions." *Geophysical Research Letters*, 44, pp. 3887–3896. DOI: 10.1002/2017GL072975.

Kirpes, R. M., A. L. Bondy, D. Bonanno, R. C. Moffet, B. Wang, A. Laskin, A. P. Ault, and K. A. Pratt (2018). "Secondary sulfate is internally mixed with sea spray aerosol and organic aerosol in the winter Arctic." *Atmospheric Chemistry and Physics*, 18, pp. 3937–3949. DOI: 10.5194/acp-18-3937-2018.

Klimach, T. (2012). "Chemische Zusammensetzung der Aerosole : Design und Datenauswertung eines Einzelpartikel-Laserablationsmassenspektrometers." PhD Thesis. Johannes Gutenberg-University, Mainz. DOI: 10.25358/openscience-4386.

Klonecki, A., P. Hess, L. Emmons, L. Smith, J. Orlando, and D. Blake (2003). "Seasonal changes in the transport of pollutants into the Arctic troposphere-model study." *Journal of Geophysical Research D: Atmospheres*, 108, pp. 15–1. DOI: 10.1029/2002JD002199.

Knudsen, E. M. et al. (2018). "Meteorological conditions during the ACLOUD/-PASCAL field campaign near Svalbard in early summer 2017." *Atmospheric Chemistry and Physics*, 18, pp. 17995–18022. DOI: 10.5194/acp-18-17995-2018.

Köllner, F. (2020). "Aerosol Particles in the Summertime Arctic Lower Troposphere: Chemical Composition, Sources , and Formation." PhD Thesis. Johannes Gutenberg-University, Mainz. DOI: 10.25358/openscience-2680.

Köllner, F., J. Schneider, M. D. Willis, T. Klimach, F. Helleis, H. Bozem, D. Kunkel, P. Hoor, J. Burkart, W. R. Leaitch, A. A. Aliabadi, J. P. D. Abbatt, A. B. Herber, and S. Borrmann (2017). "Particulate trimethylamine in the summertime Canadian high Arctic lower troposphere." *Atmospheric Chemistry and Physics*, 17, pp. 13747–13766. DOI: 10.5194/acp-17-13747-2017.

Köllner, F., J. Schneider, M. D. Willis, H. Schulz, D. Kunkel, H. Bozem, P. Hoor, T. Klimach, F. Helleis, J. Burkart, W. R. Leaitch, A. A. Aliabadi, J. P. D. Abbatt, A. B. Herber, and S. Borrmann (2021). "Chemical composition and

source attribution of sub-micrometre aerosol particles in the summertime Arctic lower troposphere." *Atmospheric Chemistry and Physics*, 21, pp. 6509–6539. DOI: 10.5194/acp-21-6509-2021.

Kondo, Y et al. (2011). "Emissions of black carbon, organic, and inorganic aerosols from biomass burning in North America and Asia in 2008." *Journal of Geophysical Research*, 116, p. D08204. DOI: 10.1029/2010JD015152.

Korhonen, H., K. S. Carslaw, D. V. Spracklen, D. A. Ridley, and J. Ström (2008). "A global model study of processes controlling aerosol size distributions in the Arctic spring and summer." *Journal of Geophysical Research*, 113, p. D08211. DOI: 10.1029/2007JD009114.

Kramshøj, M., C. N. Albers, T. Holst, R. Holzinger, B. Elberling, and R. Rinnan (2018). "Biogenic volatile release from permafrost thaw is determined by the soil microbial sink." *Nature Communications*, 9, p. 3412. DOI: 10.1038/s41467-018-05824-y.

Kramshøj, M., I. Vedel-Petersen, M. Schollert, Å. Rinnan, J. Nymand, H. Ro-Poulsen, and R. Rinnan (2016). "Large increases in Arctic biogenic volatile emissions are a direct effect of warming." *Nature Geoscience*, 9, pp. 349–352. DOI: 10.1038/ngeo2692.

Kroll, J. H. and J. H. Seinfeld (2008). "Chemistry of secondary organic aerosol: Formation and evolution of low-volatility organics in the atmosphere." *Atmospheric Environment*, 42, pp. 3593–3624. DOI: 10.1016/j.atmosenv.2008.01.003.

Kuhn, T., R. Damoah, A. Bacak, and J. J. Sloan (2010). "Characterising aerosol transport into the Canadian High Arctic using aerosol mass spectrometry and Lagrangian modelling." *Atmospheric Chemistry and Physics*, 10, pp. 10489–10502. DOI: 10.5194/acp-10-10489-2010.

Kulmala, M., H. Vehkamäki, T. Petäjä, M. Dal Maso, A. Lauri, V.-M. Kerminen, W. Birmili, and P. McMurry (2004). "Formation and growth rates of ultrafine atmospheric particles: a review of observations." *Journal of Aerosol Science*, 35, pp. 143–176. DOI: 10.1016/j.jaerosci.2003.10.003.

Kulmala, M., L. Pirjola, and J. M. Mäkelä (2000). "Stable sulphate clusters as a source of new atmospheric particles." *Nature*, 404, pp. 66–69. DOI: 10.1038/35003550.

Kürten, A., A. Bergen, M. Heinritzi, M. Leiminger, V. Lorenz, F. Piel, M. Simon, R. Sitals, A. C. Wagner, and J. Curtius (2016). "Observation of new particle formation and measurement of sulfuric acid, ammonia, amines and highly oxidized organic molecules at a rural site in central Germany." *Atmospheric Chemistry and Physics*, 16, pp. 12793–12813. DOI: 10.5194/acp-16-12793-2016.

Lampert, A., J. Hartmann, F. Pätzold, L. Lobitz, P. Hecker, K. Kohnert, E. Larmanou, A. Serafimovich, and T. Sachs (2018). "Comparison of Lyman-alpha and LI-COR infrared hygrometers for airborne measurement of turbulent fluctuations of water vapour." *Atmospheric Measurement Techniques*, 11, pp. 2523–2536. DOI: 10.5194/amt-11-2523-2018.

Lance, S. et al. (2011). "Cloud condensation nuclei as a modulator of ice processes in Arctic mixed-phase clouds." *Atmospheric Chemistry and Physics*, 11, pp. 8003–8015. DOI: 10.5194/acp-11-8003-2011.

Lange, R., M. Dall'Osto, H. Skov, J. Nøjgaard, I. Nielsen, D. Beddows, R. Simo, R. Harrison, and A. Massling (2018). "Characterization of distinct Arctic aerosol accumulation modes and their sources." *Atmospheric Environment*, 183, pp. 1–10. DOI: 10.1016/j.atmosenv.2018.03.060.

Lathem, T. L., A. J. Beyersdorf, K. L. Thornhill, E. L. Winstead, M. J. Cubison, A. Hecobian, J. L. Jimenez, R. J. Weber, B. E. Anderson, and A. Nenes (2013). "Analysis of CCN activity of Arctic aerosol and Canadian biomass burning during summer 2008." *Atmospheric Chemistry and Physics*, 13, pp. 2735–2756. DOI: 10.5194/acp-13-2735-2013.

Law, K. S. and A. Stohl (2007). "Arctic air pollution: Origins and impacts." *Science*, 315, pp. 1537–1540. DOI: 10.1126/science.1137695.

Leaitch, W. R., A. Korolev, A. A. Aliabadi, J. Burkart, M. D. Willis, J. P. Abbatt, H. Bozem, P. Hoor, F. Köllner, J. Schneider, A. Herber, C. Konrad, and R. Brauner (2016). "Effects of 20-100nm particles on liquid clouds in the clean summertime Arctic." *Atmospheric Chemistry and Physics*, 16, pp. 11107–11124. DOI: 10.5194/acp-16-11107-2016.

Leaitch, W. R., L. M. Russell, J. Liu, F. Kolonjari, D. Toom, L. Huang, S. Sharma, A. Chivulescu, D. Veber, and W. Zhang (2018). "Organic functional groups in the submicron aerosol at 82.5° N, 62.5° W from 2012 to 2014." *Atmospheric Chemistry and Physics*, 18, pp. 3269–3287. DOI: 10.5194/acp-18-3269-2018.

Leaitch, W. R., S. Sharma, L. Huang, D. Toom-Sauntry, A. Chivulescu, A. M. Macdonald, K. Von Salzen, J. R. Pierce, A. K. Bertram, J. C. Schroder, N. C. Shantz, R. Y. Chang, and A. L. Norman (2013). "Dimethyl sulfide control of the clean summertime Arctic aerosol and cloud." *Elementa*, 1, pp. 1–12. DOI: 10.12952/journal.elementa.000017.

Leck, C. and E. Svensson (2015). "Importance of aerosol composition and mixing state for cloud droplet activation over the Arctic pack ice in summer." *Atmospheric Chemistry and Physics*, 15, pp. 2545–2568. DOI: 10.5194/acp-15-2545-2015.

Lee, S.-H. (2003). "Nitrate and oxidized organic ions in single particle mass spectra during the 1999 Atlanta Supersite Project." *Journal of Geophysical Research*, 108, p. 8417. DOI: 10.1029/2001JD001455.

Leng, C. B., J. E. Roberts, G. Zeng, Y. H. Zhang, and Y. Liu (2015a). "Effects of temperature, pH, and ionic strength on the Henry's law constant of triethylamine." *Geophysical Research Letters*, 42, pp. 3569–3575. DOI: 10.1002/2015GL063840.

Leng, C., J. D. Kish, J. E. Roberts, I. Dwebi, N. Chon, and Y. Liu (2015b). "Temperature-Dependent Henry's Law Constants of Atmospheric Amines." *The Journal of Physical Chemistry A*, 119, pp. 8884–8891. DOI: 10.1021/acs.jpca.5b05174.

Levasseur, M. (2013). "Impact of Arctic meltdown on the microbial cycling of sulphur." *Nature Geoscience*, 6, pp. 691–700. DOI: 10.1038/ngeo1910.

Li, Z., K.-M. Xu, and A. Cheng (2017). "The Response of Simulated Arctic Mixed-Phase Stratocumulus to Sea Ice Cover Variability in the Absence of Large-Scale Advection." *Journal of Geophysical Research: Atmospheres*, 122, pp. 12,335–12,352. DOI: 10.1002/2017JD027086.

Liu, F., X. Bi, G. Zhang, X. Lian, Y. Fu, Y. Yang, Q. Lin, F. Jiang, X. Wang, P. Peng, and G. Sheng (2018). "Gas-to-particle partitioning of atmospheric amines observed at a mountain site in southern China." *Atmospheric Environment*, 195, pp. 1–11. DOI: 10.1016/j.atmosenv.2018.09.038.

Liu, P., P. J. Ziemann, D. B. Kittelson, and P. H. McMurry (1995a). "Generating Particle Beams of Controlled Dimensions and Divergence: I. Theory of Particle Motion in Aerodynamic Lenses and Nozzle Expansions." *Aerosol Science and Technology*, 22, pp. 293–313. DOI: 10.1080/02786829408959748.

Liu, P., P. J. Ziemann, D. B. Kittelson, and P. H. McMurry (1995b). "Generating Particle Beams of Controlled Dimensions and Divergence: II. Experimental Evaluation of Particle Motion in Aerodynamic Lenses and Nozzle Expansions." *Aerosol Science and Technology*, 22, pp. 314–324. DOI: 10.1080/02786829408959749.

Liu, P. S. K., R. Deng, K. A. Smith, L. R. Williams, J. T. Jayne, M. R. Canagaratna, K. Moore, T. B. Onasch, D. R. Worsnop, and T. Deshler (2007). "Transmission Efficiency of an Aerodynamic Focusing Lens System: Comparison of Model Calculations and Laboratory Measurements for the Aerodyne Aerosol Mass Spectrometer." *Aerosol Science and Technology*, 41, pp. 721–733. DOI: 10.1080/02786820701422278.

Liu, Z., H. Chen, Q. Li, J. Sun, L. Wang, X. Yang, H. Xiao, M. Li, and J. Chen (2020). "Size-Resolved Mixing States and Sources of Amine-Containing Particles in the East China Sea." *Journal of Geophysical Research: Atmospheres*, 125, pp. 1–15. DOI: 10.1029/2020JD033162.

Lutsch, E., E. Dammers, S. Conway, and K. Strong (2016). "Long-range transport of NH3, CO, HCN, and C2H6 from the 2014 Canadian Wildfires." *Geophysical Research Letters*, 43, pp. 8286–8297. DOI: 10.1002/2016GL070114.

Lutsch, E. et al. (2019a). "Unprecedented Atmospheric Ammonia Concentrations Detected in the High Arctic From the 2017 Canadian Wildfires." *Journal of Geophysical Research: Atmospheres*, 124, pp. 8178–8202. DOI: 10.1029/2019JD030419.

Lutsch, E. et al. (2019b). "Unprecedented Atmospheric Ammonia Concentrations Detected in the High Arctic From the 2017 Canadian Wildfires." *Journal of Geophysical Research: Atmospheres*, 124, pp. 8178–8202. DOI: 10.1029/2019jd030419.

Martin, M., R. Y. Chang, B. Sierau, S. Sjogren, E. Swietlicki, J. P. D. Abbatt, C. Leck, and U. Lohmann (2011). "Cloud condensation nuclei closure study on summer arctic aerosol." *Atmospheric Chemistry and Physics*, 11, pp. 11335–11350. DOI: 10.5194/acp-11-11335-2011.

Mason, R. H. et al. (2016). "Size-resolved measurements of ice-nucleating particles at six locations in North America and one in Europe." *Atmospheric Chemistry and Physics*, 16, pp. 1637–1651. DOI: 10.5194/acp-16-1637-2016.

Matsui, H., Y. Kondo, N. Moteki, N. Takegawa, L. K. Sahu, M. Koike, Y. Zhao, H. E. Fuelberg, W. R. Sessions, G. Diskin, B. E. Anderson, D. R. Blake, A. Wisthaler, M. J. Cubison, and J. L. Jimenez (2011a). "Accumulation-mode aerosol number concentrations in the Arctic during the ARCTAS aircraft campaign: Long-range transport of polluted and clean air from the Asian continent." *Journal of Geophysical Research*, 116, p. D20217. DOI: 10.1029/2011JD016189.

Matsui, H., Y. Kondo, N. Moteki, N. Takegawa, L. K. Sahu, Y. Zhao, H. E. Fuelberg, W. R. Sessions, G. Diskin, D. R. Blake, A. Wisthaler, and M. Koike (2011b). "Seasonal variation of the transport of black carbon aerosol from the Asian continent to the Arctic during the ARCTAS aircraft campaign." *Journal of Geophysical Research*, 116, p. D05202. DOI: 10.1029/2010JD015067.

Mauritsen, T., J. Sedlar, M. Tjernström, C. Leck, M. Martin, M. Shupe, S. Sjogren, B. Sierau, P. O. Persson, I. M. Brooks, and E. Swietlicki (2011). "An Arctic CCN-limited cloud-aerosol regime." *Atmospheric Chemistry and Physics*, 11, pp. 165–173. DOI: 10.5194/acp-11-165-2011.

May, N. W., P. K. Quinn, S. M. McNamara, and K. A. Pratt (2016). "Multiyear study of the dependence of sea salt aerosol on wind speed and sea ice conditions in the coastal Arctic." *Journal of Geophysical Research: Atmospheres*, 121, pp. 9208–9219. DOI: 10.1002/2016JD025273.

McCabe, J. R., J. Savarino, B. Alexander, S. Gong, and M. H. Thiemens (2006). "Isotopic constraints on non-photochemical sulfate production in the Arctic winter." *Geophysical Research Letters*, 33, p. L05810. DOI: 10.1029/2005GL025164.

McFarquhar, G. M. et al. (2011). "Indirect and semi-direct aerosol campaign: The impact of arctic aerosols on clouds." *Bulletin of the American Meteorological Society*, 92, pp. 183–201. DOI: 10.1175/2010BAMS2935.1.

Megaw, W. and H. Flyger (1973). "Measurement of the background atmospheric aerosol." *Journal of Aerosol Science*, 4, pp. 179–181. DOI: 10.1016/0021-8502(73)90069-4.

Mertes, S., F. Schröder, and A. Wiedensohler (1995). "The Particle Detection Efficiency Curve of the TSI-3010 CPC as a Function of the Temperature Difference between Saturator and Condenser." *Aerosol Science and Technology*, 23, pp. 257–261. DOI: 10.1080/02786829508965310.

Mertes, S., U. Kästner, and A. Macke (2019). "Airborne in-situ measurements of the aerosol absorption coefficient, aerosol particle number concentration and size distribution of cloud particle residuals and ambient aerosol particles during the ACLOUD campaign in May and June 2017". data set. Leibniz-Institut für Troposphärenforschung e.V., Leipzig. DOI: 10.1594/PANGAEA.900403.

Mioche, G., O. Jourdan, M. Ceccaldi, and J. Delanoë (2015). "Variability of mixed-phase clouds in the Arctic with a focus on the Svalbard region: a study based on spaceborne active remote sensing." *Atmospheric Chemistry and Physics*, 15, pp. 2445–2461. DOI: 10.5194/acp-15-2445-2015.

Molleker, S., F. Helleis, T. Klimach, O. Appel, H.-C. Clemen, A. Dragoneas, C. Gurk, A. Hünig, F. Köllner, F. Rubach, C. Schulz, J. Schneider, and S. Borrmann (2020). "Application of an O-ring pinch device as a constant-pressure inlet (CPI) for airborne sampling." *Atmospheric Measurement Techniques*, 13, pp. 3651–3660. DOI: 10.5194/amt-13-3651-2020.

Moore, R. H., R. Bahreini, C. A. Brock, K. D. Froyd, J. Cozic, J. S. Holloway, A. M. Middlebrook, D. M. Murphy, and A. Nenes (2011). "Hygroscopicity and composition of Alaskan Arctic CCN during April 2008." *Atmospheric Chemistry and Physics*, 11, pp. 11807–11825. DOI: 10.5194/acp-11-11807-2011.

Moore, R. H. et al. (2021). "Sizing response of the Ultra-High Sensitivity Aerosol Spectrometer (UHSAS) and Laser Aerosol Spectrometer (LAS) to changes in submicron aerosol composition and refractive index." *Atmospheric Measurement Techniques*, 14, pp. 4517–4542. DOI: 10.5194/amt-14-4517-2021.

Morrison, H., G. de Boer, G. Feingold, J. Harrington, M. D. Shupe, and K. Sulia (2012). "Resilience of persistent Arctic mixed-phase clouds." *Nature Geoscience*, 5, pp. 11–17. DOI: 10.1038/ngeo1332.

Morrison, H., J. O. Pinto, J. A. Curry, and G. M. McFarquhar (2008). "Sensitivity of modeled arctic mixed-phase stratocumulus to cloud condensation and ice nuclei over regionally varying surface conditions." *Journal of Geophysical Research: Atmospheres*, 113, n/a–n/a. DOI: 10.1029/2007JD008729.

Mungall, E. L., J. P. D. Abbatt, J. J. B. Wentzell, A. K. Y. Lee, J. L. Thomas, M. Blais, M. Gosselin, L. A. Miller, T. Papakyriakou, M. D. Willis, and J. Liggio (2017). "Microlayer source of oxygenated volatile organic compounds in the summertime marine Arctic boundary layer." *Proceedings of the National Academy of Sciences*, 114, pp. 6203–6208. DOI: 10.1073/pnas.1620571114.

Mungall, E. L., B. Croft, M. Lizotte, J. L. Thomas, J. G. Murphy, M. Levasseur, R. V. Martin, J. J. Wentzell, J. Liggio, and J. P. Abbatt (2016). "Dimethyl sulfide in the summertime Arctic atmosphere: Measurements and source sensitivity simulations." *Atmospheric Chemistry and Physics*, 16, pp. 6665–6680. DOI: 10.5194/acp-16-6665-2016.

Murphy, D. M. (2007). "The design of single particle laser mass spectrometers." *Mass Spectrometry Reviews*, 26, pp. 150–165. DOI: 10.1002/mas.20113. arXiv: NIHMS150003.

Murphy, S. M., A Sorooshian, J. H. Kroll, N. L. Ng, P Chhabra, C Tong, J. D. Surratt, E Knipping, R. C. Flagan, and J. H. Seinfeld (2007). "Secondary aerosol formation from atmospheric reactions of aliphatic amines." *Atmospheric Chemistry and Physics*, 7, pp. 2313–2337. DOI: 10.5194/acp-7-2313-2007.

NASA (2021). URL: https://firms.modaps.eosdis.nasa.gov/ (visited on 08/30/2021).

Najafi, M. R., F. W. Zwiers, and N. P. Gillett (2015). "Attribution of Arctic temperature change to greenhouse-gas and aerosol influences." *Nature Climate Change*, 5, pp. 246–249. DOI: 10.1038/nclimate2524.

Nguyen, Q. T., M. Glasius, L. L. Sørensen, B. Jensen, H. Skov, W. Birmili, A. Wiedensohler, A. Kristensson, J. K. Nøjgaard, and A. Massling (2016). "Seasonal variation of atmospheric particle number concentrations, new particle formation and atmospheric oxidation capacity at the high Arctic site Villum Research Station, Station Nord." *Atmospheric Chemistry and Physics*, 16, pp. 11319–11336. DOI: 10.5194/acp-16-11319-2016.

Norman, A. L., L. A. Barrie, D. Toom-Sauntry, A. Sirois, H. R. Krouse, S. M. Li, and S. Sharma (1999). "Sources of aerosol sulphate at Alert: Apportionment using stable isotopes." *Journal of Geophysical Research: Atmospheres*, 104, pp. 11619–11631. DOI: 10.1029/1999JD900078.

O'Dowd, C. D. and G. De Leeuw (2007). "Marine aerosol production: A review of the current knowledge." *Philosophical Transactions of the Royal Society A: Mathematical, Physical and Engineering Sciences*, 365, pp. 1753–1774. DOI: 10.1098/rsta.2007.2043.

Ogren, J. A., J. Heintzenberg, and R. J. Charlson (1985). "In-situ sampling of clouds with a droplet to aerosol converter." *Geophysical Research Letters*, 12, pp. 121–124. DOI: 10.1029/GL012i003p00121.

Orellana, M. V., P. A. Matrai, C. Leck, C. D. Rauschenberg, A. M. Lee, and E. Coz (2011). "Marine microgels as a source of cloud condensation nuclei in the high Arctic." *Proceedings of the National Academy of Sciences*, 108, pp. 13612–13617. DOI: 10.1073/pnas.1102457108.

Paris, J.-D., A. Stohl, P. Nédélec, M. Y. Arshinov, M. V. Panchenko, V. P. Shmargunov, K. S. Law, B. D. Belan, and P. Ciais (2009). "Wildfire smoke in the Siberian Arctic in summer: source characterization and plume evolution from airborne measurements." *Atmospheric Chemistry and Physics*, 9, pp. 9315–9327. DOI: 10.5194/acp-9-9315-2009.

Park, K. T., S. Jang, K. Lee, Y. J. Yoon, M. S. Kim, K. Park, H. J. Cho, J. H. Kang, R. Udisti, B. Y. Lee, and K. H. Shin (2017). "Observational evidence for the formation of DMS-derived aerosols during Arctic phytoplankton blooms." *Atmospheric Chemistry and Physics*, 17, pp. 9665–9675. DOI: 10.5194/acp-17-9665-2017.

Park, K.-T., K. Lee, Y.-J. Yoon, H.-W. Lee, H.-C. Kim, B.-Y. Lee, O. Hermansen, T.-W. Kim, and K. Holmén (2013). "Linking atmospheric dimethyl sulfide and the Arctic Ocean spring bloom." *Geophysical Research Letters*, 40, pp. 155–160. DOI: 10.1029/2012GL054560.

Patris, N., R. Delmas, M. Legrand, M. De Angelis, F. A. Ferron, M. Stiévenard, and J. Jouzel (2002). "First sulfur isotope measurements in central Greenland ice cores along the preindustrial and industrial periods." *Journal of Geophysical Research: Atmospheres*, 107, ACH 6–1–ACH 6–11. DOI: 10.1029/2001JD000672.

Pierce, J. R., B. Croft, J. K. Kodros, S. D. D'Andrea, and R. V. Martin (2015). "The importance of interstitial particle scavenging by cloud droplets in shaping the remote aerosol size distribution and global aerosol-climate effects." *Atmospheric Chemistry and Physics*, 15, pp. 6147–6158. DOI: 10.5194/acp-15-6147-2015.

Pithan, F. and T. Mauritsen (2014). "Arctic amplification dominated by temperature feedbacks in contemporary climate models." *Nature Geoscience*, 7, pp. 181–184. DOI: 10.1038/ngeo2071.

Prather, K. A. et al. (2013). "Bringing the ocean into the laboratory to probe the chemical complexity of sea spray aerosol." *Proceedings of the National Academy of Sciences*, 110, pp. 7550–7555. DOI: 10.1073/pnas.1300262110.

Pratt, K. A., L. E. Hatch, and K. A. Prather (2009). "Seasonal volatility dependence of ambient particle phase amines." *Environmental Science and Technology*, 43, pp. 5276–5281. DOI: 10.1021/es803189n.

Pratt, K. A. and K. A. Prather (2010). "Aircraft measurements of vertical profiles of aerosol mixing states." *Journal of Geophysical Research Atmospheres*, 115, pp. 1–10. DOI: 10.1029/2009JD013150.

Prenni, A. J., P. J. Demott, D. C. Rogers, S. M. Kreidenweis, G. M. McFarquhar, G. Zhang, and M. R. Poellot (2009). "Ice nuclei characteristics from M-PACE and their relation to ice formation in clouds." *Tellus B*, 61, pp. 436–448. DOI: 10.1111/j.1600-0889.2009.00415.x.

Quantel (2008). *ICE450 Power Supply-User's Manual*. LUMIBIRD (formerly Quantel-Keopsys group). Lannion, France.

Quennehen, B., A. Schwarzenboeck, A. Matsuki, J. F. Burkhart, A. Stohl, G. Ancellet, and K. S. Law (2012). "Anthropogenic and forest fire pollution aerosol transported to the Arctic: observations from the POLARCAT-France spring campaign." *Atmospheric Chemistry and Physics*, 12, pp. 6437–6454. DOI: 10.5194/acp-12-6437-2012.

Quinn, P. K., T. S. Bates, E. Baum, N. Doubleday, A. M. Fiore, M. Flanner, A. Fridlind, T. J. Garrett, D. Koch, S. Menon, D. Shindell, A. Stohl, and S. G. Warren (2008). "Short-lived pollutants in the Arctic: their climate impact and possible mitigation strategies." *Atmospheric Chemistry and Physics*, 8, pp. 1723–1735. DOI: 10.5194/acp-8-1723-2008.

Quinn, P. K., G. Shaw, E. Andrews, E. G. Dutton, T. Ruoho-Airola, and S. L. Gong (2007). "Arctic haze: current trends and knowledge gaps." *Tellus B: Chemical and Physical Meteorology*, 59, pp. 99–114. DOI: 10.1111/j.1600-0889.2006.00236.x.

Radke, L. F. and P. V. Hobbs (1984). "Airborne observations oFf Arctic Aerosols. III: Orignis And effects of airmasses." *Geophysical Research Letters*, 11, pp. 401–404.

Rahn, K. A., R. D. Borys, and G. E. Shaw (1977). "The Asian source of Arctic haze bands." *Nature*, 268, pp. 713–715. DOI: 10.1038/268713a0.

Rahn, K. A., E. Joranger, A. Semb, and T. J. Conway (1980). "High winter concentrations of SO2 in the norwegian arctic and transport from eurasia." *Nature*, 287, pp. 824–826. DOI: 10.1038/287824a0.

Rahn, K. A. and R. J. McCaffrey (1980). "On the Origin and Transport of the Winter Arctic Aerosol." *Annals of the New York Academy of Sciences*, 338, pp. 486–503. DOI: 10.1111/j.1749-6632.1980.tb17142.x.

Raschke, E., S. Kinne, W. B. Rossow, P. W. Stackhouse, and M. Wild (2016). "Comparison of Radiative Energy Flows in Observational Datasets and Climate Modeling." *Journal of Applied Meteorology and Climatology*, 55, pp. 93–117. DOI: 10.1175/JAMC-D-14-0281.1.

Raso, A. R. W., K. D. Custard, N. W. May, D. Tanner, M. K. Newburn, L. Walker, R. J. Moore, L. G. Huey, L. Alexander, P. B. Shepson, and K. A. Pratt (2017). "Active molecular iodine photochemistry in the Arctic." *Proceedings of the National Academy of Sciences*, 114, pp. 10053–10058. DOI: 10.1073/pnas.1702803114.

Rehbein, P. J. G., C.-H. Jeong, M. L. McGuire, X. Yao, J. C. Corbin, and G. J. Evans (2011). "Cloud and Fog Processing Enhanced Gas-to-Particle Partitioning of Trimethylamine." *Environmental Science & Technology*, 45, pp. 4346–4352. DOI: 10.1021/es1042113.

Reilly, P. T. A., A. C. Lazar, R. A. Gieray, W. B. Whitten, and J. M. Ramsey (2000). "The Elucidation of Charge-Transfer-Induced Matrix Effects in Environmental Aerosols Via Real-Time Aerosol Mass Spectral Analysis of Individual Airborne Particles." *Aerosol Science and Technology*, 33, pp. 135–152. DOI: 10.1080/027868200410895.

Romero-González, R., M. I. Alarcón-Flores, J. L. M. Vidal, and A. G. Frenich (2012). "Simultaneous determination of four biogenic and three volatile amines in anchovy by ultra-high-performance liquid chromatography coupled to tandem mass spectrometry." *Journal of Agricultural and Food Chemistry*, 60, pp. 5324–5329. DOI: 10.1021/jf300853p.

Roth, A., J. Schneider, T. Klimach, S. Mertes, D. van Pinxteren, H. Herrmann, and S. Borrmann (2016). "Aerosol properties, source identification, and cloud processing in orographic clouds measured by single particle mass spectrometry

on a central European mountain site during HCCT-2010." *Atmospheric Chemistry and Physics*, 16, pp. 505–524. DOI: 10.5194/acp-16-505-2016.

Roth, A. (2014). "Untersuchungen von Aerosolpartikeln und Wolkenresidualpartikeln mittels Einzelpartikel-Massenspektrometrie und optischen Methoden." PhD Thesis. Johannes Gutenberg-University, Mainz. DOI: 10.25358/openscience-4273.

Saiz-Lopez, A., C. S. Blaszczak-Boxe, and L. J. Carpenter (2015). "A mechanism for biologically induced iodine emissions from sea ice." *Atmospheric Chemistry and Physics*, 15, pp. 9731–9746. DOI: 10.5194/acp-15-9731-2015.

Scalabrin, E., R. Zangrando, E. Barbaro, N. M. Kehrwald, J. Gabrieli, C. Barbante, and A. Gambaro (2012). "Amino acids in Arctic aerosols." *Atmospheric Chemistry and Physics*, 12, pp. 10453–10463. DOI: 10.5194/acp-12-10453-2012.

Scharffe, D., F. Slemr, C. A. Brenninkmeijer, and A. Zahn (2012). "Carbon monoxide measurements onboard the CARIBIC passenger aircraft using UV resonance fluorescence." *Atmospheric Measurement Techniques*, 5, pp. 1753–1760. DOI: 10.5194/amt-5-1753-2012.

Schill, G. P., K. D. Froyd, H. Bian, A. Kupc, C. Williamson, C. A. Brock, E. Ray, R. S. Hornbrook, A. J. Hills, E. C. Apel, M. Chin, P. R. Colarco, and D. M. Murphy (2020). "Widespread biomass burning smoke throughout the remote troposphere." *Nature Geoscience*, 13, pp. 422–427. DOI: 10.1038/s41561-020-0586-1.

Schmale, J., J. Schneider, G. Ancellet, B. Quennehen, A. Stohl, H. Sodemann, J. F. Burkhart, T. Hamburger, S. R. Arnold, A. Schwarzenboeck, S. Borrmann, and K. S. Law (2011). "Source identification and airborne chemical characterisation of aerosol pollution from long-range transport over Greenland during POLARCAT summer campaign 2008." *Atmospheric Chemistry and Physics*, 11, pp. 10097–10123. DOI: 10.5194/acp-11-10097-2011.

Schmale, J., P. Zieger, and A. M. L. Ekman (2021). "Aerosols in current and future Arctic climate." *Nature Climate Change*, 11, pp. 95–105. DOI: 10.1038/s41558-020-00969-5.

Schmidt, S., J. Schneider, T. Klimach, S. Mertes, L. P. Schenk, P. Kupiszewski, J. Curtius, and S. Borrmann (2017). "Online single particle analysis of ice particle residuals from mountain-top mixed-phase clouds using laboratory

derived particle type assignment." *Atmospheric Chemistry and Physics*, 17, pp. 575–594. DOI: 10.5194/acp-17-575-2017.

Schnaiter, M. and E. Järvinen (2019). "SID-3 1Hz size distribution of cloud particles during the ACLOUD campaign in 2017". data set. Karlsruher Institut für Technologie, Institut für Meteorologie und Klimaforschung, Karlsruhe. DOI: 10.1594/PANGAEA.900261.

Schneider, J., S. Mertes, D. Van Pinxteren, H. Herrmann, and S. Borrmann (2017). "Uptake of nitric acid, ammonia, and organics in orographic clouds: Mass spectrometric analyses of droplet residual and interstitial aerosol particles." *Atmospheric Chemistry and Physics*, 17, pp. 1571–1593. DOI: 10.5194/acp-17-1571-2017.

Schnell, R. C. and W. E. Raatz (1984). "Vertical and horizontal characteristics of Arctic haze during AGASP: Alaskan Arctic." *Geophysical Research Letters*, 11, pp. 369–372.

Schollert, M., S. Burchard, P. Faubert, A. Michelsen, and R. Rinnan (2014). "Biogenic volatile organic compound emissions in four vegetation types in high arctic Greenland." *Polar Biology*, 37, pp. 237–249. DOI: 10.1007/s00300-013-1427-0.

Schroeder, W. and L. Giglio (2021). *NASA VIIRS Land Science Investigator Processing System (SIPS) Visible Infrared Imaging Radiometer Suite (VIIRS) 375 m & 750 m Active Fire Products*. Department of Geographical Sciences, University of Maryland. Maryland, US.

Schroeder, W., P. Oliva, L. Giglio, and I. A. Csiszar (2014). "The New VIIRS 375m active fire detection data product: Algorithm description and initial assessment." *Remote Sensing of Environment*, 143, pp. 85–96. DOI: 10.1016/j.rse.2013.12.008.

Sedlar, J., M. D. Shupe, and M. Tjernström (2012). "On the relationship between thermodynamic structure and cloud top, and its climate significance in the Arctic." *Journal of Climate*, 25, pp. 2374–2393. DOI: 10.1175/JCLI-D-11-00186.1.

Sedlar, J. and M. Tjernström (2009). "Stratiform Cloud—Inversion Characterization During the Arctic Melt Season." *Boundary-Layer Meteorology*, 132, pp. 455–474. DOI: 10.1007/s10546-009-9407-1.

Sedlar, J., M. Tjernström, T. Mauritsen, M. D. Shupe, I. M. Brooks, P. O. G. Persson, C. E. Birch, C. Leck, A. Sirevaag, and M. Nicolaus (2011). "A transitioning Arctic surface energy budget: the impacts of solar zenith angle, surface albedo and cloud radiative forcing." *Climate Dynamics*, 37, pp. 1643–1660. DOI: 10.1007/s00382-010-0937-5.

Seguin, A. M., A.-L. Norman, and L. Barrie (2014). "Evidence of sea ice source in aerosol sulfate loading and size distribution in the Canadian High Arctic from isotopic analysis." *Journal of Geophysical Research: Atmospheres*, 119, pp. 1087–1096. DOI: 10.1002/2013JD020461.

Seibert, P. and A. Frank (2004). "Source-receptor matrix calculation with a Lagrangian particle dispersion model in backward mode." *Atmospheric Chemistry and Physics*, 4, pp. 51–63. DOI: 10.5194/acp-4-51-2004.

Seinfeld, J. H. and S. N. Pandis (2016). *Atmospheric Chemistry and Physics: From Air Pollution to Climate Change, 3rd Edition*. John Wiley Sons. Hoboken, New Jersey.

Serreze, M. C. and R. G. Barry (2011). "Processes and impacts of Arctic amplification: A research synthesis." *Global and Planetary Change*, 77, pp. 85–96. DOI: 10.1016/j.gloplacha.2011.03.004.

Sharma, S., M. Ishizawa, D. Chan, D. Lavoué, E. Andrews, K. Eleftheriadis, and S. Maksyutov (2013). "16-year simulation of Arctic black carbon: Transport, source contribution, and sensitivity analysis on deposition." *Journal of Geophysical Research: Atmospheres*, 118, pp. 943–964. DOI: 10.1029/2012JD017774.

Shaw, G. E. (1984). "Microparticle size spectrum of Arctic haze." *Geophysical Research Letters*, 11, pp. 409–412. DOI: 10.1029/GL011i005p00409.

Shaw, G. E. (1995). "The Arctic Haze Phenomenon." *Bulletin of the American Meteorological Society*, 76, pp. 2403–2413. DOI: 10.1175/1520-0477(1995)076<2403:TAHP>2.0.CO;2.

Shaw, P. M., L. M. Russell, A. Jefferson, and P. K. Quinn (2010). "Arctic organic aerosol measurements show particles from mixed combustion in spring haze and from frost flowers in winter." *Geophysical Research Letters*, 37, n/a–n/a. DOI: 10.1029/2010GL042831.

Shindell, D. T. et al. (2008). "A multi-model assessment of pollution transport to the Arctic." *Atmospheric Chemistry and Physics*, 8, pp. 5353–5372. DOI: 10.5194/acp-8-5353-2008.

Shindell, D. and G. Faluvegi (2009). "Climate response to regional radiative forcing during the twentieth century." *Nature Geoscience*, 2, pp. 294–300. DOI: 10.1038/ngeo473.

Shupe, M. D., P. O. Persson, I. M. Brooks, M. Tjernström, J. Sedlar, T. Mauritsen, S. Sjogren, and C. Leck (2013). "Cloud and boundary layer interactions over the Arctic sea ice in late summer." *Atmospheric Chemistry and Physics*, 13, pp. 9379–9400. DOI: 10.5194/acp-13-9379-2013.

Shupe, M. D. (2011). "Clouds at Arctic Atmospheric Observatories. Part II: Thermodynamic Phase Characteristics." *Journal of Applied Meteorology and Climatology*, 50, pp. 645–661. DOI: 10.1175/2010JAMC2468.1.

Shupe, M. D. and J. M. Intrieri (2004). "Cloud radiative forcing of the Arctic surface: The influence of cloud properties, surface albedo, and solar zenith angle." *Journal of Climate*, 17, pp. 616–628. DOI: 10.1175/1520-0442(2004)017<0616:CRFOTA>2.0.CO;2.

Shupe, M. D., S. Y. Matrosov, and T. Uttal (2006). "Arctic Mixed-Phase Cloud Properties Derived from Surface-Based Sensors at SHEBA." *Journal of the Atmospheric Sciences*, 63, pp. 697–711. DOI: 10.1175/JAS3659.1.

Shupe, M. D., V. P. Walden, E. Eloranta, T. Uttal, J. R. Campbell, S. M. Starkweather, and M. Shiobara (2011). "Clouds at Arctic Atmospheric Observatories. Part I: Occurrence and Macrophysical Properties." *Journal of Applied Meteorology and Climatology*, 50, pp. 626–644. DOI: 10.1175/2010JAMC2467.1.

Si, M., E. Evoy, J. Yun, Y. Xi, S. J. Hanna, A. Chivulescu, K. Rawlings, D. Veber, A. Platt, D. Kunkel, P. Hoor, S. Sharma, W. Richard Leaitch, and A. K. Bertram (2019). "Concentrations, composition, and sources of ice-nucleating particles in the Canadian High Arctic during spring 2016." *Atmospheric Chemistry and Physics*, 19, pp. 3007–3024. DOI: 10.5194/acp-19-3007-2019.

Sierau, B., R. Y. Chang, C. Leck, J. Paatero, and U. Lohmann (2014). "Single-particle characterization of the high-Arctic summertime aerosol." *Atmospheric Chemistry and Physics*, 14, pp. 7409–7430. DOI: 10.5194/acp-14-7409-2014.

Silva, P. J., D.-Y. Liu, C. A. Noble, and K. A. Prather (1999). "Size and Chemical Characterization of Individual Particles Resulting from Biomass Burning of Local Southern California Species." *Environmental Science & Technology*, 33, pp. 3068–3076. DOI: 10.1021/es980544p.

Silva, P. J. and K. A. Prather (2000). "Interpretation of mass spectra from organic compounds in aerosol time-of-flight mass spectrometry." *Analytical Chemistry*, 72, pp. 3553–3562.

Sipilä, M. et al. (2016). "Molecular-scale evidence of aerosol particle formation via sequential addition of HIO3." *Nature*, 537, pp. 532–534. DOI: 10.1038/nature19314.

Smith, S. J., H. Pitcher, and T. Wigley (2001). "Global and regional anthropogenic sulfur dioxide emissions." *Global and Planetary Change*, 29, pp. 99–119. DOI: 10.1016/S0921-8181(00)00057-6.

Sotiropoulou, G., J. Sedlar, M. Tjernström, M. D. Shupe, I. M. Brooks, and P. O. G. Persson (2014). "The thermodynamic structure of summer Arctic stratocumulus and the dynamic coupling to the surface." *Atmospheric Chemistry and Physics*, 14, pp. 12573–12592. DOI: 10.5194/acp-14-12573-2014.

Spreen, G., L. Kaleschke, and G. Heygster (2008). "Sea ice remote sensing using AMSR-E 89-GHz channels." *Journal of Geophysical Research: Oceans*, 113. DOI: https://doi.org/10.1029/2005JC003384. eprint: https://agupubs.onlinelibrary.wiley.com/doi/pdf/10.1029/2005JC003384.

Sprenger, M. and H. Wernli (2015). "The LAGRANTO Lagrangian analysis tool - Version 2.0." *Geoscientific Model Development*, 8, pp. 2569–2586. DOI: 10.5194/gmd-8-2569-2015.

Stohl, A. (2006). "Characteristics of atmospheric transport into the Arctic troposphere." *Journal of Geophysical Research Atmospheres*, 111, pp. 1–17. DOI: 10.1029/2005JD006888.

Stohl, A., C. Forster, A. Frank, P. Seibert, and G. Wotawa (2005). "Technical note: The Lagrangian particle dispersion model FLEXPART version 6.2." *Atmospheric Chemistry and Physics*, 5, pp. 2461–2474. DOI: 10.5194/acp-5-2461-2005.

Stohl, A., Z. Klimont, S. Eckhardt, K. Kupiainen, V. P. Shevchenko, V. M. Kopeikin, and A. N. Novigatsky (2013). "Black carbon in the Arctic: the

underestimated role of gas flaring and residential combustion emissions." *Atmospheric Chemistry and Physics*, 13, pp. 8833–8855. DOI: 10.5194/acp-13-8833-2013.

Stohl, A. et al. (2007). "Arctic smoke - Record high air pollution levels in the European Arctic due to agricultural fires in Eastern Europe in spring 2006." *Atmospheric Chemistry and Physics*, 7, pp. 511–534. DOI: 10.5194/acp-7-511-2007.

Stone, R. S., G. P. Anderson, E. Andrews, E. G. Dutton, E. P. Shettle, and A. Berk (2007). "Incursions and radiative impact of Asian dust in northern Alaska." *Geophysical Research Letters*, 34, p. L14815. DOI: 10.1029/2007GL029878.

Stroeve, J. C., M. C. Serreze, M. M. Holland, J. E. Kay, J. Malanik, and A. P. Barrett (2012). "The Arctic's rapidly shrinking sea ice cover: A research synthesis." *Climatic Change*, 110, pp. 1005–1027. DOI: 10.1007/s10584-011-0101-1.

Ström, J., A.-C. Engvall, F. Delbart, R. Krejci, and R. Treffeisen (2009). "On small particles in the Arctic summer boundary layer: observations at two different heights near Ny-Ålesund, Svalbard." *Tellus B*, 61, pp. 473–482. DOI: 10.1111/j.1600-0889.2008.00412.x.

Sullivan, R. C. and K. A. Prather (2005). "Recent Advances in Our Understanding of Atmospheric Chemistry and Climate Made Possible by On-Line Aerosol Analysis Instrumentation." *Analytical Chemistry*, 77, pp. 3861–3886. DOI: 10.1021/ac050716i.

Sullivan, R. C. and K. A. Prather (2007). "Investigations of the Diurnal Cycle and Mixing State of Oxalic Acid in Individual Particles in Asian Aerosol Outflow." *Environmental Science & Technology*, 41, pp. 8062–8069. DOI: 10.1021/es071134g.

Sultana, C. M., D. B. Collins, and K. A. Prather (2017). "Effect of Structural Heterogeneity in Chemical Composition on Online Single-Particle Mass Spectrometry Analysis of Sea Spray Aerosol Particles." *Environmental Science & Technology*, 51, pp. 3660–3668. DOI: 10.1021/acs.est.6b06399.

Thomas, J. L., J.-C. Raut, K. S. Law, L. Marelle, G. Ancellet, F. Ravetta, J. D. Fast, G. Pfister, L. K. Emmons, G. S. Diskin, A. Weinheimer, A. Roiger, and H. Schlager (2013). "Pollution transport from North America to Greenland

during summer 2008." *Atmospheric Chemistry and Physics*, 13, pp. 3825–3848. DOI: 10.5194/acp-13-3825-2013.

Tilgner, A., Z. Majdik, A. Sehili, M. Simmel, R. Wolke, and H. Herrmann (2005). "SPACCIM: Simulations of the multiphase chemistry occurring in the FEBUKO hill cap cloud experiments." *Atmospheric Environment*, 39, pp. 4389–4401. DOI: 10.1016/j.atmosenv.2005.02.028.

Tjernström, M. et al. (2014). "The Arctic Summer Cloud Ocean Study (ASCOS): overview and experimental design." *Atmospheric Chemistry and Physics*, 14, pp. 2823–2869. DOI: 10.5194/acp-14-2823-2014.

Tolocka, M. P., D. A. Lake, M. V. Johnston, and A. S. Wexler (2004). "Number concentrations of fine and ultrafine particles containing metals." *Atmospheric Environment*, 38, pp. 3263–3273. DOI: 10.1016/j.atmosenv.2004.03.010.

Tunved, P., J. Ström, and R. Krejci (2013). "Arctic aerosol life cycle: Linking aerosol size distributions observed between 2000 and 2010 with air mass transport and precipitation at Zeppelin station, Ny-Ålesund, Svalbard." *Atmospheric Chemistry and Physics*, 13, pp. 3643–3660. DOI: 10.5194/acp-13-3643-2013.

Val Martin, M., R. Kahn, and M. Tosca (2018). "A Global Analysis of Wildfire Smoke Injection Heights Derived from Space-Based Multi-Angle Imaging." *Remote Sensing*, 10, p. 1609. DOI: 10.3390/rs10101609.

Van Pinxteren, M., K. W. Fomba, N. Triesch, C. Stolle, O. Wurl, E. Bahlmann, X. Gong, J. Voigtländer, H. Wex, C. Li, B. Grosselin, V. Daële, F. Senf, and D. Van (2019a). "Marine organic matter in the remote environment of the Cape Verde Islands – An introduction and overview to the MarParCloud campaign." *Atmospheric Chemistry and Physics*, pp. 1–63.

Van Pinxteren, M., K. W. Fomba, D. van Pinxteren, N. Triesch, E. H. Hoffmann, C. H. Cree, M. F. Fitzsimons, W. von Tümpling, and H. Herrmann (2019b). "Aliphatic amines at the Cape Verde Atmospheric Observatory: Abundance, origins and sea-air fluxes." *Atmospheric Environment*, 203, pp. 183–195. DOI: 10.1016/j.atmosenv.2019.02.011.

VanCuren, R. A., T. Cahill, J. Burkhart, D. Barnes, Y. Zhao, K. Perry, S. Cliff, and J. McConnell (2012). "Aerosols and their sources at Summit Greenland – First results of continuous size- and time-resolved sampling." *Atmospheric Environment*, 52, pp. 82–97. DOI: 10.1016/j.atmosenv.2011.10.047.

Wendisch, M., M. Brückner, J. Burrows, S. Crewell, K. Dethloff, K. Ebell, C. Lüpkes, A. Macke, J. Notholt, J. Quaas, A. Rinke, and I. Tegen (2017). "Understanding Causes and Effects of Rapid Warming in the Arctic." *Eos*, p. 6. DOI: 10.1029/2017EO064803.

Wendisch, M. et al. (2019). "The arctic cloud puzzle using ACLOUD/PASCAL multiplatform observations to unravel the role of clouds and aerosol particles in arctic amplification." *Bulletin of the American Meteorological Society*, 100, pp. 841–871. DOI: 10.1175/BAMS-D-18-0072.1.

Wentworth, G. R., J. G. Murphy, B. Croft, R. V. Martin, J. R. Pierce, J.-S. Côté, I. Courchesne, J.-É. Tremblay, J. Gagnon, J. L. Thomas, S. Sharma, D. Toom-Sauntry, A. Chivulescu, M. Levasseur, and J. P. D. Abbatt (2016). "Ammonia in the summertime Arctic marine boundary layer: sources, sinks, and implications." *Atmospheric Chemistry and Physics*, 16, pp. 1937–1953. DOI: 10.5194/acp-16-1937-2016.

Wenzel, R. J. and K. A. Prather (2004). "Improvements in ion signal reproducibility obtained using a homogeneous laser beam for on-line laser desorption/ionization of single particles." *Rapid Communications in Mass Spectrometry*, 18, pp. 1525–1533. DOI: 10.1002/rcm.1509.

Wernli, H. and H. C. Davies (1997). "A Lagrangian-based analysis of extratropical cyclones. I: The method and some applications." *Quarterly Journal of the Royal Meteorological Society*, 123, pp. 467–489. DOI: 10.1256/smsqj.53810.

Wex, H. et al. (2019). "Annual variability of ice-nucleating particle concentrations at different Arctic locations." *Atmospheric Chemistry and Physics*, 19, pp. 5293–5311. DOI: 10.5194/acp-19-5293-2019.

Willis, M. D., J. Burkart, J. L. Thomas, F. Köllner, J. Schneider, H. Bozem, P. M. Hoor, A. A. Aliabadi, H. Schulz, A. B. Herber, W. R. Leaitch, and J. P. Abbatt (2016). "Growth of nucleation mode particles in the summertime Arctic: A case study." *Atmospheric Chemistry and Physics*, 16, pp. 7663–7679. DOI: 10.5194/acp-16-7663-2016.

Willis, M. D., F. Köllner, J. Burkart, H. Bozem, J. L. Thomas, J. Schneider, A. A. Aliabadi, P. M. Hoor, H. Schulz, A. B. Herber, W. R. Leaitch, and J. P. Abbatt (2017). "Evidence for marine biogenic influence on summertime Arctic aerosol." *Geophysical Research Letters*, 44, pp. 6460–6470. DOI: 10.1002/2017GL073359.

Willis, M. D., W. R. Leaitch, and J. P. Abbatt (2018). "Processes Controlling the Composition and Abundance of Arctic Aerosol." *Reviews of Geophysics*, 56, pp. 621–671. DOI: 10.1029/2018RG000602.

Wilson, T. W. et al. (2015). "A marine biogenic source of atmospheric ice-nucleating particles." *Nature*, 525, pp. 234–238. DOI: 10.1038/nature14986.

Wylie, D. P. and J. G. Hudson (2002). "Effects of long-range transport and clouds on cloud condensation nuclei in the springtime Arctic." *Journal of Geophysical Research*, 107, p. 4318. DOI: 10.1029/2001JD000759.

Xu, J. W., R. V. Martin, A. Morrow, S. Sharma, L. Huang, W. Richard Leaitch, J. Burkart, H. Schulz, M. Zanatta, M. D. Willis, D. K. Henze, C. J. Lee, A. B. Herber, and J. P. Abbatt (2017). "Source attribution of Arctic black carbon constrained by aircraft and surface measurements." *Atmospheric Chemistry and Physics*, 17, pp. 11971–11989. DOI: 10.5194/acp-17-11971-2017.

Xu, L., L. M. Russell, and S. M. Burrows (2016). "Potential sea salt aerosol sources from frost flowers in the pan-Arctic region." *Journal of Geophysical Research: Atmospheres*, 121, pp. 10,840–10,856. DOI: 10.1002/2015JD024713.

Yang, X., J. A. Pyle, and R. A. Cox (2008). "Sea salt aerosol production and bromine release: Role of snow on sea ice." *Geophysical Research Letters*, 35, pp. 1–5. DOI: 10.1029/2008GL034536.

Zanatta, M., H. Bozem, F. Köllner, J. Schneider, D. Kunkel, P. Hoor, J. de Faria, A. Petzold, U. Bundke, K. Hayden, R. M. Staebler, H. Schulz, and A. B. Herber (2020). "Airborne survey of trace gases and aerosols over the Southern Baltic Sea: from clean marine boundary layer to shipping corridor effect." *Tellus, Series B: Chemical and Physical Meteorology*, 72, pp. 1–24. DOI: 10.1080/16000889.2019.1695349.

Zanatta, M. and A. Herber (2019). "Aircraft measurements of aerosol size distribution in the Arctic during the ACLOUD campaign 2017". data set. Alfred Wegener Institute, Helmholtz Centre for Polar and Marine Research, Bremerhaven. DOI: 10.1594/PANGAEA.900341.

Zelenyuk, A., D. Imre, M. Earle, R. Easter, A. Korolev, R. Leaitch, P. Liu, A. M. Macdonald, M. Ovchinnikov, and W. Strapp (2010). "In Situ Characterization of Cloud Condensation Nuclei, Interstitial, and Background Particles Using the Single Particle Mass Spectrometer, SPLAT II †." *Analytical Chemistry*, 82, pp. 7943–7951. DOI: 10.1021/ac1013892.

Zelinka, M. D., S. A. Klein, K. E. Taylor, T. Andrews, M. J. Webb, J. M. Gregory, and P. M. Forster (2013). "Contributions of Different Cloud Types to Feedbacks and Rapid Adjustments in CMIP5*." *Journal of Climate*, 26, pp. 5007–5027. DOI: 10.1175/JCLI-D-12-00555.1.

Zeppenfeld, S., M. van Pinxteren, M. Hartmann, A. Bracher, F. Stratmann, and H. Herrmann (2019). "Glucose as a Potential Chemical Marker for Ice Nucleating Activity in Arctic Seawater and Melt Pond Samples." *Environmental Science & Technology*, 53, pp. 8747–8756. DOI: 10.1021/acs.est.9b01469.

Zhang, R., A. Khalizov, L. Wang, M. Hu, and W. Xu (2012). "Nucleation and Growth of Nanoparticles in the Atmosphere." *Chemical Reviews*, 112, pp. 1957–2011. DOI: 10.1021/cr2001756.

Zuidema, P., B. Baker, Y. Han, J. Intrieri, J. Key, P. Lawson, S. Matrosov, M. Shupe, R. Stone, and T. Uttal (2005). "An Arctic Springtime Mixed-Phase Cloudy Boundary Layer Observed during SHEBA." *Journal of the Atmospheric Sciences*, 62, pp. 160–176. DOI: 10.1175/JAS-3368.1.

LIST OF FIGURES

LIST OF TABLES

ACRONYMS

ACI	aerosol-cloud interaction
ACLOUD	Arctic CLoud Observations Using airborne measurements during polar Day
AI	standard aerosol inlet
ALABAMA	Aircraft-based Laser ABlation Aerosol MAss spectrometer
AMALi	Airborne Mobile Aerosol Lidar
amm.	ammonium
AWI	Alfred Wegener Institute
BB	biomass burning
BC	black carbon
BL	boundary layer
CAO	cold air outbreak
CCI	cloud capped by inversion
CCN	cloud condensation nuclei
CII	cloud inside the inversion
CDP	Cloud Droplet Probe
CIP	Cloud Imaging Probe
CP	cold period
CPC	Condensation Particle Counter
CPI	constant pressure inlet
CPR	cloud particle residue
CRISP	Concise Retrieval of Information from Single Particles
CVI	counterflow virtual impactor
DCA	dicarboxylic acids

DEA	diethylamine
DMS	dimethyl sulfide
DPA	dipropylamine
EC	elemental carbon
ECMWF	European Centre for Medium-Range Weather Forecast
FLEXPART	FLEXible PARTicle (dispersion model)
INP	ice nucleating particle
iod.	iodine
KIT	Karlsruhe Institute of Technology
LAGRANTO	LAGRangian ANalysis TOol
LaMP	Laboratoire de Météorologie Physique
LYR	Longyearbyen
MSA	methanesulfonic acid
MSOA	marine secondary organic aerosol
NASA	National Aeronautics and Space Administration
NIST	National Institute of Standards and Technology
NOAA	National Oceanic and Atmospheric Administration
NP	neutral period
NPF	new particle formation
n. Canada	northern Canada
nss	non-sea-spray
OC	organic carbon
ODR	orthogonal distance regression
OPC	Optical Particle Counter
PASCAL	Physical feedbacks of Arctic planetary boundary level Sea ice, Cloud and AerosoL
PES	potential emission sensitivity
PMT	photomultiplier tube

pot	potassium
PSI	potential source inventory
PSL	polystyrene latex
s. N. America	southern North America
SID-3	Small Ice Detector Mark 3
sil.	silicate
SLSTR	Sentinel-3 Sea and Land Surface Temperature Radiometer
SML	sea surface microlayer
SOA	secondary organic aerosol
SPMS	single particle mass spectrometer
sulf.	sulfate
TEA	triethylamine
TMA	trimethylamine
TMP	turbo molecular pump
TPA	tripropylamine
TROPOS	Leibniz institute for tropospheric research
UHSAS	Ultra-High Sensitivity Aerosol Spectrometers
UV	ultraviolet
van.	vanadium
VIIRS	Visible Infrared Imaging Radiometer Suite
VOC	volatile organic compounds
WBF	Wegener-Bergeron-Findeisen
WP	warm period

LIST OF SYMBOLS

Symbol	Unit/Value	Description
a	s	m/z calibration coefficient (including shot-to-shot variability)
AE	-	aspiration efficiency of the CVI inlet system
b	s $\mathrm{Da}^{\frac{1}{2}}$	m/z calibration coefficient (including ion flight properties)
C_{coinc}	-	number of particle counts detected by both detection laser stages of the ALABAMA
C_{hits}	-	number of successfully ablated/ionized particles by the ablation laser of the ALABAMA
CE	-	collection efficiency
d_a	nm	aerodynamic diameter
$d_{cut-off}$	μm	cut-off diameter of the CVI inlet system
$\mathrm{d}N/\mathrm{d}\log(d_p)$	cm^{-3}	particle number concentration normalized to logarithmic size bins of d_p
d_{opt}	nm	optical diameter
d_p	nm	particle diameter
d_{va}	nm	vacuum-aerodynamic diameter
DE	-	detection efficiency
EF	-	enrichment factor of the CVI inlet system
f_{ALA}	$\mathrm{cm}^3\ \mathrm{s}^{-1}$	volumetric flow through the ALABAMA instrument
h	m asl.	altitude
h_{cr}	-	relative height inside the cloud
HR	-	hit rate
k	nm	size calibration factor
LWC	$\mathrm{g\ cm}^{-3}$	liquid water content
m/z	Da	ion mass to charge ratio

$N_{>10}$	cm^{-3}	number concentration of particles in the size range between 10 nm and 3 μm
$N_{100-1000}$	cm^{-3}	number concentration of particles in the size range between 100 nm and 1 μm
$N_{250-1600}$	cm^{-3}	number concentration of particles in the size range between 250 and 1600 nm
N_{coinc}	cm^{-3}	number concentration of particles detected by both detection laser stages of the ALABAMA
N_{drop}	cm^{-3}	cloud droplet number concentration
N_{ice}	cm^{-3}	cloud ice particle number concentration
N_{ref}	cm^{-3}	number concentration of particles obtained by a reference instrument
p	hPa	air pressure
PF	-	fraction of the specific particle type
PF_{scaled}	cm^{-3}	particle fraction (PF) of the specific species scaled by the particle number concentration detected by the ALABAMA (N_{coinc})
p_{lens}	hPa	lens pressure
RH	%	relative humidity
SE	-	sampling efficiency
T	°C	temperature
t_{ToF}	s	ion flight time
u	$m\ s^{-1}$	west-east component of the horizontal wind vector
upcount	-	time counter value between the two detection events
v	$m\ s^{-1}$	south-north component of the horizontal wind vector
v_0	$m\ s^{-1}$	gas expansion velocity
v_g	$m\ s^{-1}$	gas velocity after the expansion into the evacuated part of the ALABAMA
v_p	$m\ s^{-1}$	particle velocity
θ	K	potential temperature
λ	nm	(laser) wave length

ν_{Coinc}	s^{-1}	frequency of particle detections by both detection laser stages
ρ_0	$1\,g\,m^{-2}$	standard particle density
ρ_{PSL}	$1.05\,g\,m^{-2}$	PSL density
σ_{CE}^{vert}	-	absolute uncertainty of the vertically-resolved collection efficiency (CE)
σ_{DE}^{vert}	-	absolute uncertainty of the vertically-resolved detection efficiency (DE)
σ_{HR}^{abs}	-	absolute uncertainty of the hit rate (HR)
σ_{HR}^{vert}	-	absolute uncertainty of the vertically-resolved hit rate (HR)
σ_{PF}^{abs}	-	absolute uncertainty of the particle fraction (PF) of the specific particle type
σ_{PF}^{bg}	-	absolute uncertainty of the particle fraction (PF) of the specific particle type related to the background signal definition
σ_{PF}^{bin}	-	absolute uncertainty of the particle fraction (PF) of the specific particle type related to binomial statistics
$\sigma_{PF_{sclaed}}^{abs}$	cm^{-3}	absolute uncertainty of the scaled particle fraction (PF_{scaled}) of the specific particle type
$\sigma_{v_p}^{abs}$	$m\,s^{-1}$	absolute uncertainty of the particle velocity (v_p)
$\sigma_{upcount}^{abs}$	-	absolute uncertainty of time counter value ($upcount$)
χ	-	shape factor
χ_{CO}	ppb_v	volume mixing ratio of CO
χ_{CO_2}	ppm_v	volume mixing ratio of CO_2
χ_{H_2O}	ppm_v	volume mixing ratio of H_2O
χ_{O_3}	ppb_v	volume mixing ratio of O_3

LIST OF PUBLICATIONS

PEER REVIEWED PUBLICATIONS

DeMott, P. J., O. Möhler, D. J. Cziczo, N. Hiranuma, M. D. Petters, S. S. Petters, F. Belosi, H. G. Bingemer, S. D. Brooks, C. Budke, M. Burkert-Kohn, K. N. Collier, A. Danielczok, **O. Eppers**, L. Felgitsch, S. Garimella, H. Grothe, P. Herenz, T. C. J. Hill, K. Höhler, Z. A. Kanji, A. Kiselev, T. Koop, T. B. Kristensen, K. Krüger, G. Kulkarni, E. J. T. Levin, B. J. Murray, A. Nicosia, D. O'Sullivan, A. Peckhaus, M. J. Polen, H. C. Price, N. Reicher, D. A. Rothenberg, Y. Rudich, G. Santachiara, T. Schiebel, J. Schrod, T. M. Seifried, F. Stratmann, R. C. Sullivan, K. J. Suski, M. Szakáll, H. P. Taylor, R. Ullrich, J. Vergara-Temprado, R. Wagner, T. F. Whale, D. Weber, A. Welti, T. W. Wilson, M. J. Wolf, and J. Zenker (2018): "The Fifth International Workshop on Ice Nucleation phase 2 (FIN-02): laboratory intercomparison of ice nucleation measurements." *Atmos. Meas. Tech.*, 11, 6231–6257, DOI: 10.5194/amt-11-6231-2018.

Ehrlich, A., M. Wendisch, C. Lüpkes, M. Buschmann, H. Bozem, D. Chechin, H.-C. Clemen, R. Dupuy, **O. Eppers**, J. Hartmann, A. Herber, E. Jäkel, E. Järvinen, O. Jourdan, U. Kästner, L.-L. Kliesch, F. Köllner, M. Mech, S. Mertes, R. Neuber, E. Ruiz-Donoso, M. Schnaiter, J. Schneider, J. Stapf, and M. Zanatta (2019): A comprehensive in situ and remote sensing data set from the Arctic CLoud Observations Using airborne measurements during polar Day (ACLOUD) campaign. *Earth Syst. Sci. Data*, 11, 1853–1881, DOI: 10.5194/essd-11-1853-2019.

N. Hiranuma, K. Adachi, D. M., Bell, F. Belosi, H. Beydoun, B. Bhaduri, H. Bingemer, C. Budke, H.-C. Clemen, F. Conen, K. M. Cory, J. Curtius, P. J. DeMott, **O. Eppers**, S. Grawe, S. Hartmann, N. Hoffmann, K. Höhler, E. Jantsch, A. Kiselev, T. Koop, G. Kulkarni, A. Mayer, M. Murakami, B. J. Murray, A. Nicosia, M. D. Petters, M. Piazza, M. Polen, N. Reicher, Y. Rudich, A. Saito, G. Santachiara, T. Schiebel, G. P. Schill, J. Schneider, L. Segev, E. Stopelli, R. C. Sullivan, K. Suski, M. Szakáll, T. Tajiri, H. Taylor, Y. Tobo, R. Ullrich, D. Weber, H. Wex, T. F. Whale, C. L. Whiteside, K. Yamashita, A. Zelenyuk, and O. Möhler (2019): "A comprehensive characterization of ice nucleation by three different types of cellulose particles immersed in water." *Atmos. Chem. Phys.*, 19, 4823–4849, DOI: 10.5194/acp-19-4823-2019.

Hartmann, M., K. Adachi, **O. Eppers**, C. Haas, A. Herber, R. Holzinger, A. Hünerbein, E. Jäkel, C. Jentzsch, M. van Pinxteren, H. Wex, S. Willmes and F. Stratmann (2020): "Wintertime airborne measurements of ice nucleating particles in the high Arctic: A hint to a marine, biogenic source for ice nucleating particles." *Geophys. Res. Lett.*, 47, e2020GL087770, DOI: 10.5194/acp-19-4823-2019.

K. Nakoudi, C. Ritter, C. Böckmann, D. Kunkel, **O. Eppers**, V. Rozanov, Mei, L., V. Pefanis, E. Jäkel, A. Herber, M. Maturilli and R. Neuber (2019): "Does the Intra-Arctic Modification of Long-Range Transported Aerosol Affect the Local Radiative Budget? (A Case Study)." *Remote Sensing*, 2020, 12(13):2112, DOI: 10.3390/rs12132112.

Wendisch, M., A. Macke, A. Ehrlich, C. Lüpkes, M. Mech, D. Chechin, K. Dethloff, C. B. Velasco, H. Bozem, M. Brückner, H. Clemen, S. Crewell, T. Donth, R. Dupuy, K. Ebell, U. Egerer, R. Engelmann, C. Engler, **O. Eppers**, M. Gehrmann, X. Gong, M. Gottschalk, C. Gourbeyre, H. Griesche, J. Hartmann, M. Hartmann, M. Heinold, A. Herber, H. Herrmann, G. Heygster, P. Hoor, S. Jafariserajehlou, E. Jäkel, E. Järvinen, O. Jourdan, U. Kästner, S. Kecorius, E. M. Knudsen, F. Köllner, J. Kretzschmar, L. Lelli, D. Leroy, M. Maturilli, L. Mei, S. Mertes, G. Mioche, R. Neuber, M. Nicolaus, T. Nomokonova, J. Notholt, M. Palm, M. van Pinxteren, J. Quaas, P. Richter, E. Ruiz-Donoso, M. Schäfer, K. Schmieder, M. Schnaiter, J. Schneider, A. Schwarzenböck, P. Seifert, M. D. Shupe, H. Siebert, G. Spreen, J. Stapf, F. Stratmann, T. Vogl, A. Welti, H. Wex, A. Wiedensohler, M. Zanatta and S. Zeppenfeld (2019): "The Arctic Cloud Puzzle: Using ACLOUD/PASCAL Multiplatform Observations to Unravel the Role of Clouds and Aerosol Particles in Arctic Amplification." *Bull. Am. Meteorol. Soc.*, 100(5), 841-871, DOI: 10.1175/BAMS-D-18-0072.1.

Schneider, J., R. Weigel, T. Klimach, A. Dragoneas, O. Appel, A. Hünig, S. Molleker, F. Köllner, H.-C. Clemen, **O. Eppers**, P. Hoppe, P. Hoor, Mahnke, C., M. Krämer, C. Rolf, J.-U. Grooß, A. Zahn, F. Obersteiner, F. Ravegnani, A. Ulanovsky, H. Schlager, M. Scheibe, G. S. Diskin, J. P. DiGangi, J. B. Nowak, M. Zöger, and S. Borrmann (2021): "Aircraft-based observation of meteoric material in lower-stratospheric aerosol particles between 15 and 68°N." *Atmos. Chem. Phys.*, 21, 989–1013, DOI: 10.5194/acp-21-989-2021.

Zanatta, M., A. Herber, Z. Jurányi, **O. Eppers**, J. Schneider and J. P. Schwarz (2021): "Technical note: Sea salt interference with black carbon quantification in snow samples using the single particle soot photometer." *Atmos. Chem. Phys.*, 21, 9329–9342, DOI: 10.5194/acp-21-9329-2021.

PUBLICATIONS UNDER REVIEW

Ohata, S., M. Koike, A. Yoshida, N. Moteki, K. Adachi, N. Oshima, H. Matsui, **O. Eppers**, H. Bozem, M. Zanatta, and A. B. Herber (2021): "Arctic black carbon during PAMARCMiP 2018 and previous aircraft experiments in spring." *Atmos. Chem. Phys. Discuss.*, DOI: 10.5194/10.5194/acp-2021-349, in review.

FIRST AUTHOR CONFERENCE CONTRIBUTIONS

Eppers. O, F. Köllner, H.-C. Clemen, H. Bozem, S. Mertes, D. Kunkel, J. Schneider, P. Hoor and S. Borrmann (2018): "Single particle mass spectrometry of Arctic ambient aerosol and cloud residuals during ACLOUD." poster presentation, *POLAR 2018 – SCAR/IASC Open Science Conference*, Davos, Switzerland, June 15-26, 2018.

Eppers. O, F. Köllner, H.-C. Clemen, H. Bozem, S. Mertes, E. Järvinen, J. Schneider, P. Hoor and S. Borrmann (2018): "Chemical identification of different aerosol species in summertime Arctic clouds and ambient air". poster presentation, 2nd $(AC)^3$ Science Conference, Bremerhaven, Germany, November 12-14, 2018.

Eppers. O, J. Schneider, F. Köllner, H.-C. Clemen, H. Bozem, S. Mertes, D. Kunkel, P. Hoor and S. Borrmann (2019): "Aircraft-based single particle analysis of cloud residuals and aerosol particles in the summertime Arctic." oral presentation, *European Geoscience Union General Assembly*, Vienna, Austria, April 7-12, 2019.

Eppers. O, F. Köllner, H.-C. Clemen, J. Schneider, H. Bozem, S. Mertes, D. Kunkel, P. Hoor and S. Borrmann (2020): "Abundance of amines in residual particles from Arctic clouds – Results from aircraft-based single particle mass spectrometry." poster presentation, *European Aerosol Conference*, Aachen, Germany, August 31- 4 September, 2020.

CONTRIBUTIONS TO THIS STUDY

This study was supported by the valuable contributions of colleagues that are acknowledged here.

In Chapter 2, experiments were carried out by myself, Franziska Köllner and Hans-Christian Clemen, with critical feedback from Johannes Schneider. I operated the ALABAMA, the OPC and the trace gas instruments during different calibration measurements in the laboratory, with critical comments from Johannes Schneider, Franziska Köllner, Heiko Bozem and Peter Hoor. Data from the CVI inlet systems, CPC and UHSAS-1 were provided by Stephan Mertes. UHSAS-2 and cloud data sets were downloaded from the data servers by myself. Daniel Kunkel provided the meteorological data sets and the LAGRANTO and FLEXPART output. I analyzed the LAGRANTO and FLEXPART output. Satellite data were downloaded by myself.

In Chapters 3 and 4, Manfred Wendisch and Andreas Herber designed the research project. I operated the ALABAMA and the trace gas instruments onboard the research aircraft, with guidance of Johannes Schneider, Franziska Köllner, Hans-Christian Clemen and Heiko Bozem. Stephan Mertes operated the CVI inlet system, the UHSAS-1 and the CPC. Marco Zanatta and Andreas Herber operated the UHSAS-2 onboard the aircraft. I analyzed the ALABAMA data as well as the trace gas data for CO, CO_2 and O_3 in combination with the other data sets, with critical feedback from Johannes Schneider, Peter Hoor, Franziska Köllner, Hans-Christian Clemen, Heiko Bozem, Daniel Kunkel, Hans-Christoph Lachnitt, Stephan Mertes and Stephan Borrmann.

DANKSAGUNG

An dieser Stelle möchte ich mich bei allen Beteiligten bedanken, die mir bei der Entstehung der vorliegenden Arbeit zur Seite gestanden haben. Ohne die wertvolle Unterstüzung meiner Kolleginnen und Kollegen, meiner Freunde und meiner Familie wäre diese Arbeit nicht zu bewältigen gewesen. Die persönliche Danksagung wurde aus Datenschutzgründen von dieser Version der Dissertation entfernt.

CURRICULUM VITAE

The curriculum vitae is not included in the electronic version.

DECLARATION

I hereby declare that I wrote the dissertation submitted without any unauthorized external assistance and used only sources acknowledged in the work. All textual passages which are appropriated verbatim or paraphrased from published and unpublished texts as well as all information obtained from oral sources are duly indicated and listed in accordance with bibliographical rules. In carrying out this research, I complied with the rules of standard scientific practice as formulated in the statutes of Johannes Gutenberg-University Mainz to insure standard scientific practice.

Mainz, 9. September 2021

Oliver Eppers